A new LHC search channel for a light Higgs boson and associated QCD calculations

Mathieu Rubin

LABORATOIRE DE PHYSIQUE THEORIQUE ET HAUTES ENERGIES

THESE DE DOCTORAT DE L'UPMC

Spécialité: **Physique Théorique**

Présentée par

Mathieu RUBIN

Pour obtenir le grade de

Docteur de l'Université Pierre et Marie Curie

Sujet:

A NEW LHC SEARCH CHANNEL FOR A LIGHT HIGGS BOSON AND ASSOCIATED QCD CALCULATIONS

Soutenue le 21 juin 2010 devant le jury composé de

MM.	Abdelhak DJOUADI,	rapporteur,
	Jean-Philippe GUILLET,	examinateur,
	Fabio MALTONI,	examinateur,
	Vyacheslav RYCHKOV,	examinateur,
	Gavin SALAM,	directeur de thèse,
&	Mike SEYMOUR,	rapporteur.

Abstract

This thesis addresses various topics related to LHC studies and predictions. We were first interested in a boosted ($p_t > 200$ GeV) light Higgs boson at the LHC ($M_H \simeq 120$ GeV) in the $pp \to WH$ and $pp \to ZH$ search channels with $H \to b\bar{b}$. We showed how these challenging channels can be recovered as promising search channels using a subjet analysis procedure in two steps: a "mass-drop" analysis, which allows one to reduce the large QCD backgrounds, and a "filtering" analysis, which improves the resolution on the reconstructed Higgs jet mass. Then we focused on the filtering analysis, which allows one to suppress the diffuse background from the underlying-event and pile-up, which are mainly responsible for the bad Higgs mass resolution. We optimised its parameters using semi-analytical calculations which led us to examine the structure of the non-global logarithms that appear in this problem. Finally, we studied some processes whose perturbative series converges poorly at next-to-leading (NLO) order for some observables, a property that we had noticed in the Z+jet and W+jet processes at high-p_t during our Higgs analysis. This is important because it leads to questions about the reliability of the predictions resulting from perturbative calculations. It thus becomes necessary to examine higher-order corrections. The method that we developed, called "LoopSim", consists in approximating these higher-order corrections by merging different orders of perturbation theory such that all infra-red and collinear divergences are cancelled.

Résumé

Cette thèse a pour objet l'étude de divers sujets liés à la physique du LHC et à ses prédictions. Nous nous sommes dans un premier temps intéressés à la recherche au LHC d'un boson de Higgs léger ($M_H \simeq 120$ GeV) et "boosté" ($p_{t,H} > 200$ GeV) dans le canal $pp \to WH$ et $pp \to ZH$ avec $H \to b\bar{b}$. Nous avons montré comment, à partir d'une analyse de la sous-structure des jets en deux étapes respectivement appelées "mass-drop" et "filtering", il est possible de réduire de manière significative les divers fonds (mass-drop) et d'améliorer la résolution en masse lors de la reconstruction du Higgs (filtering). Cela nous a permis de rendre prometteur ce canal de recherche au LHC, longtemps considéré comme trop difficile. A partir de là nous nous sommes concentrés plus particulièrement sur la procédure du "filtering", qui permet de supprimer autant que possible l'effet du bruit diffus que constituent l'underlying-event et le pile-up, en majeur partie responsable de la dégradation de la résolution. Nous avons optimisé ses paramètres à partir d'une analyse semi-analytique, ce qui nous a conduits à l'étude de la structure des "non-global" logarithms qui interviennent lors du calcul de la distribution en masse du Higgs. Finalement, nous nous sommes penchés sur les processus dont la série perturbative présente une mauvaise convergence au next-to-leading (NLO) order pour certaines observables, une caractéristique que nous avions en particulier remarquée pour les processus Z+jet et W+jet à grand p_t lors de notre première étude sur le Higgs. Cet aspect est important car cette mauvaise convergence induit une perte de confiance sur les prédictions résultant des calculs perturbatifs. Il devient donc nécessaire d'examiner les ordres supérieurs, ce que permet de façon approximative un nouvel outil que nous avons élaboré, appelé "LoopSim", qui combine divers ordres de la théorie des perturbations de manière à annuler les divergences molles et collinéaires qui apparaissent inévitablement.

Remerciements

Alors que je suis sur le point de terminer ma thèse, je ne saurais partir sans remercier celles et ceux qui, de près ou de loin, m'ont aidé à la réaliser.

Mes premières pensées vont sans hésiter à mon directeur de thèse, Gavin Salam, qui fut vraiment formidable tout au long de ces (presque) quatre années durant lesquelles j'ai eu la chance de travailler à ses côtés! Il est non seulement un scientifique mondialement reconnu, mais il est aussi un grand pédagogue qui est maintes fois parvenu à me faire comprendre des aspects difficiles de la chromodynamique quantique (et il y en a beaucoup!). Je suis également admiratif de sa grande intuition physique et de la profonde compréhension des intéractions fondamentales qu'il a acquise au cours de ses diverses recherches. Mais par dessus tout, c'est son côté humain qui m'aura marqué. Il a toujours été présent pour moi: pour m'encourager lorsque tout allait bien, pour me soutenir lorsque ça allait moins bien, et de manière générale pour me guider dans mes réflexions. Bref, merci Gavin pour m'avoir permis de vivre cette belle aventure en physique des particules!

Je tiens également à remercier MM Abdelhak Djouadi, Jean-Philippe Guillet, Fabio Maltoni, Slava Rychkov et Mike Seymour d'avoir accepté de faire partie de mon jury de thèse, et en particulier mes deux rapporteurs, Abdelhak Djouadi et Mike Seymour, pour leur lecture attentive de ma thèse, leurs divers commentaires et pour les corrections qu'ils ont apportées à mon manuscrit.

Merci aussi à Jon Butterworth et Adam Davison pour la fructueuse collaboration qui a mené au premier article de ma thèse, ainsi qu'à Mike Paterson qui nous a suivis tout au long de ce très beau projet! Et un grand merci à Sebastian Sapeta avec qui j'ai eu également le plaisir de travailler pour mon dernier article. Sa gentillesse, son sérieux et sa bonne humeur ont aplani bien des difficultés et ont rendu ce travail très agréable!

Mais tout ceci n'aurait été possible sans l'accueil chaleureux du LPTHE et de ses membres à qui je souhaite donc exprimer toute ma gratitude. En particulier merci au directeur Olivier Babelon de m'avoir accepté au sein de ce laboratoire; merci aux secrétaires, notamment Annie Richard, Valérie Sabouraud, Isabelle Nicolaï et Françoise Got qui m'ont guidé dans les méandres parfois obscurs de l'administration; merci à tous ces preux chevaliers de l'informatique qui ont combattu chaque jour pour que le réseau du laboratoire fonctionne du mieux possible! Je pense notamment à Damien Brémont qui fut en outre un grand ami de tous les thésards, mais aussi à Marco Picco, Matteo Cacciari (et Gavin!) qui ont aussi largement contribué à ce dur labeur, et enfin à Lionel Pihery qui a eu la chance(!) d'arriver tout juste pour le déménagement du laboratoire et qui a dû (et doit encore) fournir un très grand effort pour que tout rentre dans l'ordre le plus vite possible. Merci aussi à Bruno Machet avec qui j'ai eu de nombreuses discussions très intéressantes et qui fut très présent tout au long de ma thèse, à Redamy Perez Ramos qui m'a également accompagné durant ma thèse, même de loin, et à Sofian Teber avec qui j'ai eu le plaisir de discuter, notamment pendant les repas de midi!

Cependant, cette thèse aurait perdu une grande partie de sa saveur sans la présence de mes frères d'armes, valeureux combattants de la physique théorique, avec qui j'ai vécu de très beaux moments! Un très grand merci donc à David Andriot, Camille Aron, Solène Chevalier Thery, Quentin Duret, Benoît Estienne, Tiago Fonseca, Joao Gomez, Nicolas Houdeau, Alexis Martin, César Moura, Clément Rousset et Alberto Sicilia qui m'ont accompagné chacun à diverses périodes de ma thèse. Mes pensées vont tout particulièrement à ceux qui furent présents durant ces grands moments des restos thésards et du Cake Challenge qui ont

contribué à nous réunir, sans oublier les fous furieux du Time Challenge, à savoir David, César (le plus fou!), Quentin, Alexis, et moi-même! Une spéciale dédicace à David qui a été contraint de partager le même bureau que moi pendant trois années: merci donc de m'avoir supporté tout ce temps à tes côtés! Mais au final, on se sera bien amusés!

Bien évidemment, je ne peux oublier les courageuses copines des thésards sus-mentionnés qui ont joué le jeu du Cake Challenge et qui nous ont préparé de si bons gateaux! Elles furent toujours de très agréable compagnie et elles nous ont apporté une touche de fraicheur dans cet univers presque exclusivement masculin de la physique théorique! J'exprime en particulier ma reconnaissance à Claire, qui m'a tiré d'une situation délicate en acceptant de préparer l'un de mes gateaux, et à Cécile dont l'aide me fut très précieuse ces derniers temps pour la préparation de mon CV.

Je ne serais jamais parvenu à ce niveau sans les divers enseignants qui, au fil des années, m'ont transmis leur savoir et leur amour de la physique, des mathématiques, et de la philosophie! Je pense en particulier à mes responsables de stage Geoffroy Prévot, Stéphane Nonnenmacher et Nicole Allard, ainsi qu'à mes anciens professeurs Michel Gonnord, Jean-Marie Mercier, Evelyne Camez, Jean-Pierre Brouillet et Gilles Favre. Merci aussi à Claude Aslangul et Claude Delalande qui m'ont donné la chance d'intégrer le magistère de l'ENS Ulm directement en deuxième année.

Pour terminer, je tiens à remercier du fond du coeur ma famille et mes amis qui m'ont tous soutenu du début à la fin de ma thèse, et pour certains même bien avant! Ma plus profonde gratitude revient à mes parents qui, chacun à leur manière, ont été près de moi et par leur amour m'ont aidé à surmonter toutes mes épreuves. Une pensée toute particulière à Pauline, qui m'a beaucoup apporté également, mais qui nous a malheureusement quittés au début de ma thèse. Merci à sa fille Muriel, à Chantal, à Samuel, et à tout le groupe des JPMU pour toutes ces belles rencontres qu'ils ont organisées et tous ces très beaux moments que j'ai eu la chance de vivre à leurs côtés tout au long de ces années. Je tiens aussi à manifester ma gratitude à mon ancienne thérapeute, Josette, qui m'a accompagné sur une partie de ma thèse et m'a vraiment aidé à m'affirmer et à vivre pleinement ma vie! Une tendre pensée pour ma si chère Stéphanie qui est entrée dans mon coeur en cette dernière année de thèse pour mon plus grand bonheur!

Et il y a enfin tous les autres vers qui se tourne mon amour ou mon amitié. Sachez que ce travail vous est également dédié.

Contents

Introduction

During much of the 20^{th} century, considerable effort has been devoted to understanding the three forces that are dominant at infinitesimal length scales, namely electromagnetism, the weak interaction and the strong interaction. Various theoretical developments and experimental results eventually led to the combination of these forces into a single framework, which is a quantum field theory now known as the *Standard Model of particle physics*. It has been widely tested and verified at various colliders and precision experiments, and though some questions remain unanswered, it currently gives very accurate predictions for a huge array of experimental measurements.

The Large Hadron Collider (LHC), which is a 27 kilometer proton-proton collider built roughly 100 meters underground near Geneva, is designed to find the one particle of the Standard Model that has not yet been observed, the so-called Higgs boson, and to probe very small-distance phenomena in order to possibly discover new physics, i.e. phenomena that cannot be explained within the framework of the Standard Model.

In the search for new physics at the LHC, one may want to reconstruct a new massive particle P. In this case, one has to adequately tag the expected decay products of P in order to possibly find it in LHC events. In general, the major issue is to reduce the Standard Model background as much as possible while enhancing the signal for P. This may usually be achieved only if one understands the properties of both the background and the expected signal in order to know how to distinguish them efficiently. New physics may also be seen in differential cross-section measurements as an excess with respect to the Standard Model expectations. In this case, one has to ensure that the observed deviation is really a signal for something new and not, for instance, a manifestation of higher order effects from the Standard Model itself that are not yet accounted for theoretically. Our confidence in a new physics explanation may depend on the accuracy to which we know the Standard Model backgrounds.

This thesis has been concerned with these two different aspects of the search for new physics at the LHC. Chapter 1 gives an introductory review of the basic properties of the Standard Model that are relevant for this work. In the two following chapters, we consider boosted massive particles at the LHC, like the W and the Higgs bosons, and in particular their hadronic decays. In this case, the strong interactions lead to final state configurations in the LHC events that can be difficult to analyse. We thus review some methods to identify them in such a "dirty" environment. Chapter 2 can be seen as an introduction to these concepts, and in chapter 3 we develop a new powerful strategy based on jet substructure that allows one to efficiently reconstruct massive particles decaying hadronically while reducing the large background from strong interactions. We apply it to the case of light Higgs searches at the LHC, where we show how the very challenging WH and ZH production modes can be recovered as promising search channels for a light Higgs. In chapter 4 we semi-analytically

optimize the reconstruction strategy used in the preceding chapter. The calculations are carried out in the leading single-logarithmic large-N_c approximation. Finally, chapter 5 deals with higher order corrections of the Standard Model. Many calculations have already been performed at NLO but only a few are available at NNLO. However, we have found that some processes can be highly enhanced at NLO compared to LO calculations, which raises the question of the reliability of the predictions one makes for these processes at the LHC. Would the NNLO calculation reveal a further large enhancement too? And what about theoretical uncertainties on the calculation? We will present in this chapter a new calculational tool which will help investigate these questions by merging in a novel way different orders of perturbation theory.

Chapter 1

The Standard Model at the LHC

In this introductory chapter, we review the fundamental aspects of the Standard Model that are relevant to understand the various topics and issues that we will address throughout this thesis. Section 1.1 gives a brief overview of the electroweak interactions. We focus more precisely on the electroweak symmetry breaking mechanism, at the origin of the Higgs boson, for which we discuss the current experimental constraints and expectations for the LHC. In section 1.2, we study the theoretical aspects of the strong interaction, which induces the main backgrounds to many LHC searches for new physics. The concept of jets is introduced in section 1.3. Jets are important objects to consider when studying hadronic events in any collider experiment, and they constitute the central part of this thesis. Finally, section 1.4 describes some fundamental non-perturbative aspects of strong interactions relevant for the LHC.

1.1 Electroweak (EW) interactions

There are many very good textbooks that introduce in a pedagogical way the electroweak interactions as well as quantum field theories in general (see for instance [1–5]). Here we summarise the main ideas, useful in the context of this thesis, that constitute the theory of electroweak interactions, but without entering into much detail.

1.1.1 The $SU(2)_L \times U(1)$ theory

With the success of *quantum electrodynamics* (QED), offering a relativistic and quantum description of the interaction between electrons and photons in terms of fields through abelian $U(1)$ symmetry, physicists were led to examine various possibilities of quantum field theories to unify electroweak interactions with electromagnetism. The model which is now known as the *Standard Model of electroweak interactions* was originally proposed by S. L. Glashow in 1961 [6], and later extended by S. Weinberg in 1967 [7] and A. Salam in 1968 [8] who both incorporated the Higgs mechanism (section 1.1.2) into the model. We are going to present its modern formulation.

In 1956, Lee and Yang predicted that parity was violated in weak interactions [9], which was later confirmed by Wu *et al.* [10] in a famous experiment involving β decay. It was then established that only left-handed neutrinos, i.e. neutrinos with negative helicity, are sensitive to weak interaction. These helicity eigenstates are referenced with a subscript L

or R, for instance:

$$\nu_L = \frac{1-\gamma_5}{2}\nu\,, \tag{1.1}$$

$$\nu_R = \frac{1+\gamma_5}{2}\nu\,, \tag{1.2}$$

where the $\{\gamma_{i=0\ldots3}, \gamma_5\}$ are the usual Dirac matrices. Therefore, the simplest idea that was found was to introduce a *weak isospin*, i.e. doublets of $SU(2)_L$, where L serves as a reminder that only left-handed fermions appear in the doublet. We introduce lepton spinors U_L and quark spinors Q_L. For instance:

$$U_L = \begin{pmatrix} \nu_{e_L} \\ e_L^- \end{pmatrix} \quad Q_L = \begin{pmatrix} u_L \\ d_L \end{pmatrix},$$

and similarly for the two other families. The right-handed fermions belong to singlets of $SU(2)$.

The lagrangian $\mathcal{L}_{EW}$ of the electroweak interactions, invariant under the $SU(2)_L \times U(1)$ symmetry which mixes weak and electromagnetic interactions,[1] can then be written in the following form:

$$\mathcal{L}_{EW} = \mathcal{L}_0 + \mathcal{L}_{gauge} + \mathcal{L}_{int} + \mathcal{L}_{EWSB}\,. \tag{1.3}$$

$\mathcal{L}_0$ corresponds to the free propagation of the fields:

$$\mathcal{L}_0 = \bar{U}_L \left(i\partial\!\!\!/\right) U_L + \bar{e}_R \left(i\partial\!\!\!/\right) e_R + \bar{Q}_L \left(i\partial\!\!\!/\right) Q_L + \bar{u}_R \left(i\partial\!\!\!/\right) u_R + \bar{d}_R \left(i\partial\!\!\!/\right) d_R\,, \tag{1.4}$$

where $\partial\!\!\!/ \equiv \gamma^\mu \partial_\mu$. $\mathcal{L}_{gauge}$ corresponds to the gauge bosons' propagation and interactions:

$$\mathcal{L}_{gauge} = -\frac{1}{4} W_i^{\mu\nu} W^i_{\mu\nu} - \frac{1}{4} B_{\mu\nu} B^{\mu\nu}\,, \tag{1.5}$$

where the B and W^i fields are related to the physical photon, $W^\pm$ and Z^0 fields by some simple transformations that we do not describe here (see for instance [2]). We will return to this type of term in the simpler case of strong interactions in section 1.2. $\mathcal{L}_{int}$ concerns the interactions between the fermions and the gauge bosons:

$$\mathcal{L}_{int} = g\left(W^+_\mu J^{\mu+}_W + W^-_\mu J^{\mu-}_W + Z^0_\mu J^\mu_Z\right) + eA_\mu J^\mu_A\,, \tag{1.6}$$

where the vector currents can be expressed in terms of fermions fields as:

$$J^{\mu+}_W = \frac{1}{\sqrt{2}} \left(\bar{\nu}_{e_L} \gamma^\mu e_L + \bar{u}_L \gamma^\mu d_L\right)\,, \tag{1.7}$$

$$J^{\mu-}_W = \frac{1}{\sqrt{2}} \left(\bar{e}_L \gamma^\mu \nu_{e_L} + \bar{d}_L \gamma^\mu u_L\right)\,. \tag{1.8}$$

The constant g is the coupling of the $SU(2)_L$ group, while e is the electromagnetic coupling. The reader is referred to [2] for the other currents. $\mathcal{L}_{EWSB}$ corresponds to the electroweak symmetry breaking that will be explained in section 1.1.2. We only considered the first family in the expression of the Lagrangian, but we can include the two other families in a very similar way. The 3 families are completely independent unless we introduce mixing terms, which is done through the *Cabibbo-Kobayashi-Maskawa* (CKM) matrix, but this goes beyond the scope of this thesis and we will not enter into details here.

[1] We do not discuss the weak hypercharge Y corresponding to the $U(1)$ part of the group because it will be irrelevant for the rest of this thesis.

1.1.2 The Higgs mechanism as a model for electroweak symmetry breaking

The problem with the Lagrangian $\mathcal{L}_0 + \mathcal{L}_{int}$ is the absence of mass terms for the fermions and the gauge bosons. If we take the electron as an example, one could imagine introducing a simple mass term of the form:

$$\begin{aligned} \mathcal{L}_{mass} &= -m_e \bar{e} e \,, \\ &= -m_e (\bar{e}_L e_R + \bar{e}_R e_L) \,. \end{aligned} \tag{1.9}$$

Unfortunately, this term breaks the $SU(2)_L \times U(1)$ symmetry because e_L and e_R belong to different $SU(2)$ representations. But experiments have revealed that almost all particles have a mass. So how can we deal with these two apparent contradictions?

The answer is given in the $\mathcal{L}_{EWSB}$ term. It incorporates the idea of the Higgs mechanism which was proposed in a series of famous papers in 1964 by three different teams [11,12] and also [13] (for a review, see [14]) We introduce a new complex $SU(2)$ doublet field ϕ which couples to the fermions:[2]

$$\mathcal{L}_\phi = -\lambda_e \bar{U}_L \phi e_R + h.c. \,, \tag{1.10}$$

where λ_e is called the *Yukawa coupling* of the electron, with similar terms for the other fermions. The $\mathcal{L}_{EWSB}$ part of the lagrangian can then be written as:

$$\mathcal{L}_{EWSB} = (D_\mu \phi)^\dagger D^\mu \phi + \mathcal{L}_\phi - V(\phi) \,. \tag{1.11}$$

The first term corresponds to the free propagation of the field ϕ and its interaction with the gauge bosons, summarised in the covariant derivative D_μ, that we do not express for brevity. $\mathcal{L}_\phi$ covers the ϕ terms for all the fermions whereas $V(\phi)$ corresponds to the self-coupling of ϕ, which, due to renormalisability constraints, is usually expressed as:

$$V(\phi) = -\mu^2 \phi^\dagger \phi + \lambda \left(\phi^\dagger \phi \right)^2 \,. \tag{1.12}$$

The starting point of the Higgs mechanism is to say that the expectation value of ϕ in the vacuum is a certain value, usually denoted by $\frac{v}{\sqrt{2}}$, different from 0. This is possible if $\mu^2 > 0$ in eq. (1.12), in which case v is given by:

$$v = \sqrt{\frac{\mu^2}{\lambda}} \,. \tag{1.13}$$

The idea is to expand the field ϕ around its ground state:

$$\phi(x) = \begin{pmatrix} 0 \\ \frac{v}{\sqrt{2}} \end{pmatrix} + \frac{1}{\sqrt{2}} U(x) \begin{pmatrix} 0 \\ h(x) \end{pmatrix} , \tag{1.14}$$

where we choose a particular direction around the circle of minima of the potential (fig. 1.1). $h(x)$ is a real field with $\langle h(x) \rangle = 0$ in the vacuum. $U(x)$ is a general $SU(2)$ transformation that allows one to obtain any doublet:

$$U(x) = e^{i \vec{\alpha}(x) . \vec{\sigma}} \,, \tag{1.15}$$

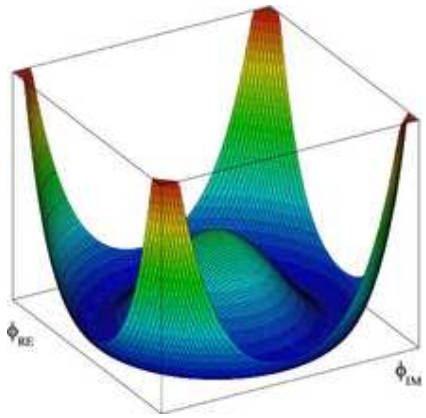

Figure 1.1: The Higgs potential, eq. (1.12), also known as the "Mexican hat". There are an infinite number of minima, all obtained by a simple rotation of the ϕ components from one given equilibrium position.

with $\vec{\alpha}$ a three-dimensional real vector depending on the space-time position x, and $\vec{\sigma}$ corresponds to the usual three Pauli matrices, which form the basis of the $SU(2)$ algebra. With this parametrisation, eq. (1.10) is rewritten as:

$$\mathcal{L}_\phi = -m_e \bar{e}e - \frac{m_e}{v} h\bar{e}e + h.c\,, \tag{1.16}$$

with

$$m_e = \lambda_e \frac{v}{\sqrt{2}}\,, \tag{1.17}$$

and similar terms for quarks. Notice that $U(x)$ was removed by a simple gauge transformation.

Eq. (1.16) introduces 2 important terms. The first one is a mass term for fermions, which was one of the motivations for the Higgs mechanism, and the second one is a coupling term of the fermions to a new field, called the *Higgs field*, corresponding to a new particle. The stronger the coupling λ, the larger the mass of the particle. Expanding the kinetic term in eq. (1.11) also results in mass terms for the W and Z bosons as well as couplings of these bosons to the Higgs. As we started from an explicitly gauge invariant expression (eq. (1.10)), the result of eq. (1.16) is also gauge invariant, contrary to the simple mass term of eq. (1.9). But the gauge invariance is not manifest: it is *hidden* by the non-zero expectation value in the vacuum of the Higgs field. In this case, we say that the $SU(2)_L \times U(1)$ symmetry is *spontaneously broken* into a $U(1)$ symmetry corresponding to electromagnetism.

Concerning the gauge bosons W and Z, they acquire a mass through the term $(D_\mu\phi)^\dagger D^\mu\phi$ in eq. (1.11). It can be written in terms of the fields $h(x)$, $W^\pm$ and Z in the following form [14]:

$$(D_\mu\phi)^\dagger D^\mu\phi = \frac{1}{2}(\partial_\mu h)^2 + M_W^2 W_\mu^+ W^{\mu-} + 2\frac{M_W^2}{v} h W_\mu^+ W^{\mu-} + \frac{1}{2}M_Z^2 Z_\mu Z^\mu + \frac{1}{2}\frac{M_Z^2}{v} h Z_\mu Z^\mu\,, \tag{1.18}$$

[2] *h.c.* means "hermitian conjugate".

where g' is the coupling constant of the $U(1)_Y$ group. The quantities M_W and M_Z are mass terms for the W and Z bosons:

$$M_W = \frac{1}{2} v g \,, \tag{1.19}$$

$$M_Z = \frac{1}{2} v \sqrt{g^2 + g'^2} \,. \tag{1.20}$$

The massive gauge bosons couple to the Higgs field with a strength proportional to their mass squared.

1.1.3 Constraints on the Higgs boson

As eq. (1.16) reveals, giving mass to fermions and gauge bosons implies the existence of a new scalar particle h which couples to fermions via the Yukawa couplings λ_i. Up to now, this particle has never been observed in any collider experiment. It might be worth wondering whether there is a chance that it is observed in a near future for instance at the LHC, or if it might be completely out of reach. For that, we have to know if the Higgs boson should be relatively light ($< \mathcal{O}(1 \text{ TeV})$), or if it must be very massive ($\gg 1$ TeV). The Standard Model does not predict its mass. But some theoretical constraints can be derived, that rely on some assumptions. The most important one concerns WW scattering at high energy. As discussed in [15], if one computes the WW scattering cross-section in perturbation theory taking into account the Higgs coupling with the W, one finds an upper limit on the Higgs mass:

$$M_H < \sqrt{\frac{8\sqrt{2}\pi}{3G_F}} \approx 1 \text{ TeV} \,, \tag{1.21}$$

that comes from the application of the optical theorem. If the Higgs mass is above this limit, this means that *perturbative unitarity* is violated. This is not unitarity itself. The consequence would be that perturbative theory cannot be applied at high energies, i.e. weak interactions become strong. By itself, this is an important motivation to build hadronic colliders running at some TeV scales: At $\mathcal{O}(1 \text{ TeV})$, either we see a Higgs boson, or we see strong interactions of the electroweak bosons, or maybe both, but at least we *ought to* see something new. Another constraint can be derived from the running of the Higgs self-coupling λ [16–20]. On the one hand, if λ is large enough, then it increases with the scale and we do not want to reach the Landau pole before Λ_{NP}, the scale at which new physics appear. One can show that if $\Lambda_{NP} \sim M_{\text{Planck}}$, then $M_H < 175$ GeV, but if $\Lambda_{NP} \sim 1$ TeV, then $M_H \sim 1$ TeV also. On the other hand, if the Higgs boson is light, so if λ is small ($M_H = \sqrt{2\lambda} v$), then λ can become negative because of top loops, leading to an unstable vacuum. To avoid it, the Higgs boson cannot be too light, and more precisely $M_H > 70$ GeV or $M_H > 130$ GeV assuming no new physics respectively below 1 TeV or below the Planck scale. If the vacuum is metastable, then this lower limit is reduced.

There are also experimental constraints. In 2003, from the study of various Higgs production processes, LEP and LEP2 excluded with 95% confidence level a Higgs boson with a mass below 114 GeV [21].[3] Another very important constraint comes from electroweak precision measurements. Indeed, the radiative corrections to some Standard Model quantities, like the W mass, can be computed, which involve the Higgs boson mass as a parameter

[3] Though some studies envisage the possibility of an "hidden Higgs sector" that would still allow it to be lighter than 114 GeV, e.g. [22].

of the result. These expressions can then be fitted to experimental measurements of the related quantities. The current best fit is $M_H = 87^{+35}_{-26}$ GeV with an upper limit of 157 GeV at 95% confidence level [23]. It is also worth noticing that the CDF and D0 experiments at the Tevatron were recently able to exclude a Higgs with a mass between 162 and 166 GeV [24, 25], though a more recent study [26] questions these exclusion limits.

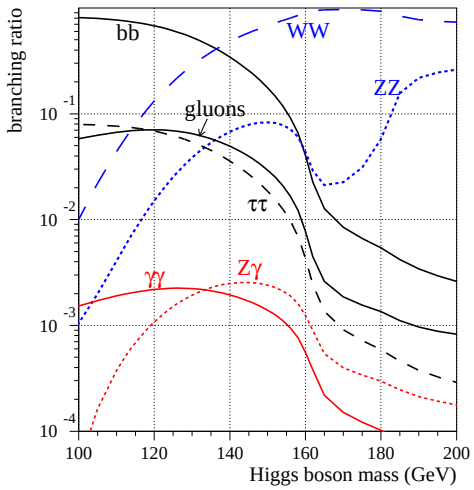

Figure 1.2: The various branching ratios for the Higgs boson depending on its mass computed using HDECAY 2.0 [27] (picture taken from [28]).

Therefore, if the Standard Model Higgs boson exists, it seems that it is light enough to be seen at the current hadronic colliders, either at the Tevatron or at the LHC. Fig. 1.2 shows the computed branching ratios of the Higgs boson as a function of its mass, assumed to be relatively light, between 100 and 200 GeV. However, the current experimental constraints on the Higgs mass M_H favours a Higgs with a mass just above the LEP2 exclusion limit, i.e. around 120 GeV. In this case, the Higgs is not heavy enough to decay into vector bosons. Therefore, it mainly decays into fermions, the most massive of which below this scale is the b quark. It can also decay into $\gamma\gamma$, γZ and gluon-gluon via quantum loops. The Higgs coupling with a fermion is proportional to the fermion's mass (eq. (1.16)), which explains why the branching ratio into $b\bar{b}$ is so important (around 70%). In this thesis, we will be mainly interested in a light Higgs boson, as it is the most probable scenario for a Standard Model Higgs, and we will thus particularly focus on the Higgs decaying into $b\bar{b}$ in order to possibly discover it through this decay channel and also be able to measure its Yukawa coupling λ_b to the b quark.

1.1.4 New physics at the LHC

One has to be aware that the Higgs mechanism formulated in the Standard Model is not the only way that one might find to explain electroweak symmetry breaking, i.e. the possibility for particles to acquire a mass without spoiling gauge invariance. Actually, though theoretically consistent and experimentally very well verified, the Standard Model in its present formulation has some deficiencies (for instance too many free parameters, natural-

ness,...) and some unsolved issues (dark matter, neutrino mass,...) which lead theorists to think about more fundamental theories beyond it. For instance, to explain electroweak symmetry breaking, one can also consider supersymmetric Higgs [29], little Higgs models [30], gauge-Higgs unification scenarios [31, 32] and Higgsless extra-dimension scenarios [33].

With its unprecedented centre of mass energy reach of 14 TeV in proton-proton collisions,[4] the LHC is now the ideal machine to examine the electroweak breaking sector as well as theories beyond the Standard Model in general. However, since the LHC is a hadronic collider operating at high luminosity, one major difficulty that will be encountered in studying LHC events arises from the large importance of strong interactions. For each event, they may produce hundreds of hadrons that make data hard to analyse. Strong interactions, though interesting by themselves, thus also appear as a large background to many LHC studies involving for instance the search for new particles or the measurement of fundamental Standard Model parameters. It is therefore mandatory to control and to understand as well as possible these hadronic backgrounds in order to have a chance to extract any interesting information in the LHC data. The three remaining sections of this chapter will thus describe the theory of strong interactions, emphasising the aspects that will be used throughout this thesis (section 1.2) and that are moreover fundamental in hadronic colliders experiments in general (sections 1.3, 1.4). Some important results derived later in this thesis will show how we can deal with strong interaction issues when reconstructing hadronically decaying boosted massive particles.

1.2 Strong interactions (QCD)

1.2.1 The $SU(3)$ theory of colour

M. Gell-Mann [34] and G. Zweig [35,36] introduced the idea of quarks bound inside hadrons to explain the observed hadron spectrum. But it was soon realised that the 3 quarks in spin-$\frac{3}{2}$ baryons have to be in a completely symmetric state, which is in contradiction with Fermi-Dirac statistics, which imposes the total antisymmetry of the wave-function. To solve this problem, a new degree of freedom was introduced, called *colour*. The minimal number of colours required is 3 in order for the wave function of the 3 quarks to be antisymmetric in the colour indexes. Many experiments have confirmed the hypothesis of 3 colours [37].

The question that arose was to understand how the colour degree of freedom could explain the strong interactions, i.e. the dynamical role of colour. The simplest way to implement it was to consider a new symmetry group $SU(N_c)$, where $N_c = 3$ stands for the number of colours, and to build a quantum field theory based on invariance under local transformations of this symmetry group, as was done for electroweak interactions. This theory was called *quantum chromodynamics* (QCD). The QCD lagrangian, invariant under $SU(3)$, can be written in the following way [38]:[5]

$$\mathcal{L}_{QCD} = -\frac{1}{4} F^A_{\mu\nu} F_A^{\mu\nu} + \sum_j \bar{q}_{j,a} \left(i \not{D} - m_j \right)_{ab} q_{j,b} \,. \tag{1.22}$$

In this expression, the index j refers to the various quark flavours, a, b refer to the $N_c = 3$ quark colours, and A refers to the $N_c^2 - 1 = 8$ colours of the gauge bosons. The form of

[4] Currently 7 TeV, but which should be increased to 14 TeV in the next years.

[5] We do not consider the gauge-fixing and ghost terms in the lagrangian. Although important in general, they will not bring us any insight in the context of this thesis.

the lagrangian is similar to that of the electroweak one, except that we do not include any symmetry breaking term, because $SU(3)$ is seen as an exact symmetry of nature. The first term corresponds to the propagation and self-interactions of the gauge bosons, called *gluons*, with an implicit sum over the $N_c^2 - 1 = 8$ degrees of freedom of the gluon field $\mathcal{A}$:

$$F_{\mu\nu}^A = \partial_\mu \mathcal{A}_\nu^A - \partial_\nu \mathcal{A}_\mu^A - g_s \, f^{ABC} \mathcal{A}_\mu^B \mathcal{A}_\nu^C \, . \tag{1.23}$$

g_s is the coupling constant of the strong interactions, and f^{ABC} corresponds to the structure constants of the group $SU(3)$: if we denote by t^A the 8 matrices generating the $SU(3)$ algebra, then

$$[t^A, t^B] = i f^{ABC} t^C \, . \tag{1.24}$$

The second term of the lagrangian deals with free quark propagation and interactions between quarks and gluons. The important terms are all included in the covariant derivative D of the quark field:[6]

$$D_\mu q = \partial_\mu q + i g_s \, t^A \mathcal{A}_\mu^A q \, . \tag{1.25}$$

The mass term in eq. (1.22) does not break the fundamental symmetry, contrary to the case of electroweak interactions. Though added in QCD as an input, one should be aware that this mass actually comes from the electroweak symmetry breaking mechanism (section 1.1.2).

Let us mention that the lagrangian of eq. (1.22) can be rewritten under the form:

$$\mathcal{L}_{QCD} = \mathcal{L}_0 + \mathcal{L}_{int} \, , \tag{1.26}$$

where $\mathcal{L}_0$ involves the propagation terms of the free fields, and $\mathcal{L}_{int}$ groups all the interaction terms, which are proportional to g_s or g_s^2.

1.2.2 Perturbative QCD

Once the lagrangian is known, the next step is to compute cross-sections, which are the main measurable quantities in particle physics. We usually start from a scattering process involving 2 particles in an initial state $|i\rangle$, and we want to compute the probability to reach a given final state denoted by $|f\rangle$. If these particles are only sensitive to strong interactions, then we have to calculate the following quantity:

$$S_{if} = \langle f | \, T e^{i \int d^4x \mathcal{L}_{int}} \, | i \rangle \ , \tag{1.27}$$

which is the scattering amplitude from state i to state f through strong interactions ($\mathcal{L}_{int}$ was defined in the previous section and T corresponds to the time-ordered product of operators). The ultimate goal is to be able to compute all the elements S_{if} of the so-called *scattering matrix* S, that are the basic quantities that give us access to cross-sections. Unfortunately, we do not know yet how to do such a calculation exactly. We have to resort to approximations, whose main one considers that the coupling constant g_s is small enough so that we can expand the exponential operator in powers of g_s. This is the *perturbative* theory of strong interactions, or perturbative QCD:

$$S_{if} \simeq \delta_{if} + i \int d^4x \, \langle f | \, \mathcal{L}_{int}(x) \, | i \rangle - \frac{1}{2} \int d^4x \, d^4y \, \langle f | \, T \left(\mathcal{L}_{int}(x) \mathcal{L}_{int}(y) \right) | i \rangle + \dots \tag{1.28}$$

[6] This derivative ensures that the lagrangian is invariant under transformations of $SU(3)$.

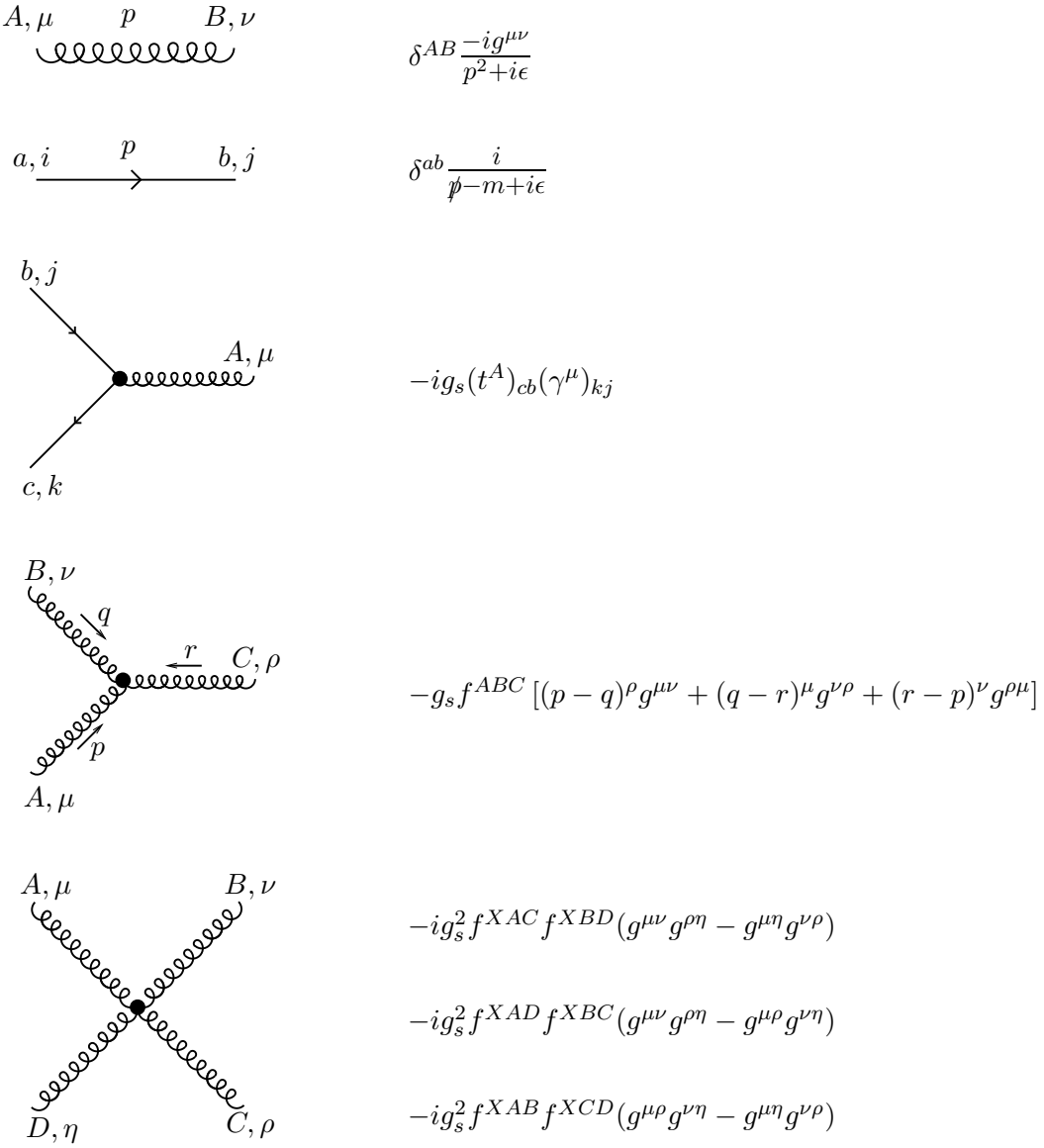

Figure 1.3: Feynman rules for propagators and vertices in QCD where gluons are represented by curly lines and quarks by solid lines. Notice that the gluon's propagator is written in the Feynman gauge, but we do not consider the ghosts that appear in loop diagrams to suppress the unphysical gluon polarizations as we will never use them.

where the remaining (non-written) terms are at least of order $\mathcal{O}(g_s^3)$. To deal with all these terms, Feynman invented a diagrammatic picture of the interactions, where particles propagate along lines and interaction points are represented as vertices of the diagrams. We will not enter the details of how the calculations are implemented in practice because this is done in many textbooks in quantum field theory (see for instance [1–3]) and also because we will use them later in particular cases. We limit ourselves to giving in fig. 1.3 the main Feynman rules for QCD.

In explicit QCD cross-sections calculations, one always has to deal with some colour algebra involving the structure constants or the fundamental matrices of the $SU(3)$ group. As an example, we present in fig. 1.4 some one-loop Feynman diagrams whose colour structure calculation gives the two fundamental constants of the $SU(N_c)$ group, denoted by C_F and C_A. These 2 constants are present in almost every QCD calculation.

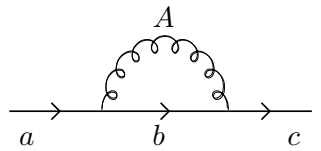

$$\propto t^A_{cb} t^A_{ba} = C_F \delta_{ca},\ C_F = \frac{N_c^2 - 1}{2N_c}$$

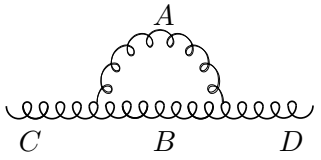

$$\propto f^{ABC} f^{ABD} = C_A \delta^{CD},\ C_A = N_c$$

Figure 1.4: The C_F and C_A constants for a general $SU(N_c)$ group which appear when we apply the Feynman rules of fig. 1.3 at the vertices of the diagrams. Here we only consider the colour structure of the Feynman diagrams, and not their spinor structure.

For the particular QCD case $N_c = 3$, these constants become:

$$C_F = \frac{4}{3}\,, \tag{1.29}$$

$$C_A = 3\,. \tag{1.30}$$

It should be noted that in perturbative QCD the asymptotic states are quarks and gluons, which have never been seen in any collider.[7] But in non-perturbative QCD, which corresponds to solving directly eq. (1.27) without any approximation, the asymptotic states are the hadrons that we observe in nature. We will return to this important point in section 1.4.

1.2.3 Running coupling

When one applies the Feynman rules to loop diagrams like those presented in fig. 1.5 that appear at higher orders in perturbation theory, one has to deal for instance with integrals of the form

$$I^{\mu\nu}(p) \propto \int d^4k \frac{k^\mu k^\nu}{k^2 (k-p)^2}\,, \tag{1.31}$$

[7] Though we have many sources of indirect experimental evidence for their existence.

which correspond to the spinor part of diagram (a) if quarks are supposed massless. One immediately notices that this integral diverges quadratically when k becomes large. To subtract this divergence, one has to *renormalise* the theory, which unavoidably leads to the introduction of a new scale μ, the point where the subtraction procedure is performed. The parameters of the theory, like masses and couplings, then depend on μ. This is the case for the strong coupling α_s, which is defined as:

$$\alpha_s = \frac{g_s^2}{4\pi}\,, \tag{1.32}$$

in analogy with the fine structure constant of QED. However, physical cross-sections should not depend on this unphysical arbitrary scale μ. This would indeed be the case if we could compute them directly from eq. (1.27). However, when carrying out perturbative calculations, the truncation of the perturbative series to a given order introduces a dependence on μ, and the size of this dependence gives an idea of the importance of the neglected higher-order corrections. This will be essential for the last chapter.

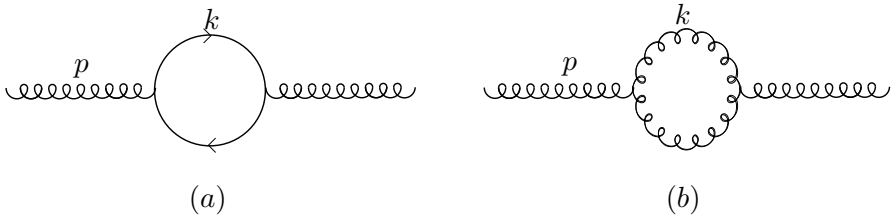

Figure 1.5: Example of one loop diagrams contributing to the β function.

The coupling α_s itself depends on μ, and this dependence is controlled by the β function:

$$\mu^2 \frac{\partial \alpha_s}{\partial \mu^2} = \beta(\alpha_s)\,. \tag{1.33}$$

Fig. 1.5 shows some of the diagrams that contribute to the calculation of the β function at one loop. The result is the following:

$$\beta(\alpha_s) = -\beta_0 \alpha_s^2 + \mathcal{O}(\alpha_s^3)\,, \tag{1.34}$$

with

$$\beta_0 = \frac{11 C_A - 2 n_f}{12\pi}\,, \tag{1.35}$$

where n_f is the number of active light flavours, i.e. the number of quark flavours with masses much smaller than the scale μ at which α_s is computed. Solving eq. (1.34) leads to the evolution of α_s at one loop with respect to a reference scale μ_0:

$$\alpha_s(\mu^2) = \frac{\alpha_s(\mu_0^2)}{1 + \beta_0 \alpha_s(\mu_0^2) \ln \frac{\mu^2}{\mu_0^2}}\,. \tag{1.36}$$

For $n_f \leq 16$ (which is actually the case) one notices that $\beta_0 > 0$ in QCD, so that α_s decreases when μ increases. This means that the strong interactions become weak at small distances,

and are really strong at large distances. This property, called *asymptotic freedom*, seems to be at the heart of *confinement*, i.e. the fact that quarks are bound into hadrons[8] and cannot propagate freely on macroscopic distances. In practical calculations, one usually considers $\mu = Q$, where Q is some characteristic scale of the problem, like the centre of mass energy of the collision. We say that the coupling α_s runs with the scale Q, i.e. α_s is a *running coupling* constant. This property has been verified experimentally (fig. 1.6).

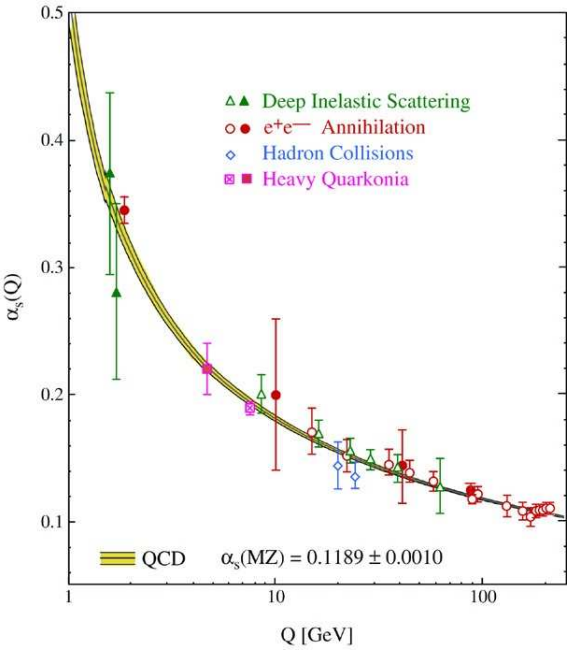

Figure 1.6: The running of the strong coupling α_s, measured by various experiments, and compared to the theoretical expectation (figure taken from [39])

We can rewrite eq. (1.36) as ($\mu = Q$):

$$\alpha_s(Q^2) = \frac{1}{\beta_0 \ln \frac{Q^2}{\Lambda^2}}\,, \tag{1.37}$$

introducing a new parameter Λ. Λ represents the scale at which $\alpha_s(\mu)$ diverges, i.e. when $1 + \beta_0 \alpha_s(\mu_0^2) \ln \frac{\mu^2}{\mu_0^2} = 0$, assuming one could apply perturbation theory at such a scale. This scale is measured to be roughly a couple of hundred MeV:

$$\Lambda \sim 200 \text{ MeV}\,. \tag{1.38}$$

Perturbation theory is valid only when $Q \gg \Lambda$.

1.2.4 Angular ordering

We are now going to derive the very important property of angular ordering [40–44], which we will often use in the following chapters. To explain it, we start with a concrete example

[8] And behave as free particles inside the hadrons.

of a calculation where angular ordering is manifest. Let us assume that we study the Higgs boson decaying into $b\bar{b}$. We have already mentioned this decay in section 1.1.3, which is by far the dominant one if the Higgs has a mass around 115 GeV, and which is also at the heart of various chapters of this thesis. We would like to compute the probability $P(E_0, E_1)$ to emit one gluon with energy E from the $b\bar{b}$ dipole, with E in a given range $[E_0, E_1]$.[9]

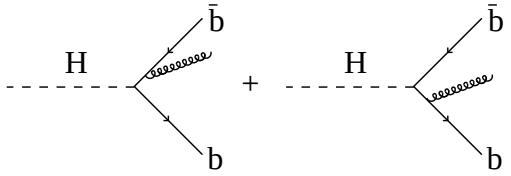

Figure 1.7: Feynman diagrams for Higgs decaying into $b\bar{b}$ and subsequent one-gluon emission from the $b\bar{b}$ dipole.

For that, we first have to sum the 2 amplitudes depicted in fig. 1.7 using the Feynman rules. If the gluon is *soft*, i.e. if its energy is significantly smaller than that of the b quarks, then one can easily show that this amplitude squared can be written [40]:

$$M(k) = 4\pi\alpha_s C_F \frac{2p_b.p_{\bar{b}}}{(p_b.k)(p_{\bar{b}}.k)}\,, \tag{1.39}$$

with p_b, $p_{\bar{b}}$ and k being respectively the momenta of b, $\bar{b}$ and the gluon. From there, the probability $P(E_0, E_1)$ is simply:

$$\begin{aligned} P(E_0, E_1) &= \int \frac{d^3\vec{k}}{(2\pi)^3 2|\vec{k}|} M(k)\Theta(|\vec{k}| - E_0)\Theta(E_1 - |\vec{k}|)\,, \\ &= \frac{\alpha_s C_F}{\pi}\int_{E_0}^{E_1}\frac{d|\vec{k}|}{|\vec{k}|}\int\frac{d^2\Omega}{4\pi}\,\frac{2(b\bar{b})}{(bk)(\bar{b}k)}\,, \\ &= \frac{\alpha_s C_F}{\pi}\ln\frac{E_1}{E_0}\int\frac{d^2\Omega}{4\pi}\,\frac{2(b\bar{b})}{(bk)(\bar{b}k)}\,. \end{aligned} \tag{1.40}$$

We have introduced the notation:

$$(ij) \equiv 1 - \cos\theta_{ij}\,, \tag{1.41}$$

and $d^2\Omega$ is the integration over all the angular phase space. Let us now rewrite:

$$\frac{2(b\bar{b})}{(bk)(\bar{b}k)} = I_b(k) + I_{\bar{b}}(k)\,, \tag{1.42}$$

with

$$I_b(k) = \frac{1}{(bk)}\left(1 + \frac{(b\bar{b}) - (bk)}{(\bar{b}k)}\right)\,, \tag{1.43}$$

$$I_{\bar{b}}(k) = \frac{1}{(\bar{b}k)}\left(1 + \frac{(b\bar{b}) - (\bar{b}k)}{(bk)}\right)\,. \tag{1.44}$$

[9] This observable is not collinear safe (cf section 1.3.1), as we should introduce a cut-off for emitting a gluon too close to the b quarks, or to compute instead the probability to emit a third *jet*. But as we will not do the full angular integration, we will just hide this problem for now, returning to it later.

As a first step, using angular coordinates (θ_{bk}, ϕ_{bk}) with respect to the b quark direction, i.e. $d^2\Omega = d\cos\theta_{bk} d\phi_{bk}$, we carry out the ϕ_{bk} integration for the $I_b(k)$ part of eq. (1.40):[10]

$$\begin{aligned}\int_0^{2\pi} \frac{d\phi_{bk}}{2\pi} I_b(k) &= \frac{1}{(bk)} \left(1 + \frac{\cos\theta_{bk} - \cos\theta_{b\bar{b}}}{2\pi} \int_0^{2\pi} \frac{d\phi_{bk}}{1 - \cos\theta_{b\bar{b}}\cos\theta_{bk} + \sin\theta_{b\bar{b}}\sin\theta_{bk}\cos\phi_{bk}}\right), \\ &= \frac{1}{(bk)} \left(1 + \frac{\cos\theta_{bk} - \cos\theta_{b\bar{b}}}{|\cos\theta_{bk} - \cos\theta_{b\bar{b}}|}\right), \\ &= \frac{2}{(bk)} \Theta(\theta_{b\bar{b}} - \theta_{bk}) \,. \end{aligned} \tag{1.45}$$

Now defining the angular variables with respect to $\bar{b}$, we can do exactly the same thing for the $I_{\bar{b}}$ part of eq. (1.40). This leads to the following expression for $P(E_0, E_1)$:

$$P(E_0, E_1) = \frac{\alpha_s C_F}{2\pi} \ln\frac{E_1}{E_0} \left(\int \frac{d\cos\theta_{bk}}{1 - \cos\theta_{bk}} \Theta(\theta_{b\bar{b}} - \theta_{bk}) + \int \frac{d\cos\theta_{\bar{b}k}}{1 - \cos\theta_{\bar{b}k}} \Theta(\theta_{b\bar{b}} - \theta_{\bar{b}k}) \right). \tag{1.46}$$

This remarkable result shows that the probability $P(E_0, E_1)$ does not receive any contribution from soft gluons emitted outside 2 cones of radius $\theta_{b\bar{b}}$ centred respectively on b and $\bar{b}$ (fig. 1.8). This is the *angular ordering* property.

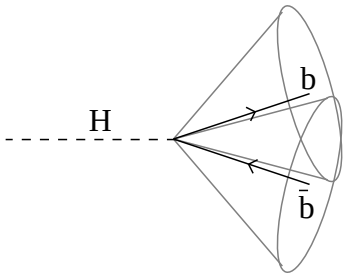

Figure 1.8: The part of the perturbative radiation from the $b\bar{b}$ dipole emitted inside the 2 cones is the one that contributes most to physical observables. The angular ordering approximation neglects gluons emitted at larger angles.

Here, we studied a simple observable which is independent of the angular region. For more complicated observables, one does not find *strict* angular ordering, but only an approximate version: as a first approximation, one can neglect soft gluons emitted outside the 2 cones of fig. 1.8 when computing physical observables.

The angular ordering property of soft emission is an example of a coherence effect: a gluon emitted at large angle with respect to the splitting angle $\theta_{b\bar{b}}$ does not resolve the splitting into $b\bar{b}$, it only sees the Higgs colour charge, which is 0. Therefore, our previous calculation is also valid for any colour neutral $q\bar{q}$ dipole. We could have for instance also considered $\gamma^*, Z \to q\bar{q}$, which would have worked identically. If we do the same calculation

[10] We use $(\bar{b}k) = a + b\cos\phi_{bk}$ with $a = 1 - \cos\theta_{b\bar{b}}\cos\theta_{bk}$ and $b = \sin\theta_{b\bar{b}}\sin\theta_{bk}$, which is easy to derive, and then the integration over ϕ_{bk} is performed with:

$$\int_0^{2\pi} \frac{d\phi}{2\pi} \frac{1}{a + b\cos\phi} = \frac{1}{\sqrt{a^2 - b^2}} \,,$$

if $|a| > |b|$.

for a gluon g_1 splitting into $q\bar{q}$, then the radiation pattern from this colour field can be shown to have contributions outside the 2 bremsstrahlung cones of fig. 1.8. But the angular ordering property states that a second gluon g_2 emitted outside these 2 cones only sees the overall $q\bar{q}$ colour charge, which is that of g_1.

1.2.5 Large-N_c limit

Let us now introduce another approximation that reveals itself very useful for calculating higher order corrections. The large-N_c limit was proposed by 't Hooft [45] as a way to help understand the strong interactions. The idea is to consider the limit $N_c \to \infty$ with $\alpha_s N_c$ fixed. In this limit, 't Hooft found that a considerable simplification occurs: one is left only with *planar* Feynman diagrams (see below). One might think that this approximation is not good for QCD where $N_c = 3$, which is not really greater than 1. But, as we will see in the following examples, the large-N_c limit actually corresponds to an expansion in powers of $1/N_c^2$, which is close to the perturbative QCD expansion at the M_Z scale: $\alpha_s(M_Z) \simeq 0.12$. Furthermore, as Witten pointed out in [46], if one examines the value of e in QED, with $e^2/4\pi \simeq 1/137$, one finds $e \simeq 0.302$, not much smaller than $1/N_c$.

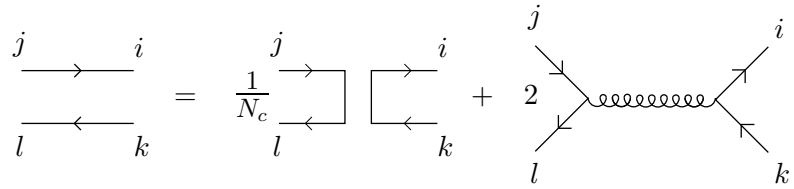

Figure 1.9: Diagrammatic view of the Fierz identity eq. (1.47).

To understand the large-N_c limit, let us start with the *Fierz identity*, which is valid for any $SU(N_c)$ group (see appendix A):

$$\delta^i_j \delta^l_k = \frac{1}{N_c}\delta^i_k \delta^l_j + 2(t^A)^i_k (t^A)^l_j \,. \tag{1.47}$$

This identity is the decomposition of the N_c^2 colour states of a $q\bar{q}$ system into the colour singlet and colour octet representations. Using the colour part of the Feynman rules in fig. 1.3, one finds the corresponding pictorial representation of this identity, presented in fig. 1.9.

When $N_c \to \infty$, the $1/N_c$ singlet term disappears, and we can then deduce with fig. 1.9 the colour representation of the gluon in the large-N_c limit:[11]

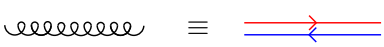

This means that the gluon is represented by a $q\bar{q}$ pair with different colours. Fig. 1.10 shows a few examples of Feynman diagrams and their corresponding large-N_c limit representation. The computation of their colour factor is done in appendix A. Here we only comment on the results.

[11] The factor of 2 is just a normalisation factor of the t^A matrices that are present at the two vertices ($2 = 1/T_R$, see appendix A).

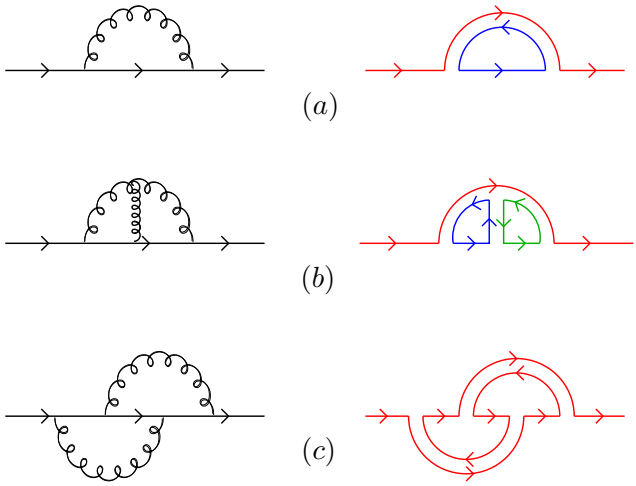

Figure 1.10: Some Feynman diagrams and their corresponding colour representation in the large-N_c approximation. The Feynman diagrams represent either virtual gluon loops, or real gluons emission amplitudes squared.

If we average over the N_c colours of the incoming quark and we sum over the colours of the final quark, we obtain (appendix A):

$$(a) = \frac{\alpha_s}{N_c}\mathrm{Tr}(t^A t^A) = \mathcal{O}(\alpha_s N_c)\,, \tag{1.48}$$

$$(b) = \frac{\alpha_s^2}{N_c}\mathrm{Tr}(t^A t^B t^C) i f^{ABC} = \mathcal{O}(\alpha_s^2 N_c^2)\,, \tag{1.49}$$

$$(c) = \frac{\alpha_s^2}{N_c}\mathrm{Tr}(t^A t^B t^A t^B) = \mathcal{O}(\alpha_s^2)\,. \tag{1.50}$$

Diagrams (a) and (b) are both planar. Each one gives a leading contribution in the large-N_c limit: for each power of α_s we obtain one power of N_c. On the contrary, diagram (c) is an example of a non-planar graph. To see why, one can first notice that the emitted gluons correspond to $q\bar{q}$ pairs of the *same* colour, which is never the case for planar diagrams. Another way to see this is to draw diagram (c) in a slightly different but equivalent way. This is the diagram of fig. 1.11. One notices that one of the gluon has to "jump" over the other one, i.e. we cannot draw a colour flow in one continuous line. This graph is thus non-planar and this is manifest in the colour factor: it is a next-to-leading contribution because a factor N_c^2 is missing with respect to diagram (b).

Figure 1.11: Diagram (c) of fig. 1.10 drawn such that it becomes explicitly non-planar.

1.3 Jet physics at the LHC

Though possible in some cases, it is usually hard to talk about the potential discovery of new physics at the LHC without considering *jets*. Jets are a direct consequence of 2 fundamental properties of QCD: asymptotic freedom and infra-red limit of QCD (soft and collinear). We have already studied asymptotic freedom in section 1.2.3, and section 1.3.1 will introduce the latter property. Jets form an essential part of any event study at collider experiments, and especially at the LHC where the hadronic activity is very important.

1.3.1 Origin of jets: the soft and collinear limit of QCD

As an introduction, let us first consider an explicit QCD calculation: the total hadronic cross-section in e^+e^- annihilation at next-to-leading order (NLO). For that, one has to sum the real and virtual part of the cross-section whose diagrams are represented in fig. 1.12.

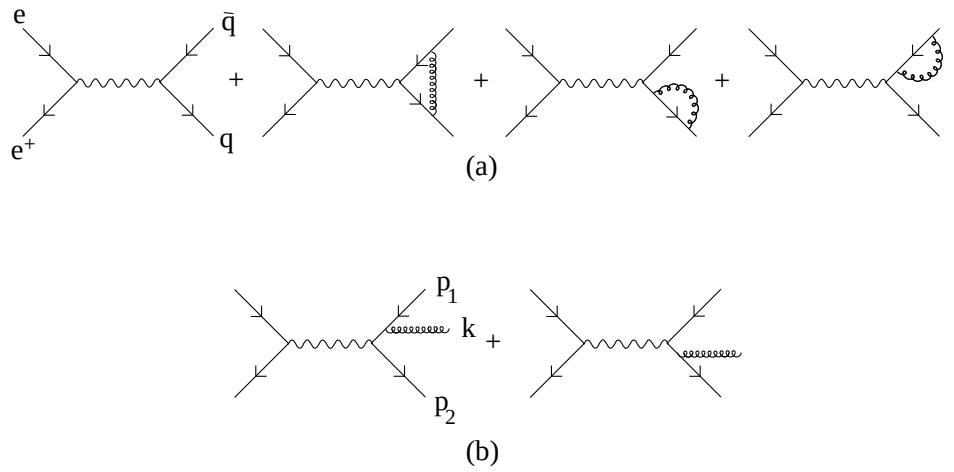

Figure 1.12: Diagrams entering in the calculation of the total NLO hadronic cross-section in e^+e^- annihilation. (a) LO + virtual NLO diagrams, (b) real NLO diagrams.

Using the Feynman rules for the real diagrams (b), integrating over the momenta of the q, $\bar{q}$ and the gluon g, and summing over all the final state colours and gluon's polarisations, one finds the real NLO contribution to the total cross-section when $m_q = 0$ [47, 48]:

$$\sigma^{q\bar{q}g} = \sigma_0 N_c \sum_f Q_f^2 \int_0^1 dx_1 \int_0^1 dx_2 \frac{\alpha_s C_F}{2\pi} \frac{x_1^2 + x_2^2}{(1-x_1)(1-x_2)}\,, \tag{1.51}$$

where Q_f is the electromagnetic charge of quark flavour f, and:

$$x_1 = \frac{2E_q}{\sqrt{s}}\,, \tag{1.52}$$

$$x_2 = \frac{2E_{\bar{q}}}{\sqrt{s}}\,, \tag{1.53}$$

$$\sigma_0 = \frac{4\pi\alpha^2}{3s}\,. \tag{1.54}$$

s is the total centre of mass energy of the e^+e^- collision, α is the fine structure constant of QED, and E_i is the energy of particle i. We notice that the integrals in eq. (1.51) diverge at $x_i = 1$. As one can show that

$$1 - x_1 = \frac{x_2 E_g (1 - \cos\theta_{1g})}{\sqrt{s}}\,, \tag{1.55}$$

$$1 - x_2 = \frac{x_1 E_g (1 - \cos\theta_{2g})}{\sqrt{s}}\,, \tag{1.56}$$

this means that the divergence occurs either when the gluon is *collinear* to q or $\bar{q}$ ($\theta_{ig} \to 0$), or when the gluon is *soft*, i.e. its energy is very low ($E_g \to 0$). To understand where this divergence comes from, let us zoom on one of the real NLO diagrams in fig. 1.12, which leads to fig. 1.13. Using the Feynman rules (fig. 1.3), the expression for the quark propagator in red is roughly ($m = 0$):

$$\frac{i}{\not{p}_1 + \not{k}} = \frac{i(\not{p}_1 + \not{k})}{(p_1 + k)^2}\,, \tag{1.57}$$

with:

$$(p_1 + k)^2 = 2E_{p_1} E_k (1 - \cos\theta_{1k})\,. \tag{1.58}$$

When the gluon becomes either soft or collinear to the quark, the propagator thus diverges and this is what we observe in eq. (1.51).

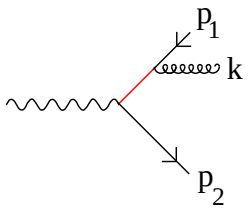

Figure 1.13: When the gluon becomes either soft or collinear to the quark, the quark internal line drawn in red becomes on-shell, and its propagator thus diverges.

This divergence is not actually a problem because it will cancel with the virtual diagrams that have exactly the same soft and collinear divergences in the gluon loop. As in the context of renormalisation, we have to regularise this expression, for instance using a space-time dimension $4 - 2\epsilon$ with $\epsilon < 0$ (called dimensional regularisation [49–52]). We thus obtain for the virtual and real parts at NLO [38]:

$$\sigma^{q\bar{q}g}(\epsilon) = \sigma_0 N_c \sum_f Q_f^2 \frac{\alpha_s C_F}{2\pi} H(\epsilon) \left[\frac{2}{\epsilon^2} + \frac{3}{\epsilon} + \frac{19}{2} - \pi^2 + \mathcal{O}(\epsilon)\right]\,, \tag{1.59}$$

$$\sigma^{q\bar{q}}(\epsilon) = \sigma_0 N_c \sum_f Q_f^2 + \sigma_0 N_c \sum_f Q_f^2 \frac{\alpha_s C_F}{2\pi} H(\epsilon) \left[-\frac{2}{\epsilon^2} - \frac{3}{\epsilon} - 8 + \pi^2 + \mathcal{O}(\epsilon)\right]\,. \tag{1.60}$$

where $H(\epsilon) = 1 + \mathcal{O}(\epsilon)$. One notices on eqs. (1.59,1.60) that the divergences manifest themselves as poles in $1/\epsilon$. But the physical cross-section, which is obtained by adding the real and virtual parts, is regular in the limit $\epsilon \to 0$:

$$\sigma_{tot}^{NLO} = \sigma_0 N_c \sum_f Q_f^2 \left(1 + \frac{\alpha_s}{\pi} + \mathcal{O}(\alpha_s^2)\right)\,, \tag{1.61}$$

where we used $C_F = 4/3$. This cancellation of divergences between real and virtual diagrams is a particular case of a more general theorem which states that suitably defined inclusive quantities will indeed be free of singularities in the massless limit. This theorem was first demonstrated in the case of QED by Bloch and Nordsieck [53] (soft singularities only) and in more general cases, including QCD, by Kinoshita [54] and Lee and Nauenberg [55] (soft and collinear singularities). But what do suitably defined inclusive quantities mean?

To answer this question, let us consider a simple example. Assume that we want to compute the probability to have 3 partons in the final state. In this case, only the diagrams (*b*) in fig. 1.12 contribute, and the expression for the probability is proportional to eq. (1.59), which diverges in 4 dimensions, i.e. when $\epsilon \to 0$. The result is thus meaningless, or non-physical. This example shows that we cannot compute *everything* in perturbative QCD: the probability to obtain 3 partons in the final state is not a suitably defined inclusive quantity. In fact, the derivation of the Kinoshita-Lee-Nauenberg theorem assumes that we can sum over degenerate final and initial states configurations. So we are led to the fundamental concept of *infra-red and collinear safety*, which is a simple way to be sure that we suitably define inclusive quantities [38]: *for an observable's distribution to be calculable in perturbation theory, the observable should be infra-red and collinear safe, i.e. insensitive to the emission of soft and collinear gluons. In particular, if $\vec{p}_i$ is any momentum occurring in its definition, it must be invariant under the branching $\vec{p}_i \to \vec{p}_j + \vec{p}_k$ whenever $\vec{p}_j$ and $\vec{p}_k$ are parallel (collinear safety) or one of them is very soft (infra-red safety).*

One may argue that due to finite detector resolutions in angle and energy, experiments always measure infra-red and collinear (IRC) safe quantities. This is true, but theoretical IRC safety is crucial as soon as we want to compare theoretical predictions with measurements.

As an example, the probability to emit a gluon in the energy range $[E_0, E_1]$ that we considered in section 1.2.4 is an infra-red safe quantity (for $E_0 > 0$) but is not collinear safe. This was manifest in the divergent integrals over θ_{bk} and $\theta_{\bar{b}k}$ (eq. (1.46)). Event shape variables such as thrust [56, 57], spherocity [58], energy correlations [59–61] and C-parameter [62] are examples of IRC safe quantities. A jet, that we are going to study now, is an example of an IRC safe way to view a parton.

1.3.2 An approach to jets

We saw in the previous section that the probability to find 3 partons in the final state is ill-defined because if is not IRC safe. Sterman and Weinberg made one of the first attempts to define a related probability in an IRC safe way. Instead of considering the 3-parton cross-section, they computed the 3-*jet* cross-section [63]. In their approach, a final state is classified as two-jet-like (or two-"parton"-like) if all but a fraction ε of the total available energy is contained in a pair of cones of half-angle δ. The 3-jet cross-section is an IRC safe observable because emitting a soft or collinear gluon does not change the number of jets (fig. 1.14).

Sterman and Weinberg found a 3-jet cross-section equal to:

$$\sigma_3^{NLO} = \sigma_{tot}^{NLO} \frac{4C_F\alpha_s}{\pi} \left[\ln\frac{1}{\delta} \ln\left(\frac{1}{2\varepsilon} - 1\right) + \ln\frac{1}{\delta}\left(-\frac{3}{4} + 3\varepsilon\right) + \frac{\pi^2}{12} - \frac{7}{16} - \varepsilon + \frac{3}{2}\varepsilon^2 + \mathcal{O}(\delta^2 \ln\varepsilon) \right], \tag{1.62}$$

where σ_{tot}^{NLO} is given in eq. (1.61). We now obtain a finite cross-section, because divergences

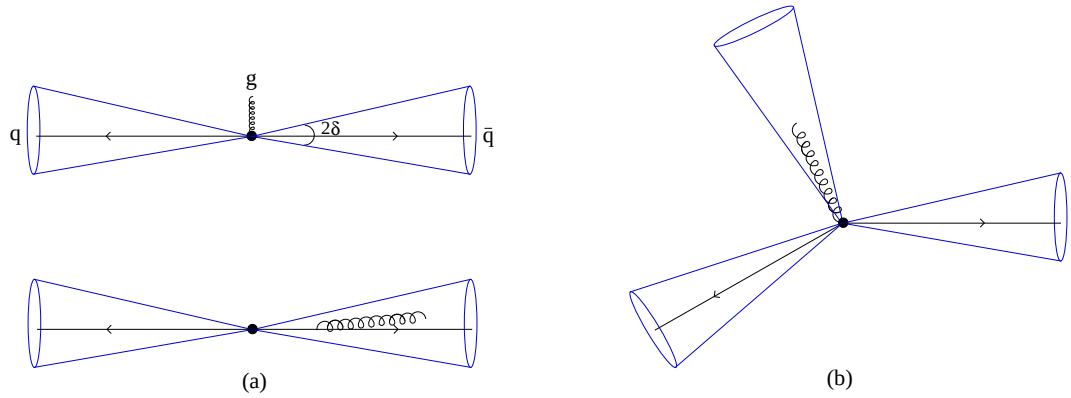

Figure 1.14: (*a*) Examples of 2-jet events in the Sterman and Weinberg approach: the gluon is either too soft or too collinear to be accounted as a separate jet; (*b*) Example of a 3-jet event where the gluon is energetic enough and sufficiently separated in angle to be seen as an additional jet.

are regularised using the ε and δ parameters. However, one notices that if $\delta \ll 1$ or $\varepsilon \ll 1$, the cross-section becomes enhanced by logarithms of $1/\delta$ and $1/\varepsilon$. This means that the $\mathcal{O}(\alpha_s)$ term can become as large as we want. This is a manifestation of the soft and collinear divergences: though being cancelled, if we reduce δ or ε, we also reduce the phase space region in which this cancellation occurs.

If we compute the higher-order corrections, we can find a leading term of the form

$$J_n(\delta, \varepsilon) = \alpha_s^n \ln^n \frac{1}{\delta} \ln^n \frac{1}{\varepsilon}\,, \tag{1.63}$$

which can be even larger than the $\mathcal{O}(\alpha_s)$ term for δ and ε small enough. An immediate consequence of this enhancement is a breakdown of the perturbative expansion: we cannot trust it if higher order corrections become so important. Therefore, one has to take into account at least the dominant term at all-orders. This procedure is called *resummation*. We will return to this very important point later, but for now, we are going to see the phenomenological implication for a collider experiment of such an enhancement.

1.3.3 The parton shower

The higher order enhancement of the cross-section observed in the previous section becomes manifest if we compute the probability to emit a gluon with energy E at an angle θ from a quark (fig. 1.15). In the soft and collinear limit, one can easily show the following property:

$$d\sigma_3 = d\sigma_2 \frac{2C_F\alpha_s}{\pi} \frac{dE}{E} \frac{d\theta}{\theta}\,. \tag{1.64}$$

The quantity $d\sigma_2$ is the differential cross-section to produce a $q\bar{q}$ pair, which depends on the details of the process. The quantity $d\sigma_3$ is the differential cross-section to produce an additional gluon. Therefore, the expression

$$d\Phi_g \equiv \frac{2C_F\alpha_s}{\pi} \frac{dE}{E} \frac{d\theta}{\theta}\,, \tag{1.65}$$

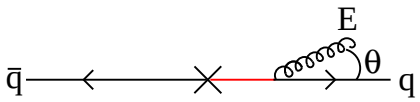

Figure 1.15: Production of a $q\bar{q}$ pair via an unspecified process (cross) with subsequent emission of a gluon with energy E at an angle θ from $q\bar{q}$. The propagator of the quark (in red) goes on shell when $E, \theta \to 0$.

can be viewed as the probability we were looking for. Notice that the coupling α_s should be computed at the emission's energy scale, which is roughly given by the transverse momentum $k_t \simeq E\theta$ of the gluon with respect to the quark. So, when $E \to 0$ or $\theta \to 0$, not only do we observe a divergent logarithmic enhancement of the emission probability, but also the coupling α_s enters the non-perturbative regime (cf discussion about asymptotic freedom in section 1.2.3). As already stated in the previous section, this means that perturbation theory is not suited to describe very soft or collinear emissions, which belong to large-distance physics. In spite of that, the enhancement of the emission probability has an observable consequence, usually referred as *parton-showering*: once a parton (quark or gluon) is produced in a hard scattering process (for instance $e^+e^- \to q\bar{q}$), it undergoes many successive soft and/or collinear splittings. This "cascade" of partons results, after hadronisation, in collimated sprays of hadrons that have often been observed in experiments. This is what we usually call *jets* (figs. 1.16, 1.17). The first experimental evidence for these jets was reported by SLAC in 1975 [64]. One should be aware that a parton-showering process can occur on initial state as well as final state partons. In the former case, we talk about Initial State Radiation (ISR), and in the latter case, we talk about Final State Radiation (FSR).

This picture gives an intuitive view of a jet, but jets can only be suitably defined using jet algorithms (see next section). The original definition of a jet from Sterman and Weinberg (section 1.3.2) can actually be seen as the first jet algorithm, i.e. a way to see the event as "two-parton-like" or more depending on the choice of the parameters ε and δ. However, it turned out experimentally and theoretically that this definition was not well suited to study multijet events, and alternative jet algorithms were thus proposed, that we are now going to describe.

1.3.4 Jet algorithms

Fig. 1.17 showed an example of 2 and 3 jet events at LEP. For these events, it seems to be rather clear how many jets there are, especially for the 2-jet event. But for the 3-jet case, how can we be sure that there are really 3 jets and not 4? Maybe there are 2 jets close to each other that we do not distinguish well on the picture. Therefore, we need a good definition of what we call a jet, that can be used to compute cross-sections as in the Sterman-Weinberg approach. Moreover, the events shown come from LEP, which was a leptonic collider. We expect much more hadronic activity from a hadronic collider like the LHC, leading to final states far more complex where it can be impossible to distinguish any jet by eye.

The goal of a jet algorithm is to solve this issue in a fully automated way so as to be able to deal with millions of events. More precisely, given a set of N hadrons with momenta $\{p_i\}$, a jet algorithm returns a set of n jets, $n \leq N$. As we saw in section 1.3.1, the procedure to obtain the final jets should be IRC safe, in order for the theoretical results to

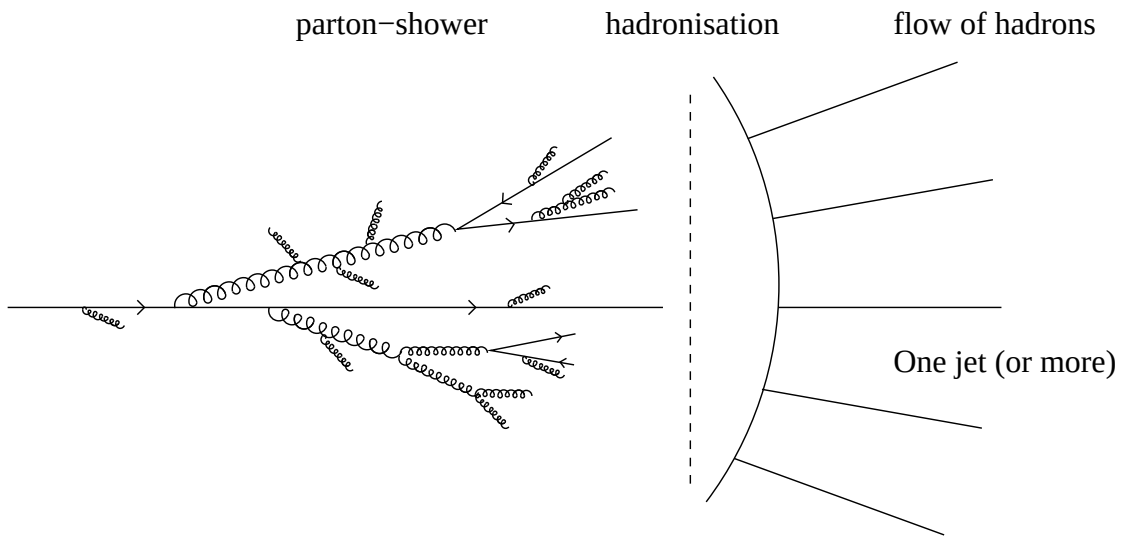

Figure 1.16: The parton-showering process from an initial quark. After hadronisation, it results in a flow of hadrons that gives one jet or more according to the jet algorithm chosen (see section 1.3.4).

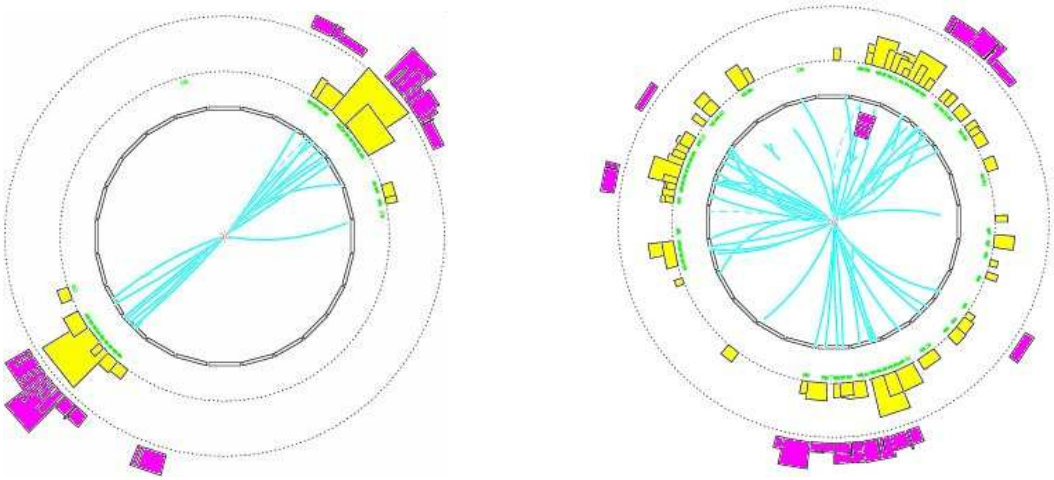

(a) (b)

Figure 1.17: Pictures taken from the website of the OPAL experiment at LEP [65]: (a) two-jet event interpreted as a hard process $e^+e^- \to q\bar{q}$; (b) three-jet event interpreted as a hard process $e^+e^- \to q\bar{q}g$.

be comparable with experimental data. This means that the addition of a soft particle, or the splitting of a particle into 2 collinear particles, should change neither the number of jets nor their momentum. One example of class of jet algorithms is provided by the *sequential recombination* algorithms, defined here for hadronic colliders:[12] let $\{i\}_{i=1..N}$ be the set of all hadrons produced in an event. Define 2 distances d_{ij} and d_{iB} respectively between 2 particles i and j and between a particle i and the beam. Then iterate the following procedure [66, 67]:[13]

1. Find the minimum d_{min} of all the distances d_{ij} and d_{iB}.
2. If d_{min} is a d_{ij}, merge particles i and j into a new particle (or "pseudo-jet") k. If it is a d_{iB}, declare particle i to be a final state jet and remove it from the list.
3. Repeat from step (1) until no particles are left.

The distance measures should be chosen longitudinally invariant, i.e. they do not change if we make a boost along the beam axis. When d_{ij} is the smallest distance found, one has to decide how to recombine particles i and j into a new particle k, which is called the *recombination scheme*. The simplest way to do it is to sum the 4 momenta:

$$p_k = p_i + p_j \,. \tag{1.66}$$

This is the E-scheme, which is the most widely used nowadays. Other schemes exist but we will not consider them. An inclusive sequential recombination algorithm as defined above is necessarily IR unsafe, because the emission of an arbitrarily soft particle can become a jet. Therefore, one also has to provide a cut on the minimal transverse momentum for a jet.

Important examples of IRC safe sequential recombination algorithms in hadronic colliders[14] are the k_t [66, 67] and Cambridge/Aachen (C/A, [71, 72]) algorithms whose longitudinally invariant distance measures are given by:

$$k_t: \quad d_{ij} = \min(p_{t_i}^2, p_{t_j}^2)\frac{\Delta R_{ij}^2}{R^2}\,, \tag{1.67}$$

$$d_{iB} = p_{t_i}^2\,, \tag{1.68}$$

$$C/A: \quad d_{ij} = \frac{\Delta R_{ij}^2}{R^2}\,, \tag{1.69}$$

$$d_{iB} = 1\,, \tag{1.70}$$

where p_t is the transverse momentum with respect to the beam. The angular distance ΔR_{ij} in the (y, ϕ) plane between particles i and j is defined as:

$$\Delta R_{ij}^2 \equiv (y_i - y_j)^2 + (\phi_i - \phi_j)^2\,. \tag{1.71}$$

[12] For an e^+e^- collider, the d_{iB} distance is useless because partons cannot be emitted from the beam.

[13] We present only the inclusive version of the algorithm, defined in [67]. The exclusive version is described in [66].

[14] The first example of a sequential recombination algorithm was provided by the JADE collaboration in e^+e^- collisions [68, 69]. Though IRC safe, it suffered from some bad issues and was progressively replaced by the e^+e^- version of the k_t algorithm [70]

R is a parameter of the algorithm, called the *jet radius*. If R is reduced, then we analyse the event on a finer scale and we resolve more "partons" that participated to the hard process. R is equivalent to the δ parameter of the Sterman-Weinberg's approach. This implies that there is a non-unique way to see an event. This ambiguity seems disturbing at first sight but actually reveals a great richness of the physics: what you see clearly depends on the scale at which you look at things. One should be aware that the possibility to look at an event at different scales reveals itself very powerful to understand its structure and we will intensively use this opportunity to reduce the QCD background and enhance possibly new physics signals in the following chapters.

The k_t and C/A algorithms provide physically relevant descriptions of a parton-shower because their distance measures are closely related to the soft and collinear divergences of QCD. The C/A algorithm essentially measures the angle between 2 partons and recombines them if they are close enough, and the k_t distance is related to the emission probability of a gluon, because eq. (1.65) can be equivalently rewritten, in the collinear limit ($\theta \ll 1$), as:

$$d\Phi_g = \frac{2C_F\alpha_s}{\pi}\frac{dp_{t_g}\, d\Delta R_{qg}}{p_{t_g}\,\Delta R_{qg}}\,, \tag{1.72}$$

where p_{t_g} is the gluon transverse momentum with respect to the beam axis.

Another important class of jet algorithms is the so-called *cone* algorithms. The Sterman-Weinberg definition of a jet can be seen as one of that kind. Contrary to the sequential recombination algorithms, they give a top-down approach: the goal is to find coarse regions of energy flow (represented as stable cones) and define them as jets. This is a simple and maybe more intuitive view of a parton-shower, which should work well because QCD only modifies energy flow on small angular scales. But cone algorithms are more difficult to implement in practice, and the various definitions that have long been used were all infra-red and/or collinear unsafe. This was revealed by the work of [73, 74], and [74] also implemented a new IRC safe cone algorithm called SISCone. We will not say more about cone algorithms because we will hardly use them in this thesis, but the reader is referred to section 2.1 of [75] for a review.

One major problem of all the sequential recombination jet algorithms was the time required to cluster one event. For each of them, this was of the order of N^3 where N is the number of hadrons in the event, and this was found too large for the LHC, where $N \sim 1000$. However, in 2005, Cacciari and Salam found a clever way to reduce this time to $\mathcal{O}(N \ln N)$ for the k_t algorithm [76], which is far more attractive for practical use at the LHC. They also developed a new tool, FastJet [77], which implements this method in a C++ program that is now widely used among the experimental community. In FastJet, one can find the k_t, C/A and SISCone algorithms, as well as plugins to various other jets algorithms. But there is also another new jet algorithm that will be useful for chapter 4 of this thesis, called the anti-k_t algorithm [78]. It is a sequential recombination algorithm with distance measures:

$$d_{ij} = \min\left(\frac{1}{p_{t_i}^2}, \frac{1}{p_{t_j}^2}\right)\frac{\Delta R_{ij}^2}{R^2}\,, \tag{1.73}$$

$$d_{iB} = \frac{1}{p_{t_i}^2}\,. \tag{1.74}$$

Contrary to k_t, the anti-k_t algorithm clusters hard particles first, so that the hardest jets are usually circular.

1.3.5 Splitting functions

We saw in section 1.3.3 that there is a high probability to emit a soft and collinear gluon. The enhancement of the emission probability manifests itself as a parton-shower, whose main consequence is to develop a jet structure that is experimentally analysed using jet algorithms (section 1.3.4). This can also be analytically described thanks to resummation that consists in extracting the logarithmically enhanced terms at each order of perturbation theory. This was briefly mentioned in section 1.3.2 where we noticed that the dominant terms have powers of logarithms that counterbalance the smallness of α_s. Given an IRC safe observable τ that we study in the region $\tau \ll 1$, we talk about leading-logarithmic (LL) resummation if one considers only the leading term at each order of the expansion of its integrated distribution $\Sigma(\tau)$:

$$\Sigma(\tau) = \sum_{k=0}^{\infty} c_k \alpha_s^k \ln^{2k} \tau \,. \tag{1.75}$$

For each power of α_s, one has up to two large logarithms: one for soft emissions, one for collinear emissions. This is a *double-log* resummation. At this accuracy, one can use eq. (1.65) for the emission probability of a gluon, because this expression contains the leading part of the soft and collinear divergences.

However, in resummation, one sometimes has to face observables that only give rise either to a collinear large logarithm, or to a soft large logarithm, but not both. It is also possible that one may want to go beyond the double leading-log approximation and thus consider next-to-leading-log (NLL) corrections with down to only one large logarithm for each power of α_s. In chapter 4, we will have an example of such an observable, for which we will resum the leading soft logarithms only and treat angular distributions using as few approximations as possible. In this case, we talk about *single-log* resummation. However, at this accuracy, eq. (1.65) cannot be used anymore, because it does not take into account the full energy or angular distributions. In chapter 4, we will study the matrix elements in the soft approximation. Therefore we will not examine them in this section. Instead, we are going to study the collinear approximation without assuming that the emitted gluons are soft. The collinear approximation is important for Monte-Carlo programs that usually use it to simulate the parton-showering process (see next section).

To study the collinear approximation for a splitting $i \to jk$ where i, j and k are quarks or gluons, we define 2 kinematic variables: z and t. The variable z is the fraction of parton i's energy carried by parton j:

$$E_j = zE_i \,, \tag{1.76}$$

$$E_k = (1-z)E_i \,, \tag{1.77}$$

and t is the virtuality of parton i:

$$t \equiv p_i^2 = (p_j + p_k)^2 \,. \tag{1.78}$$

The problem is to compute, in the collinear limit, the probability $\frac{d^2P}{dt\,dz}dt\,dz$ for a parton i to split into j and k with invariant mass squared t and with j carrying the fraction z of parton i's energy. One can show that this splitting probability is process independent, and that we can always write in the final state [79]:

$$d\sigma_{n+1} = d\sigma_n \frac{d^2P}{dt\,dz} dt\,dz \,, \tag{1.79}$$

where $d\sigma_n$ is the differential cross-section to produce n particles in the final state from a certain process. All the information about the process is contained within $d\sigma_n$, $\frac{d^2P}{dt\,dz}$ does not depend on it. This is a particular case of *factorisation* that allows one to separate short and long distance physics, a collinear emission being part of the long-distance physics (see section 1.4.1 for more details about factorisation).

The LO splitting probability can be written in the following form:

$$\frac{d^2P}{dt\,dz} = S_{ji}\frac{\alpha_s}{2\pi}\frac{P_{ji}(z)}{t}\,, \tag{1.80}$$

where $S_{ji} = 1/2$ for i and j identical and $S_{ji} = 1$ otherwise. $P_{ji}(z)$ is called a *splitting function*. In QCD, there are 4 splitting functions represented in fig. 1.18.[15]

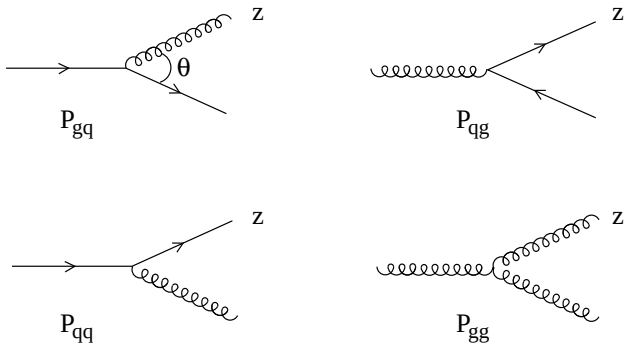

Figure 1.18: The QCD branchings at LO in the collinear approximation ($\theta \ll 1$) and their corresponding splitting functions.

At LO, the splitting functions can be written as [79]:

$$P_{qq}(z) = C_F\frac{1+z^2}{1-z}\,, \tag{1.81}$$

$$P_{gq}(z) = C_F\frac{1+(1-z)^2}{z}\,, \tag{1.82}$$

$$P_{qg}(z) = T_R\left(z^2+(1-z)^2\right)\,, \tag{1.83}$$

$$P_{gg}(z) = 2C_A\left(\frac{1-z}{z}+\frac{z}{1-z}+z(1-z)\right)\,. \tag{1.84}$$

The factor S_{ji} in eq. (1.80) is 1/2 only for P_{gg} and 1 otherwise. One can notice interesting symmetries among these splitting functions [80], for instance if we permute the decay products:

$$P_{qq}(z) = P_{gq}(1-z)\,, \tag{1.85}$$

$$P_{qg}(z) = P_{qg}(1-z)\,, \tag{1.86}$$

$$P_{gg}(z) = P_{gg}(1-z)\,, \tag{1.87}$$

or the crossing relations:

$$\frac{P_{ji}(z)}{C_{ji}} = (-1)^{2s_j-2s_i+1}\frac{1}{z}\frac{P_{ij}\left(\frac{1}{z}\right)}{C_{ij}}\,, \tag{1.88}$$

[15]This is true at LO, though at higher orders one must also distinguish quarks and antiquarks as well as the various quark flavours.

where s_k is the spin of parton k and $C_{ji} = C_F$, T_R or C_A, is the colour factor related to the splitting function P_{ji}.

1.3.6 Numerical tools for the LHC

To analyse data, or to predict how well a particular kind of new physics can be seen at the LHC, one usually needs to calculate cross-sections. For instance, if one wants to compute the distribution $d\sigma/dx$ of an observable X at the LHC, one has to carry out the following integration:

$$\frac{d\sigma}{dx} = \sum_k \frac{1}{k!} \int \frac{d^3\vec{p}_1}{(2\pi)^3 2|\vec{p}_1|} \cdots \int \frac{d^3\vec{p}_k}{(2\pi)^3 2|\vec{p}_k|} M(p_1, \ldots, p_k) \delta(X(p_1, \ldots, p_k) - x)\,, \qquad (1.89)$$

where the sum over k actually runs over all the processes $pp \to p_1 \ldots p_k$ at the LHC and $M(p_1, \ldots, p_k)$ is the matrix element squared. Unfortunately, this kind of integration is very complex to perform in general, in part because one often also wants to add some particular kinematic cuts, for example $|y_i| < 2.5$,[16] to simulate the detector's range.

The Monte-Carlo method is a particularly suited tool for multi-dimensional integrations with phase space cuts as complex as one can imagine. In principle, it is simple to implement. One first chooses a particular process and randomly generates some momenta $p_1 \ldots p_k$ (that we call an "event"). Then, one checks if the event passes the various kinematic cuts. If not, one generates another event. If yes, one computes the matrix element squared $M(p_1, \ldots, p_k)$ for this process and defines the weight of the event as being the matrix element times the phase space factors. Eventually, one obtains the differential distribution $d\sigma/dx$ by defining an histogram for X, computing the value $X(p_1, \ldots, p_k)$, and filling the corresponding bin of the histogram with the event weight. If needed, one can do the same for different processes and sum the resulting histograms. With this method, one can thus obtain any desired distribution.

Unfortunately, in general, life is not as easy as the simple description we have just given. For instance, one would like to generate more events in phase space regions where the event weight is enhanced. Moreover, we have seen in section 1.3.1 that the matrix element can diverge in the soft or collinear limits, so that one usually has to face with numerical instabilities. Therefore, the integration has to be carried out in a clever way in order to obtain reliable results in a sufficiently short computing time.

Various Monte-Carlo programs have already been implemented to study different kinds of processes. One class of programs corresponds to the *fixed-order* Monte-Carlo programs. This means that the matrix element is computed exactly at LO, NLO, and nowadays up to NNLO. Beyond LO, we know that the real and virtual parts are separately divergent (section 1.3.1), but their sum is finite. To deal with these kinds of integrals, some methods have been found among which the Catani-Seymour dipole subtraction method [81] and the Frixione-Kunszt-Signer (FKS) approach [82,83] are the most commonly used in NLO Monte-Carlo programs, whereas sector decomposition (see [84] for a review) and antenna subtraction [85–87] are preferred for NNLO calculations. Sector decomposition first disentangles all the singularities before extracting the poles and subtracting them. The dipole and antenna subtraction methods as well as the FKS methods use the fact that a real matrix element can only become singular when one final state parton becomes soft or when 2 partons become collinear, in

[16] $y_i \equiv \frac{1}{2} \ln \frac{E_i + p_{z,i}}{E_i - p_{z,i}}$ is called the rapidity of particle i.

which case the singular behaviour becomes universal and very well-known (see for instance the previous section on splitting functions). These methods are implemented in various Monte-Carlo programs at NLO, for instance MCFM [88, 89] and NLOJET++ [90] that we will both later use, FeynCalc/FormCalc [91], GOLEM [92], and a new generation of programs like Rocket [93], BlackHat [94], and HELAC/CutTools [95, 96] that allow one to compute diagrams with an arbitrary number of external legs at one-loop.

Another class of programs is parton-shower Monte-Carlo event generators. In this case, each parton in the initial state undergoes successive branchings to simulate ISR (section 1.3.3), and each final state parton is also "showered" in order to simulate FSR. For that, one has to compute a Sudakov form factor $\Delta(\tau_0, \tau)$ which gives the probability that there is no emission between scales τ_0 and τ. This form factor simply sums all the virtual diagrams and can be roughly written under the following form:[17]

$$\Delta_q(\tau_0, \tau) = e^{-\frac{\alpha_s}{2\pi}\int_{\tau_0}^{\tau}\frac{d\tau}{\tau}\int_{z_0}^{1-z_0} dz\, P_{qq}(z)}\,, \tag{1.90}$$

$$\Delta_g(\tau_0, \tau) = e^{-\frac{\alpha_s}{2\pi}\int_{\tau_0}^{\tau}\frac{d\tau}{\tau}\int_{z_0}^{1-z_0} dz\, (P_{qg}(z)+\frac{1}{2}P_{gg}(z))}\,, \tag{1.91}$$

for the quark and gluon form factors respectively. This is simply the exponentiation of the one gluon-emission probability that depends on the splitting functions (eq. 1.80). z_0 and τ_0 define the cut-offs for long-distance physics, or so called *unresolvable* emissions below which a gluon is too soft or too collinear to be detected. To take into account effect of coherent branching which manifests itself as angular ordering that we derived in section 1.2.4, one can define the scale τ to be related to the angle of the emission, for instance [97]

$$\tau = \frac{p_j.p_k}{E_j E_k} = 1 - \cos\theta_{jk}\,, \tag{1.92}$$

for a branching $i \to jk$ with j and k massless, and impose angular-ordered emissions $\tau_{n+1} < \tau_n$ for successive emissions. In this case, eqs. (1.90,1.91) correctly describe collinear emissions and the coherence property of soft emissions. The parton-showering process expressed in terms of Sudakov form factors Δ_q and Δ_g is implemented in parton-showers Monte-Carlo like HERWIG [97, 98] which uses eq. (1.92) as the ordering variable, and like PYTHIA [99] and Sherpa [100] which both take a different approach to angular ordering.

Another important issue is the possibility of merging parton-showers with fixed-order Monte-Carlo programs beyond LO. The problem is that when a parton-shower Monte-Carlo simulates the parton-showering process from a LO configuration, it also generates a part of the higher-order contributions, those that are soft or collinear enhanced. Therefore, one has to find a way to avoid double counting. How to achieve this requirement at NLO is nicely explained through a toy-model in [101]. This led to the creation of the MC@NLO program that we will also use later.

1.4 Some non-perturbative aspects of QCD

In sections 1.2−1.3, we mainly considered perturbative QCD. However, many important properties of QCD cannot be derived within the perturbative framework. In spite of that, they can usually be studied using a combination of theoretical understanding and experimental analysis. In this part, we review the non-perturbative aspects of QCD relevant for hadronic colliders, and in particular for LHC studies.

[17] α_s should depend on the emission's scale but, for this simple explanation, we do not take it into account.

1.4.1 Parton distribution functions

The Feynman rules studied in section 1.2.2 involve point-like objects, which are the quarks and gluons. So, to make an explicit perturbative QCD calculation, we assume we have incoming quarks or gluons, and we compute the amplitude to obtain a certain final state. However, in hadronic colliders, we always have hadrons and not quarks or gluons in the initial state. Said another way, the asymptotic states of perturbative QCD are not the same as those of the full QCD theory. To take this property into account, we usually define *parton distribution functions* $q(x, Q^2)$, which are non-perturbative objects. We can introduce parton distribution functions for each hadron, but with the LHC in mind, we will only consider the proton as the reference hadron. $q(x, Q^2)$ is then defined as the probability to find a quark with flavour q carrying a longitudinal fraction x of the proton's momentum when the proton is probed at scale Q^2. One can similarly define $g(x, Q^2)$ for the gluon distribution. These distributions can be studied for instance in Deep Inelastic Scattering (DIS) experiments, where electrons scatter off protons (fig. 1.19).

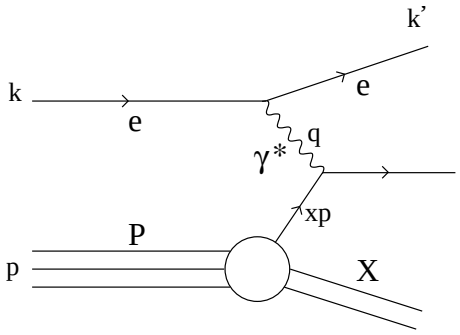

Figure 1.19: DIS event in the Feynman's parton model: the exchanged virtual photon hits one of the quarks that constitute the proton. The momentum fraction x carried by the hit quark can be calculated within the framework of the Feynman's parton model to be $x = \frac{Q^2}{2(p.q)}$, with $Q^2 = -q^2$. This can be experimentally measured using only the deviation of the electron because $q = k - k'$.

The parton distribution functions were first introduced by Feynman [102] to explain *Bjorken scaling* [103] of the structure functions of the proton (for example, see [3, 5]), which can be translated by the independence of the functions q with respect to Q^2 when $Q^2 \to \infty$. However, in QCD, this scaling can only be approximate. Indeed, a quark can emit a gluon, thus acquiring a large transverse momentum k_t with a probability $\alpha_s dk_t/k_t$. The integration of this quantity up to scale $\sim Q^2$ leads to contributions that behave like $\alpha_s \ln Q^2$ and are at the origin of the Bjorken scaling violation. The QCD picture of this effect is shown in fig. 1.20.

From a theoretical point of view, one can derive the evolution equation with Q^2 of the parton distribution functions. They are known as the Dokshitzer-Gribov-Lipatov-Altarelli-

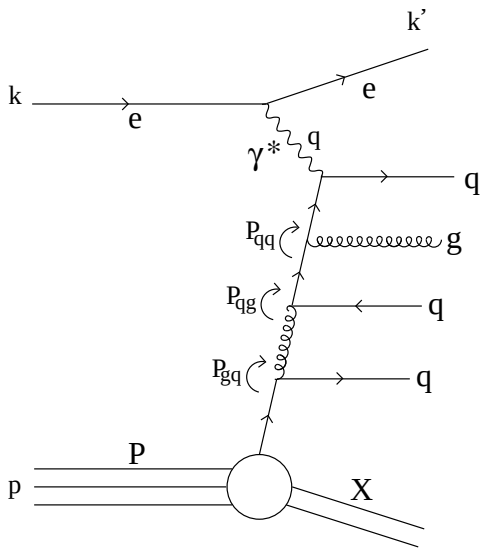

Figure 1.20: A more realistic picture of DIS in which the struck quark has acquired a non-zero transverse momentum due to successive parton splittings.

Parisi (DGLAP) equations [79, 104–106] and can be written in the following way:

$$Q^2\frac{\partial q_i}{\partial Q^2}(x,Q^2) = \frac{\alpha_s}{2\pi}\int_x^1 \frac{dz}{z}\sum_j \left(P_{q_iq_j}\left(\frac{x}{z},\alpha_s(Q^2)\right)q_j(z,Q^2) + P_{q_ig}\left(\frac{x}{z},\alpha_s(Q^2)\right)g(z,Q^2)\right)\,, \tag{1.93}$$

$$Q^2\frac{\partial g}{\partial Q^2}(x,Q^2) = \frac{\alpha_s}{2\pi}\int_x^1 \frac{dz}{z}\sum_j \left(P_{gq_j}\left(\frac{x}{z},\alpha_s(Q^2)\right)q_j(z,Q^2) + P_{gg}\left(\frac{x}{z},\alpha_s(Q^2)\right)g(z,Q^2)\right)\,. \tag{1.94}$$

The sum over j takes into account all the quarks and antiquarks flavours, so that we have to deal with $2n_f - 1$ coupled equations. The functions P_{ji} are called the *evolution kernels*, or the splitting functions, that we have already encountered in section 1.3.5. Here, the difference is that we take into account the virtual corrections, and therefore these functions become distributions whose expressions at LO are:[18]

$$P_{qq}(x) = C_F\left[\frac{1+x^2}{(1-x)_+} + \frac{3}{2}\delta(1-x)\right]\,, \tag{1.95}$$

$$P_{gq}(x) = C_F\left[\frac{1+(1-x)^2}{x}\right]\,, \tag{1.96}$$

$$P_{qg}(x) = T_R\left[x^2+(1-x)^2\right]\,, \tag{1.97}$$

$$P_{gg}(x) = 2C_A\left[\frac{x}{(1-x)_+} + \frac{1-x}{x} + x(1-x)\right] + 2\pi\beta_0\delta(1-x)\,, \tag{1.98}$$

with β_0 given by eq. (1.35). We use the same notation as in eqs. (1.81−1.84) because, away from $x = 1$, they are the same functions which can still be interpreted as a probability

[18] $T_R = \frac{1}{2}$ is the usual normalisation factor of the t^A matrices in QCD, see appendix A.

density for partons splitting. The "plus" prescription has the following meaning: for every smooth function f, we get

$$\int_0^1 dx \, \frac{f(x)}{(1-x)_+} = \int_0^1 dx \, \frac{f(x) - f(1)}{1-x} \,, \tag{1.99}$$

and for $x < 1$,

$$\frac{f(x)}{(1-x)_+} = \frac{f(x)}{1-x} \,. \tag{1.100}$$

Eqs. (1.95−1.98) give only the first order terms of a series expansion in α_s. The evolution kernels are actually known at NLO [107–109] and up to NNLO in the unpolarised case [110, 111].

In contrast to the QED case, we cannot find the exact physical solution when solving these differential equations because the initial condition $q(x, Q_0^2)$ at a given scale $Q = Q_0$ is non-perturbative, thus analytically unknown, and has to be extracted from experiment. An analytical formula can be guessed for $q(x, Q_0^2)$ and fitted with the experimental results. This is done by different fitting collaborations like CTEQ [112] and MRST/MRSW [113]. With this in hand, one can solve the DGLAP equations to obtain $q(x, Q^2)$ at any value of Q^2 large enough to remain in the perturbative region. The DGLAP equations led to many discussions about its numerical solutions (see for instance [114–118]). The reason for such a keen interest is because the parton distribution functions are at the heart of the predictions one can make in collisions involving hadrons, so that an accurate analytical or numerical knowledge is required. The main property that is used to compute physical cross-sections is called *factorisation*. It means that we can separate the long and short distance physics, i.e. the perturbative and non-perturbative parts of QCD. This has been proved to all-orders in perturbation theory using 2 different methods (see [119] for a review).

In DIS where a proton with momentum P collides with an electron of momentum k at a characteristic scattering scale Q, this property translates mathematically as the expression of the corresponding total cross-section $\sigma(P, k)$:

$$\sigma(P,k) = \sum_{f=q_i,g} \int_0^1 dx \, f(x, \mu_F^2) \hat{\sigma}_f \left(xP, k, \frac{Q^2}{\mu_F^2} \right) . \tag{1.101}$$

f runs over all the partons flavours. $\hat{\sigma}$ is the cross-section calculated from perturbative QCD, with a parton of momentum xP in the initial state instead of the proton itself. μ_F is called the *factorisation scale*, which separates the long and short distance physics. The long-distance physics reveals itself in the perturbative evolution of the parton distribution functions as collinear singularities. Because they arise in the initial state, they are not taken into account by the Kinoshita-Lee-Nauenberg theorem and remain at the end of the calculation. Roughly speaking, we factorise them in the $f(x, \mu_F^2)$ function if they involve a transverse momentum smaller than μ_F. Of course, physical cross-sections should not depend on μ_F but, as we truncate the perturbative series, we actually observe a dependence on it that we have to examine when computing uncertainties.

One of the most important concepts for parton distribution functions is that of *universality*. It means that if we extract the functions $f(x, \mu_F^2)$ from DIS experiments, we can use these functions to study hadron-hadron collisions. In other words, parton distribution functions should not depend on the process under study. For instance, if we collide 2 protons

p with momenta P_1 and P_2, the resulting total cross-section $\sigma(P_1, P_2)$ for some hard process $pp \to X$ ($X = Z$, WW, 2 jets,...) is:

$$\sigma(P_1, P_2) = \sum_{f_1, f_2 = q_i, g} \int_0^1 \int_0^1 dx_1 dx_2 \, f_1(x_1, \mu_F^2) f_2(x_2, \mu_F^2) \hat{\sigma}_{f_1 f_2 \to X} \left(x_1 P_1, x_2 P_2, \frac{Q^2}{\mu_F^2} \right) , \tag{1.102}$$

where f_1 and f_2 can be extracted from DIS experiments.

1.4.2 Hadronisation

In section 1.3.3, we examined the parton-showering process that develops both in the initial state and the final state of the hard collision. In Monte-Carlo generators, the final-state parton-shower is implemented until a scale Q_0 is reached, below which we enter the non-perturbative regime where the final state partons are transformed into the observed hadrons. This process is called *hadronisation*. It is fundamentally a non-perturbative property of QCD as it involves the transition from partons to hadrons. It may be seen as the inverse process of extracting a parton from the proton using parton distribution functions. Here, we have to deal with *fragmentation functions* D_i^h instead. $D_i^h(z)$ represents the probability for a parton i to fragment into a particular hadron h carrying the fraction z of the parton's energy. These functions obey DGLAP like equations, i.e. their evolution with energy is controllable using perturbation theory. We will not enter into details here.

Perturbation theory seems to work rather well down to very low scales of ~ 1 GeV, i.e. a few times Λ_{QCD}. This leads to the hypothesis of *local parton-hadron duality* [120], which states that the flow of momentum and quantum numbers at the hadron level tends to follow the flow established at the parton level. Of course, this is only an approximation because the formation of hadrons induces an irreducible smearing of order Λ_{QCD}.

The string model [121–124] is one of the two important hadronisation models that follow the local parton-hadron duality. The basic property of this model is the following: when a colour connected $q\bar{q}$ pair separates itself, it loses some energy to the colour field which is supposed to collapse into a stringlike configuration. The string finally breaks up into hadron-sized pieces through spontaneous $q\bar{q}$ pair production in its intense colour field. Each gluon that remains at the end of the parton showering process produces a kink on the string which changes the angular distribution of hadrons in a way which is in good agreement with experiment (see for instance [125]).

Another important hadronisation model is the cluster model [126–128], which relies on the formation, after the parton-showering process, of colour singlet clusters of partons which further decay into hadrons. An example of such clusters can be colour-connected neighbouring $q\bar{q}$ pairs (assuming all the final state gluons split into $q\bar{q}$). This model also usually leads to good agreement with experiment.

1.4.3 Underlying-event and pile-up

Underlying event (UE) and pile-up (PU) are important aspects of QCD specific to hadronic colliders. They are really simple to describe in an intuitive way but very hard to understand analytically: UE and PU concern soft interactions and therefore cannot be dealt with using perturbative QCD. As for the hadronisation process, one thus has to rely on models that are

fitted to experimental data. For the purpose of this thesis, it will be sufficient to describe UE and PU without entering into the details of these models.

Let us first consider the UE. When two protons collide, we saw in section 1.4.1 that two partons participate in the hard interaction, one from each proton. The probability for one particular parton to interact is proportional to the corresponding parton distribution function. However, it seems very unlikely that *only* one parton from each proton interacts. Several other partons can also interact between the two protons. So one has to face with *multiple parton interactions*. But it is also very unlikely that 2 different parton interactions lead to a hard process in the same proton-proton collision. Instead, these additional interactions result in soft emissions of a few GeV. Several models exist to simulate them [129–133]. Each model usually has a certain number of free parameters in it that have to be tuned in order to give an accurate description of the experimental data (see for instance [134]). The simulation of multi-parton interactions with their tunes is implemented in Monte-Carlo event generators like PYTHIA [99], HERWIG with JIMMY [130], SHERPA [100], and Phojet [135].

We now turn to PU. At the LHC, the proton beam consists of bunches of protons. Therefore, if the beam is sufficiently collimated or dense, it often happens that several protons interact during the same bunch crossing. As for the UE, it is very unlikely that two different proton-proton interactions give rise to a hard interaction in one bunch crossing, so that PU is also made of soft particles. But it is believed that one PU collision results in less hadronic activity than UE. Indeed, it seems logical to state that the collision which leads to the hard interaction is more central than the other ones, i.e. UE involves the whole proton structure whereas PU interactions are more peripheral (fig. 1.21). However, there can be many different proton-proton collisions in the same bunch crossing. PU will become very important during the high luminosity running of the LHC: PU activity is expected to reach values up to $10 - 20$ GeV per unit area (in the (y, ϕ) plane) [136, 137] whereas UE activity will range around $2 - 3$ GeV per unit area [138]. Notice that this PU activity corresponds to roughly 20 collisions per bunch crossing [138]. PU interactions are modelled to be of the minimum-bias type in PYTHIA (see [99] for more details).

UE and PU are very important sources of noise at the LHC. They can really distort jet mass reconstructions for instance by adding a large amount of additional activity in the jet's neighbourhood. An important aspect of this thesis concerns the way one can remove this kind of noise using a subjet analysis procedure.

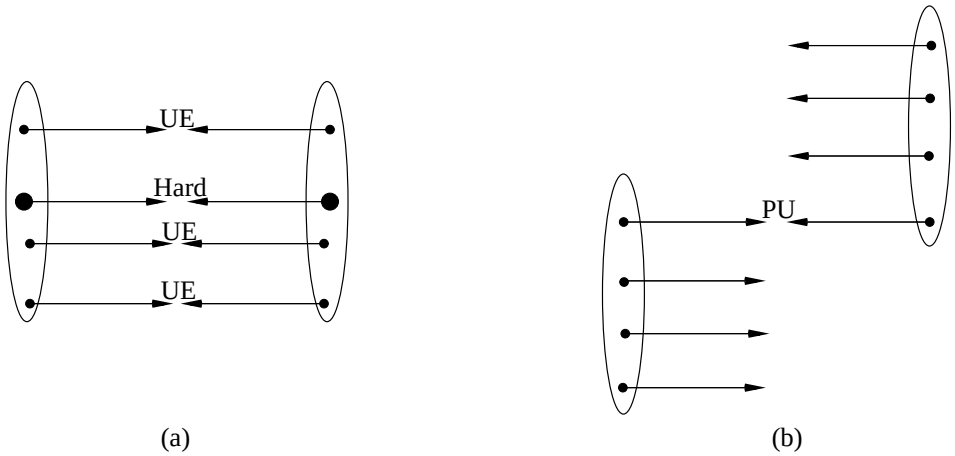

Figure 1.21: (*a*) Central proton-proton collision involving multiple parton interactions leading to the hard process and to several UE interactions; (*b*) Peripheral proton-proton collision leading to one PU interaction whereas the other partons do not participate in any interaction.

Chapter 2

Boosted massive particles decaying hadronically

One major issue at the LHC, and at any collider in general, is to identify (new) massive particles in order to study their properties (mass, spin, couplings,...) or to tag an event (see later). Many of the particles of interest nowadays have a very short lifetime and decay before reaching the detectors. Therefore, the question that arises is to know how to identify them using their decay products. There are essentially two kinds of decays:

- *leptonic decays* where the massive particle decays into leptons and/or neutrinos (like $Z \to \mu^+\mu^-$ or $W^+ \to e^+\nu$)

- *hadronic decays* where the massive particle decays into quarks (like $H \to b\bar{b}$ or $W^+ \to u\bar{d}$)

A particle can undergo a 3-body decay (or even more), like in the case of the top quark where we have for instance $t \to bW^+ \to be^+\nu$.

Leptonic decays are usually more easily tagged because electrons and muons can be very efficiently reconstructed in the detectors [139, 140]. To recognise a Z boson decaying into $\mu^+\mu^-$, one just has to compute the invariant mass of the pair and if it is around $M_Z \simeq 91$ GeV, then they likely originated from a Z boson. In contrast, hadronic decays are much harder to study. The first reason is that there is often a large number of hadrons in an event coming from the parton showering process (cf section 1.3.3), and reconstructing the branching history[1] is not an easy task (jet algorithms do such a job, but there's an ambiguity in the one to use, with all their parameters which should be chosen adequately according to the process under study [141]). Moreover, there is also noise from soft particles due to pile-up and underlying events (see section 1.4.3), which is very difficult to suppress, although some methods already exist [138].[2] Finally, there is a very large QCD background from hard processes like, for instance, $g \to b\bar{b}$ which can look similar to $Z \to b\bar{b}$. All of these make hadronic decays difficult to study.

[1] Of course, this is a classical point of view. Due to quantum interferences, there is not really a branching history, but it can be thought of this way.

[2] The filtering analysis that we will discuss in the next chapter is another method to reduce the effect of this kind of noise.

In this chapter we are going to explain how hadronic decays can be treated, considering at the moment only the reduction of the hard QCD background.[3] In section 2.1 we examine the general method to implement this reduction, and in section 2.2 we focus more particularly on the light Higgs boson when it decays into $b\bar{b}$.

2.1 Jets from a massive particle vs QCD jets

2.1.1 A simple introductory example

We first take as an example non-boosted $t\bar{t}$ production, which has been very well studied at Tevatron [142–144], in order to show the generality of this topic and to emphasise the differences with boosted processes that are a central part of this thesis. The top quark decays before it can hadronise. Therefore, to recognise a $t\bar{t}$ event, one has to study the possible decays of the top. This leads us to consider 3 different final state configurations for $t\bar{t}$ production, usually called 3 different *search channels* (fig. 2.1):

The *all-leptonic channel*: the 2 W's decay leptonically, so that the final state consists of 2 b quarks (seen as jets after parton-showering and hadronisation), 2 leptons (where we only consider electrons and muons because τ leptons are massive enough to decay hadronically and thus need separate study in general), and 2 neutrinos identified as missing energy whose transverse momentum can be computed using momentum conservation. This channel has a clean signature and backgrounds are not very large (with respect to QCD backgrounds [144, 145]), but it suffers from a low branching ratio ($\sim 5\%$, if we do not take the τ leptons into account) and the fact that the 2 W's cannot be fully reconstructed.

The *semi-leptonic channel*: one W decays leptonically and the other one hadronically. So what we want to see in the detector is 1 lepton, missing energy, and roughly 4 jets (2 from the b's and 2 from the W). This channel usually gives the best results with its large branching ratio ($\sim 30\%$) and its rather clean signature. But if we look at a 4 jet event like the one in fig. 2.2, we see that we get a combinatorial background due to the fact that we do not know which jets come from the W decay, and which ones come from the b quarks.[4] So, to reconstruct the W, do we have to recombine jet 1 with jet 2, or jet 1 with jet 3, or ...?

The *all-hadronic channel*: the 2 W's decay hadronically. So we expect to see up to 6 jets. This channel is interesting in the sense that we can in principle fully reconstruct both of the W bosons, but in spite of its large branching ratio ($\sim 44\%$), it is a challenging channel for $t\bar{t}$ studies because the QCD background is very large and the combinatorial background is important.

This non-boosted example allowed us to review some different ways to tag an event. We are now going to focus on channels involving hadronic decays, like in the semi-leptonic and fully hadronic channels in $t\bar{t}$. There are two reasons for that. Firstly, as several studies have already shown [146–148],[5] hadronic decays will play a very important role at the LHC and it will become necessary to be able to deal with them. Secondly, we will describe in the next chapter a new method using jet substructure that allows an efficient reconstruction of

[3] The other aspects will be seen in the next chapter.

[4] b-tagging is used to solve this problem, but for more general processes involving no b-quarks, this would not be the case.

[5] plus many other references that will be given in the following chapters.

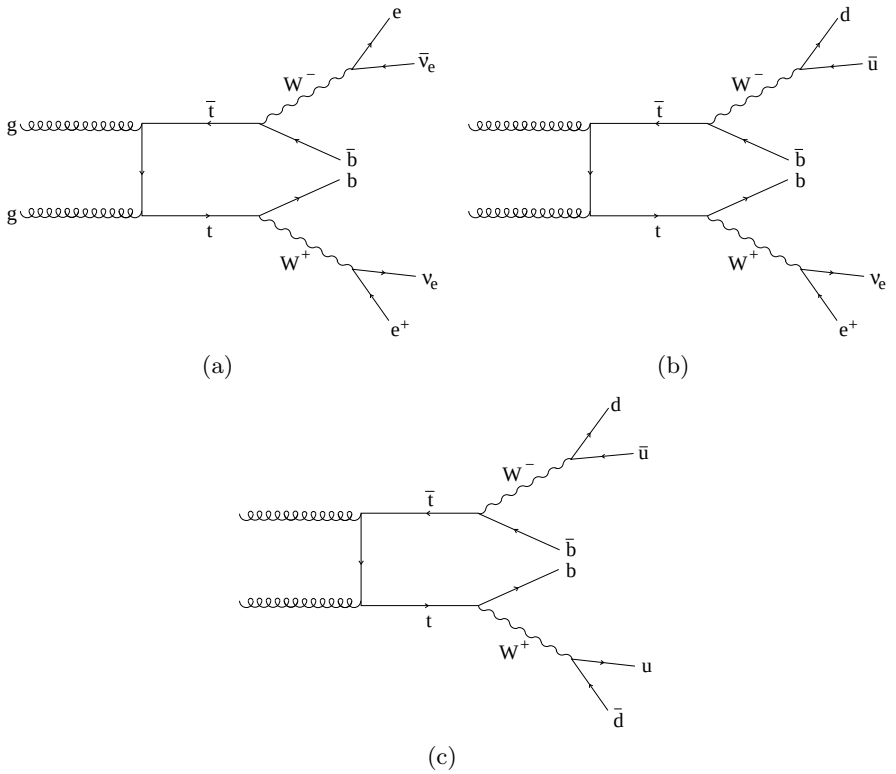

(a) (b) (c)

Figure 2.1: $t\bar{t}$ production from a gg process and its analysis through (a) the dilepton channel, (b) the semi-leptonic channel, and (c) the all-hadronic channel

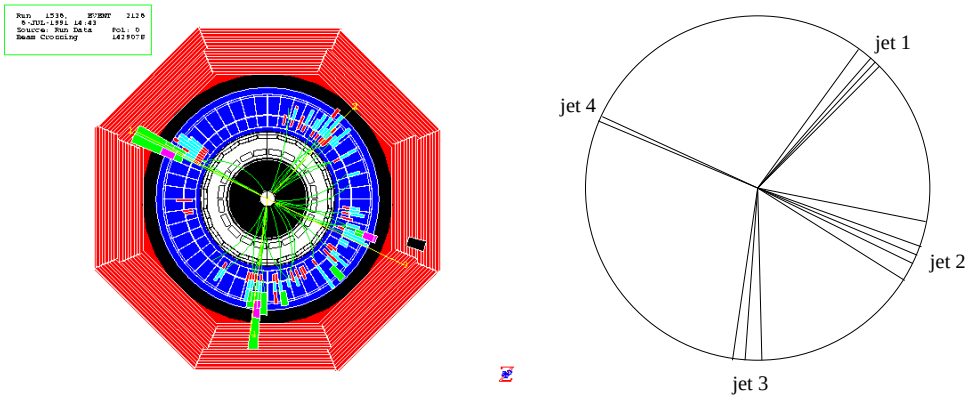

(a) (b)

Figure 2.2: (a) Example of a four jet event from SLAC and (b) its schematic representation

boosted massive particles decaying hadronically as well as an efficient reduction of the QCD background. Therefore, this chapter can be seen as an introduction to that topic.

2.1.2 Considering boosted massive particles

With the LHC starting, we will be able to reach centre of mass energies of several TeV in the hard parton-parton interaction. Therefore, LHC events may either produce very massive new particles, like SUSY ones, or *very boosted* Standard Model (SM) objects like vector bosons, "very boosted" meaning a large transverse momentum p_t compared to the particle's mass M, $p_t \gg M$. Concerning the new particles, most models predict that they will decay into SM particles.[6] A large difference of mass between the new massive particles and the SM ones, or the Lightest Supersymmetric Particle (LSP), also implies that SM particles are very boosted. Therefore, in many cases, we will have to face high-p_t (massive) objects at the LHC. At first sight it can seem that it is a problem as jets from boosted massive particles are collimated and therefore look similar to QCD splittings (because of the collinear divergence of QCD, see section 1.3.1). However, as a high-p_t splitting usually results in only one jet instead of two if the radius of the jet algorithm is large enough,[7] one avoids the combinatorial background mentioned above.

So, henceforth, we will essentially consider high-p_t jets. The goal of this analysis is to be able to distinguish jets from a boosted massive particle from QCD jets.

2.1.3 Use of a discriminating variable: the jet mass

Hadronic decays are challenging because QCD backgrounds can swamp the signal. For example, $W^+ \to u\bar{d}$ which gives 1 jet in the final state (boosted case), can be very hard to distinguish from a QCD jet that contains for instance a hard splitting $g \to gg$. One variable that can be used to gain an information is to compute the mass of the jets, which is a powerful discriminator as the mass distribution is of course very different for a QCD jet and a W jet (fig. 2.3).

As can be seen on these plots, approximately 10% and 16% of the quark and gluon jets respectively are kept in a mass range around the W mass ($M_W \pm 10$ GeV) while 60% of the W jets are kept. Notice the tails in the W plot: the tail on the left, towards low masses, results from the loss of perturbative radiation as well as from events where the W decays into 2 separated jets, whereas the tail towards high masses is due to hadrons entering the jet and which have nothing to do with it (essentially initial state radiation here, though in real life underlying event and pile-up can deeply change the shape of the mass distribution, see next chapter). This cut on the jet mass is a first important step to reduce the background but is not enough, as the QCD background cross-section is usually orders of magnitude above the signal cross-section.[8] So we need to go further, using another discriminating variable.

[6] with the exception of the dark matter candidate, which should be stable.

[7] For a splitting $i \to jk$, the angular distance R_{jk} between j and k is $\mathcal{O}\left(\frac{M_i}{p_{t_i}}\right)$, see eq. (2.7) later.

[8] for instance, with a minimum p_t of 200 GeV, the WH signal that will be studied later has a cross-section around 70 fb, whereas $W+$ jet, which is its major background for a low mass Higgs boson, has a cross-section around 180000 fb. Of course, b-tagging and adequatly chosen cuts on transverse momentum or rapidity are also used to reduce this large difference.

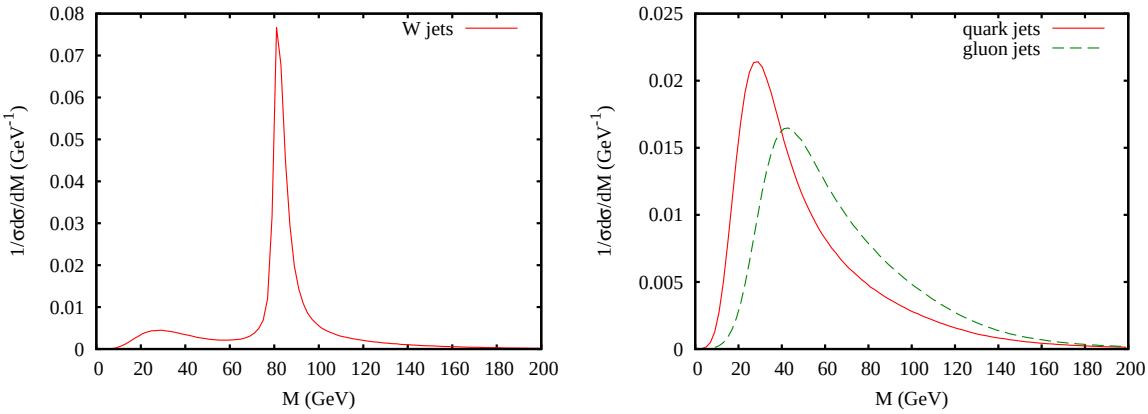

(a) (b)

Figure 2.3: Mass distribution for (a) W jets, and (b) QCD jets. To generate these plots, we used PYTHIA 6.4 with $p_{t_{min}} = 200$ GeV, and k_t algorithm with $R = 1$. Notice that the underlying event was switched off. For each event, only the hardest jet was considered.

2.1.4 Another discriminating variable

After averaging over the azimuthal angle ϕ, only 2 independent variables remain to characterise a branching $i \to jk$: the energy fraction z and the angle θ (fig. 2.4), where z is defined as

$$z = \min\left(\frac{E_j}{E_i}, \frac{E_k}{E_i}\right) , \tag{2.1}$$

with E_l the energy of particle l. This definition implies $0 < z < \frac{1}{2}$, and in the boosted limit, when particles j and k become almost collinear, it can be equivalently written in terms of transverse momenta (sometimes more convenient because invariant under longitudinal Lorentz boosts):

$$z = \frac{\min(p_{t_j}, p_{t_k})}{p_{t_j} + p_{t_k}} . \tag{2.2}$$

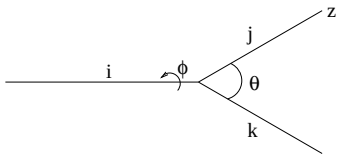

Figure 2.4: kinematic variables for a branching $1 \to 2$

With the help of a jet algorithm, eq. (2.1) can be used in Monte-Carlo studies or experimentally. However, for theoretical studies, it can be sometimes more convenient to consider z as the energy fraction carried by a particular decay product (like the b quark as opposed to $\bar{b}$, or the gluon as opposed to a quark), as we did for instance in section 1.3.5 when we talked about splitting functions. In this case, z can be in the range $0 < z < 1$. In all this chapter, we may switch from one definition to another, but the physics obviously remains the same.

Coming back to the mass variable, we can write it as a combination of z and θ:

$$M^2 \quad = \quad 2z(1-z)E^2(1-\cos\theta)\,. \tag{2.3}$$

Therefore, once M is known, we can either choose z or θ, or any other combination of these two variables different from M. This variable must have a powerful discriminating strength. For instance, due to the collinear divergence of QCD and the fact that the massive particles are boosted, θ is not very convenient because it will be small for both QCD jets and boosted massive jets. However, we can use instead the soft divergence of QCD, which tells us that z is small most of the time when a gluon is emitted, which means that the z distribution is peaked towards 0 for QCD jets whereas it is not the case for massive particles jets (fig. 2.5(a)). z is convenient because directly related to splitting functions.

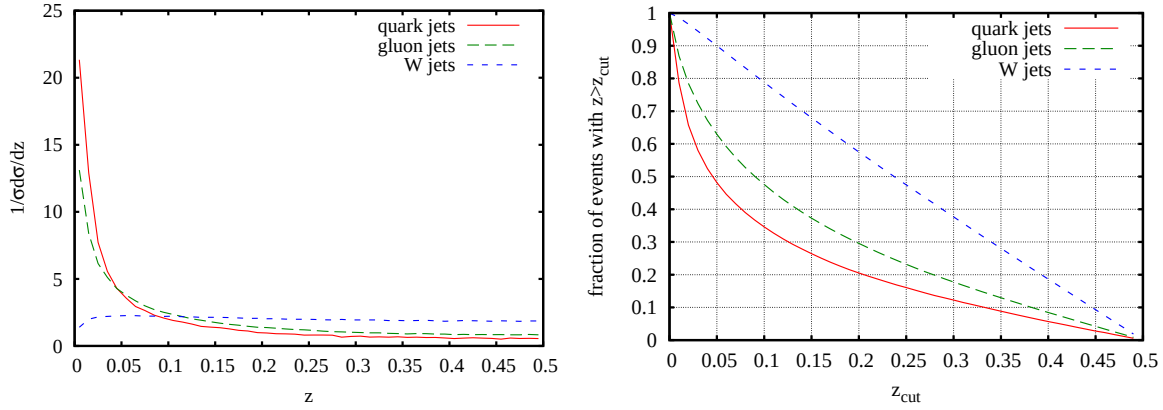

(a) (b)

Figure 2.5: (a) z distribution for W, quark, and gluon jets respectively using PYTHIA with a large $p_{t_{min}}$ of 1000 GeV in order not to be constrained by kinematic limits. For each event, we considered the hardest jet and we applied to it a Mass Drop (MD) analysis (but with $y_{cut} = 0$), whose details will be described in the next chapter. We then computed the z fraction for each event whose hardest jet after the MD has a mass within $[M_W - 10$ GeV, $M_W + 10$ GeV$]$. The clustering was done using the C/A algorithm with $R = 0.8$. Notice that PYTHIA does not take into account spin correlations for the W decay in the WW process that was used to generate the W distribution, so its distribution is like the one for a massive scalar particle; (b) fraction of events which would pass a cut $z > z_{cut}$ as a function of z_{cut} for W, quark, and gluon jets.

Demanding a z greater than z_{cut} allows one to significantly reduce the QCD background with respect to the signal, here W boson production. If z is too small, i.e. $z < z_{cut}$, then we say it's background, otherwise we keep it as signal. For instance, using $z_{cut} = 0.1$, fig. 2.5(b) shows that 79% of the signal remains whereas we only keep about 34% and 48% of the quark and gluon jets respectively. In the next section, we will see what this implies in terms of signal significance.

One should be aware that we can imagine other variables to study a splitting [149] but they are almost all equivalent for a $1 \to 2$ process. In spite of that, let us mention the k_t distance d_{jk} (eq. (1.67)) which may be used instead of z. Applying eq. (2.7), which will be

seen in the next section, we find in the boosted limit:

$$\begin{aligned} d_{jk} &\equiv \min\left(p_{t_j}^2, p_{t_k}^2\right) \Delta R_{jk}^2 \,, \\ &\simeq z^2 p_{t_i}^2 \frac{1}{z(1-z)} \frac{M_i^2}{p_{t_i}^2} \,, \\ &\simeq \frac{z}{1-z} M_i^2 \,. \end{aligned} \tag{2.4}$$

Therefore, the dimensionless variable

$$y_{jk} \equiv \frac{d_{jk}}{M_i^2} \,, \tag{2.5}$$

is equivalent to z when $p_{t_i} \gg M_i$ at leading order.

2.1.5 Theoretical consequence of the z cut

Before continuing discussing the importance of the z cut, we derive a very simple but useful formula that we will often refer to in this thesis. For that we consider a splitting $i \to jk$ of a massive particle i into 2 massless particles j and k. Let M_i and p_t respectively be the mass and the transverse momentum of particle i. We define z to be the energy fraction of particle i carried by particle j. We can write:

$$M_i^2 = 2z(1-z)p_t^2 \left(\cosh \Delta y_{jk} - \cos \Delta\phi_{jk}\right) \,, \tag{2.6}$$

with $\Delta y_{jk} = y_j - y_k$ and $\Delta\phi_{jk} = \phi_j - \phi_k$. In the boosted limit, $M_i \ll p_t$, or equivalently $\Delta y_{jk}, \Delta\phi_{jk} \ll 1$, one can deduce:

$$R_{jk}(z) \simeq \frac{1}{\sqrt{z(1-z)}} \frac{M_i}{p_t} \,, \tag{2.7}$$

where we remind the reader that R_{jk} is the angular distance in the (y, ϕ) plane between j and k (eq. (1.71)):

$$R_{jk}^2 = \Delta y_{jk}^2 + \Delta\phi_{jk}^2 \,. \tag{2.8}$$

We now return to the cut on z analysed in section 2.1.4. The question that arises is the following: what do we really gain in terms of reduction of QCD backgrounds by using a cut on z? More precisely, given a mass M_0, we want to compute the probability to find a quark jet with a mass M in the range $\left[M_0 - \frac{\Gamma}{2}, M_0 + \frac{\Gamma}{2}\right]$, $\Gamma \ll M_0$, depending on whether we impose a z cut or not. For this purpose, we recall that the probability for a quark with (virtual) invariant mass squared t to split into a quark and a gluon with energy fraction z is given by (eq. (1.80)):

$$\frac{d^2P}{dtdz} = \frac{\alpha_s}{2\pi} \frac{P_{gq}(z)}{t} \,, \tag{2.9}$$

so that

$$\frac{d^2P}{dMdz} = \frac{\alpha_s}{\pi} \frac{P_{gq}(z)}{M} \,. \tag{2.10}$$

We assume that we cluster the event using a jet algorithm with a certain radius $R_0 \sim 1$. As we still work in the boosted limit, we require the quark and the gluon to be in the same

jet. Thus, if we define M and p_t to be respectively the jet mass and the jet transverse momentum, eq. (2.7) implies in a sufficiently boosted limit where $\frac{M^2}{R_0^2 p_t^2} \ll 1$:

$$z > \frac{M^2}{R_0^2 p_t^2}\,. \tag{2.11}$$

Therefore:

$$\begin{aligned}\frac{1}{\sigma}\frac{d\sigma}{dM_0} &= \int dM dz \frac{d^2P}{dM dz}\delta(M - M_0)\,,\\ &= \frac{\alpha_s C_F}{\pi}\int \frac{dM}{M}\int_{\frac{M^2}{R_0^2 p_t^2}}^1 dz \frac{1+(1-z)^2}{z}\delta(M-M_0)\,.\end{aligned} \tag{2.12}$$

The upper bound should be $1-\frac{M^2}{R_0^2 p_t^2}$ with our current definition for z, but replacing it with 1 leads to small corrections scaling like $\mathcal{O}\left(\frac{M^2}{p_t^2}\right)$ that we neglect here. Without any additional cut on z, we thus obtain:

$$\frac{1}{\sigma}\frac{d\sigma}{dM} = \frac{\alpha_s C_F}{\pi}\frac{1}{M}\left(4\ln\left(\frac{R_0 p_t}{M}\right) - \frac{3}{2} + \mathcal{O}\left(\frac{M^2}{p_t^2}\right)\right)\,. \tag{2.13}$$

Therefore, the probability $P_\Gamma(M_0)$ for the quark jet to be in an interval of width Γ around M_0 can be approximately written

$$P_\Gamma(M_0) \simeq \frac{\alpha_s C_F}{\pi}\frac{\Gamma}{M_0}\left(4\ln\left(\frac{R_0 p_t}{M_0}\right) - \frac{3}{2}\right)\,. \tag{2.14}$$

As $\Gamma \ll M_0$, we can write the result as the product of the interval width with the differential distribution evaluated at M_0. Now, if we impose $z > z_{cut}$, with $z_{cut} > \frac{M^2}{4p_t^2}$, then eq. (2.12) has to be replaced by:

$$\frac{1}{\sigma}\frac{d\sigma}{dM_0} = \frac{\alpha_s C_F}{\pi}\int \frac{dM}{M}\int_{z_{cut}}^1 dz \frac{1+(1-z)^2}{z}\delta(M-M_0)\,. \tag{2.15}$$

Once again, we neglect terms of order z_{cut}, so that the upper bound for the integral is 1 instead of $1 - z_{cut}$. This leads to

$$\frac{1}{\sigma}\frac{d\sigma}{dM} = \frac{\alpha_s C_F}{\pi}\frac{1}{M}\left(2\ln\left(\frac{1}{z_{cut}}\right) - \frac{3}{2} + \mathcal{O}\left(z_{cut}\right)\right)\,. \tag{2.16}$$

We immediately notice that the effect of the z cut is to replace the large logarithm $\ln\left(\frac{R_0^2 p_t^2}{M^2}\right)$ in the limit $p_t \gg M$ by $\ln\left(\frac{1}{z_{cut}}\right)$. This effect is shown in fig. 2.6.

Consequently, the probability for a quark jet to be in a mass range of width Γ around M_0 and also pass the z cut is given by:

$$P_\Gamma(M_0, z_{cut}) \simeq \frac{\alpha_s C_F}{\pi}\frac{\Gamma}{M_0}\left(2\ln\left(\frac{1}{z_{cut}}\right) - \frac{3}{2}\right)\,. \tag{2.17}$$

As p_t increases, the probability to find a quark jet that passes both cuts on mass and z does not change much, whereas it increases logarithmically if we only impose the mass cut.

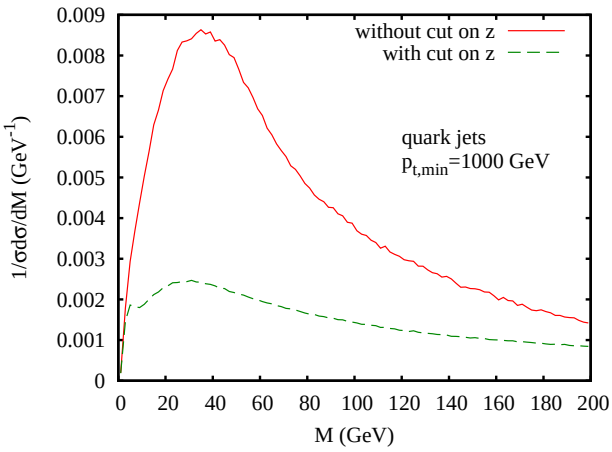

Figure 2.6: Mass distribution for quark jets at $p_{t_{min}} = 1000$ GeV, obtained with PYTHIA in the same way as for fig. 2.5. We compare the full mass distribution to the curve obtained when we only consider the jets that fulfil the condition $z > z_{cut}$, with $z_{cut} = 0.1$.

Consequently, selecting jets with $z > z_{cut}$ among all the QCD jets that passed the mass cut implies that we only keep a fraction f of background events given by

$$\begin{aligned} f &= \frac{P_\Gamma(M_0, z_{cut})}{P_\Gamma(M_0)} \\ &\simeq \frac{2\ln\left(\frac{1}{z_{cut}}\right) - \frac{3}{2}}{4\ln\left(\frac{R_0 p_t}{M_0}\right) - \frac{3}{2}} \end{aligned} \tag{2.18}$$

This very simple analysis would have to be supplemented with a resummed calculation for very high $\frac{p_t}{M}$ values, but here we get the main idea, which is that the cut on z kills one large logarithm, as long as z_{cut} not too small.

2.2 Application to light Higgs searches for the LHC: an introduction

In this section, we would like to apply these ideas to Higgs searches at the LHC. When it is light (i.e. M_H around 120 GeV, just above the LEP2 exclusion limit [21]), we saw in section 1.1.3 that it mainly decays hadronically, roughly 70% of the time according to HDECAY [27]. After reviewing the main search channels at the LHC, we will focus on Higgs production in association with a vector boson in order to estimate an optimal z_{cut} in this case. This is in view of the following chapter which will use the basic concepts that will be introduced here.

2.2.1 Higgs boson studies for the LHC

As was explained in section 1.1.2, the Higgs boson plays a very important role in the Standard Model as it is the remnant of electroweak symmetry breaking, allowing particles

to acquire a mass. Moreover, since it is the only particle of the Standard Model that is still to be observed, there has been a large amount of work in computing more precisely its production cross-sections (because of the information we want to extract from them), while refining the procedures that should allow one to observe it, if it exists, at high energy colliders experiments.

There are essentially 4 ways to produce a Higgs at hadron colliders [14], as depicted in figure 2.7. Fig. 2.8 shows their respective cross-sections at the LHC. All production modes have been computed exactly at NLO in QCD: gluon-gluon fusion [150, 151], vector boson fusion [152,153], associated production with a vector boson [154] and with a $t\bar{t}$ pair [155,156]. It is worth noticing that the gluon-gluon fusion process has been calculated up to NNLO in the heavy top quark limit [157–159] with NLO electroweak corrections [160–163], and that the WH/ZH production modes have been computed exactly at NNLO in QCD [157,164,165] with also NLO electroweak corrections [166]. Monte-Carlo programs have been written dedicated to NNLO Higgs production (see for instance the program HNNLO [167] or FEHiP [168]). This illustrates how much importance is given to the Higgs search.

Because it is so important in the Standard Model, we saw in section 1.1.3 that high-energy experiments at LEP or Tevatron have devoted significant resources to searching for the Higgs boson over the past years, leading to various constraints on its mass. In the meantime, two of the LHC experiments, ATLAS and CMS, have devoted part of their studies to predicting their respective sensitivity to a potential Higgs discovery [140, 169]. This sensitivity depends on the experimental apparatus (resolution of the detectors, LHC luminosity,...) as well as on theoretical considerations (how well the properties of QCD allow one to distinguish signal from backgrounds).

To do that, the ATLAS and CMS experiments rely on Monte-Carlo programs like PYTHIA or HERWIG to simulate signal and backgrounds in realistic events, and on other programs like Geant4 [170] to simulate the response and the geometry of the various detectors. Combining these programs leads to realistic predictions of the observations that may be made at the LHC. During the last few years, the two experiments published technical reports on the results of such simulations for many physics topics [140,169], and in particular for Higgs searches. For instance, the results for the ATLAS experiment can be summed up in fig. 2.9.

The high significance that one can notice in fig. 2.9 when $M_H = 150 - 180$ GeV comes from the large $H \to WW$ branching ratio in this mass range and the clean signature of such a process when the 2 W's decay leptonically. On the other hand, the Higgs boson seems far more difficult to observe when its mass is below 130 GeV. The reason for that is the dominant decay mode into $b\bar{b}$ of the Higgs when it has a low mass (fig. 1.2): such a signal being completely swamped by very large continuum $b\bar{b}$ production from QCD, it is not easily recognisable. That is why, in spite of their low branching ratios, experiments instead rely on $H \to \gamma\gamma$, $H \to \tau\tau$ and $H \to ZZ^*$ decay modes to efficiently tag the Higgs decay products, as they have a much cleaner signature.

Nevertheless, if the Higgs mass is low (below 130 GeV, which we recall is favoured by precision electroweak fits), this picture is not so satisfactory. Not only the combined significance is not large, but also the $Hb\bar{b}$ coupling, which drives the main decay channel, cannot be measured experimentally [171].[9] With this in mind, one could imagine recovering

[9]One could think of diffractive Higgs production to measure the coupling, but the conclusion from the ATLAS Forward Report concerning the $H \to b\bar{b}$ decay is pretty definitive: "Our current understanding

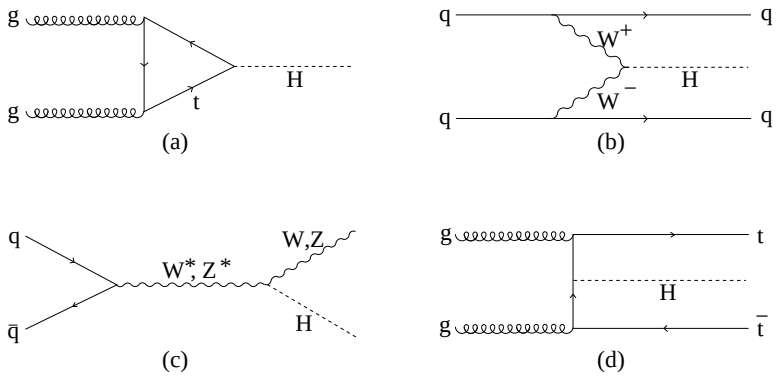

Figure 2.7: The various leading order Feynman diagrams contributing to the production of the Higgs boson: (a) gluon-gluon fusion through a top loop, (b) associated production with 2 jets, (c) associated production with vector bosons (W or Z), (d) associated production with a $t\bar{t}$ pair.

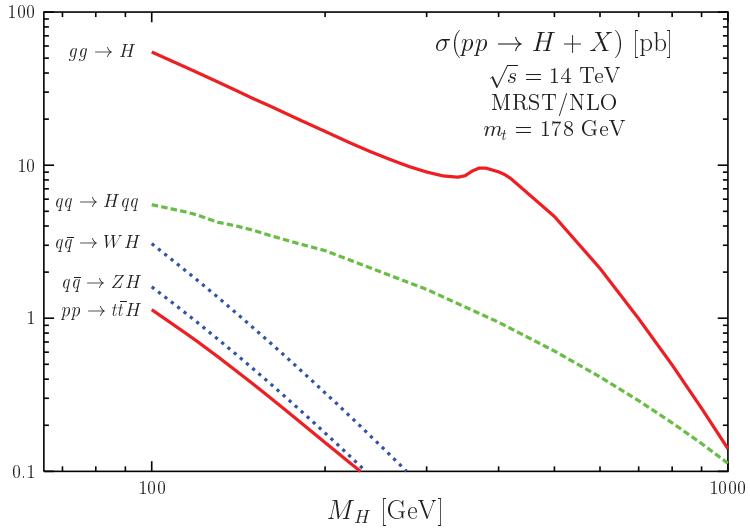

Figure 2.8: Higgs production cross-sections at exact NLO in QCD as a function of the Higgs mass (plot taken from [14]). The NNLO QCD corrections as well as the NLO electroweak corrections are also included for the WH and ZH production modes.

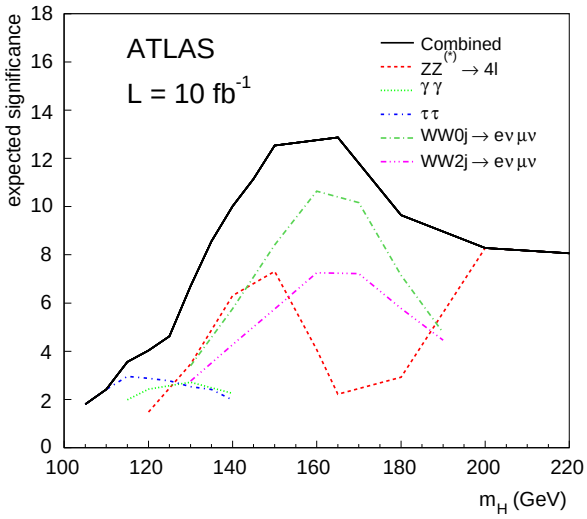

Figure 2.9: The predicted ATLAS significance for the search of the Higgs boson with a luminosity of 10 fb^{-1} at the LHC as a function of the Higgs mass. $H \to ZZ^*$, $H \to \gamma\gamma$, and $H \to WW0j$ involve Higgs production via gluon-gluon fusion. $H \to \tau\tau$ involves Higgs production via vector boson fusion. The last one $WW2j$ involves both gluon-gluon fusion and vector boson fusion.

the $H \to b\bar{b}$ signal using associated production of the Higgs boson with vector bosons (W and Z) or $t\bar{t}$. These processes have smaller cross-sections than the 2 dominant ones, gg fusion and VBF (see fig. 2.8), but they offer a cleaner signature because we also have the decay products of the W, Z, or $t\bar{t}$ that can help identify these events. Of course, CMS and ATLAS simulated what would be expected for these studies, and the fact that the results do not appear on the plot 2.9 means that they were not found good enough.

However $H \to b\bar{b}$ is the main decay when the Higgs boson is light, and there are many motivations for going further into this study (see next chapter). In this section, as in the next chapter, we consider boosted light Higgs searches, and we are going to carry out a leading order (LO) analysis on the ZH channel so as to optimise the use of the z cut introduced in the previous section. This analysis will be very approximate but will give us an idea of which z_{cut} one should use.

2.2.2 Signal and Backgrounds

The signal $H \to b\bar{b}$ suffers from large QCD background due to parton branchings which result in a jet with a mass around the Higgs mass (fig. 2.10).

Even though a splitting like $g \to gg$ looks very similar to $H \to b\bar{b}$ at high p_t in the final state (after parton-shower and hadronisation), the two can actually be distinguished thanks to *b-tagging*. Indeed, b quarks hadronise into B-mesons which have a long lifetime and therefore, they can travel a lot before decaying. This results in a *secondary vertex*, i.e. a vertex point displaced with respect to the beam axis, from where the decay products of

after detailed studies is consistent with the previous generator-level studies, namely that under realistic assumptions, the enhanced cross sections predicted by BSM Higgs models are required to observe the Higgs Boson in the $H \to b\bar{b}$ channel" [172]

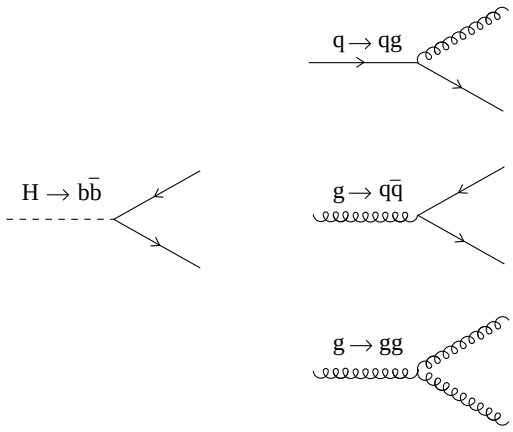

Figure 2.10: Higgs signal vs QCD backgrounds

the B meson come from. If we could always perfectly find this secondary vertex without a mistake, i.e. if the b-tagging was perfect, then the only background to $H \to b\bar{b}$ at LO would be $g \to b\bar{b}$ as we would have to see a double b-tagged jet. Unfortunately this is not the case, and one usually defines 2 numbers related to this:

1. the probability r to identify a B-hadron produced in an event,

2. the probability f to tag a jet as containing a B-hadron even though there's no B in it.

r is called the b-tag efficiency, and f the fake tag rate. These rates depend on what we are considering. Values often used by experimentalists range up to 70% for the b-tag efficiency, and down to 1% for the fake tag rate. The fact that r is not 1 implies that some signal will be lost as it will not be seen as containing 2 b's. The fact that f is not 0 means that all the three backgrounds mentioned in fig. 2.10 have to be considered. This is all the more true given that the splitting $g \to gg$ occurs much more often than $g \to b\bar{b}$.

With this in hand, we now focus on the process $q\bar{q} \to ZH$ with $H \to b\bar{b}$, which will be studied in more detail in the next chapter. The ultimate goal will be to improve the results obtained by ATLAS and CMS on this search channel. For the moment, we are going to make use of b-tagging in order to find an optimal z_{cut} to discriminate this signal against backgrounds.

2.2.3 z distribution for the Higgs boson

To find the optimal z_{cut}, one has to know the distribution of z for the signal and the backgrounds. At LO, we have already seen that the z distribution for the background in the collinear limit is given by the splitting functions (section 1.3.5). Therefore, we now have to know the probability for a high-p_t Higgs boson to decay into a quark with energy fraction z in the lab frame. In a first place, and for more generality, we do not need to suppose that the Higgs is boosted, and thus we do not consider the effect of the jet radius, even if we will come back to that point later.

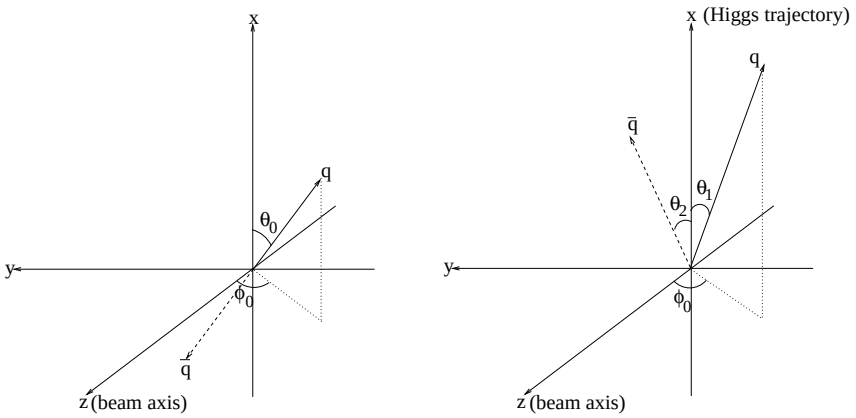

Figure 2.11: Higgs decay (a) in its rest frame, (b) in the lab frame (up to a longitudinal boost which does not matter as the result does not depend on it).

The Higgs is a scalar particle, so it decays uniformly in its rest frame. Given that, we just make a boost of this decay from the rest frame into the lab frame (fig. 2.11). A straightforward calculation using a massless b quark shows that, if we start from the configuration of fig. 2.11(a) in the Higgs rest frame, the momenta of b and $\bar{b}$ can be written in the lab frame under the following form:

$$p_b = \begin{cases} |\vec{p_b}| &= \frac{M_H}{2}\sqrt{\frac{1+x}{x}}\left(1+\frac{1}{\sqrt{1+x}}\cos\theta_0\right) \\ p_{b_x} &= \frac{M_H}{2}\sqrt{\frac{1+x}{x}}\left(\cos\theta_0+\frac{1}{\sqrt{1+x}}\right) \\ p_{b_y} &= \frac{M_H}{2}\sin\theta_0\sin\phi_0 \\ p_{b_z} &= \frac{M_H}{2}\sin\theta_0\cos\phi_0 \end{cases} \qquad p_{\bar{b}} = \begin{cases} |\vec{p_{\bar{b}}}| &= \frac{M_H}{2}\sqrt{\frac{1+x}{x}}\left(1-\frac{1}{\sqrt{1+x}}\cos\theta_0\right) \\ p_{\bar{b}_x} &= \frac{M_H}{2}\sqrt{\frac{1+x}{x}}\left(-\cos\theta_0+\frac{1}{\sqrt{1+x}}\right) \\ p_{\bar{b}_y} &= -\frac{M_H}{2}\sin\theta_0\sin\phi_0 \\ p_{\bar{b}_z} &= -\frac{M_H}{2}\sin\theta_0\cos\phi_0 \end{cases} , \tag{2.19}$$

where

$$x = \frac{M_H^2}{p_t^2}\,, \tag{2.20}$$

with M_H the mass of the Higgs boson, and p_t its transverse momentum. Therefore, the energy fraction z of the Higgs splitting in the lab frame according to the definition of eq. 2.1 is

$$z = \frac{1}{2}\left(1-\frac{1}{\sqrt{1+x}}|\cos\theta_0|\right)\,. \tag{2.21}$$

Using this equation and the uniform decay of the scalar Higgs in its rest frame (which is equivalent to $(\cos\theta_0, \phi_0)$ uniformly distributed), we obtain the property that the z distribution is uniform in the range

$$\frac{1}{2}\left(1-\frac{1}{\sqrt{1+x}}\right) < z < \frac{1}{2}\,. \tag{2.22}$$

Said another way:

$$\frac{d\sigma}{dz} = 2\sqrt{1+x}\,\Theta\left(z-\frac{1}{2}+\frac{1}{2\sqrt{1+x}}\right)\Theta\left(\frac{1}{2}-z\right)\,. \tag{2.23}$$

This equation is valid for any value of the Higgs transverse momentum. Returning to the boosted case ($x \ll 1$), one can evaluate the effect of choosing a jet radius R_0 to cluster the event. If we demand the b and $\bar{b}$ to be in the same jet, then eq. (2.7) tells us that the reconstructed Higgs boson has a uniform distribution in the range:

$$\frac{M_H^2}{R_0^2 p_{t_H}^2} < z < \frac{1}{2}\,. \tag{2.24}$$

The z distribution for the Higgs looks like that of the W boson plotted in fig. 2.5(a) because PYTHIA is lacking spin correlations and the W thus appears as a scalar particle. The drop of the distribution at small z is due to kinematic limits (finite p_t).

2.2.4 Optimising the use of the z cut

Choosing an adequate z_{cut} depends on the process under study and all its possible backgrounds as well as their relative importance. That's why we have to be more specific here, and we decide to study ZH events with a low mass Higgs boson (so that its main decay is into a $b\bar{b}$ pair). The reason for that is because this process as well as WH will be studied in more depth in the next chapter. The problem is now the following: we want to discriminate as much as possible the ZH signal against the Zq and Zg backgrounds at high p_t[10] using the "best" z_{cut}. "The best" means that the ratio $\frac{N_S}{\sqrt{N_B}}$, i.e. the number of signal events over the square root of background events passing the z cut, is maximised. For that, we suppose that the mass of the QCD jets are roughly equal to M_H, which means that they have already successfully passed the mass cut. Moreover, we require 2 b tags in the jets.

Given a number N_S and N_B respectively of signal and background events that passed the mass cut, we have to compute the significance $\omega(z_{cut})$ which is the ratio

$$\begin{aligned}\omega(z_{cut}) &= \frac{N_s S(z_{cut})}{\sqrt{N_B B(z_{cut})}}\,,\\ &= C\frac{S(z_{cut})}{\sqrt{B(z_{cut})}}\,,\end{aligned} \tag{2.25}$$

where $S(z_{cut})$ and $B(z_{cut})$ are respectively the fraction of signal and background events that pass the z cut for a given z_{cut}, and C is a constant independent of z_{cut}. The goal is thus to maximise $\omega(z_{cut})$.

$S(z_{cut})$ is computed using the uniform z distribution of the Higgs decay in the lab frame. If we take z to be the energy fraction carried for instance by the b quark, we obtain

$$\begin{aligned}S(z_{cut}) &= r^2 \int_{z_{cut}}^{1-z_{cut}} dz\,,\\ &= r^2(1-2z_{cut})\,.\end{aligned} \tag{2.26}$$

The r^2 factor comes from the fact that we have to recognise 2 b quarks in the event, this being done with a probability r for each b (cf section 2.2.2).

Concerning $B(z_{cut})$, we have to distinguish $B_q(z_{cut})$ and $B_g(z_{cut})$, i.e. the fraction of quark and gluon jets respectively that pass the z cut. We first consider B_q. The Zb

[10] There are other possible backgrounds like $t\bar{t}$ or dijets, but these should be reducible in a large part using leptonic cuts on the Z decay.

background can lead to a jet that is similar to the Higgs jet when b splits into bg where b is adequately tagged as a real b jet whereas g is mistagged as a b jet. The Zq background (with $q \neq b$) can also lead to a jet that is similar to the Higgs jet when q splits into qg where the q and g are both mistagged as b jets. We thus have to make a difference between a b jet and another flavor jet[11] ($q = u, d, s, c$) because they will not have the same influence depending on the b tag efficiency r and the fake tag rate f. If we remember that the probability for the splitting $q \to qg$ to occur with energy fraction z is given by the splitting function $P_{gq}(z)$ (section 1.3.5), then B_q can be written as:[12]

$$B_q(z_{cut}) = \frac{1}{\sigma_{Zb} + \sum_q \sigma_{Zq}} \int_{z_{cut}}^{1-z_{cut}} dz \left(rf P_{gb}(z)\sigma_{Zb} + \sum_q f^2 P_{gq}(z)\sigma_{Zq} \right) , \tag{2.27}$$

where the sum over q only concerns light flavours ($q \in \{u, d, s, c\}$). For the first term concerning $b \to bg$ splitting, the factor rf means that we have to properly tag the b quark (factor r) and that we have to mistag the gluon as a b quark (factor f). For the second term, we have no b quark produced, so we have to double mistag the jet (factor f^2). We also include the cross-sections σ_{Zb} and σ_{Zq} to produce a Z boson with respectively a b quark and a light quark at LO, in order to have their relative importance.

The reasoning is similar for B_g and we obtain:

$$B_g(z_{cut}) = \int_{z_{cut}}^{1-z_{cut}} dz \left(r^2 P_{bg}(z) + \sum_q f^2 P_{qg}(z) + f^2 P_{gg}(z) \right) . \tag{2.28}$$

We can now combine everything and write:

$$\begin{aligned} B(z_{cut}) &= \frac{1}{\Sigma_{Z+jet}} \left(\left(\sigma_{Zb} + \sum_q \sigma_{Zq} \right) B_q(z_{cut}) + \sigma_{Zg} B_g(z_{cut}) \right) , \\ &= \frac{1}{\Sigma_{Z+jet}} \Bigg[\frac{1}{3} \left(2r^2 T_R + f^2 (2(n_f - 1)T_R - C_A) \right) \left((1 - z_{cut})^3 - z_{cut}^3 \right) \sigma_{Zg} + \\ &\quad + f \left(f C_A \sigma_{Zg} + f C_F \sum_q \sigma_{Zq} + r C_F \sigma_{Zb} \right) \left(2 \ln \left(\frac{1 - z_{cut}}{z_{cut}} \right) + 3 z_{cut} - \frac{3}{2} \right) \Bigg] , \end{aligned} \tag{2.29}$$

with $n_f = 5$ is the number of quark flavours to be taken into account. In this expression, we explicitly wrote the normalisation factor $\Sigma_{Z+jet} = \sum_q \sigma_{Zq} + \sigma_{Zb} + \sigma_{Zg}$, even though it is not very useful because it will only change the constant C in eq. (2.25). In the second line, we used the expressions for the splitting functions eqs. (1.81−1.84) and integrated them.

Eq. (2.29) can be understood in a more familiar way by taking the limit $z_{cut} \to 0$. In this case, a term proportional to $\ln \frac{1}{z_{cut}}$ survives, which is a manifestation of the gluon soft divergence. A constant term D also survives, which can be written:

$$D = -\frac{3}{2} C_F \left(f^2 \sum_q \sigma_{Zq} + rf\sigma_{Zb} \right) - f^2 \left(\frac{11}{6} C_A - \frac{2}{3}(n_f - 1)T_R \right) \sigma_{Zg} + \frac{2}{3} r^2 T_R \sigma_{Zg} . \tag{2.30}$$

[11] As $M_{top} > M_H$, top quark is not considered as a background here.

[12] up to an overall normalisation factor entering the constant C in eq. (2.25). We thus do not write for instance the α_s factor that appears in all the splitting functions.

The first term is the well-known $-\frac{3}{2}C_F$ from quark splitting, the second and third terms are the other well-known $\frac{11}{6}C_A - \frac{2}{3}(n_f - 1)T_R$ from gluon splitting, separated because of b-tagging.

At this stage, we still have to know the cross-sections σ_{Zg}, $\sum_q \sigma_{Zq}$, and σ_{Zb} at LO. These can be obtained using PYTHIA or HERWIG. If we take the HERWIG values for $p_t > 200$ GeV, we obtain:

$$\sigma_{Zg} \simeq 7.8 \text{ pb}\,, \tag{2.31}$$

$$\sum_q \sigma_{Zq} \simeq 47 \text{ pb}\,, \tag{2.32}$$

$$\sigma_{Zb} \simeq 1.9 \text{ pb}\,. \tag{2.33}$$

These values can be a little different according to the generator chosen or the parton distribution function set used. But this is not so important here as we just would like to get an idea of the optimal z_{cut}.

Now, we have all the elements to determine $\omega(z_{cut})$ depending on the value of $\kappa \equiv \frac{f}{r}$. In fig. 2.12, we take as an example some particular values for r and f, where the choice $(r, f) = (60\%, 2\%)$ will be used in the next chapter. Here only the shape is important because the overall normalisation is not included.

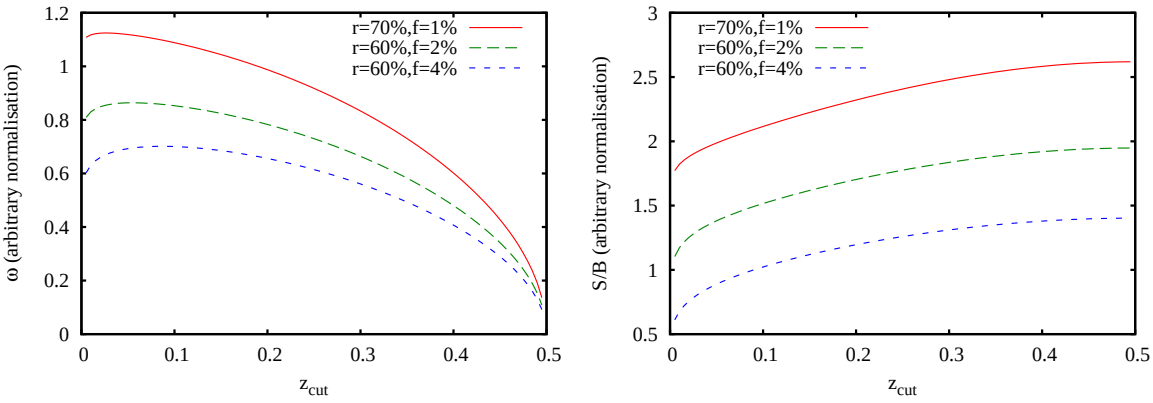

(a) (b)

Figure 2.12: (a) The significance of the signal as a function of z_{cut} for 3 different values of the couple (r, f); (b) $\frac{S}{B}$ as a function of z_{cut} for the same values of (r, f).

So the optimal z_{cut} values are found to be:

- For $(r, f) = (70\%, 1\%)$, $z_{opt} \simeq 0.026$.
- For $(r, f) = (60\%, 2\%)$, $z_{opt} \simeq 0.055$.
- For $(r, f) = (60\%, 4\%)$, $z_{opt} \simeq 0.086$.

As we can see, there is a trade-off: if z_{cut} is too small, then we keep too much of the backgrounds with fake tags.[13] If z_{cut} is too large, then we lose too much of signal. But, actually, with the values used for f and r, the optimal z_{cut} is still small, roughly between

[13] if the b-tagging was perfect, the optimal z_{cut} would be 0.

0.02 and 0.1. If we considered a worse b-tagging, i.e. κ increasing, then the optimal z_{cut} would also increase as we would have to reject more and more backgrounds from fake tags, which are essentially the ones with a soft divergence.[14]

Of course, the values given above for z_{opt} are to be taken with care. They give an idea about which z_{cut} we can choose, but are not very precise. The first reason for that is experimental. In experiments, one also has to deal with *systematic uncertainties*. One of these uncertainties comes from the fact that the ratio S/B can be low, even if $S/\sqrt{B}$ is rather large. In fig. 2.12(b), one sees that taking larger z_{cut} increases S/B, and thus decreases the systematic uncertainties. Another reason is that in a real analysis, there would be other kind of reducible backgrounds like dijets for instance that would come into the game, also favouring larger z_{cut}. Finally, one has to be aware that we only did a LO analysis. At NLO, one would obtain diagrams like the ones in fig. 2.13. Therefore, even with perfect b-tagging, the branchings $q \to qg$ and $g \to gg$ would have to be considered, leading to an even larger z_{cut}.

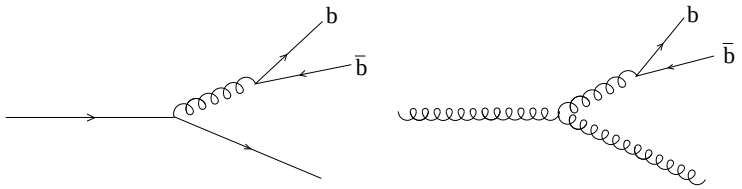

Figure 2.13: NLO background diagrams that can be suppressed thanks to the z cut.

As a conclusion, we would say that z_{cut} should be roughly chosen between 0.05 and 0.15,[15] but of course it depends on the physical process we are studying and on the importance of systematic uncertainties.

2.2.5 Effect of the jet radius

In the previous section we chose the z_{cut} according to a LO analysis depending on the parameters of the b-tagging. But in real studies, we have to deal with parton-showering, initial state radiation, underlying event and pile-up that enter the game and complicate a lot the analysis. The basic question that one has to face before any data analysis is the following: which jet algorithm and which jet radius should we choose to reconstruct the event? This question is relevant for the studies of the previous sections because the ability to compute the mass of a jet or the fraction z of a splitting obviously depends on the way the event is first reconstructed. Concerning the jet algorithm, this depends on the analysis and will be explained in detail in the next chapter. But let us say a few words about the jet radius which is closely related to the cut imposed on z.

Let R_0 be the radius of the jet algorithm used to cluster the event. We recall (eq. (2.7)) that if the b quark resulting from the Higgs splitting into $b\bar{b}$ carries a fraction z of the Higgs energy, then we can write:

$$R_{bb}(z) \simeq \frac{1}{\sqrt{z(1-z)}} \frac{M_H}{p_{t_H}} \,. \tag{2.34}$$

[14] with the exception of $g \to q\bar{q}$, $q \neq b$.

[15] if the only background was arising from the splitting $g \to gg$ for instance, then the optimal z_{cut} would be 0.14.

For now, eq. (2.34) tells us that b and $\bar{b}$ are clustered together only if $R_0 > R_{bb}(z)$. Therefore, besides the z_{cut} parameter, the radius R_0 of the clustering naturally cuts on small z and we would like to understand the interplay that exists between R_0 and z_{cut}. The analysis of the previous section did not actually take R_0 into account.

Let us assume that the p_t of the Higgs boson is fixed. In this case, if we choose $R_0 < R_{bb}(z_{cut})$, then we will not reconstruct the Higgs splittings that occur with a fraction z such that $z_{cut} < z < z_0$, where z_0 is defined by $R_0 = R_{bb}(z_0)$. Therefore, one could equivalently take $z_{cut} = z_0$, which has the advantage that it is more discriminative against backgrounds. On the other hand, if we choose $R_0 > R_{bb}(z_{cut})$, then we will reconstruct Higgs splittings with $z_0 < z < z_{cut}$ that will be later cut by the z_{cut} parameter, and they are thus useless. Moreover, with R_0 large, we increase the importance of the background because we capture a larger noise from ISR, UE, and PU. Therefore, for p_t fixed, it seems that one should choose $R_0 = R_{bb}(z_{cut})$ for better efficiency.

Now the p_t of the Higgs boson is not the same from one event to the next, and the interplay between R_0 and z_{cut} becomes much more difficult to study. In the next chapter, we will introduce the Mass Drop Analysis procedure that allows us to be very flexible concerning the choice of R_0. Indeed, it significantly reduces the effect of the background on the Higgs jet and therefore we can reconstruct it using large R_0 values, so that the interplay between R_0 and z_{cut} does not play a major role anymore.

2.3 Conclusion

The ability to tag an event and recognise signal amidst its backgrounds is dependent on the signature that we are expecting. At a hadronic collider like LHC, dealing with hadronic decays reveals itself to be a hard task because of the very large QCD background. In this chapter, we have considered the case of boosted massive particles that decay into a single jet and we have shown how variables like the jet mass and the z fraction of the splitting (eq. (2.1)) can greatly help us to reconstruct the signal while rejecting backgrounds. An important aspect of the cut on z is that it kills one large logarithm in the relatively low-mass distribution of the quark and gluon jets in the boosted limit.

We applied these considerations to the particular case of the light Higgs boson, whose main decay is into $b\bar{b}$. We showed that the z distribution of its decay is uniform within some kinematic limits, which allowed us to make a simple but insightful LO analysis on the optimal z_{cut} that should be chosen in order to maximise the significance of the ZH signal with respect to its main backgrounds depending on the parameters of the b-tagging. This analysis revealed that a good value for z_{cut} should be around 0.1 in presence of both tagged and mis-tagged light jets. We finally roughly examined the important interplay between the initial radius R_0 of the clustering and z_{cut}, which may in general be non-trivial. The Mass Drop analysis that will be studied in the following chapter will however suppress a large part of their interaction, essentially the R_0 dependence.

Chapter 3

Light Higgs searches at the LHC using jet substructure

In the previous chapter we studied how to reconstruct boosted massive particles decaying hadronically, where the most important difficulty arises from the ability to distinguish them from QCD jets. We also focused on a particular case: the Higgs boson decaying into $b\bar{b}$ in the ZH channel. In this chapter, we are going to apply these considerations to a full analysis of the WH and ZH search channels at the LHC, where we have to deal not only with very large QCD backgrounds, but also with underlying event (UE) and pile-up (PU). After having examined these channels in more details (section 3.1), we will show how it is possible to efficiently reconstruct the Higgs boson using a subjet analysis procedure that we will describe (section 3.2). Sections 3.3 and 3.4 will present the numerical Monte-Carlo study that validates our Higgs reconstruction procedure and improves significantly on the previous results concerning WH and ZH channels. Finally, in section 3.5 we will estimate the NLO corrections to this analysis.

3.1 A challenging search channel at the LHC

In chapter 2, we saw that the associated production of a light Higgs boson with W or Z was found not to be a good search channel at the LHC by the ATLAS and CMS experiments. In this section we analyse it more deeply: we start by examining in detail the old approach from ATLAS (similar to that of CMS) before giving some ideas that led us to go further.

3.1.1 Previous studies on the WH/ZH channels

We would like to briefly review the original study on WH/ZH channels in order to understand why it was found so difficult to deal with (cf section 2.2.1). When we talk about WH and ZH channels with H decaying into $b\bar{b}$, we actually consider 3 different search channels:

1. the *dilepton* channel: $pp \to ZH$ with $Z \to l^+l^-$,
2. the *missing-E_t* channel: $pp \to ZH$ with $Z \to \nu\bar{\nu}$,
3. the *semi-leptonic* channel: $pp \to WH$ with $W \to l\nu_l$,

where l is either electron or muon. The ATLAS study [139] focused on the semi-leptonic channel. This is because the dilepton channel suffers from a rate that is 6 times lower, and despite its cleaner signature it seems it cannot improve the results. And concerning the $ZH \to \nu\bar{\nu}b\bar{b}$ channel, it cannot be efficiently tagged, as the missing-E_t ($\equiv \not{E}_t$) required is too small, leading to very large experimental backgrounds.

We thus focus on $WH \to l\nu_l b\bar{b}$ events. The expected signature is 1 lepton (taken with $p_t >$ a few GeV), a small missing-E_t and 2 tagged b-jets ($p_t > 15$ GeV for each of them). Unfortunately, many kind of backgrounds can look similar to this signature, like continuum $Wb\bar{b}$ production, single top $pp \to W^* \to tb \to Wb\bar{b}$, W with 2 jets where at least one of the jets is mistagged, i.e. seen as a b-jet whereas there's no b inside, and $t\bar{t} \to WWb\bar{b}$ where one of the leptons from the decay of the two W's is not seen in the detector, or where one W decays hadronically but both resulting jets are soft. To suppress as much as possible these backgrounds, beyond the above-mentioned cuts on transverse momenta, one usually vetoes events with additional leptons and jets.

Higgs mass (GeV)	100	120
WH, $H \to b\bar{b}$	416	250
WZ, $Z \to b\bar{b}$	545	220
$Wb\bar{b}$	3650	2000
$t\bar{t} \to WWb\bar{b}$	3700	3700
tb, tbq	740	740
Wbj, Wjj	7600	4160
Total background	16235	10820
S/B	2.5%	2.3%
$S/\sqrt{B}$	3.3	2.4
$S/\sqrt{B}$ incl. syst.	1.9	1.7

Table 3.1: Expected WH, $H \to b\bar{b}$ signal and background rates inside a mass window of ± 22 GeV around the Higgs mass for two different Higgs boson masses, assuming a b-tagging efficiency of 60% and an integrated luminosity of 30 fb^{-1} (table taken from [139]).

Despite all these cuts, table 3.1 shows that the backgrounds were found to remain very large with respect to the signal, an important fraction coming from mistagged light QCD jets in Wbj and Wjj, though $Wb\bar{b}$ and $t\bar{t}$ are important too. This is also due to a poor detector acceptance: it often happens that one of the decay products reaches the detector in a region where it cannot be well measured. The presence of the Z peak ($Z \to b\bar{b}$ in the WZ background) also degrades the visibility of the Higgs mass peak. Eventually, the background shape shown in fig. 3.1(a) makes it hard to identify the Higgs signal above the summed backgrounds. If we impose an additional cut on the rapidity separation between b and $\bar{b}$, for instance $|y_b - y_{\bar{b}}| < 1$, the systematics uncertainties resulting from this particular shape can be reduced. Indeed, imposing $|y_b - y_{\bar{b}}| < 1$ leads to the dashed curve of fig. 3.1(b) for the $t\bar{t}$ background, to be compared with the one obtained with the ATLAS cuts only (using a simple LO analysis with MCFM 5.3 [88,89]). We notice that the background shape is significantly flattened.

The significance found by ATLAS was below 2σ with 30 fb^{-1} for Higgs masses around 120 GeV, which is far too small to be a competitive search channel at the LHC or to allow precision measurements of the $Hb\bar{b}$, WWH and ZZH couplings. At this point, the

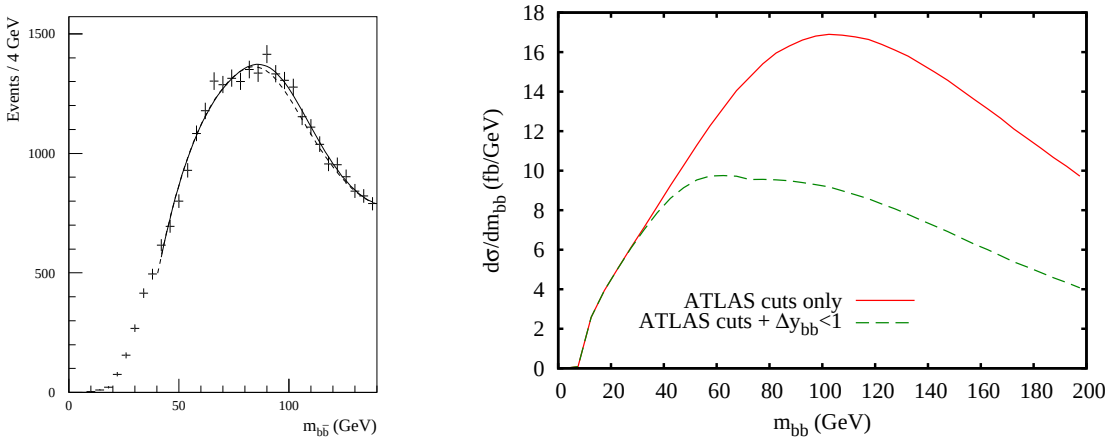

(a) (b)

Figure 3.1: (a) WH signal above the summed backgrounds, represented by a dashed line (picture taken from [139]). The Higgs mass is assumed to be 100 GeV; (b) The $t\bar{t}$ background simulated at LO with MCFM using the ATLAS cuts (solid curve) or imposing an additional cut on the rapidity separation between b and $\bar{b}$ ($|y_b - y_{\bar{b}}| < 1$) (dashed curve).

conclusion from the ATLAS TDR published in 1999 about WH and ZH production reveals a lot: "The extraction of a signal from $H \to b\bar{b}$ decays in the WH channel will be very difficult at the LHC, even under the most optimistic assumptions [...]" [139].

However, this search channel is important, and it can be worth trying to analyse it more deeply. We are thus going to show how the difficulties encountered by CMS and ATLAS in their analysis can be overcome, and that we can recover the WH and ZH channels as promising search channels at the LHC for a low-mass Higgs boson [173]. Notice that the same kind of analysis was later done for the $t\bar{t}H$ channel [174] using methods similar to those that will be described here.

3.1.2 Some ideas for improvement

Looking for boosted Higgs bosons

When considering the ATLAS analysis, and as already touched on in section 2.2, an idea that one might have would be to see what happens at higher Higgs p_t.[1] At high p_t the problem of detector acceptance is almost eliminated because the W and the Higgs bosons mainly decay in the central region of the detector (fig. 3.2).

But this is not the whole story. At high p_t, the b and $\bar{b}$ from the Higgs decay are close to each other because, we recall, the angular distance R_{bb} between them can be written (eq. 2.7):

$$R_{bb} \simeq \frac{1}{\sqrt{z(1-z)}} \frac{M_H}{p_{t_H}}, \tag{3.1}$$

with z the energy fraction carried by the b or $\bar{b}$. Therefore, one can require the b and $\bar{b}$ to be in the same jet. The cut-induced background shape that was observed in the ATLAS

[1] This is not a new idea as works on boosted Higgs searches go back to the 80's [175], there in the context of $H \to \tau^+\tau^-$.

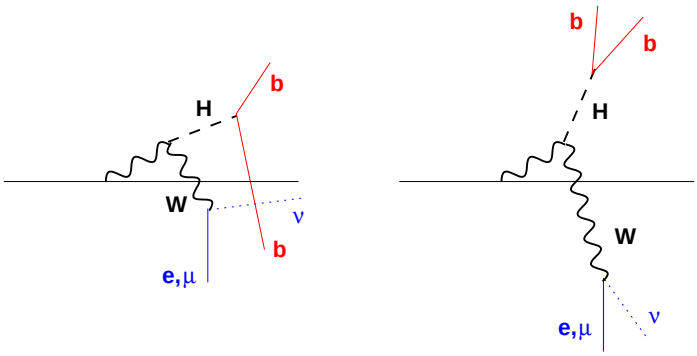

Figure 3.2: Higgs and W bosons decay (a) at small p_t and (b) at high p_t.

study (fig. 3.1(a)) may thus be suppressed (cf fig. 3.1(b)). Moreover, the backgrounds cross-sections fall somewhat more quickly with p_t than signal: in fig. 3.3 are represented the p_t distributions of the signal and backgrounds cross-sections when we impose the cut $R_{bb} < R_0 = 1.2$. With this cut, the $t\bar{t}$ background is actually greatly suppressed. This is due to kinematical constraints: it is very unlikely that the b and $\bar{b}$ resulting from the decay of 2 boosted tops flying in opposite directions will be in the same phase space region, and this explains the sharp drop in the $t\bar{t}$ cross-section at high-p_t. Concerning the signal at low p_t, there's no chance for the $b\bar{b}$ pair from the Higgs decay to be within angular distance 1.2 from each other because of eq. (3.1), which explains why the WH cross-section is null in this region. Notice that on this plot we did not require the mass of the $b\bar{b}$ jet to be around the Higgs mass, which would reduce the backgrounds even more with respect to the signal. Finally, going to high-p_t makes it possible to tag more efficiently the $Z \to \nu\bar{\nu}$ decay because of the large missing-E_t expected (no experimental background anymore).

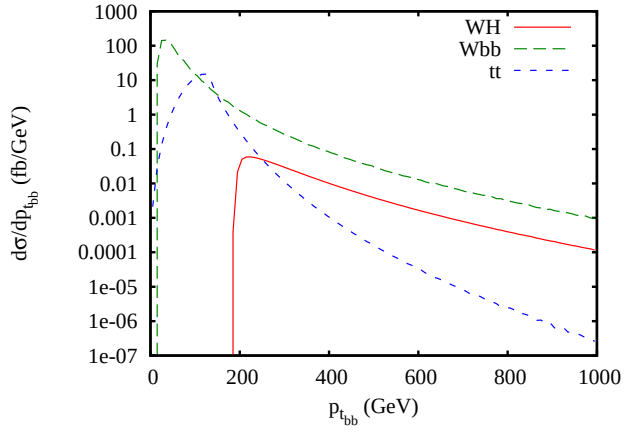

Figure 3.3: Differential $p_{t_{bb}}$ distributions for the WH channel and its major backgrounds at high p_t: W+jets and $t\bar{t}$. The only cut required is that b and $\bar{b}$ are within angular distance $R_0 = 1.2$ from each other.

One might think that using a large p_t cut, i.e. $p_{t_H} > p_{t_{min}}$ with $p_{t_{min}}$ of at least a couple

of hundred GeV, would result in too important a loss of signal events. This is partially true: there is a very important drop of the signal cross-section. However, the problem in the ATLAS study was not a lack of signal events, but a very large number of background events. Therefore, it seems that this idea of working in the boosted regime might be worth exploiting.

All the arguments given here only result from boosted kinematics. But one can also use the knowledge of the QCD soft divergence mentioned in the previous chapter in order to further reduce the backgrounds.

Using the discriminating power of the z_{cut} parameter

From now on, we assume that the Higgs is sufficiently boosted such that the b and $\bar{b}$ resulting from its decay are clustered into the same jet. Such a jet is called a *Higgs candidate*.

The most important noise present in the ATLAS study was due to mistagged light QCD jets. At high-p_t, these jets mostly come from a splitting, quark $\to$ quark-gluon or gluon $\to$ gluon-gluon, hard enough to give rise to a jet mass around M_H. If one or two of the final partons are wrongly tagged as b, such a jet can look very similar to a Higgs jet. We know that the energy fraction z carried by the partons are different for light QCD jets and Higgs jets: we recall that $z \ll 1$ usually for a QCD splitting whereas $z \sim 1/2$ for a Higgs splitting. And thanks to eq. (2.18), we also know that this fundamental property leads to a significant reduction of the QCD backgrounds when using an adequate cut on z.

The problem is now: once a Higgs candidate is identified, how can we measure the energy fraction z? The main idea, which goes back to the work of [146, 147], is to look into the substructure of the jets.[2] One method is to cluster the event using the k_t algorithm, which has the property, due to its k_t ordering, that it clusters the hardest splitting at the last step of the clustering. Therefore, it is enough to undo the last stage of the clustering in order to obtain the 2 separated b-tagged jets. One can then easily measure z and discriminate signal against QCD background.[3]

This is a good starting point but is not enough. Indeed, at the LHC there will be an important contamination from non-perturbative effects like underlying event (UE) and pile-up (PU). And we would like to get rid of these too. We are now going to see how a deeper analysis into the substructure of the jets can help us achieve this.

3.2 The Mass Drop and Filtering Analysis

Though we will discuss the full event selection procedure for the WH and ZH channels in the next section, we are now going to examine the main step of this selection concerning the hadronic part of the event. As before, we assume that we clustered our event and found a Higgs candidate, i.e. a jet with 2 b's inside. The first question that one might ask is the following: is it a Higgs jet or a background QCD jet?

We would like to find a subjet analysis procedure on the Higgs candidate jet that helps one to answer this question and improve the mass resolution on the Higgs signal. In this section, we first show how the reduction of the background can be achieved by what we

[2] [146] was the first to talk about subjets to reconstruct hadronic decays, but the present formulation using also the z_{cut} parameter (in its more or less equivalent form $y_{cut}p_t^2$) was first introduced by [147].

[3] as mentioned in the previous chapter, only the QCD splitting $g \to b\bar{b}$ is not distinguishable from $H \to b\bar{b}$ with this method. But it has a low rate compared to the $g \to gg$ splitting.

call the *Mass Drop analysis* (MD), which is the first part of the procedure. Then, we study the *Filtering analysis* whose aim is to "clean" the Higgs jet from a large number of UE/PU particles present in it. We finally conclude by examining the effects of this subjet analysis procedure on both the background and the signal.

3.2.1 The Mass Drop Analysis (MD)

The reduction of the QCD background is similar in spirit to what was explained before: we cut on small z energy fractions because they are more likely to come from a pure soft QCD splitting. However, a novel aspect in our reduction strategy is to be aware of the large importance of the UE at the LHC which can greatly spoil the Higgs jet. Therefore one should make a distinction between the soft particles from the UE and the soft perturbative radiation from the original $b\bar{b}$ pair. Because the Higgs is colour neutral, the important property of angular ordering [40–44] implies that almost all the perturbative radiation from the $b\bar{b}$ dipole is present in 2 cones of radius R_{bb} respectively centred on b and $\bar{b}$. Consequently, once a Higgs candidate jet is observed in an event, one should find a strategy that gets rid of all the particles outside these cones, because we know that they are not related to the Higgs (but to UE, PU, or Initial State Radiation). And in our study, this will also be very important for the filtering analysis (see next subsection).[4]

The idea is to go back into the clustering history of the jet, as was explained above for the k_t algorithm. But instead of considering only the last stage of the clustering, one can go deeper in the jet's clustering history. Figure 3.4 and its caption explain why the method using the k_t algorithm is not suited for very "dirty" environments like the ones that will be encountered at the LHC. The fact that the k_t-algorithm d_{ij} distance involves the particles' transverse momentum and that the b and $\bar{b}$ are the hardest objects imply that they are clustered together after all the other particles in their neighbourhood were clustered, and therefore, when we go back into the clustering history, we separate them *before* we could treat all the junk particles. Instead, if we consider for instance the C/A algorithm, then the major part of the particles that are outside the 2 cones will cluster *after* the b and $\bar{b}$ jets get unified, as they are all at a distance from b and $\bar{b}$ greater than R_{bb}.

That is a nice idea, but how do we know that the b and $\bar{b}$ jets were separated? This is crucial to measure z, and thus to be able to reduce the QCD background if we find it below z_{cut}. Of course, thanks to b-tagging, we can answer this question.[5] But it is a particular case, and we would like to find a general way to do it, that could work for instance to reconstruct a W boson decaying hadronically at the LHC, for instance $W^+ \to u\bar{d}$. Here, there is no particular means to tag the u and d quarks. The central part of the MD analysis, where its name comes from, is to realise that the splitting responsible for the large jet mass is precisely the Higgs decaying into $b\bar{b}$. All the splittings that occur afterwards (i.e. the parton showering) give a mass to the b and $\bar{b}$ jets respectively, but small compared to the Higgs mass (figure 3.5). This works the same way for QCD jets, W jets and Z jets.

Once the "hard" splitting is identified, one can measure its energy fraction z (eq. (2.1)). If $z > z_{cut}$, the splitting is considered to be more or less symmetric and we keep the jet as a good Higgs candidate. Otherwise, it looks like a mistagged QCD jet and we reject it. These are the main ideas. In [173], we formulated it using a different variable: instead

[4] Moreover, we get more precisely the relevant quantities like z, p_t or R_{bb}, whose measurement can be distorted by all the additional UE/PU particles entering into the jet.

[5] Notice that experiments need individual b jets to do the tagging.

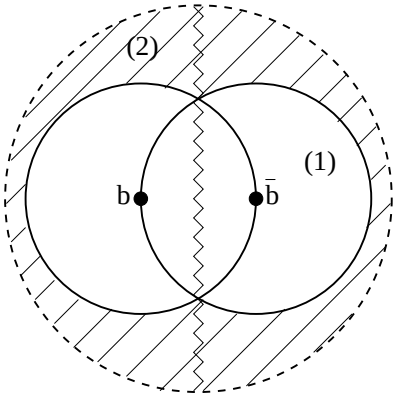

Figure 3.4: An idealised view in the (y, ϕ) plane of the Higgs candidate jet just after the whole event was clustered (largest dashed circle) and its 2 main regions: (1) the 2 cones around b and $\bar{b}$ where one can find almost all the perturbative radiation and (2) the dashed region outside these 2 cones composed almost exclusively from UE/PU/ISR particles. The k_t algorithm separates this jet roughly along the broken line when going back into the clustering history. The C/A algorithm first eliminates all the dashed region before separating the 2 cones.

of measuring z, we measure the k_t distance[6] $d_{j_1,j_2} \equiv \min(p^2_{t_{j_1}}, p^2_{t_{j_2}})\Delta R^2_{j_1,j_2}$ between the 2 subjets j_1 and j_2 and we check the condition $d_{j_1,j_2} > y_{cut} M_j^2$ where y_{cut} is a dimensionless parameter. However, thanks to formula eq. (2.4), we know that it is equivalent to $z > z_{cut}$ with

$$y_{cut} = \frac{z_{cut}}{1 - z_{cut}}\,, \tag{3.2}$$

at least at LO.

We now describe the MD analysis more precisely. Let us suppose we found a hard jet[7] j reconstructed when clustering the event using the C/A algorithm with some radius R_0. We then use the following iterative procedure in order to recognise if j is a boosted heavy particle or a pure QCD jet:

1. Break the jet j into two subjets by undoing its last stage of clustering. Label the two subjets j_1 and j_2 such that $m_{j_1} > m_{j_2}$.

2. If there was a significant mass drop, $m_{j_1} < \mu M_j$, and the splitting is not too asymmetric, $d_{j_1,j_2} > y_{cut} M_j^2$, then deem j to be the heavy-particle neighbourhood and exit the loop.

3. Otherwise redefine j to be equal to j_1 and go back to step 1.

In the MD analysis, we introduce two parameters: μ and y_{cut}. Using section 2.2.4, we know that y_{cut} should be chosen somewhere between 0.05 and 0.18 in order to efficiently reduce the QCD background. In [173], we decided to take $y_{cut} = 0.09$. Concerning the mass drop threshold itself, controlled by μ, there is also the question of how one should choose it: if

[6] As usual, $\Delta R^2 = \Delta y^2 + \Delta\phi^2$.

[7] b-tagged or not, this can work for boosted W decaying hadronically for instance.

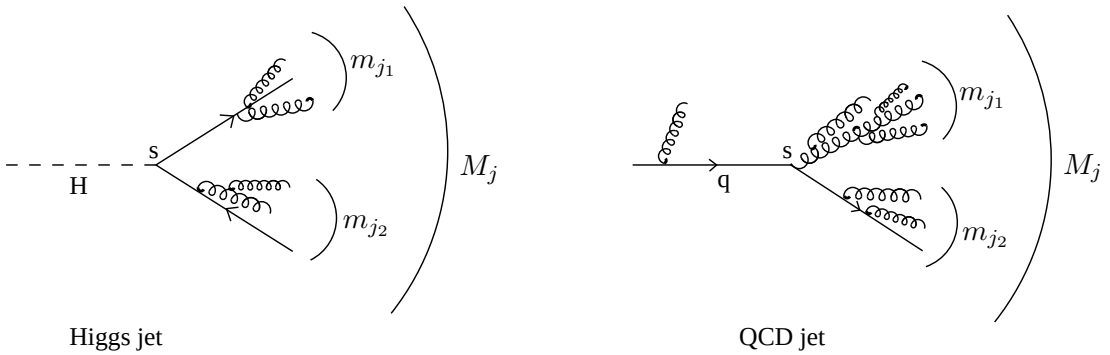

Higgs jet QCD jet

$$m_{j_1}, m_{j_2} \ll M_j$$

Figure 3.5: The origin of the MD analysis. Regardless of whether the Higgs candidate jet j is really a Higgs jet or a QCD jet satisfying $M_j \simeq M_H$, there usually is a splitting hard enough, denoted by s on the figure, that gives rise to the major part of the jet mass M_j. The 2 subjets j_1 and j_2 acquire their mass due to soft and collinear emissions from the parton showering.

too large (~ 1) then any splitting gives a significant mass drop and this parameter becomes useless, but if too small then the mass drop condition will be hard to obtain because the b and $\bar{b}$ subjets acquire mass due to parton showering, and we will thus lose too much signal. At the very least, we decided that the mass drop condition should be fulfilled if the Higgs decays into a Mercedes $b\bar{b}g$ configuration in its rest frame, i.e. $\mu > 1/\sqrt{3}$. But to be a little more precise, we made a plot (fig. 3.6) for the signal reconstruction efficiency depending on this parameter μ, and also on the original jet algorithm radius R_0, which is supposed to be large enough to cluster together the b and $\bar{b}$ at moderately high p_t thus allowing one to find the Higgs candidate jet.

This figure was originally designed not only to find efficient μ and R_0 parameters, but also to distinguish between 2 kind of MD analysis. The "y_{cut} after" curves mean that we check only the mass-drop condition while we go back into the clustering history, and *then*, once we find a splitting with a sufficient mass-drop, we check the y_{cut} condition: if it succeeds, we say that it is signal, otherwise we reject the event. This is different from the procedure given above where we do not reject the event if the y_{cut} condition fails: instead we continue to go back into the clustering history of the jet. When we started thinking about this analysis, we were doing it the first way. And by doing so, we saw that if R_0 is large (> 1.2), there is a drop in the efficiency, which was unexpected (the "y_{cut} after" curves in fig. 3.6).[8] This can be explained in the following way: when R_0 is large, the jet captures a large amount of UE/PU/ISR and there is a large probability that a fake mass drop occurs before we would expect it. Being aware of that, this is the reason why we decided to slightly modify the procedure: if the y_{cut} condition fails, this can be because we see a fake mass-drop due to UE/PU particles (which are usually soft like perturbative radiation and therefore the z cut

[8]The same behaviour is observed when R_0 is too small (< 1), because in this case the b and $\bar{b}$ are often too far away from each other to be clustered together.

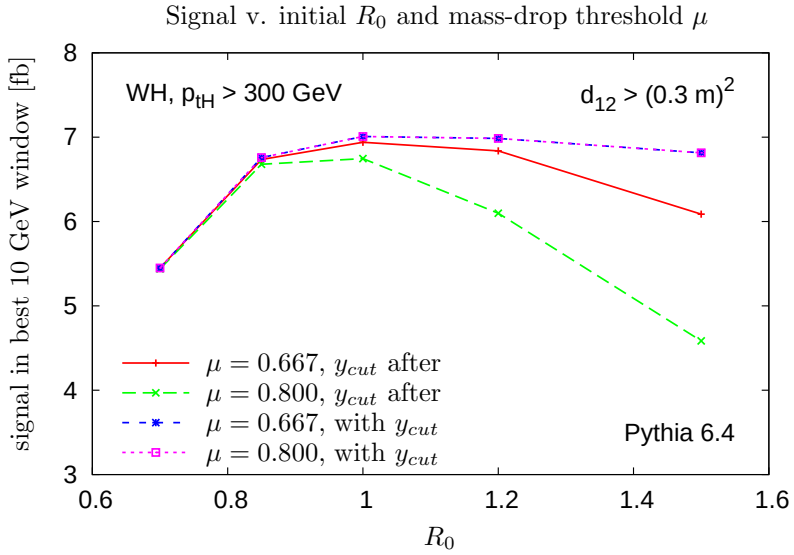

Figure 3.6: Reconstruction efficiency of the Higgs candidate jet in the best 10 GeV mass window with respect to the original clustering radius R_0 for 2 values of the mass drop threshold and for 2 different MD procedures: we examine the y_{cut} condition either after we find a sufficient mass-drop ("y_{cut} after"), or while testing the mass-drop condition ("with y_{cut}"). We take $y_{cut} = 0.09$ in both cases.

should also reject them efficiently). We thus continue our descent into the clustering history of the heaviest jet as it is presented above. The consequence of such a subtle modification is represented by the curves "with y_{cut}" in fig. 3.6: we not only improve the efficiency of the reconstruction procedure at intermediate R_0, but we keep it efficient even at larger values of R_0, which is important because we do not want our procedure to depend too much on R_0, and we want it to be robust even in a very noisy environment, for instance during the high luminosity running of the LHC. This modification ensures that these 2 conditions are satisfied and that we reduce much of the interplay between y_{cut} and R_0 which was mentioned in section 2.2.5.

Concerning the precise value of μ, we can see on the plot that taking $\mu = 0.667$ or $\mu = 0.8$ (but still larger than $1/\sqrt{3}$) does not change anything for the most efficient version of the MD analysis. Therefore we decided to take $\mu = 0.667$, which worked better for the old version, and is also more discriminative. Note that we finally chose $R_0 = 1.2$.

3.2.2 The Filtering analysis

We have just presented the MD analysis, which is an iterative subjet analysis procedure that allows one to identify boosted massive particles decaying hadronically while rejecting a large part of the backgrounds made up by QCD jets. At the end of the MD procedure, one should be left with 2 subjets, each of them originating from one of the partons of the hard splitting (these are represented by the 2 cones of the figure 3.4). These 2 subjets are called the "Higgs neighbourhood".

At the LHC, we know that this procedure will not be sufficient as the UE/PU particles

that are present in the Higgs neighbourhood will significantly degrade the mass resolution on the Higgs jet. Their effect on the reconstructed Higgs mass scales as R_{bb}^4 [176]. Therefore, the idea is to recluster ("filter") the particles resulting from the MD analysis in the Higgs neighbourhood with a radius $R_{\text{filt}} < R_{bb}$ and to take the 3 hardest jets obtained. By doing so, we reduce the effect of the UE/PU particles on the reconstructed Higgs mass to $\mathcal{O}\left(R_{\text{filt}}^2 R_{bb}^2\right)$ (see next chapter). Unfortunately, we also lose some perturbative radiation from the $b\bar{b}$ pair. So there is a compromise to make between these 2 effects.

The filtering procedure is the following:

1. Define $R_{\text{filt}} = \min\left(0.3, \frac{R_{bb}}{2}\right)$.
2. Cluster the Higgs neighbourhood using the C/A algorithm with R_{filt}.
3. Sum the 3 highest-p_t jets obtained: this is the final Higgs jet.

Using some numerical simulations, this choice for R_{filt} was found to be rather effective in suppressing the UE effect while keeping as much perturbative radiation as possible from the $b\bar{b}$ dipole. Taking the 3 hardest jets ensures that we capture the dominant $\mathcal{O}(\alpha_s)$ radiation from the Higgs decay as well as the b and $\bar{b}$ jets. The whole subjet analysis procedure is summed up in fig. 3.7.

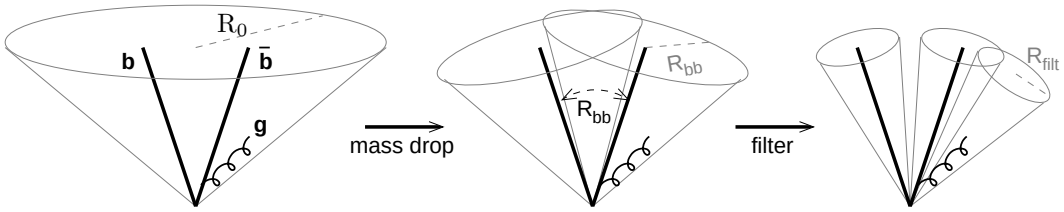

Figure 3.7: The Mass Drop and Filtering analysis (picture taken from [173]). First, we cluster the event with a large radius R_0. Then we do the MD analysis until we separate the b and $\bar{b}$. Eventually, we filter the Higgs neighbourhood with a smaller radius R_{filt} in order to get rid of many UE particles while keeping the major part of the perturbative radiation.

An important consideration in this analysis, already discussed in [146], is the possibility to flexibly adapt the reconstruction strategy to the p_t of the Higgs boson, which is related to R_{bb} by eq. (3.1). The MD analysis reduces the size of the Higgs candidate jet to a $\mathcal{O}(R_{bb})$ which is just large enough to contain (almost) all the QCD radiation from the Higgs decay. And the filtering analysis uses a radius that depends on R_{bb}, and so on p_{t_H}. This is an important aspect of our procedure and is fundamental for the LHC as it will involve different energy and angular scales from one event to the next.

One last point that one should be aware of concerns the difference between the k_t and the C/A algorithms for the MD analysis, discussed in the previous subsection, but which is also related to the filtering. Indeed, if we use the k_t algorithm instead of C/A for the MD analysis, then we keep all the UE particles from the original jet. Therefore, applying the filtering procedure to this structure would mean that the third hardest jet, which is supposed to correspond to the $\mathcal{O}(\alpha_s)$ perturbative radiation at an angular distance $\sim R_{bb}/2$ from the Higgs boson direction, may instead be composed by UE particles at an angular

distance $\sim \mathcal{O}(R_0)$ from the Higgs, thus leading to a distortion of the reconstructed Higgs mass measurement. This would result in a loss of efficiency for this procedure.

Now that our MD and filtering procedures are well defined, let us examine their practical impact on Higgs jets and background QCD jets before considering the actual event generation and selection procedures for the boosted Higgs search in the WH and ZH channels in section 3.3.

3.2.3 Effects of the Mass Drop and Filtering analysis on Higgs and background jets

First, we would like to check that we effectively gain something using our analysis with respect to more standard ones. In table 3.2 taken from [173], we compare our procedure (MD+filtering) with the original subjet analysis proposal using the k_t algorithm, instead of C/A, with the same y_{cut} as was described previously. We also compare it with an analysis using SISCone based only on the jet mass. We generate parton showered events using HERWIG [97, 98], and we add UE with the JIMMY program [130]. For the C/A and k_t algorithms, we require each subjet to be b-tagged. For SISCone, that does not take the underlying substructure into account, we require 2 b's inside the jet. In the first column we determine, for each of these analysis, the cross section for identified Higgs decays in a mass window around the Higgs boson mass (taken as 115 GeV) in ZH events. In the second column we compute the cross-section for tagging QCD jets as Higgs jets in $Z + b\bar{b}$ events in the same mass window. The significance $S/\sqrt{B}$ is calculated in the third column. All these cross sections were obtained for a roughly optimal R_0 value that depends on the analysis.

Jet definition	σ_S/fb	σ_B/fb	$S/\sqrt{B \cdot \text{fb}}$
C/A, $R_0 = 1.2$, MD-F	0.57	0.51	0.80
k_t, $R_0 = 1.0$, y_{cut}	0.19	0.74	0.22
SISCone, $R_0 = 0.8$	0.49	1.33	0.42

Table 3.2: Cross section for the $Z + H$ signal and the $Z +$ jets background for $200 < p_{t_Z}$ (GeV) < 600 and $110 < m_J$ (GeV) < 125, with perfect b-tagging; shown for the MD+filtering procedure and other standard ones at near optimal R_0 values.

Due to the use of the y_{cut}, the k_t algorithm performs well on background rejection, but it cannot get rid of the UE particles that degrade the Higgs peak, and therefore it loses many signal events (so S is small and B is small). On the contrary, SISCone takes fewer UE particles and therefore can more efficiently reconstruct the signal. But as it ignores the underlying substructure of the jet, it cannot distinguish it from QCD background (so S is large and B is large). Concerning our MD+filtering procedure, it does well on both fronts (S is large and B is small). So we really gain in term of significance.

To go a little further, we compare the effect of the MD and filtering analysis respectively on Higgs jets and QCD light jets at high p_t. For that we generate parton showered ZH and dijet events using HERWIG and we still add UE with the JIMMY program. In figure 3.8 we plot the mass distributions obtained for the hardest jet at various stages of the analysis. First, let us comment on the signal distributions. If we just cluster the event using the C/A algorithm with a radius $R_0 = 1.2$ ("raw jet" curves) and compute the resulting Higgs candidate jet mass, one observes that the Higgs mass peak is broadened towards higher masses. This simply means that the UE greatly spoils the Higgs neighbourhood and thus

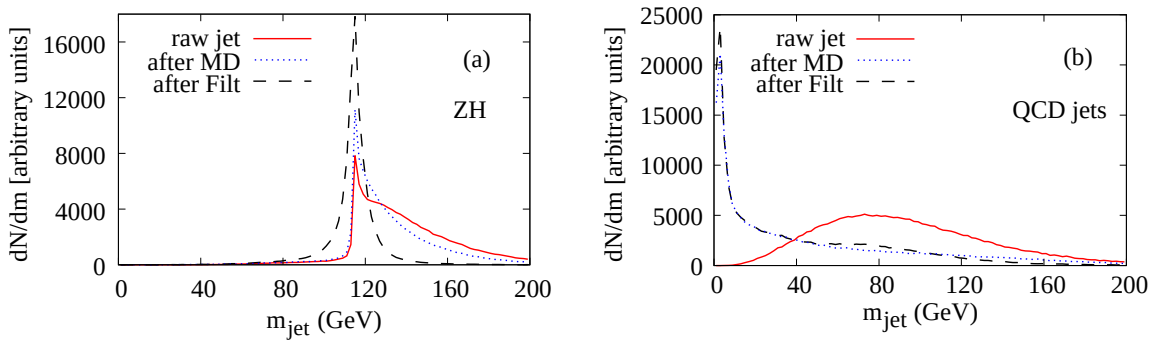

Figure 3.8: (a) Effect of the subjet analysis procedure on the signal: ZH events ($M_H = 115$ GeV) with UE were generated using HERWIG and JIMMY, with a p_t cut of 200 GeV, and clustered using C/A with $R_0 = 1.2$. We plot the Higgs candidate jet mass distribution before any subjet analysis (solid curve), after MD analysis (dotted curve), and after filtering analysis (dashed curve). We assumed perfect b-tagging. (b) The same for a generic dijet background, where the hardest jet mass distributions are plotted (we do not apply any b-tagging requirement).

degrades the mass resolution. Then, if we only do the MD analysis without filtering ("after MD" curves), we gain a little in mass resolution because we get rid of all the UE particles outside the angular ordering region corresponding to the Higgs decay (see section 3.2.1). But, the dispersion of the distribution still remains very important. Finally, thanks to the filtering analysis ("after Filt" curves), we clearly recover a nice peak, relatively narrow (68% of events contained within a window of ~ 14 GeV). Notice the small tail towards low masses which comes from the unavoidable loss of perturbative radiation during the filtering process. In chapter 4, we will see how it is possible to optimise this procedure in order to obtain the narrowest possible peak centred on M_H.

We now turn to the effect of the whole procedure on QCD jets. Without the MD and filtering analysis, high-p_t QCD jets have a very broad distribution centred around 80 GeV. This explains why the QCD background is so important around the Higgs mass region. If we apply the MD procedure to these jets, we significantly reduce this background (by roughly a factor of 3 around 115 GeV): the major part of the distribution is shifted towards very low masses of a few GeV. This means that the cut on d_{ij} is efficient. Applying the filtering analysis does not significantly change the light QCD jet mass distribution around the Higgs mass, though it seems to reduce it even more at higher masses (by a factor of 5 around 200 GeV).

Therefore, the MD analysis works well in reducing the QCD background, whereas the filtering analysis essentially results in a major improvement for the Higgs mass resolution. We are now going to describe the signal and background events generation for the boosted WH and ZH channels. We recall that they are our original motivation for developing the MD and filtering analysis, which we are now going to incorporate into the event selection procedure.

3.3 Event generation and selection

3.3.1 Event generation

Now that we know how to identify a hadronically decaying Higgs boson in a complex environment, let us return to the original problem, which is to look for a light Higgs boson at the LHC in the WH and ZH channels. We recall (see section 3.1) that we focus on 3 different search channels, each of them involving $H \to b\bar{b}$ decay:

(a) ZH with $Z \to l^+l^-$, $l = e, \mu$.

(b) ZH with $Z \to \nu\bar{\nu}$.

(c) WH with $W \to l\nu_l$.

We do not consider the possible hadronic decay of the vector bosons, though they could perhaps be investigated with the same MD and filtering analysis used for the Higgs, which may be an interesting topic for future work in order to possibly further improve the results that will be obtained in this chapter.

We used HERWIG and JIMMY to simulate signal and background events with UE, Fastjet to cluster each event, and PYTHIA to cross-check the results. For each of the 3 search channels, the backgrounds considered were WW, WZ, ZZ, Zj, Wj, jj, $t\bar{t}$, single top. Notice that in our original analysis, we only considered the single-top production via $q\bar{q} \to W^* \to tb$ and $qg \to qtb$, but as the ATLAS collaboration later pointed out (see section 3.4.3), we actually missed the Wt background, which is important for our study. The WZ and ZZ backgrounds ($Z \to b\bar{b}$) are only critical when the Higgs mass is too close to the Z mass, otherwise the mass peaks of the 2 bosons can be separated. But as our Higgs boson is light ($M_H \geq 115$ GeV), this has to be carefully examined. All the samples were generated with a luminosity ≥ 30 fb^{-1}, except for the dijet background where the very high cross-section makes this impractical. Instead, we assumed that the selection efficiency of a leptonically-decaying boson factorises from the hadronic Higgs selection. This assumption was tested and found to be a good approximation in the signal region of the mass plot.

The main results that will be plotted in this chapter correspond to a b-tag efficiency of 60% and a mistag rate of 2%. However, as these parameters have an important impact on our results, we will mention what happens if they are varied.

3.3.2 Event selection

Once events are generated, the important point is to be able to recognise a Higgs boson decaying into $b\bar{b}$ while discarding as much as possible all the other backgrounds.

Leptonic cuts

Before looking for the Higgs boson, we need to tag a W or a Z boson that is produced in association with the Higgs. This greatly helps us to reduce the very large QCD background from dijet events for instance. As we mentioned in section 3.1.2 and used for the Higgs subjet analysis in the previous one, we study boosted Higgs and vector bosons, with $p_t > p_{t_{min}}$. In the main analysis we use $p_{t_{min}} = 200$ GeV, though the effect of raising this cut to $p_{t_{min}} = 300$ GeV will also be considered later. Depending on the search channel, we require:

(a) a *Z candidate* in the dilepton channel: an e^+e^- or $\mu^+\mu^-$ pair with an invariant mass 80 GeV $< m <$ 100 GeV and $p_{t_Z} > p_{t_{min}}$. Each lepton is required to have $p_t > 30$ GeV.

(b) a *Z candidate* in the missing-E_t channel: $\not{E}_T > p_{t_{min}}$.

(c) a *W candidate* in the semi-leptonic channel: one lepton e or μ with $p_t > 30$ GeV and $\not{E}_T > 30$ GeV, consistent with a W of nominal mass (see below) with $p_{t_W} > p_{t_{min}}$.

In order to be within detector acceptance, we also cut on the leptons' rapidity: $|y| < 2.5$ (channels (a) and (c)). We add another cut for background rejection: we require no other leptons than the ones necessary to identify the signal with $|y| < 2.5$ and $p_t > 30$ GeV. This cut also ensures that the 3 channels are completely independent from one another. Notice that in the original analysis of [173], the cut on the additional lepton was forgotten in channel (b), so that some events from channel (c) were actually considered as part of channel (b) and not of channel (c).

Concerning channel (c), we cannot reconstruct the W mass exactly because we lack the information about the neutrino direction, and more precisely p_{z_ν}. We only know its transverse momentum $\vec{p_{t_\nu}}$. However, for a given $\vec{p_{t_\nu}}$, only two p_{z_ν} values would solve the equation

$$(p_e + p_\nu)^2 = M_W^2 \,. \tag{3.3}$$

Expanding this equation implies:

$$4(m_e^2 + p_{t_e}^2)p_{z_\nu}^2 - 4p_{z_e}A_{e\nu}p_{z_\nu} - A_{e\nu}^2 + 4E_e^2 p_{t_\nu}^2 = 0 \,, \tag{3.4}$$

with

$$A_{e\nu} = M_W^2 - m_e^2 + 2\vec{p_{t_e}}.\vec{p_{t_\nu}} \,. \tag{3.5}$$

This quadratic equation in p_{z_ν} has solutions only if its discriminant is positive, which is equivalent to

$$M_W^2 + 2\vec{p_{t_e}}.\vec{p_{t_\nu}} \geq 2p_{t_e}p_{t_\nu} \,. \tag{3.6}$$

This condition, expressed in terms of measurable quantities in the event, is the one we check when we say that the lepton and missing-E_t must be consistent with a W of nominal mass.

Hadronic cuts

Once the vector boson was identified with all the previous requirements, we look at the hadronic part of the event. We now require the presence of a good *Higgs candidate* jet J, that is a jet with 2 b-tagged subjets, satisfying $p_t > p_{t_{min}}$ and passing the MD and filtering analysis procedures explained in section 3.2. Notice that J is accepted only if the 2 hardest subjets coming from the filtering analysis are b-tagged. Here again, in order to reject backgrounds, we require no other b-tagged jets in the range $|y| < 2.5$ with $p_t > 50$ GeV (ZH channels (a) and (b)). For channel (c) (WH), where the $t\bar{t}$ background is severe, these cuts are strengthened: we do not want to see *any* other jet with $|y| < 3$ and $p_t > 30$ GeV, b-tagged or not.

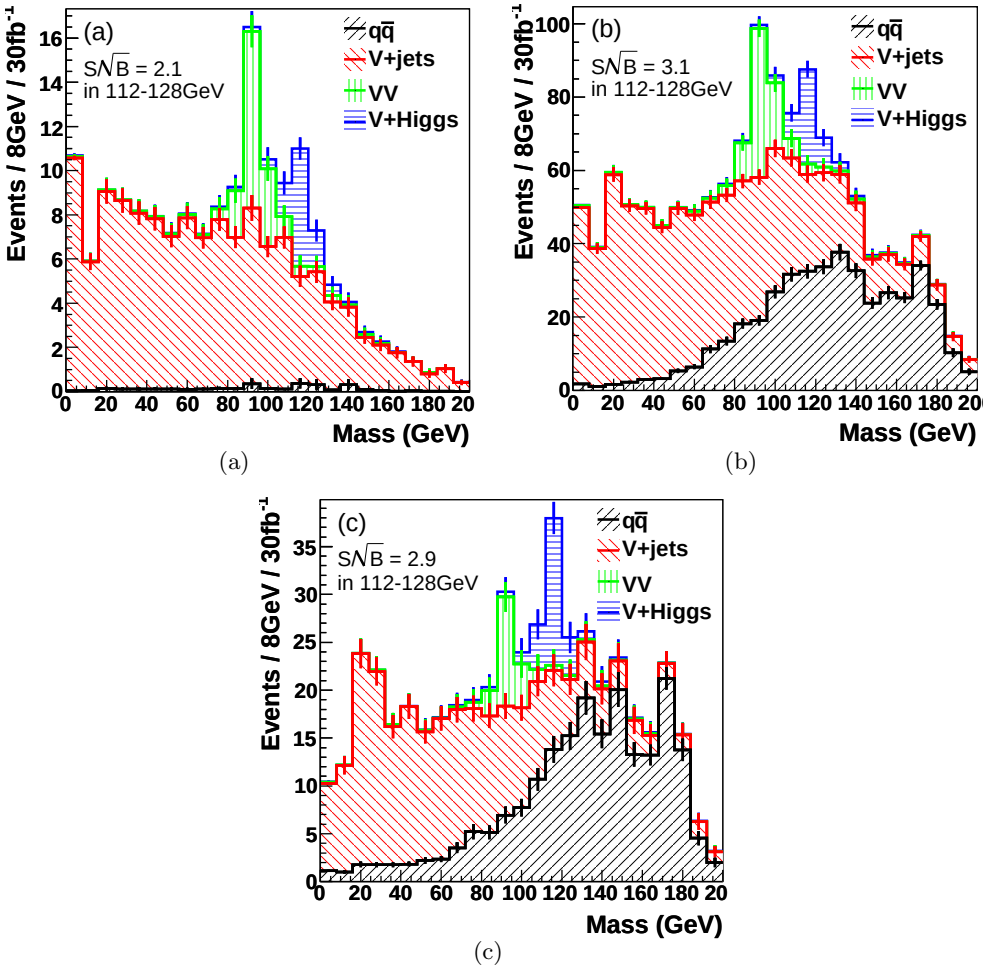

Figure 3.9: Signal and background for $b\bar{b}$ jet mass distributions in channels (a), (b) and (c) respectively for a luminosity of 30 fb^{-1} at the LHC with $M_H = 115$ GeV. A b-tag efficiency of 60% is assumed as well as a mistag rate of 2%. The $q\bar{q}$ sample includes dijets and $t\bar{t}$, of which the latter dominates. The errors reflect the statistical uncertainty on the simulated samples, and correspond to integrated luminosities > 30 fb^{-1}.

3.4 Results

3.4.1 Each channel separately

Generating all the signal and background events for each channel, and using the cuts described previously, one arrives at the plots shown in fig. 3.9 for the $b\bar{b}$ jet mass distributions at hadron level. The significance is computed by summing the number of signal (S) and background (B) events in the mass range $112 - 128$ GeV, and then calculating $S/\sqrt{B}$. On each plot, we can clearly see the Z peak coming from WZ and ZZ backgrounds near the Higgs one. However, it seems that it is not a critical background for our analysis as it hardly reaches the Higgs mass region. For the dilepton channel (a), the largest (and almost only) background is from Z+jets. Such a channel has a very clean signature which leads to very few backgrounds, but suffers from a low cross-section because of a small branching ratio $Z \to l^+l^-$, $l = e, \mu$ (6.8%). This is why the significance of 2.1σ is the lowest of the 3 search channels. On the contrary, the missing-E_t channel (b) has a cross-section which is 3 times greater, but the backgrounds are also very important because of a less clean signature. Notice that in this channel, the V+jets background is in fact equally shared between W+jets and Z+jets. A W+jets event looks like the signal topology when the lepton from the W is below the leptonic cut and when the single neutrino is highly boosted. This is almost the same for the $t\bar{t}$ background which also contributes significantly: in principle, it should result in 2 leptons, b, $\bar{b}$, and missing-E_t, but if the 2 leptons are either not seen or not energetic enough to be cut, then it can look like what we expect for the signal.[9] The significance of 3.1σ that we found was actually overestimated compared to the other channels, because as explained in section 3.3.2, some events from channel (c) were considered as belonging to this channel. Concerning the semi-leptonic channel (c), the 2 most important backgrounds are $t\bar{t}$ and W+jets. Such a channel is intermediate between the 2 first ones: it offers a relatively clean signature and the branching ratio $W \to l\nu_l$, $l = e, \mu$ is large (22.2%).

3.4.2 Combined results

The sum of the 3 search channels is shown in figure 3.10. The major backgrounds are $t\bar{t}$, Z+jets and W+jets. The conclusion of our study is that a Higgs with $M_H = 115$ GeV is visible with a significance of 4.5σ, which is a great improvement compared to previous studies on the same search channels, and validates our subjet analysis procedure. However, different b-tagging efficiencies as well as larger Higgs masses can have an important impact on these results, and that's why we also examined their effect (fig. 3.11). Most scenarios are above 3σ, but to be a significant discovery channel, our approach requires decent b-tagging, low-mass Higgs, and good experimental resolution.

We also looked at what happens if we take $p_{t_{min}} = 300$ GeV instead of 200 GeV. As $p_{t_{min}}$ is increased, the background is reduced even more with respect to the signal and it becomes more and more probable to reconstruct the decay $H \to b\bar{b}$ into a single jet. However, the signal cross-section itself decreases by a factor of $\sim 3-4$, so that the number of signal events become very small. Fig. 3.11 indicates that this trade-off seems to be in favour of a lower $p_{t_{min}}$.

[9] If one of the W decays hadronically, then the $t\bar{t}$ event results in 1 lepton, 1 jet, b, $\bar{b}$, missing-E_t. If the jet and the lepton are not tagged, then it also looks like a signal event.

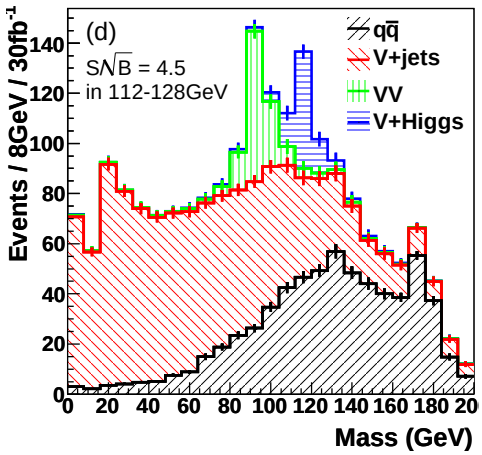

Figure 3.10: Signal and backgrounds $b\bar{b}$ jet mass distributions for the sum of the 3 search channels, when the luminosity is 30 fb^{-1} at the LHC. The Higgs mass was taken as 115 GeV. We assumed a b-tag efficiency of 60% and a mistag rate of 2%.

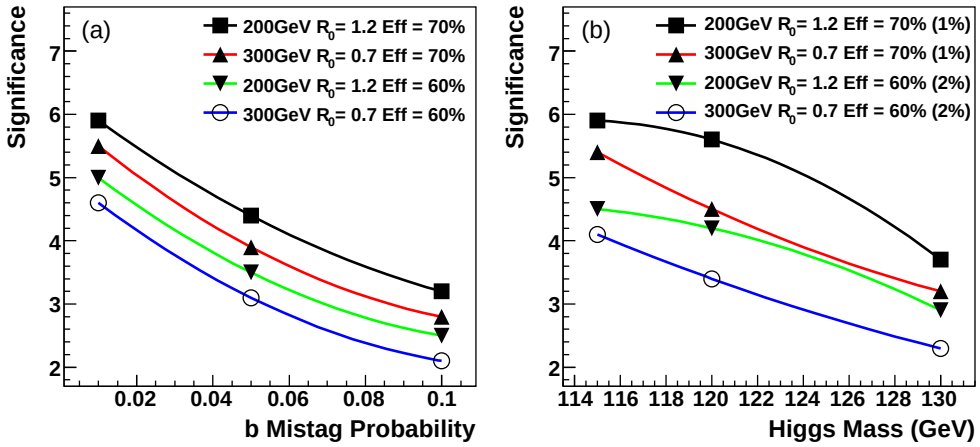

Figure 3.11: (a) Expected significance as a function of the mistag rate for different b-tag efficiencies and $p_{t_{min}}$ (shown at optimal R_0 values). (b) Expected significance as a function of the Higgs mass.

3.4.3 ATLAS results

Motivated by these promising results, the ATLAS collaboration repeated this analysis including a full simulation of their detectors[10] and a more sophisticated statistical combination of the different channels in order to check if it remains viable in a more realistic environment [177]. Some of the cuts were slightly changed, experimental cuts were added (like isolation criteria), but the main analysis was kept very similar to what we presented here. However, they also took into account the Wt background that we neglected, but which can lead to a topology close to the signal. Indeed we obtain one W on one side and a top quark on the other side decaying into bW. If the W decays into a c or b jet (and another one not detected), than it can fake the $Wb\bar{b}$ signal in the WH channel. A c quark can be mistagged as b because the D mesons resulting from the hadronisation of the c quark have a long lifetime, not that much smaller than that of B mesons. The results for each channel are presented in figure 3.12 (taken from [177]).

An important point to notice is the result of roughly 1.6σ for channel (b), to be compared with our 3.1σ. As explained in section 3.3.2, this comes from the cut on the additional lepton that was not considered in the missing-E_t channel of [173], thus increasing the relative significance of channel (b) with respect to channel (c) in our original analysis.

The ATLAS conclusion is that a 120 GeV Higgs boson can be seen with a significance of 3.7σ, which is a little less good than our results but is still promising. Including systematics, this significance can drop to 3σ. But in all cases it remains comparable to the ATLAS sensitivity for the other Higgs search channels in this low-mass region [169].

3.4.4 Possible improvements

The method that we used to recover the Higgs signal from the WH and ZH channels is designed to be efficient while remaining simple. But it can be improved in various ways.

On the one hand, we may be able to enhance the reconstructed signal a little more if we filter the Higgs neighbourhood with an optimally chosen radius R_{filt} for the filtering. This way will be explored in the next chapter. On the other hand, we can further reduce the background by employing specific top vetoes [147, 149, 174, 178, 179]. One can also try to reconstruct hadronically decaying Z and W bosons, using the MD and filtering procedure. Indeed, almost 70% of the vector bosons decays are hadronic. It has therefore the potential to significantly increase the number of reconstructed signal events. But as we would then have to deal with purely hadronic events, we would have to check that the rejection of background events still remains efficient. Finally, one could separate the high-p_t region into various bins like [200 GeV, 300 GeV], [300 GeV, 400 GeV] and so on, and then do a complete analysis in each of these bins. Combining the various results obtained in a clever way could lead to increased significance.

From an experimental point of view, the ATLAS collaboration also mentioned some improvements that can be expected in their analysis. For instance the b-tagging efficiency can be optimised for boosted b quarks, the background can be directly extracted from the data, and one can use sophisticated multivariate techniques.

[10] Actually, they did a full simulation of the ATLAS inner detector and muon system and a fast simulation of the calorimeter in its full granularity. But the WH signal was passed through a full detector simulation and it was shown that the differential distributions are correctly reproduced.

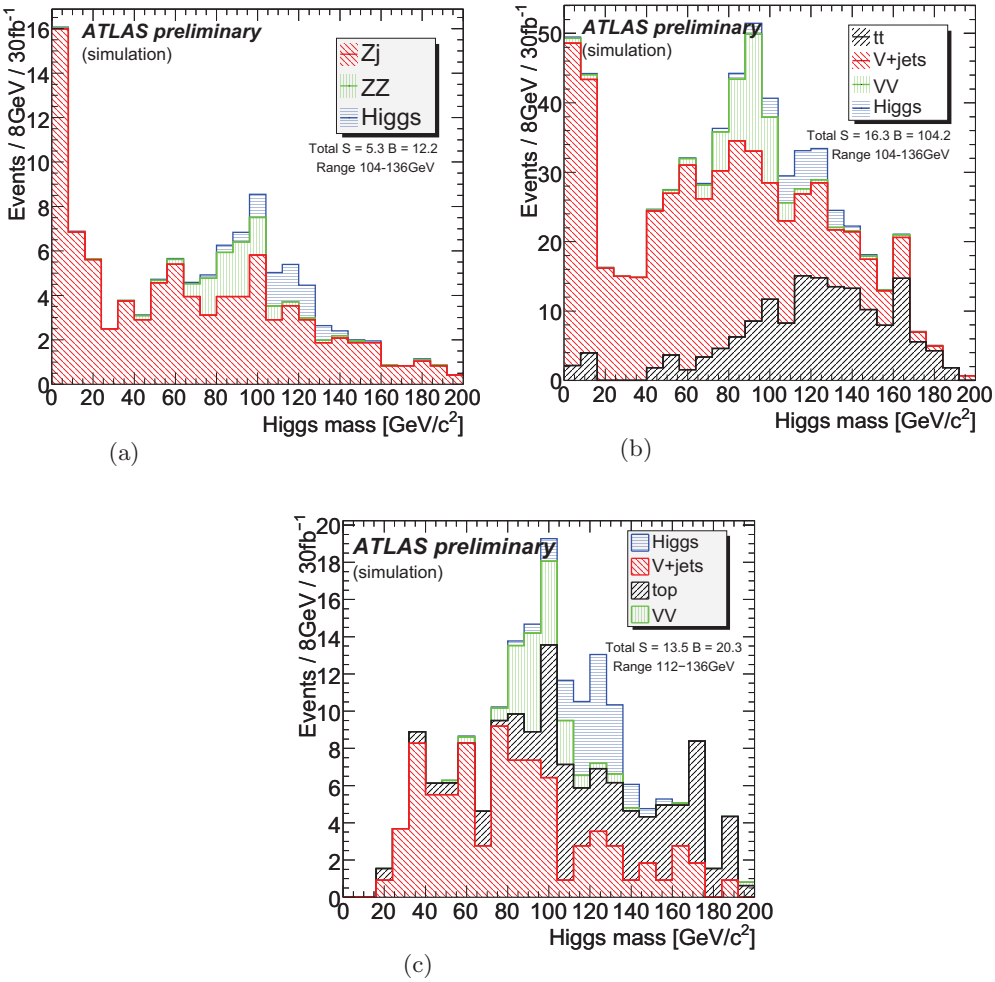

Figure 3.12: ATLAS results from (almost) full detector simulation for the distribution of the invariant mass of the Higgs candidate ($M_H = 120$ GeV) in (a) the dilepton channel, (b) the missing-E_t channel, (c) the semi-leptonic channel. The "top" background in the legend of channel (c) is a combination of $t\bar{t}$ and Wt.

All this suggests that better results may be possible for these channels, though further studies would be of value to check that explicitly.

3.5 Effect of NLO corrections

All the results that were obtained in this chapter are LO+parton-shower (with of course UE and hadronisation). But to be confident with these results, one should check how NLO corrections can change them. In fig. 3.13 we plot the differential p_t distribution of the Higgs candidate jet at LO and NLO for the $Z+H$ and $Z+$jet processes with MCFM [88, 89]. Though our main backgrounds come from $Zb\bar{b}$ and $Wb\bar{b}$, some of the issues that arise are more simply understood in $Z+$jet as a first step.

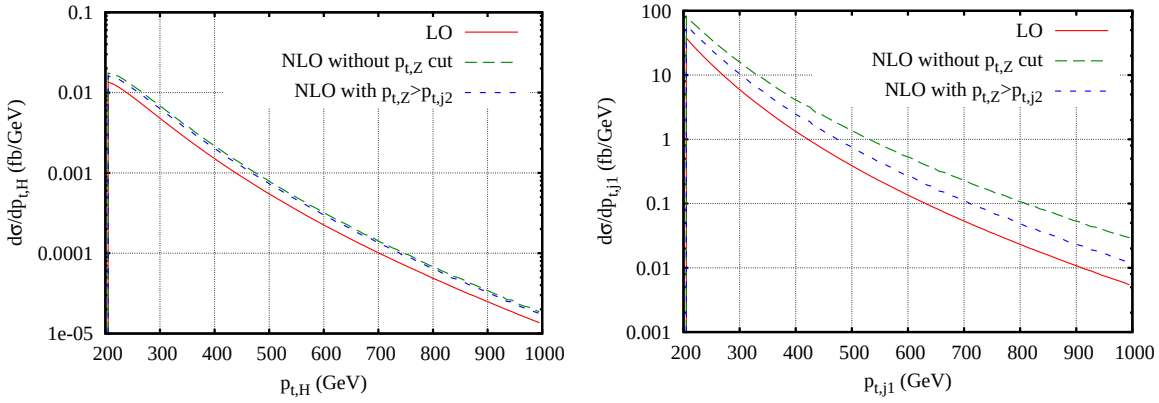

(a) (b)

Figure 3.13: (a) $p_{t,H}$ distribution for the ZH process at LO and NLO, with or without the requirement that p_{t_Z} should be greater than the p_t of the second hardest jet of the event (the hardest jet is required to be the Higgs jet). We cluster events with the C/A algorithm using a radius $R = 1.2$ and we require the hardest jet to be double b-tagged (perfect b-tagging). We used MCFM 5.3 with CTEQ6L1 for LO and CTEQ6M for NLO. The factorisation and renormalisation scales are set to $\mu = \sqrt{M_Z^2 + p_{t,Z}^2}$; (b) The same for the main Zj background concerning the p_t distribution of the hardest jet, except that we have no b-tagging requirement and the scale used is $\mu = \sqrt{M_Z^2 + p_{t,j1}^2}$.

We define the K-factor, as a function of p_t, to be the following quantity:

$$K(p_t) = \frac{\left(\frac{d\sigma}{dp_t}\right)_{NLO}}{\left(\frac{d\sigma}{dp_t}\right)_{LO}}, \tag{3.7}$$

i.e. σ_{NLO}/σ_{LO} for the differential p_t distribution. Concerning $Z+H$, we observe that the K-factor is around $1.4-1.5$ for $p_{t,H} > 200$ GeV, which is in the general ballpark that we would expect. However, when we did this study for the first time, the bad surprise came from the $Z+j$ distribution without the $p_{t,Z}$ cut. Here, the K-factor becomes large at high-p_t, up to 6. Of course, if it were the definitive answer, it would then importantly reduce the significance. Nevertheless, such a large K-factor has to be understood: where does it

come from? Actually, this K-factor results from electroweak double logarithms, when the $Z+2j$ process, which is the real NLO part of $Z+j$, is seen as an electroweak correction to a dijet process (fig. 3.14). This correction leads to soft and collinear logarithms $\ln \frac{p_{t,j1}}{M_Z}$ when $M_Z, p_{t,Z} \ll p_{t,j1}$, which do not have any virtual counterpart in $Z + j$ at one-loop (QCD higher-order corrections only). To check this interpretation, we also plotted in fig. 3.13 the NLO differential distributions when we force the Z to be more energetic than the second hardest jet of the event ($p_{t,Z} > p_{t,j2}$). This cut is designed to kill the contribution from the diagram 3.14(b). We see that the background K-factor is then greatly reduced and is more under control (~ 2), whereas that for the signal is almost unchanged.

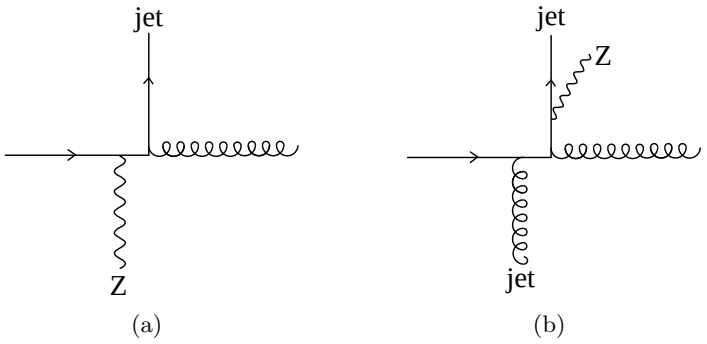

Figure 3.14: (a) One of the diagrams contributing to $Z + j$ at LO in which $p_{t,Z} = p_{t,j1}$. (b) One of the dominant real NLO diagrams in which $p_{t,Z} \ll p_{t,j1}$, which leads to a large K-factor.

These K-factors for signal and backgrounds only concern the differential p_t distributions. To see the effect on our results, one should perform the NLO calculation including all the analysis (MD+filtering as well as the various selection cuts) ideally with parton-showering, UE and hadronisation for the signals ZH and WH as well as for the main backgrounds $Zb\bar{b}$, $Wb\bar{b}$ and $t\bar{t}$. We did it for the signal using MC@NLO v3.3 [101], which matches NLO computations with parton-showers. The K-factor of around 1.5 found in the p_t distribution was confirmed for a mass of the Higgs candidate jet in [110 GeV, 126 GeV].

Unfortunately, the $Zb\bar{b}$ and $Wb\bar{b}$ backgrounds are not available in MC@NLO v3.3. What we did is that we first compared the MCFM LO results for $Zb\bar{b}$ and $Wb\bar{b}$ with HERWIG after applying all selection cuts and found a good agreement between the 2 results (see table 3.3 as an example). This is not unexpected since the background has a continuum $m_{b\bar{b}}$ distribution, which means that the MCFM LO results should not be significantly modified by the parton showering process.

This agreement reinforces the idea that we can estimate the K-factor for the backgrounds by applying all the selection cuts directly on MCFM LO and NLO events. One should be aware that this part demanded substantial work because we had to enter deep into the MCFM program in order to include our analysis, which is of course not available within the default MCFM options. The results for $W^-b\bar{b}$, $W^+b\bar{b}$ and $Zb\bar{b}$ are shown in fig. 3.15.

Consequently, for the Higgs candidate jet around 120 GeV, we find a K-factor of 1.6 for $Zb\bar{b}$, 2.6 for $W^+b\bar{b}$ and 2.8 for $W^-b\bar{b}$. We think that the larger K-factors that one observes without the MD procedure come from jets with a large mass and a collimated $b\bar{b}$ pair (i.e. the $b+\bar{b}$ is not responsible for the jet mass). Concerning $t\bar{t}$, we only checked the total cross-

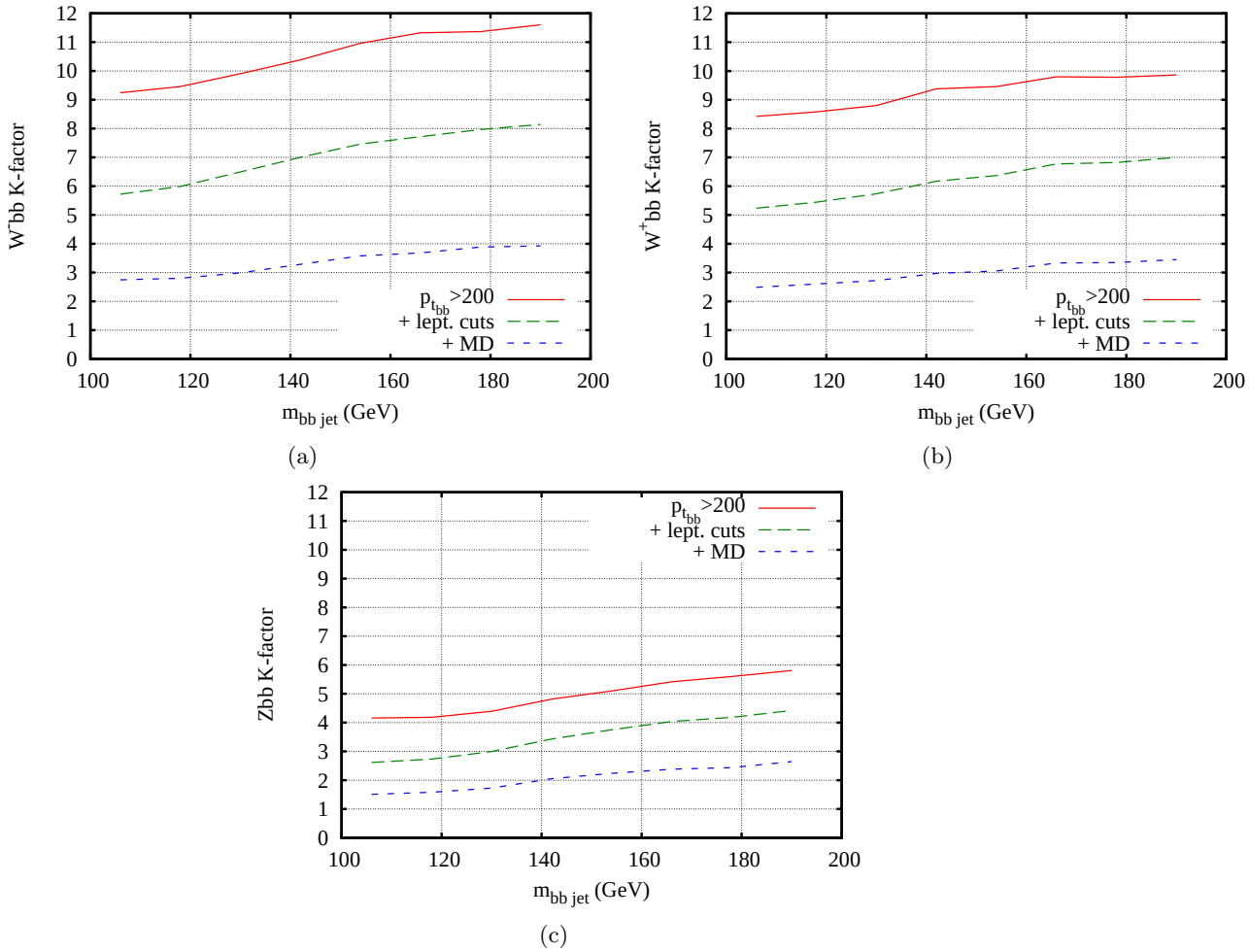

Figure 3.15: (a,b) K-factors for the $W^-b\bar{b}$ and $W^+b\bar{b}$ processes respectively. In each case, require a jet with $p_t > 200$ GeV containing a $b + \bar{b}$ pair and plot the mass of the jet without the MD procedure (red curve), then do the same with the leptonic cuts (green curve), i.e. $|y_{lep}| < 2.5$, $p_{t_{lep}} > 30$ GeV, $\not{E}_t > 30$ GeV, $p_{t_W} > 200$ GeV, and finally plot the mass of the jet after the MD analysis (blue curve); (c) The same for the $Zb\bar{b}$ process, where the leptonic cuts are replaced by: $|y_{lep}| < 2.5$, $p_{t_{lep}} > 30$, $p_{t_Z} > 200$ GeV. As before, we used CTEQ6L1 for LO and CTEQ6M for NLO. The factorisation and renormalisation scales are set to $\mu = \sqrt{M_Z^2 + p_{t,jet}^2}$.

HERWIG	MCFM LO	MCFM NLO
$110 < m_{bb} < 125$, all cuts	$110 < m_{bb} < 125$, all cuts	$110 < m_{bb} < 125$, all cuts
0.51 fb	0.49 fb	0.82 fb

Table 3.3: Cross-sections including $Z \to e^+e^-, \mu^+\mu^-$ branching ratios for the Higgs candidate jet to have a mass in [110 GeV, 125 GeV], computed with HERWIG at LO, and MCFM at LO and NLO for the $Zb\bar{b}$ background. We assume perfect b-tagging and include all the selection cuts except the jet veto cut. CTEQ6L1 is used for LO cross-sections and CTEQ6M for NLO cross-sections. The renormalisation and factorisation scales are set to $\mu = \sqrt{M_Z^2 + p_{t,Z}^2}$.

section, and found a K-factor of roughly $1.5 - 2$. We can thus conclude that the impact of the NLO corrections on our estimates for the significance $S/\sqrt{B}$ seems to be small, but the ratio S/B which controls a part of the systematic uncertainties is somewhat reduced for the WH channel.

3.6 Conclusion

The Higgs boson is the only particle of the Standard Model that has not been observed yet. The ATLAS and CMS experiments, which are the two main LHC experiments involved in Higgs hunting, have devoted a large amount of time to developing optimal strategies in order to find it (if it exists). It is difficult to observe when its mass is below 130 GeV because the main decay of the Higgs into $b\bar{b}$ is hidden behind the large QCD backgrounds. First analyses from ATLAS and CMS separately revealed that the decay $H \to b\bar{b}$, which might be possible to observe in the WH, ZH and $t\bar{t}H$ channels, was out of reach at a luminosity of 30 fb^{-1} at the LHC.

In this chapter we showed, contrary to what was believed, that the WH and ZH channels with $H \to b\bar{b}$ are actually promising search channels at the LHC for a low-mass Higgs boson. Indeed, at high-p_t we are able to recover the Higgs signal with a significance of 4.5σ at 30 fb^{-1} (3.7σ with a full detector simulation). These channels not only greatly help in observing the Higgs boson, but they also provide very important information on WWH, ZZH and $b\bar{b}H$ couplings [171]. The main point in this study is the ability to reconstruct the Higgs decaying into $b\bar{b}$ thanks to a new subjet analysis procedure which can be decomposed in 2 steps: a mass-drop analysis that allows one to reduce the large QCD background, and a filtering analysis that is designed to suppress as much as possible the effect of UE on the jet mass, thus improving mass resolution on jets. This procedure reconstructs the expected angular pattern of the perturbative radiation from the Higgs splitting and is able to adapt itself to the Higgs p_t, which can be substantially different from one event to the next, leading to different angular scales. We finally estimated the various NLO corrections that we expect for our analysis and we found that they do not strongly affect our $S/\sqrt{B}$ estimates based on LO results.

In this work we aimed to perform a simple analysis, and we thus observe that there is still room left for theoretical and experimental improvements. Our methods can also be used to identify a W or a Z boson for instance, as well as any new colourless resonance decaying hadronically that might be found at the LHC, and they can therefore have an important

impact in many other phenomenological studies that will be carried out.

Chapter 4

Non-global logarithms in filtered jet algorithms

In the previous chapter, we have shown how it is possible to recover the signal from a light Higgs boson decaying into $b\bar{b}$ at the LHC using a deep analysis into the substructure of the Higgs candidate jet. This kind of jets study has been widely used in recent years in order to identify more generally a boosted massive particle decaying hadronically, for instance the W boson [146, 147, 180, 181], top quarks [149, 174, 178, 179], supersymmetric particles [148, 182] and heavy resonances [183–185] (see also [186] for related work on general massive jets). Let us briefly recall our approach. After having clustered the event with a radius R_0 large enough to catch the b and $\bar{b}$ from the Higgs decay into a single jet,[1] this jet can be analysed in two steps:

- A Mass Drop (MD) analysis that allows one to identify the splitting responsible for the large jet mass, i.e. separate the b and $\bar{b}$ and thus measuring the angular distance R_{bb} between them, while suppressing as much QCD background as possible.

- A Filtering analysis where one reclusters the 2 resulting subjets with a smaller radius and takes the 3 highest-p_t subjets obtained in order to keep the major part of the perturbative radiation while getting rid of as many underlying event (UE) and pile-up (PU) particles as possible (which was later used also in [141, 174, 187], and a variant is proposed in [188]).

Concerning the MD analysis, the only thing we need to know is that we end up with 2 b-tagged jets, each with a radius roughly equal to R_{bb}. Notice that due to angular ordering [40–44], these 2 jets should capture most of the perturbative radiation from the $b\bar{b}$ dipole. The whole procedure is depicted in fig. 3.7.

In this chapter, we are going to focus on the filtering analysis. One can generalise it with respect to its original definition using 2 parameters, n_{filt} and η_{filt} (as discussed also in [188]): after the MD analysis was carried out, one reclusters the 2 resulting subjets with a radius $R_{\text{filt}} = \eta_{\text{filt}} R_{bb}$ and takes the n_{filt} hardest jets obtained. Obviously, the larger the value of η_{filt} the more perturbative radiation we keep, but also the more the UE/PU degrades the Higgs peak. The same holds for n_{filt}. So there is a compromise to make between losing too much perturbative radiation and being contaminated by soft particles from UE/PU. In

[1] The value chosen was $R_0 = 1.2$.

the previous chapter, we used for example $n_{\text{filt}} = 3$ and $\eta_{\text{filt}} = \min(0.3/R_{bb}, 1/2)$. However, these values had been chosen based on a brief Monte-Carlo event generator study and one would like to gain a little more analytical control over them. One question would be for instance to understand even approximately how the optimal (n_{filt},η_{filt}) values change when one increases the Higgs p_{t_H} cut, or when the PU becomes more and more important during the high luminosity running of the LHC. Though the MD and Filtering analysis were originally designed to identify a light Higgs boson, one should be aware that similar calculations may apply in other uses of filtering, for instance to study any boosted colourless resonance decaying hadronically, including W and Z bosons.

This chapter will be devoted in large part to the study of the dependence of the perturbative radiation loss with respect to the filtering parameters. As usual in this kind of work, large logarithms arise due to soft or collinear gluon emissions, and one is forced to deal with them in order to obtain reliable results in the region where the observable is sensitive to this kind of emission. We will thus compute analytically the two first orders in the leading soft logarithmic (LL) approximation when $n_{\text{filt}} = 2$ and to all-orders in the large-N_c limit[2] when $n_{\text{filt}} = 2$ or 3 for small enough values of η_{filt} (section 4.1). With these in hand, and using a program that allows one to carry out all-orders leading-log calculations in the large-N_c approximation, we check the analytical results and examine if the small-η_{filt} limit and/or the truncation of the LL expansion can be trusted to estimate the loss of perturbative radiation in practice (section 4.2). Finally, in section 4.3, we will analyse the Higgs mass peak width due respectively to the loss of perturbative radiation and to the presence of UE/PU, before combining them in a simple and approximate but physically reasonable way in order to be able to conclude about the optimal parameters choices.

4.1 Non-Global structure: analytical insights

4.1.1 The filtered Higgs mass: a Non-Global observable

It is now very well known [189–204] that soft or collinear gluons can give rise, in multiscale problems, to the appearance of large logarithms in the perturbative expansion of an observable, and more precisely in a region of phase space where it is sensitive to the soft or collinear divergences of QCD. In this chapter, the observable considered is $\Delta M = M_H - M_{\text{filtered jet}}$, where $M_{\text{filtered jet}}$ is the reconstructed Higgs-jet mass and M_H is its true mass. ΔM has the property that it is 0 when no gluon is emitted. We are interested in $\Sigma(\Delta M)$, the probability for the difference between the reconstructed and true Higgs masses to be less than a given ΔM. In this case, large soft logarithms have to be resummed at all-orders to obtain a reliable description of the small ΔM distribution.

Note that ΔM is taken to be positive definite, which is justified by the fact that we neglect Initial State Radiation (ISR). This is partially for a question of simplicity of the analysis, but also because the results of work such as [141,176] suggest that for LHC processes whose hard scales are few hundred GeV, the crucial interplay is that between Final State Radiation (FSR) and UE/PU. This is evident in the preference for small R values in dijet mass reconstructions in those references, where ISR is not playing a major role. Similarly we believe that the optimal values of η_{filt} that we will determine here will have limited impact

[2] $N_c = 3$ denotes as usual the number of QCD colours, see section 1.2.5 for more details about the large-N_c limit.

from ISR, though we shall not check this explicitly.

For the ΔM observable, soft gluons emissions lead to powers of $\ln \frac{M_H}{\Delta M}$, whereas collinear gluons emissions leads to powers of $\ln \frac{R_{bb}}{R_{\text{filt}}}$. In this study, gluons are strongly ordered in energy (the first emitted gluon being the most energetic one, and so on), and we aim to control the $\left(\alpha_s \ln \frac{M_H}{\Delta M}\right)^k$ series, in a region where

$$\ln \frac{M_H}{\Delta M} \gg \ln \frac{R_{bb}}{R_{\text{filt}}} \,. \tag{4.1}$$

Therefore, at leading-log accuracy, one has to resum terms like

$$I_k(\Delta M) = f_k \left(\frac{R_{bb}}{R_{\text{filt}}}\right) \left(\alpha_s \ln \frac{M_H}{\Delta M}\right)^k \,, \tag{4.2}$$

where all the f_k are functions to be computed. We thus disregard all the sub-leading terms, i.e. those suppressed by at least one power of $\ln \frac{M_H}{\Delta M}$. Unfortunately, such a calculation is highly non-trivial due to the fact that the observable is *non-global*. This property, first studied in [199], means that it is sensitive to radiation in only a part of the phase space. In the case of ΔM, only emissions of gluons outside the filtered jets region contribute to the observable (cf figure 4.1). As a consequence of this property, one must consider

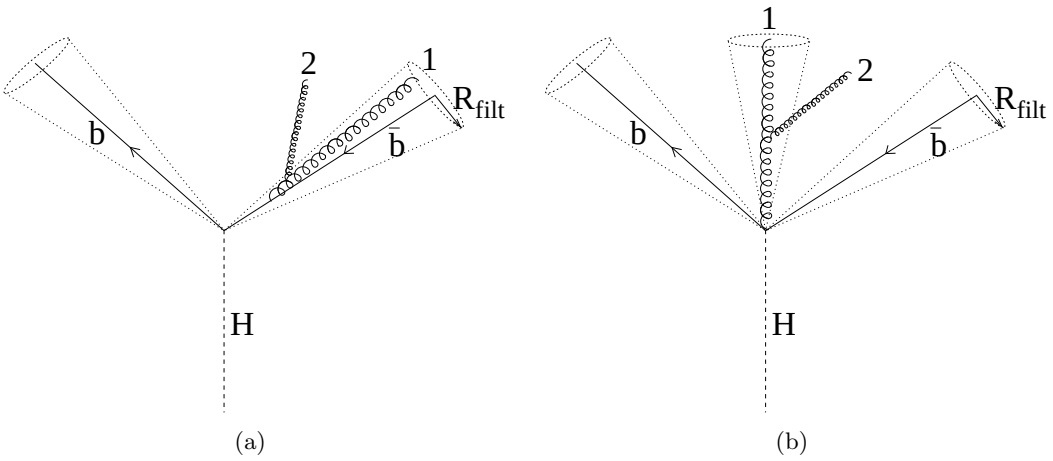

Figure 4.1: Configurations leading to non-global logarithms when (a) $n_{\text{filt}} = 2$ and (b) $n_{\text{filt}} = 3$. In each case, the hardest gluon 1, which is inside the filtered jet region, emits a softer gluon 2 outside the filtered jet region.

soft gluons emissions not just from the $b\bar{b}$ dipole (usually called primary emissions, the only ones that would be present in QED) but also from the whole ensemble of already emitted gluons [199, 205]. As the number of gluons is increased, the geometry and the colour structure of all these gluons become rapidly too complex to perform an analytical calculation. Therefore, to deal with this, one is forced to apply numerical Monte-Carlo calculations that can easily take care of the geometry. But the colour structure remains prohibitive, and one must usually also resort to the large-N_c approximation in order to go beyond the 2 first orders in perturbation theory [199, 205–207] (though some authors

have derived some analytical results in special cases [208, 209] and others have examined contributions beyond the leading large-N_c approximation [210, 211]).

However, before considering numerical calculations, some results can be derived analytically at 2^{nd} order for $n_{\text{filt}} = 2$ (where f_1 and f_2 are computed exactly) and $n_{\text{filt}} = 3$ (where only the leading behaviour of the f_k in $\ln \frac{R_{bb}}{R_{\text{filt}}}$ and N_c is looked for).

4.1.2 Some results for $n_{\text{filt}} = 2$

Perturbatively, one can write $\Sigma(\Delta M)$ as

$$\Sigma(\Delta M) = 1 + \sum_{k=1}^{\infty} I_k(\Delta M)\,, \tag{4.3}$$

where $I_k(\Delta M)$ is the $\mathcal{O}\left(\alpha_s^k\right)$ contribution to the observable. To simplify the calculation, $\Sigma(\Delta M)$ will be computed using the anti-k_t algorithm [78], even if the numerical study will be done using the C/A algorithm [71, 72] to be in accordance with the choice made in the previous chapter. However, the anti-k_t algorithm is enough to catch the dominant behaviour of the leading-log series, in the sense that it does not affect the leading large collinear logarithm in the function f_k at small R_{filt}:

$$f_k\left(\frac{R_{bb}}{R_{\text{filt}}}\right) = a_k \ln^k\left(\frac{R_{bb}}{R_{\text{filt}}}\right) + \mathcal{O}\left(\ln^{k-1}\left(\frac{R_{bb}}{R_{\text{filt}}}\right)\right)\,, \tag{4.4}$$

i.e. a_k is unchanged when moving from C/A to anti-k_t.[3] This jet algorithm gives simpler results because the gluons outside the filtered jet region tend not to cluster with the ones inside. It is this property which ensures that the hardest jets in an event are generally perfect cones, as particles usually cluster with the hardest ones in their neighbourhood first [78].

As a first step, primary emissions are considered, defined to be those one would obtain if gluons were only emitted from the $b\bar{b}$ dipole (as for photons in QED).

Primary emissions

Due to the use of the anti-k_t algorithm, the result of the primary emissions can be easily shown to exponentiate, as will be roughly seen in the next section with the $\mathcal{O}\left(\alpha_s^2\right)$ analysis. Here, we just review the very well known result that the contribution to $\Sigma(\Delta M)$ from primary emissions, denoted $\Sigma^{(P)}(\Delta M)$, can be written as:[4]

$$\Sigma^{(P)}(\Delta M) = e^{I_1(\Delta M)}\,, \tag{4.5}$$

with:

$$I_1(\Delta M) = \int \frac{d^3\vec{k}_1}{(2\pi)^3 2|\vec{k}_1|} M(k_1) \left(\Theta\left(\vec{k}_1 \in J_{b\bar{b}}\right) + \Theta\left(\vec{k}_1 \notin J_{b\bar{b}}\right)\Theta\left(\Delta M - \Delta M(\vec{k}_1)\right) - 1\right)\,. \tag{4.6}$$

[3] When $R_{\text{filt}} \sim \frac{R_{bb}}{2}$, the discarding of the $\mathcal{O}\left(\ln^{k-1}\left(\frac{R_{bb}}{R_{\text{filt}}}\right)\right)$ terms is not a priori justified, but fig. 4.4, which compares numerical results obtained using C/A with analytical estimates using anti-k_t, supports the dominance of the leading collinear logarithms.

[4] The superfix (P) serves as a reminder that only primary emissions are being accounted for.

$M(k_1)$ is the matrix element squared for emitting one soft gluon from the $b\bar{b}$ dipole (the b quark is taken to be massless):

$$M(k_1) = 4\pi\alpha_s C_F \frac{2(p_b.p_{\bar{b}})}{(p_b.k_1)(k_1.p_{\bar{b}})}\,. \tag{4.7}$$

Concerning the notations, $\Theta\left(\vec{k}_1 \in J_{b\bar{b}}\right)$ equals 1 when gluon 1 is emitted inside the jet regions around b and $\bar{b}$, denoted by $J_{b\bar{b}}$ (and is 0 otherwise), which, for $R_{\text{filt}} < R_{bb}$, is just 2 cones of radius R_{filt} centred on b and $\bar{b}$ (figure 4.1(a)). Then, concerning the expression in brackets in eq. (4.6), we separate the 2 different regions where the gluon can be: either inside or outside the filtered Higgs jet. The first term $\Theta(\vec{k}_1 \in J_{b\bar{b}})$ means that the gluon does not contribute to the observable (as it is kept in the Higgs jet, the reconstructed Higgs mass is the true Higgs mass: $\Delta M(k_1) = 0$). If the gluon is outside the filtered jet region (second term), then it does contribute to the observable:

$$\Delta M(k) \sim k_t \frac{M_H}{p_{t_H}}\,, \tag{4.8}$$

up to prefactors that can be neglected in the leading-log approximation, see appendix B. Finally, the -1 stands for the virtual corrections, for which there's obviously no loss of mass for the Higgs, and whose matrix element is just the opposite of the soft real one.[5] One thus obtains:

$$I_1(\Delta M) = -\int_{\vec{k}_1 \notin J_{b\bar{b}}} \frac{d^3\vec{k}_1}{(2\pi)^3 2|\vec{k}_1|} M(k_1)\Theta\left(\Delta M(k_1) - \Delta M\right)\,. \tag{4.9}$$

The computation of this integral in the boosted regime, where $p_{tH} \gg M_H$, or equivalently $R_{bb} \ll 1$, is done in appendix B. From now on, we will essentially use $\eta_{\text{filt}} = R_{\text{filt}}/R_{bb}$ instead of R_{filt} and we define $n \equiv n_{\text{filt}}$ and $\eta \equiv \eta_{\text{filt}}$ for more clarity in mathematical formulae. In order to keep in mind that it depends on the 2 parameters of the Filtering analysis, the distribution $\Sigma(\Delta M)$ is renamed $\Sigma^{(n)}(\eta, \Delta M)$. What we obtain at fixed coupling is the following:[6]

$$\Sigma^{(2),(P)}(\eta, \Delta M) = e^{-\frac{\alpha_s C_F}{\pi} J(\eta) \ln \frac{M_H}{\Delta M}}\,, \tag{4.10}$$

with

$$J(\eta) = 2\ln\left(\frac{1-\eta^2}{\eta^2}\right) \qquad \text{if } \eta < \frac{1}{2}\,, \tag{4.11}$$

$$= \frac{8}{\pi}\int_{\eta}^{+\infty} \frac{du}{u(u^2-1)} \arctan\left(\frac{u-1}{u+1}\sqrt{\frac{2u+1}{2u-1}}\right) \text{ if } \frac{1}{2} < \eta < 1\,. \tag{4.12}$$

We give the value of $J(1)$, a quantity that is important to discuss some aspects of the results obtained in the following sections:

$$J(1) \simeq 0.646\,. \tag{4.13}$$

[5] Even if the result seems obvious here, this way of doing the calculation can be easily generalised to higher orders and other kinds of jet algorithms.

[6] To obtain the result at running coupling, one simply makes the replacement (see eqs. (4.31,4.32) later in this chapter):

$$\alpha_s \ln\frac{M_H}{\Delta M} \to \frac{1}{2\beta_0}\ln\left(\frac{1}{1 - 2\beta_0\alpha_s(M_H)\ln\frac{M_H}{\Delta M}}\right)\,.$$

Notice that the case $\eta > 1$ will not be used in this study, but is mentioned in appendix B. The function $J(\eta)$ is plotted in figure 4.2.

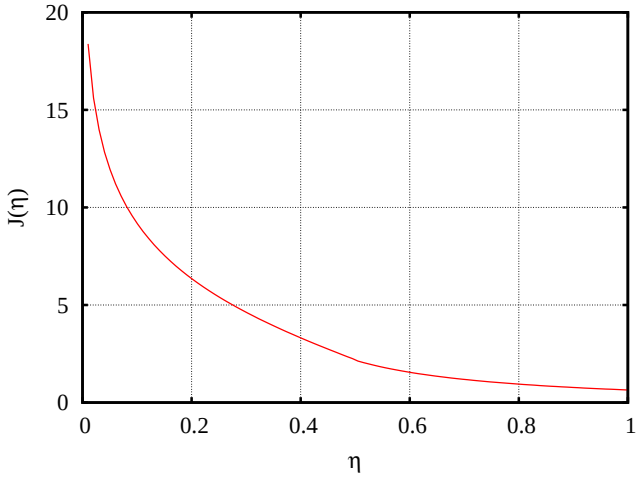

Figure 4.2: The coefficient $J(\eta)$ in front of the primary soft logarithm $\ln \frac{M_H}{\Delta M}$.

Two remarks can be made:

1. The result does not depend on the energy fraction z of the Higgs splitting into $b\bar{b}$.
2. When $\eta \ll 1$, another large logarithm $\ln \frac{1}{\eta}$ appears due to collinear enhancement.

Non-global contributions

Now, we turn to the $\mathcal{O}\left(\alpha_s^2\right)$ term, and more precisely to the contribution of the non-global terms that have to be added to the primary logarithms computed in the previous section. That corresponds to the analysis of $I_2(\Delta M)$ in the perturbative expansion of $\Sigma(\Delta M)$ from eq. (4.3). The matrix element squared for 2 real gluons emission is expressed as [40, 199, 212, 213]:

$$M(k_1 \text{ real}, k_2 \text{ real}) = (4\pi\alpha_s)^2 (W_1 + W_2)\,, \tag{4.14}$$

with

$$W_1 = 4C_F^2 \frac{(p_b.p_{\bar{b}})}{(p_b.k_1)(k_1.p_{\bar{b}})} \frac{(p_b.p_{\bar{b}})}{(p_b.k_2)(k_2.p_{\bar{b}})}\,, \tag{4.15}$$

$$W_2 = 2C_F C_A \frac{(p_b.p_{\bar{b}})}{(p_b.k_1)(k_1.p_{\bar{b}})} \left(\frac{(p_b.k_1)}{(p_b.k_2)(k_2.k_1)} + \frac{(p_{\bar{b}}.k_1)}{(p_{\bar{b}}.k_2)(k_2.k_1)} - \frac{(p_b.p_{\bar{b}})}{(p_b.k_2)(k_2.p_{\bar{b}})} \right). \tag{4.16}$$

This expression is valid when there is a strong energy ordering between the two real gluons 1 and 2, either $E_1 \gg E_2$ or $E_2 \gg E_1$ (the formula is completely symmetric under the interchange $k_1 \leftrightarrow k_2$). For the cases with one or both gluons being virtual, the following matrix elements are obtained, valid only when $E_1 \gg E_2$ [213]:

$$M(k_1 \text{ real}, k_2 \text{ virt}) = -(4\pi\alpha_s)^2 (W_1 + W_2)\,, \tag{4.17}$$

$$M(k_1 \text{ virt}, k_2 \text{ real}) = -(4\pi\alpha_s)^2 W_1\,, \tag{4.18}$$

$$M(k_1 \text{ virt}, k_2 \text{ virt}) = (4\pi\alpha_s)^2 W_1\,. \tag{4.19}$$

Using these properties, separating the 4 phase space regions depending on whether the gluons are inside or outside the filtered jet region in the same way as was done for I_1, and defining dk as:

$$dk = \frac{d^3\vec{k}}{(2\pi)^3 2|\vec{k}|}\,, \tag{4.20}$$

we can then write I_2 in the following form:

$$\begin{aligned}
I_2 = \int dk_1 dk_2 (4\pi\alpha_s)^2 \Theta(E_1 - E_2)\big\{ & \\
& \Theta(k_1 \in J_{b\bar{b}})\Theta(k_2 \in J_{b\bar{b}})\big((W_1+W_2) - (W_1+W_2) - W_1 + W_1\big) \\
& + \Theta(k_1 \in J_{b\bar{b}})\Theta(k_2 \notin J_{b\bar{b}})\big((W_1+W_2)\Theta(\Delta M - \Delta M(k_2)) - (W_1+W_2) - W_1\Theta(\Delta M - \Delta M(k_2)) + W_1\big) \\
& + \Theta(k_1 \notin J_{b\bar{b}})\Theta(k_2 \in J_{b\bar{b}})\big((W_1+W_2)\Theta(\Delta M - \Delta M(k_1)) - (W_1+W_2)\Theta(\Delta M - \Delta M(k_1)) - W_1 + W_1\big) \\
& + \Theta(k_1 \notin J_{b\bar{b}})\Theta(k_2 \notin J_{b\bar{b}})\big((W_1+W_2)\Theta(\Delta M - \Delta M(k_1,k_2)) - (W_1+W_2)\Theta(\Delta M - \Delta M(k_1)) \\
& \qquad - W_1\Theta(\Delta M - \Delta M(k_2)) + W_1\big)\big\}\,.
\end{aligned} \tag{4.21}$$

For each phase space region, the 4 terms

$$(k_1,k_2) = \text{ (real,real) } - \text{ (real,virt) } - \text{ (virt,real) } + \text{ (virt,virt)}$$

are considered. The strong energy ordering $E_1 \gg E_2$ implies that $\Delta M(k_1,k_2) = \Delta M(k_1)$, and one immediately gets:

$$\begin{aligned}
I_2 = & \int dk_1 dk_2 (4\pi\alpha_s)^2 \Theta(E_1 - E_2)\Theta(k_1 \notin J_{b\bar{b}})\Theta(k_2 \notin J_{b\bar{b}}) W_1 \Theta(\Delta M(k_2) - \Delta M) \\
& - \int dk_1 dk_2 (4\pi\alpha_s)^2 \Theta(E_1 - E_2)\Theta(k_1 \in J_{b\bar{b}})\Theta(k_2 \notin J_{b\bar{b}}) W_2 \Theta(\Delta M(k_2) - \Delta M)\,, \\
= & \; I_2^{(P)}(\Delta M) + I_2^{(NG)}(\Delta M)\,,
\end{aligned} \tag{4.22}$$

where $I_2^{(P)}(\Delta M)$ corresponds to the first integral containing the function W_1 whereas $I_2^{(NG)}(\Delta M)$ corresponds to the second integral with the function W_2. $I_2^{(P)}$ is just the second order contribution to the primary emissions, already computed above. To be convinced, one can notice that $(4\pi\alpha_s)^2 W_1$ can be expressed as the product of 2 one-gluon matrix elements $M(k_1)M(k_2)$ and, when $E_1 \gg E_2$,

$$\Theta\left(\Delta M(k_2) - \Delta M\right) = \Theta\left(\Delta M(k_2) - \Delta M\right)\Theta\left(\Delta M(k_1) - \Delta M\right)\,, \tag{4.23}$$

if k_1 and k_2 belong to the same phase space region. Therefore $I_2^{(P)}$ can be written in a more symmetric way:

$$\begin{aligned}
I_2^{(P)}(\Delta M) &= \frac{1}{2}\int dk_1 dk_2 (4\pi\alpha_s)^2 \Theta(k_1 \notin J_{b\bar{b}})\Theta(k_2 \notin J_{b\bar{b}}) W_1 \Theta(\Delta M(k_1) - \Delta M)\Theta(\Delta M(k_2) - \Delta M)\,, \\
&= \frac{1}{2}\left(\int dk \Theta(k \notin J_{b\bar{b}}) M(k) \Theta(\Delta M(k) - \Delta M)\right)^2\,, \\
&= \frac{1}{2}\left(I_1(\Delta M)\right)^2\,,
\end{aligned} \tag{4.24}$$

so that it corresponds to the second order perturbative expansion of the result eq. (4.5), obtained with primary emissions only.

The important term for this section is the one containing W_2, denoted by $I_2^{(NG)}$. As mentioned in section 4.1.1, it receives a non-zero contribution when the hardest gluon 1 is emitted inside the filtered jet region whereas the softest gluon 2 is emitted outside. For the opposite configuration, there is an exact cancellation between gluon 2 being real and virtual. Here again the computation of $I_2^{(NG)}$ is postponed to appendix B, giving directly what will help to interpret some results later. S_2 is defined such that

$$I_2^{(NG)}(\eta, \Delta M) = \frac{1}{2} C_F C_A \left(\frac{\alpha_s}{\pi} \ln \left(\frac{M_H}{\Delta M} \right) \right)^2 S_2(\eta) \,, \tag{4.25}$$

where we explicitly introduce the dependence on η and we factorise out the soft divergence, still revealed in the large logarithm $\ln \frac{M_H}{\Delta M}$. When $\eta < 1/2$, the result for S_2 can be written as:

$$\begin{aligned} S_2(\eta) &= -\frac{\pi^2}{3} + 8 \int_0^1 \frac{du_1}{u_1} \int_0^1 \frac{du_2}{u_2} \left(\frac{1}{\sqrt{(1-\eta^2(u_1^2+u_2^2))^2 - 4\eta^4 u_1^2 u_2^2}} - \frac{1}{1-\eta^2(u_1^2+u_2^2)} \right) , \\ &= -\frac{\pi^2}{3} + 4\eta^4 + 12\eta^6 + \mathcal{O}\left(\eta^8\right) . \end{aligned} \tag{4.26}$$

The important point to notice in this result is the absence of collinear logarithms, which would appear as $\ln \frac{1}{\eta}$, contrary to the primary emission case (eq. (4.11)). So that the primary emissions dominate for this observable, at least for η sufficiently small.

As mentioned in previous studies [199, 214], one notices the presence of "π^2 terms" in non-global results at second order.

4.1.3 Some results for $n_{\text{filt}} = 3$

The goal in this section is to have an estimate of the analytical behaviour in the large N_c limit of $\Sigma^{(n)}(\eta, \Delta M)$ for $n = 3$, which is the probability of having no second gluon emission leading to a $\Delta M'$ greater than ΔM. Notice that, contrary to the previous part where we obtained the function $\Sigma^{(2)}$, only the leading behaviour in $L = \ln \frac{1}{\eta}$ and N_c will be derived, so that in this context $\Sigma^{(2)}$ can be simply written:[7]

$$\Sigma^{(2)}(L, t) = e^{-4N_c L t} \tag{4.27}$$

where for further convenience we introduce the parameter $t = \frac{\alpha_s}{2\pi} \ln \frac{M_H}{\Delta M}$ and we change the arguments of Σ which becomes now a function of L and t. In this formula, $2L = 2 \ln \frac{R_{b\bar{b}}}{R_{\text{filt}}}$ can be interpreted as the "logarithmic size" of the $b\bar{b}$ dipole, i.e. the allowed phase space in rapidity for an emission from this dipole (in its centre of mass frame) outside the jet region. The parameter t means that this emission cannot occur with a t' between 0 and t.

Now we turn to $\Sigma^{(3)}(L, t)$. To have no second gluon emission in $[0, t]$, either there is no first gluon emission in $[0, t]$ outside the jet region (which corresponds to $\Sigma^{(2)}(L, t)$), or there is such an emission but the new dipole configuration is prohibited from emitting a second gluon in $[0, t]$ outside the jet region. This is depicted in figure 4.3. As the calculation is done in the large-N_c limit, after the emission of a first gluon, the second one cannot be

[7] This results simply from the combination of equations (4.10) and (4.11) with $\eta \ll 1$, and $C_F = \frac{N_c}{2}$ in the large N_c limit.

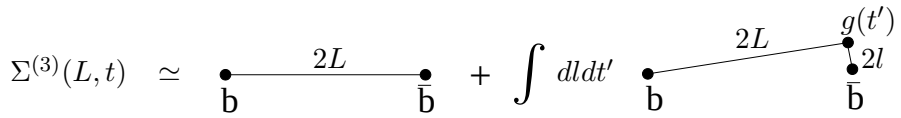

Figure 4.3: How to compute the leading behaviour of $\Sigma^{(3)}(L,t)$ from $\Sigma^{(2)}(L,t)$ when $L \gg 1$ and $N_c \gg 1$. In the second term, t' is the gluon's emission scale.

emitted from the $b\bar{b}$ dipole, but only from the bg and $\bar{b}g$ ones. Fig. 4.3 can be translated mathematically as:

$$\Sigma^{(3)}(L,t) \simeq \Sigma^{(2)}(L,t) + \int_0^t dt' 4N_c \Sigma^{(2)}(L,t') \int_0^L dl\ \Sigma^{(2)}(L,t-t')\Sigma^{(2)}(l,t-t')\,. \qquad (4.28)$$

Notice that L_{bg}, the logarithmic size of the bg dipole in figure 4.3, does not depend on l in the leading collinear log approximation.[8] In this expression, $4N_c L\Sigma^{(2)}(L,t')dt'$ is the probability not to emit the first gluon in $[0,t']$ and to emit it only at $t \in [t', t'+dt']$. The remaining part $\frac{1}{L}\int_0^L dl\,\Sigma^{(2)}(L,t-t')\Sigma^{(2)}(l,t-t')$ is the probability to emit no second gluon from the bg and $\bar{b}g$ dipoles in $[t',t]$. Using eq. (4.27) for $\Sigma^{(2)}$, $\Sigma^{(3)}$ is then given by:

$$\Sigma^{(3)}(L,t) \simeq e^{-4N_c Lt}\left(1 + \int_0^{4N_c Lt} dt' \frac{1-e^{-t'}}{t'}\right)\,. \qquad (4.29)$$

Two limits can be considered:

$$\Sigma^{(3)}(L,t) \simeq \begin{cases} 1 - \frac{3}{4}(4N_c Lt)^2 + \mathcal{O}\left((4N_c Lt)^3 + N_c t\right) & \text{if } 4N_c Lt \ll 1\,, \\ e^{-4N_c Lt}\left(\ln\left(4N_c Lt\right) + \mathcal{O}(1)\right) & \text{if } 4N_c Lt \gg 1\,. \end{cases} \qquad (4.30)$$

The limit $4N_c Lt \ll 1$ reveals two important aspects:

1. One can notice the absence of the $\mathcal{O}(Lt)$ term, which is indeed the goal of the filtering analysis as it was presented in its original version (section 3.2.2): it is intended to catch the major part of the $\mathcal{O}(\alpha_s)$ perturbative radiation. It cannot catch *all* the

[8] One can easily show the following relation:

$$L_{bg} = 2L + \mathcal{O}\left(e^{l-L}\right)\,.$$

If we introduce the neglected component of L_{bg} in the $\Sigma^{(3)}$ calculation eq. (4.28), then we have to compute an integral of the form

$$\int_0^L dl\,\frac{1-e^{(l+\mathcal{O}(e^{l-L}))t}}{l+\mathcal{O}(e^{l-L})}\,.$$

Expanding the exponential and keeping the term of order k gives

$$\int_0^L dl\,\left(l+\mathcal{O}(e^{l-L})\right)^{k-1} t^k = \frac{(Lt)^k}{k} + \mathcal{O}(L^{k-2}t^k)\,.$$

The leading $\mathcal{O}\left((Lt)^k\right)$ term is already taken into account in eq. (4.29). Therefore, including the l dependent component of L_{bg} gives rise to terms of the form $N_c^k L^{k-2} t^k$ at order k, suppressed by 2 powers of L with respect to the leading one.

$\mathcal{O}(\alpha_s)$ contribution because a hard gluon emitted at an angle $\theta > R_{bb}$ from the b and $\bar{b}$ escapes the filtering process as it is rejected by the Mass Drop analysis. Therefore, when $4N_c Lt \ll 1$, the expansion eq. (4.30) misses a term $\mathcal{O}(N_c t)$, but this is legitimate in a leading collinear log estimate. Notice that the missing term is simply $-J(1)N_c t$ where $J(\eta)$ was given in eq. (4.12).

2. it shows that the purely non-global result for $n = 3$ contains large collinear logarithms L, contrary to the case $n = 2$ (eq. (4.26)). Indeed, the primary result for $n = 3$ at second order can be proved to behave as[9] $-32C_F^2(Lt)^2$ at order α_s^2, so that the S_2 term for $n = 3$ should be equivalent to $-8C_F C_A(Lt)^2$ at large L.

Having understood some analytical features of the Filtering analysis, we now examine what can be learnt from a numerical calculation of the reconstructed Higgs mass observable.

4.2 Non-Global structure: numerical results

In all that follows t is defined so as to gather all the information about the soft logarithms in a running coupling framework:

$$\begin{aligned} t &= \frac{1}{2\pi}\int_0^{p_{t_H}} \frac{dk_t}{k_t}\alpha_s\left(k_t\frac{M_H}{p_{t_H}}\right)\Theta\left(\Delta M(k) - \Delta M\right) , \\ &= \frac{1}{2\pi}\int_{p_{t_H}\frac{\Delta M}{M_H}}^{p_{t_H}} \frac{dk_t}{k_t}\alpha_s\left(k_t\frac{M_H}{p_{t_H}}\right) , \\ &= \frac{1}{4\pi\beta_0}\ln\left(\frac{1}{1-2\beta_0\alpha_s(M_H)\ln\frac{M_H}{\Delta M}}\right) , \end{aligned} \tag{4.31}$$

where the last equality holds at the one-loop level and $\beta_0 = \frac{11C_A - 2n_f}{12\pi}$. The argument of α_s was taken as the gluon's transverse momentum with respect to the Higgs boson direction, of order $k_t\frac{M_H}{p_{t_H}}$, k_t being its transverse momentum with respect to the beam. In the case of a fixed coupling constant α_s, the definition for t here coincides with that of section 4.1.3:

$$t = \frac{\alpha_s}{2\pi}\ln\frac{M_H}{\Delta M} . \tag{4.32}$$

But from now on, and unless stated otherwise, t is given in the running coupling framework, eq. (4.31), and the function $\Sigma(\eta, \Delta M)$ is rewritten as $\Sigma(\eta, t)$.

To get an idea of the range of values covered by t, table 4.1 presents a few t values corresponding to a given ΔM for a Higgs mass of 115 GeV ($\alpha_s(M_H) = 0.114$). It reveals that the physical values for t are below 0.15.

To numerically investigate non-global observables, two approaches can be followed:

[9] In fact, one can show the following general estimate for the primary emissions in the leading soft and collinear approximations:

$$\Sigma^{(n)}(L,t) = e^{-8C_F Lt}\sum_{k=0}^{n-2}\frac{(8C_F Lt)^k}{k!} .$$

ΔM (GeV)	1	2	5	10	20	50	115
t	0.141	0.108	0.075	0.054	0.036	0.016	0

Table 4.1: Correspondence between ΔM and t for some particular values.

- an all-orders approach where one resums the leading-logs at all-orders in the large-N_c limit, the output being the function $\Sigma(t)$, i.e. the probability that the loss of perturbative emission results in a Higgs mass in the range $[M_H - \Delta M(t), M_H]$, with

$$\Delta M(t) = M_H e^{-\frac{1}{2\beta_0\alpha_s}\left(1-e^{-4\pi\beta_0 t}\right)}, \tag{4.33}$$

  simply obtained by inverting the relation eq. (4.31).

- a fixed-order approach where the first few coefficients from the expansion of $\Sigma(t)$ are computed in the large-N_c limit. More precisely, if $\Sigma(t) = \sum_{k=0}^{\infty} \frac{c_k}{k!} (N_c t)^k$, then the program returns the first few coefficients c_k.

From a numerical point of view, the way to write a fixed-order and all-orders programs is explained in appendix D. A result at fixed-order may be obtained by developing a systematic approach like the one presented at second order in eq. (4.21). For the filtered Higgs jet mass observable, we used the Fastjet package [76] to perform the clustering (and mass-drop + filtering) with the C/A algorithm, consistently with the choice made in section 3.2.

As the all-orders program gives immediately what we are looking for, which is $\Sigma(t)$, we will use it (section 4.3.1) to compute the perturbative Higgs width. But in order to check it and be confident with the results obtained, we compare them with the previous analytical estimates and see how well the perturbative leading log series fits them. This leads us to study the behaviour of the higher order terms and to gain a better understanding of the convergence and structure of the non-global series. Though treated in more details in appendix E, the main points are mentioned in this section.

4.2.1 Comparison with analytics

Using the all-orders Monte-Carlo program, a comparison between the all-orders numerical curves obtained using the C/A algorithm and their corresponding analytical estimates obtained previously with anti-k_t in eqs. (4.27,4.29) can be done. The results are presented in figure 4.4 and show good agreement, at least in the region of physical t values.

Notice that the slight discrepancy between analytical estimations and numerics starts to occur at $t > 0.1$, which is at the edge of the physical region (cf table 4.1), beyond which ΔM would be below the perturbative scale of around 1 GeV. This agreement manifests that:

- In the physical region, the leading terms in $(\alpha_s L t)^k$, with $L = \ln \frac{1}{\eta}$ seem to completely dominate and we do not need to compute the sub-leading corrections.

- One can use these analytical expressions to get an accurate estimate of the reconstructed Higgs peak width.

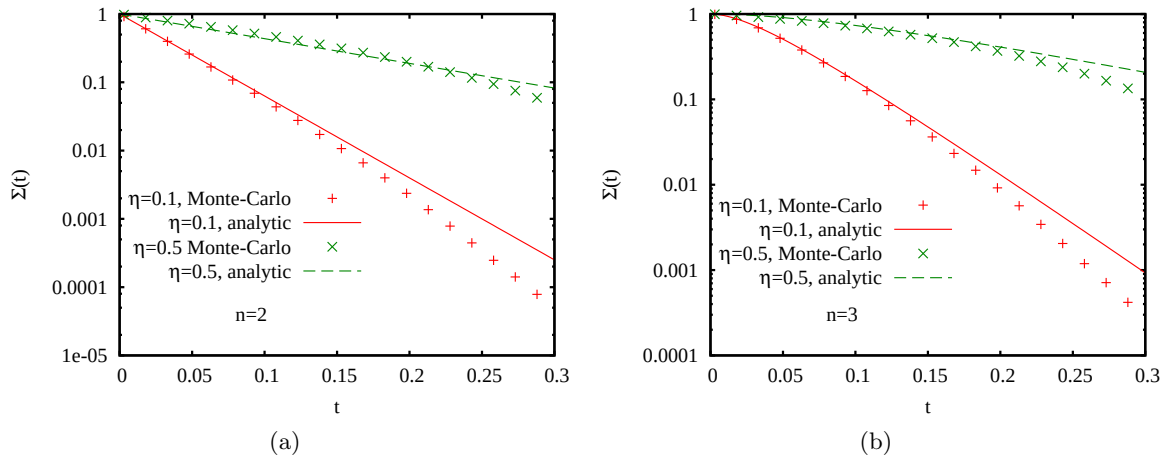

Figure 4.4: Comparison between numerical all-orders result (obtained using C/A algorithm) and leading collinear logarithm estimate of $\Sigma(t)$ derived with anti-k_t for (a) $n = 2$ and (b) $n = 3$ for 2 values of η: 0.1 and 0.5.

4.2.2 Comparison with fixed-order results

The structure of the non-global series at fixed-order is now examined so as to independently cross-check the all-orders program and to understand if the perturbative leading-log series can be usefully truncated.

As an example, figure 4.5 compares the all-orders result to the fixed-order ones up to α_s^5 for $n = 2$ and two different values of η (only the coefficients with an uncertainty of at most a few percent are plotted[10]). The curves are represented up to $t = 0.3$, which is far beyond the physical region but is instructive to study the convergence of the series.

The left plot for $\eta = 0.3$ shows a nice convergence of the perturbative series eq. (4.3), as the t range for which the all-orders and fixed-order curves coincide grows with k. However, the second plot for $\eta = 0.9$ gives an unexpected result: the fourth order diverges with respect to the third one, in the sense that the point of disagreement is shifted to smaller t. The question arises whether this divergence will remain at higher orders. To answer it, one needs to go further in perturbation theory. In appendix E, a parallel is made between the filtered Higgs jet observable and the slice observable, studied for instance in [205], for which, due to computational speed, it is possible to obtain reliable coefficients up to order 6. The same effect is observed and is even enhanced at orders 5 and 6. Therefore, it seems that the fixed-order information cannot be safely used in general: one has to be aware that the leading-log large-N_c non-global series may be divergent for any value of t.

4.3 Choice of the filtering parameters

In the previous sections we examined the structure and convergence of the perturbative leading-log series, analytically and numerically. We could then cross-check the analytical expressions and the fixed-order approach with the all-orders program, which we are going

[10]This uncertainty obviously increases with the perturbative order, but also with η because at small η, the coefficients are sensitive to the large logarithm $\ln \frac{1}{\eta}$, which is easy to compute.

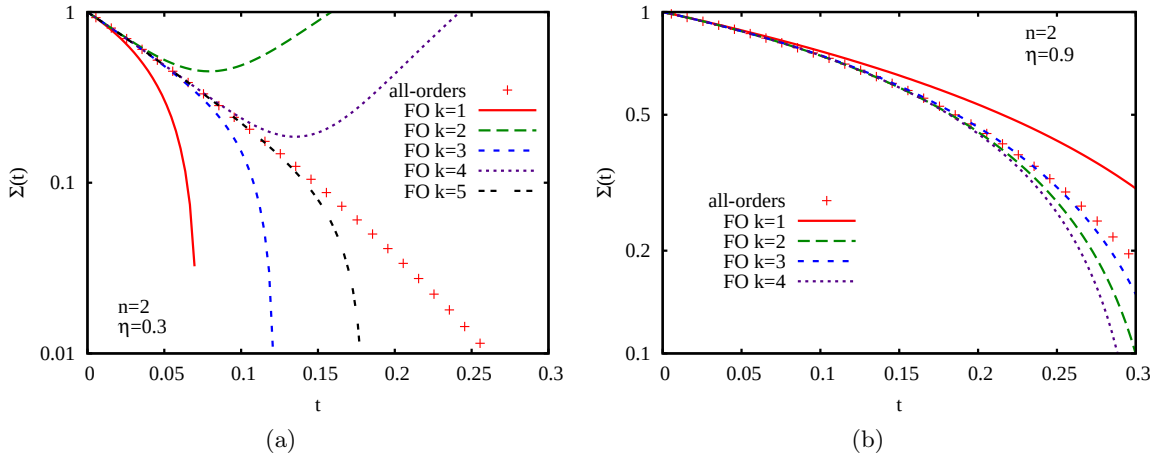

(a) (b)

Figure 4.5: Comparison between fixed-order (FO) expansion and all-orders result when $n = 2$ for (a) $\eta = 0.3$ and (b) $\eta = 0.9$. Both fixed-order and all-orders results were obtained using the C/A algorithm.

to use throughout this part.

We would like to decide how one should choose the filtering parameters (n,η) depending on the level of UE and PU as well as the p_t of the Higgs boson. Here, we do not claim to make an exact and complete analysis, but we want to obtain some estimates. First, we consider the width of the Higgs mass distribution separately in presence of perturbative radiation (using the all-orders results) and UE/PU (using a simple model for it). Then, we try to minimise the Higgs width in presence of both of these effects. Finally, we will estimate hadronisation corrections.

In all this part, we set the Higgs mass M_H at 115 GeV, as in the previous chapter.

4.3.1 Study of the Higgs perturbative width

As we could see in the previous sections, even without considering additional particles from UE/PU, $\Delta M \equiv M_H - M_{\text{filtered jet}} \neq 0$ because of the loss of perturbative radiation. The Higgs boson thus acquires a perturbative width, denoted δM_{PT}. At first sight, knowing the distributions $\Sigma^{(n)}(\eta, \Delta M)$, one might simply define it as:

$$\delta M_{PT} = 2\sqrt{\langle \Delta M^2 \rangle - \langle \Delta M \rangle^2}\,, \tag{4.34}$$

as we do for gaussian distributions for instance. Unfortunately, if we simply take $n = 2$ as an example and if we consider the primary emission result eq. (4.10), we can deduce the following distribution for ΔM:

$$\frac{d\Sigma^{(2)}(\eta, \Delta M)}{d\Delta M} = \frac{\alpha_s C(\eta)}{M_H^{\alpha_s C(\eta)}} \frac{1}{\Delta M^{1-\alpha_s C(\eta)}}\,, \tag{4.35}$$

with

$$C(\eta) = \frac{C_F J(\eta)}{\pi}\,. \tag{4.36}$$

Computing $\langle \Delta M \rangle$ and $\langle \Delta M^2 \rangle$ implies dealing with integrals of the form

$$\int_0^{M_H} \frac{d\Delta M}{\Delta M^{1-\alpha_s C(\eta)}} \Delta M = \int_0^{M_H} d\Delta M \, \Delta M^{\alpha_s C(\eta)} \,, \tag{4.37}$$

$$\int_0^{M_H} \frac{d\Delta M}{\Delta M^{1-\alpha_s C(\eta)}} \Delta M^2 = \int_0^{M_H} d\Delta M \, \Delta M^{1+\alpha_s C(\eta)} \,. \tag{4.38}$$

Such integrals give a large importance to the $\Delta M \sim M_H/2$ region, where there should be very few events, and do not describe what happens in the neighbourhood of the peak near $\Delta M = 0$. Therefore, the definition eq. (4.34) does not seem adequate for the perturbative width. That's why we shall adopt another definition, adapted from [215]. The Higgs perturbative width is defined as the size δM_{PT} for which a given fraction f of events satisfy $0 < \Delta M < \delta M_{PT}$. Using the all-orders function previously computed, this is equivalent to solving the equation $\Sigma^{(n)}(\eta, \Delta M) = f$. This leads to the width function $\delta M_{PT}(n, \eta, f)$.

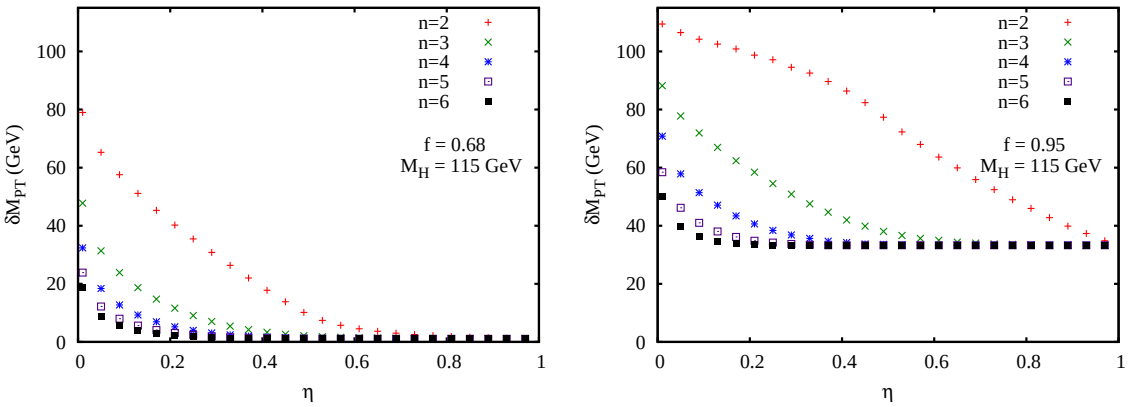

Figure 4.6: Perturbative width of the Higgs boson (in GeV) as a function of η for several values of n when (a) $f = 0.68$ and (b) $f = 0.95$.

Fig. 4.6 shows δM_{PT} as a function of η for $n = 2 \ldots 6$. When $\Delta M \sim 50$ GeV (i.e. $\sim M_H/2$), one should be aware that soft approximation loses sense and results on these plots should no longer be taken seriously. We chose the values $f = 0.68$ and $f = 0.95$, corresponding respectively to full widths of 2σ and 4σ for gaussian distributions, to show that the Higgs mass perturbative distribution is not gaussian (otherwise, going from 2σ to 4σ would have multiplied the width by a factor of 2, see also eq. (4.35)). One important thing to notice is a kind of "saturation" effect that one observes for η close enough to 1 for every fraction f. It manifests itself as a flat curve at a value $\delta M_{PT} = \delta M_{sat}(f)$, independent of n. For instance, $\delta M_{sat}(f = 0.68) \simeq 1$ GeV and $\delta M_{sat}(f = 0.95) \simeq 33$ GeV. This can be understood simply by considering that when the radius of the filtering is large enough, say $\eta > \eta_{sat}(n)$, it captures (almost) all the particles resulting from the Mass Drop analysis, i.e. all those that are within angular distance R_{bb} from b or $\bar{b}$, but it still fails to capture particles outside the Mass Drop region.[11] Of course, the larger n, the smaller $\eta_{sat}(n)$ as we keep more jets. This saturation property is equivalent to saying that all the functions $\Sigma^{(n)}(\eta, \Delta M)$ become independent of n and η when $\eta > \eta_{sat}(n)$.

[11] The probability to emit a gluon outside the MD region in $[0, t]$ is roughly given by $1 - e^{-J(1)N_c t}$.

For the rest of this analysis we keep the value $f = 0.68$, even if it is not clear which value should be chosen, and more generally what should be the relevant definition of the Higgs perturbative width. However, we will mention in section 4.3.4 what happens if we vary f between $f = 0.5$ and $f = 0.8$, so as to obtain a measure of the uncertainty of the calculations.

The curves in figure 4.6 only give us an overview of the scales involved in the Higgs boson width. But one can go a little further. At small η, we should get a large collinear enhancement revealing itself as a large logarithm $L = \ln \frac{1}{\eta}$ multiplying t. The perturbative expansion is thus a series in $(N_c L t)^k$. As a direct consequence, at small η, the all-orders function $\Sigma^{(n)}(\eta, t)$ can be written as a function of a single variable $\Sigma^{(n)}(N_c L t)$. Solving the "width equation"

$$\Sigma^{(n)}(N_c L t) = f \,, \tag{4.39}$$

gives

$$t_{PT} = \frac{C_{PT}(n, f)}{L} \,, \tag{4.40}$$

where t_{PT} is simply related to δM_{PT} by

$$t_{PT} = \frac{1}{4\pi\beta_0} \ln \left(\frac{1}{1 - 2\beta_0 \alpha_s(M_H) \ln \frac{M_H}{\delta M_{PT}}} \right) \,, \tag{4.41}$$

and where $C_{PT}(n, f)$ is a function, independent of η, which increases with n and decreases when f increases. This is confirmed by figure 4.7(a) which shows that $t_{PT} L$ is indeed independent of η as long as η and n are not too large.

As an example, for $n = 2$, let us take the simple result $\Sigma^{(2)}(L, t) = e^{-4 N_c L t}$ from eq. (4.27) in the small η limit. It was shown in section 4.2.1 that this result is very close to the all-orders one in the physical t region. Solving $\Sigma^{(2)}(L, t) = f$ immediately implies

$$C_{PT}(2, f) = \frac{\ln \frac{1}{f}}{4 N_c} \,, \tag{4.42}$$

which, for $f = 0.68$, gives $C_{PT} \simeq 0.032$ in accordance with figure 4.7(a).

One observes that $t_{PT} L$ is not strictly speaking a constant for higher n values. This may be due to the saturation effects discussed above. Indeed, even at large L, the perturbative expansion is not only a function of Lt but also of t for the lowest orders, as mentioned at the end of section 4.1.3:

$$\Sigma^{(n)}(L, t) = 1 + \sum_{k=1}^{n-2} a_k t^k + \sum_{k=n-1}^{+\infty} \left(a_k (Lt)^k + \mathcal{O}\left(L^{k-1} t^k \right) \right) \,, \tag{4.43}$$

If we only had QED like emissions, i.e. primary ones, with the use of the anti-k_t jet algorithm, we would obtain $a_k = \frac{(-J(1) N_c)^k}{k!}$ for $k \leq n - 2$, where $J(\eta)$ was derived in section 4.1.2. As n increases, the term $a_1 t$ becomes more and more important with respect to $a_{n-1}(Lt)^{n-1}$, leading to larger and larger deviations from the simple law $t_{PT} L = \text{constant}$. However, until $n = 5$, assuming $t_{PT} L$ is a constant at small η seems a good approximation. Therefore, using eq. (4.41), one can model the Higgs perturbative width in the following form:

$$\delta M_{PT}(n, L, f) = \begin{cases} M_H e^{-\frac{1}{2\beta_0 \alpha_s} \left(1 - e^{-4\pi\beta_0 \frac{C_{PT}(n,f)}{L}} \right)} & \text{if } \eta < \eta_{sat}(n, f) \,, \\ \delta M_{sat}(f) & \text{if } \eta > \eta_{sat}(n, f) \,. \end{cases} \tag{4.44}$$

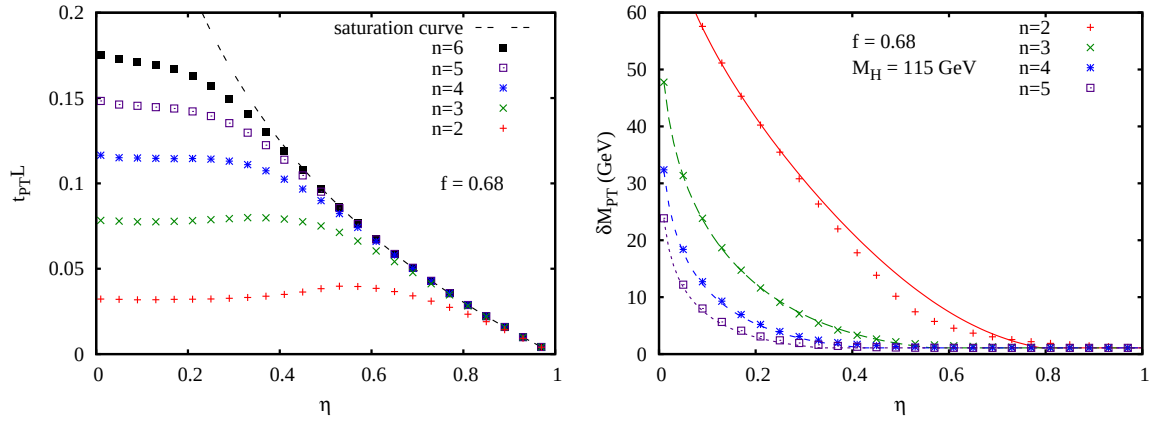

Figure 4.7: (a) $t_{PT}L$ as a function of η for $f = 0.68$ and different values of n. The saturation curve simply comes from the fact that all widths saturate to the same constant δM_{sat} for η large enough, and its equation is therefore given by $t_{sat}L$ (with $t_{sat}(f = 0.68) \simeq 0.136$). (b) δM_{PT} as a function of η for $f = 0.68$ and different values of n (curves with points). For each n is also represented the corresponding approximate width (lines) given by eq. (4.44).

n	2	3	4	5
C_{PT}	0.032	0.078	0.117	0.149
η_{sat}	0.79	0.56	0.42	0.34

Table 4.2: C_{PT} and η_{sat} as a function of n when $f = 0.68$.

$\eta_{sat}(n, f)$ is given by the intersection between the curve $t_{PT} = C_{PT}/L$ and $t_{PT} = t_{sat}$. Therefore:

$$\eta_{sat}(n, f) = e^{-\frac{C_{PT}(n,f)}{t_{sat}}} . \tag{4.45}$$

Table 4.2 shows C_{PT} and η_{sat} for $f = 0.68$ and different n values. Figure 4.7(b) shows the curves corresponding to the parametrisation eq. (4.44). We can see that it works rather well for all values of n except $n = 2$ in the region $\eta \sim 0.4 - 0.6$. This can be improved using the relation $J(\eta)t_{PT} =$ constant, which works better for $n = 2$ because it is exact for primary emissions with anti-k_t. But implementing it would not change the main conclusions presented in sections 4.3.3-4.3.5. Therefore, for the sake of simplicity, we will not use it here: we keep eq. (4.44) as the expression for δM_{PT} for the rest of this study.

Of course, were it only for the perturbative radiation, it would be nicer to choose $\eta \geq \eta_{sat}$ in order to catch as many gluons as possible, leading to $\delta M_{PT} \to \delta M_{sat}$. But we also have to take into account Initial State Radiation (ISR) and non-perturbative effects like PU and UE that can spoil our Higgs neighbourhood, thus increasing the jet mass.

Note that for the purpose of this analysis, as already mentioned previously, we will only add UE and PU to the Final State Radiation (FSR) effect studied above, and thus ignore ISR.

4.3.2 Study of the Higgs width due to underlying event and pile-up

For this simple analysis, which does not aim to give precise numbers but only an estimate of the influence of the UE/PU on the mass of the Higgs jet when we vary for instance η, n, or when the Higgs boson becomes more and more boosted, we model the UE and PU as soft particles uniformly distributed in the (y, ϕ) plane [216,217], and with transverse momentum per unit area denoted by ρ. In order to get this estimate, we consider the simple case of a symmetric ($z = 1/2$) Higgs decay along the x axis. In the limit $M_H \ll p_{t_H}$, the Higgs momentum p_H is given by:

$$p_H = \left(p_{t_H} + \frac{M_H^2}{2p_{t_H}}, p_{t_H}, 0, 0\right) . \tag{4.46}$$

The UE/PU momentum, denoted p_{UE},[12] is simply the sum of all the UE/PU particles g belonging to the filtered jet J. Still in the limit $M_H \ll p_{t_H}$, we recall the following formula (eq. (3.1)):

$$R_{bb} \simeq \frac{1}{\sqrt{z(1-z)}} \frac{M_H}{p_{t_H}} . \tag{4.47}$$

Throughout this section, we will apply it with $z = 1/2$. We can now write $\Delta M = M_{\text{filtered jet}} - M_H$ as:

$$\begin{aligned} \Delta M &= \frac{1}{2M_H} \left((p_H + p_{UE})^2 - M_H^2\right) , \\ &\simeq \frac{1}{M_H} \sum_{g \in J} p_{t_g} p_{t_H} \left(\frac{\theta_{gH}^2}{2} + \frac{M_H^2}{2p_{t_H}^2}\right) , \\ &\simeq \frac{M_H}{p_{t_H}} \sum_{g \in J} p_{t_g} . \end{aligned} \tag{4.48}$$

In the last line we used the approximation:

$$\theta_{gH} \sim \theta_{bH} = \frac{R_{bb}}{2} , \tag{4.49}$$

which comes from the fact that the UE and PU particles tend to cluster around the perturbative radiation, which is usually close to the b and $\bar{b}$ because of the collinear logarithmic divergence of QCD. As all the filtered UE/PU particles flow approximately in the same direction, the remaining sum is just the total transverse momentum of the UE which, by definition of ρ, is equal to ρA, A being the total area of the filtered jets.[13] We thus obtain

$$\Delta M \simeq \frac{\rho A M_H}{p_{t_H}} , \tag{4.50}$$

with

$$\langle A \rangle \simeq n\pi\eta^2 R_{bb}^2 , \tag{4.51}$$

[12] For brevity, we define p_{UE} to be the sum of the UE and/or PU particles' momentum but without referencing the PU dependence, which will always be implicit.

[13] in the active sense, see [216].

for the C/A jet algorithm, taking into account the anomalous dimension that comes from the fact that there should be some perturbative radiation in the jets (cf figure 14 in [216]). Notice that eq. (4.51) is only true if all the jets do not overlap, so usually when η is small enough. But this is sufficient for the purpose of our study, and we shall use this formula in all the following calculations. The correction eq. (4.50) for ΔM only induces a shift towards higher masses of the Higgs mass peak. However, there are 3 sources of fluctuations that give a width to this Higgs peak:

1. ρ is not strictly uniform in the (y, ϕ) plane in a given event.
2. ρ is not the same from one event to the next.
3. The jets' area fluctuates.

Following [216], we can write the total UE/PU transverse momentum contributing to the Higgs p_t as

$$p_{t_{UE}} = \rho A \pm \left(\sqrt{A}\sigma + A\delta\rho + \rho\Sigma\right) , \tag{4.52}$$

where

$$\sigma = \sqrt{\langle\rho^2\rangle - \langle\rho\rangle^2} \quad \text{with } \langle ...\rangle \text{ a spatial average in a given event} , \tag{4.53}$$

$$\delta\rho = \sqrt{\langle\rho^2\rangle - \langle\rho\rangle^2} \quad \text{with } \langle ...\rangle \text{ an average over events} , \tag{4.54}$$

$$\Sigma = \sqrt{\langle A^2\rangle - \langle A\rangle^2} \quad \text{with } \langle A\rangle \text{ the average over events of the filtered jets' area} . \tag{4.55}$$

For pure UE events, i.e. without PU, these terms can be estimated [216, 217]:

$$\rho_{UE} \simeq 2 - 3 \text{ GeV/area} , \tag{4.56}$$

$$\sigma_{UE} \simeq 0.6\rho_{UE} , \tag{4.57}$$

$$\delta\rho_{UE} \simeq 0.8\rho_{UE} , \tag{4.58}$$

$$\Sigma \simeq 0.26\sqrt{n}\pi\eta^2 R_{bb}^2 . \tag{4.59}$$

Though ρ_{UE} seems to be around 2 GeV/area, the tuning used in [173] was closer to 3 GeV/area, the value that we choose here. In presence of PU, i.e. when there is more than 1 pp collision per bunch crossing at the LHC (thus leading to the emission of other soft particles), ρ, σ and $\delta\rho$ have to be modified. We define N_{PU} to be the number of pp collisions in a bunch crossing except the one at the origin of the hard interaction. We use a simple model to write the parameters of the UE/PU as:

$$\rho \simeq \left(1 + \frac{N_{PU}}{4}\right)\rho_{UE} , \tag{4.60}$$

$$\sigma \simeq \sqrt{1 + \frac{N_{PU}}{4}}\sigma_{UE} , \tag{4.61}$$

$$\delta\rho \simeq \sqrt{1 + \frac{N_{PU}}{4}}\delta\rho_{UE} . \tag{4.62}$$

Some comments are needed: since ρ measures the level of noise, it should grow like N_{PU}. In the expression $1 + N_{PU}/4$, the 1 corresponds to the pp collision that leads to the UE and to the hard interaction, whereas the $N_{PU}/4$ term simply corresponds to the other pp

interactions and could be derived from the numbers given in [138]. The intra and inter events fluctuations of ρ are modelled as growing like $\sqrt{\rho}$: we thus just give σ and $\delta\rho$ the factor $\sqrt{1+N_{PU}/4}$, though further studies might be of value to parametrise these terms in a more adequate manner. Notice that the value given for $\delta\rho$ ignores the fluctuations in the number of PU events from one bunch crossing to the next, but this is beyond the accuracy of our model here. At high luminosity at LHC, N_{PU} is expected to be ~ 20, which implies $\rho \sim 10 - 20$ GeV [136–138].

Assuming gaussian distributions for these three kinds of fluctuations, one can deduce the Higgs width due to the presence of UE/PU,[14] $\delta M_{UE} = 2\sqrt{\langle \Delta M^2 \rangle - \langle \Delta M \rangle^2}$:

$$\delta M_{UE} = 2\sqrt{A\sigma^2 + A^2\delta\rho^2 + \rho^2\Sigma^2}\frac{M_H}{p_{t_H}}\,. \tag{4.63}$$

For a gaussian peak, defining a 2σ width means that we keep roughly 68% of the events around the average, which is in correspondence with the value $f = 0.68$ chosen for the perturbative calculation.

We now have all the important results in hand to consider both UE/PU and FSR simultaneously.

4.3.3 Study of the Higgs width in presence of both UE/PU and perturbative radiation

The purpose of this part is to give an estimate of how one should choose the couple of filtering parameters (n,η). For that, one has to convolute the effects of UE/PU and perturbative radiation and compute the resulting reconstructed Higgs peak width, and then minimise it with respect to the filtering parameters. This is highly non trivial to do analytically and we leave it for future work. The simple choice made here is to say that, for a given n, the optimal η, denoted η_{opt}, is the one for which the two widths are equal. This is obviously not true in general, but seems reasonable to obtain an estimate (figure 4.8) and to understand how η_{opt} changes when we vary p_{t_H} and N_{PU}. Notice that, using this method, we have to impose $\eta_{opt} < \eta_{sat}$ where η_{sat} is the saturation point (eq. (4.45)), because beyond η_{sat}, increasing η makes δM_{UE} larger without decreasing δM_{PT}, thus solving the equation $\delta M_{PT} = \delta M_{UE}$ has no sense in this region. Finally, we numerically minimise $\sqrt{\delta M_{PT}^2 + \delta M_{UE}^2}$, calculated at $\eta = \eta_{opt}(n)$, with respect to n in order to find n_{opt}.

First, we would like to understand how η_{opt} evolves with respect to the physical parameters. The equality $\delta M_{PT} = \delta M_{UE}$ gives an equation in $L = \ln\frac{1}{\eta}$:

$$M_H e^{-\frac{1}{2\beta_0\alpha_s}\left(1-e^{-4\pi\beta_0\frac{C_{PT}}{L}}\right)} = 2\sqrt{c_\sigma^2 e^{-2L} + c_{\delta\rho}^2 e^{-4L} + c_\Sigma^2 e^{-4L}}\rho_{UE}\frac{M_H}{p_{t_H}}\,, \tag{4.64}$$

[14] Here again, for brevity, we define δM_{UE} to be the Higgs width in presence of UE and/or PU without referencing the PU dependence. Actually it serves only to distinguish the width due to UE/PU from the perturbative width δM_{PT}.

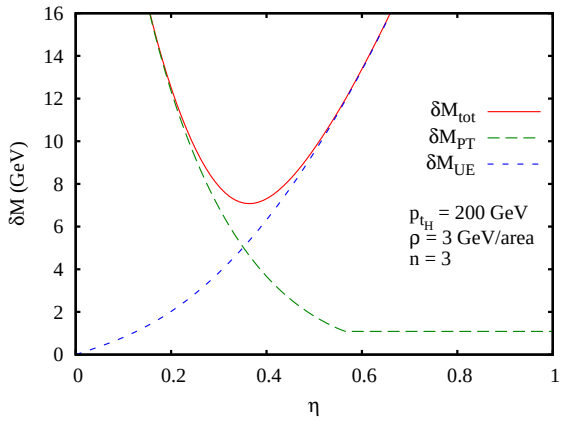

Figure 4.8: The Higgs width due to UE/PU and loss of perturbative radiation, combined as if the 2 distributions were gaussian, i.e. $\delta M_{tot} = \sqrt{\delta M_{PT}^2 + \delta M_{UE}^2}$ when $n = 3$. In this case, η_{opt}, though slightly larger, is approximately given by the intersection of the 2 curves, at least as long as η is not in the saturation region.

where the coefficients c_σ, $c_{\delta\rho}$ and c_Σ can be easily calculated using eqs. (4.51,4.56-4.62,4.63):

$$c_\sigma(n, N_{PU}, R_{bb}) \simeq 0.6\sqrt{\pi}\sqrt{n}R_{bb}\sqrt{1 + \frac{N_{PU}}{4}}\,, \tag{4.65}$$

$$c_{\delta\rho}(n, N_{PU}, R_{bb}) \simeq 0.8\pi n R_{bb}^2\sqrt{1 + \frac{N_{PU}}{4}}\,, \tag{4.66}$$

$$c_\Sigma(n, N_{PU}, R_{bb}) \simeq 0.26\pi\sqrt{n}R_{bb}^2\left(1 + \frac{N_{PU}}{4}\right)\,. \tag{4.67}$$

If the solution of eq. (4.64) for a given n is found to be above $\eta_{sat}(n, f)$, then $\eta_{opt} = \eta_{sat}(n, f)$ in order to take the saturation of δM_{PT} into account. We start by solving this equation numerically. In figure 4.9 we show η_{opt} as a function of p_{t_H} and N_{PU} for different values of n. As it should, η_{opt} increases with p_{t_H} at fixed N_{PU}. Indeed, if p_{t_H} grows at fixed η, R_{bb} decreases and so does the effect of UE/PU, whereas the perturbative radiation is kept fixed (no dependence on R_{bb}). Notice also, for $n = 3$, that the values obtained for η_{opt} are roughly consistent with the choice made in the previous chapter where we had $\eta = \min(0.3/R_{bb}, 1/2)$. The saturation comes into effect at relatively low p_{t_H}, around $400 - 500$ GeV. Above this value, the total width is small and hadronisation corrections start to become relevant, so that the results presented on these plots become not very reliable. However, for $p_t >\sim 500$ GeV and $\eta > \eta_{sat}$, the Higgs width due to perturbative radiation and UE/PU vary slowly with η and we thus believe that the precise value chosen for η is not so important: one can take any value above η_{sat} without changing the result too much. The decrease of η_{opt} with N_{PU} seems to be weaker than one might have expected *a priori*. However, in fig. 4.8, we can see that the negative slope of the perturbative width is very large, and therefore increasing the noise from PU will not change too much the η_{opt} value.

It would be interesting to understand analytically the evolution of η_{opt} with respect to the physical parameters p_{t_H} and N_{PU}. Unfortunately, eq. (4.64) cannot be easily dealt with. That's why we have to make an approximation: in this equation, one of the 3 terms under

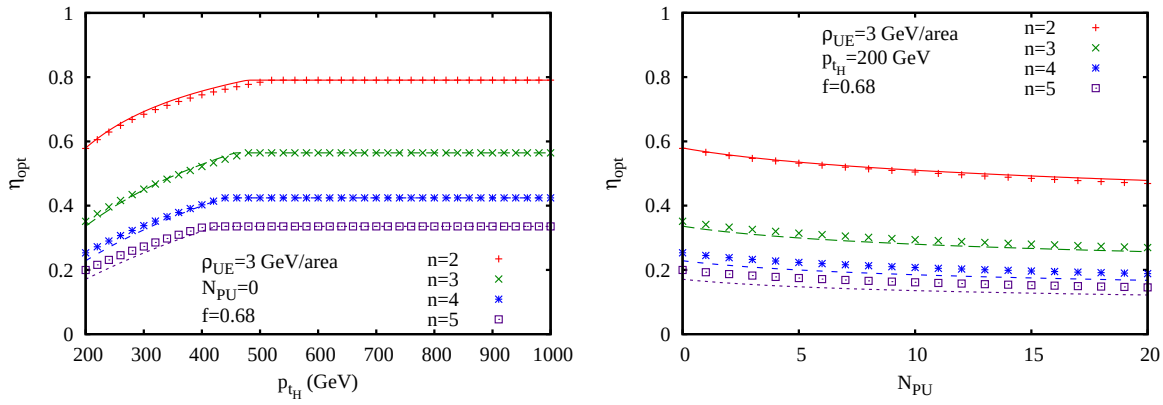

(a) (b)

Figure 4.9: The numerical solutions (points) of eq. (4.64) shown for different values of n: (a) as a function of p_{t_H} when $N_{PU} = 0$, and (b) as a function of N_{PU} when $p_{t_H} = 200$ GeV. We also show the corresponding approximate analytical solutions (lines) derived in eq. (4.75).

the square root may be dominant when $\eta = \eta_{opt}$. At first sight, one would expect that at low η_{opt}, the $c_\sigma^2 e^{-2L}$ term, which scales like η^2, should be the largest, whereas at large N_{PU}, it should be the $c_\Sigma^2 e^{-4L}$ term that is the largest one as it scales like N_{PU}^2. But figure 4.10 for $n = 3$ reveals that the $c_{\delta\rho}$ term surprisingly brings the largest contribution to δM_{UE} for physical values of the parameters (the same holds for other values of n). Therefore, to simplify things a little, one can consider eq. (4.64) and put $c_\sigma = c_\Sigma = 0$. However, to be more general, and to consider the possible situation where one of the other terms might be dominant,[15] we rewrite eq. (4.64) in the following approximate form:

$$M_H e^{-\frac{1}{2\beta_0\alpha_s}\left(1-e^{-4\pi\beta_0\frac{C_{PT}}{L}}\right)} = C_{UE}\rho_{UE}e^{-pL}R_{bb}^p\frac{M_H}{p_{t_H}}\,, \tag{4.68}$$

where $p = 1$ if the c_σ term dominates and $p = 2$ otherwise. Moreover:

$$C_{UE}(n, N_{PU}) = \begin{cases} 1.2\sqrt{\pi}\sqrt{n}\sqrt{1+\frac{N_{PU}}{4}}\,, & \text{if the } c_\sigma \text{ term is dominant,} \\ 1.6\pi n\sqrt{1+\frac{N_{PU}}{4}}\,, & \text{if the } c_{\delta\rho} \text{ term is dominant,} \\ 0.52\pi\sqrt{n}\left(1+\frac{N_{PU}}{4}\right)\,, & \text{if the } c_\Sigma \text{ term is dominant.} \end{cases} \tag{4.69}$$

Eq. (4.68) can be written in a slightly different way:

$$\frac{B_{PT}}{L} = \ln\left(\frac{1}{B_{UE} - 2\beta_0\alpha_s pL}\right)\,, \tag{4.70}$$

with:

$$B_{PT} = 4\pi\beta_0 C_{PT}\,, \tag{4.71}$$

$$B_{UE} = 1 - 2\beta_0\alpha_s\ln\left(\frac{p_{t_H}}{C_{UE}\rho_{UE}R_{bb}^p}\right)\,. \tag{4.72}$$

[15] The subtraction procedure proposed in [138] seems to eliminate most of the fluctuations from the $c_{\delta\rho}$ and c_Σ terms, so that the remaining c_σ term would be dominant in this case.

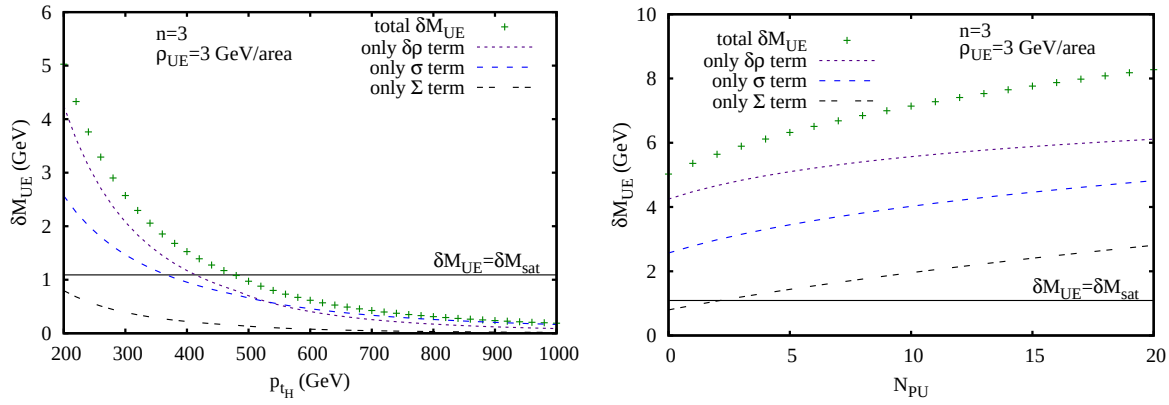

(a) (b)

Figure 4.10: δM_{UE} computed at $\eta = \eta_{opt}$ with respect to (a) p_{t_H} when $N_{PU} = 0$ and (b) N_{PU} when $p_{t_H} = 200$ GeV. On these plots is also represented the contribution to δM_{UE} of each term separately. When the UE/PU width falls below the saturation line $\delta M_{UE} = \delta M_{sat}$, then $\eta_{opt} = \eta_{sat}$.

Despite its simpler form, eq. (4.70) for L cannot be solved analytically. Here comes the second approximation, which is to make a perturbative expansion:

$$\frac{B_{PT}}{L} = \ln \frac{1}{B_{UE}} + \frac{2\beta_0 \alpha_s p}{B_{UE}} L + \mathcal{O}\left((\alpha_s L)^2\right) . \tag{4.73}$$

Neglecting the $\mathcal{O}\left((\alpha_s L)^2\right)$ term, the resulting quadratic equation immediately implies

$$L_{opt} = \frac{-B_{UE} \ln \frac{1}{B_{UE}} + \sqrt{B_{UE}^2 \ln^2 \frac{1}{B_{UE}} + 8\beta_0 \alpha_s p B_{UE} B_{PT}}}{4\beta_0 \alpha_s p} . \tag{4.74}$$

Taking into account the saturation effect, η_{opt} is then given by:

$$\eta_{opt} = \begin{cases} e^{-L_{opt}} , & \text{if } L_{opt} > -\ln \eta_{sat} , \\ \eta_{sat} , & \text{otherwise} . \end{cases} \tag{4.75}$$

We used this expression with C_{UE} corresponding to the $\delta\rho$ term in eq. (4.69) and $p = 2$ in order to plot the approximate solutions in figure 4.9. This reveals that the above relation for η_{opt} (eq. (4.75)) works rather well, within a few %.

As a second step, we would like to find the optimal n, denoted n_{opt}. This also should depend on the way UE/PU and perturbative radiation are combined. However, as a simple approximation, one can combine them as if they were both gaussian distributions. Therefore, one should minimise

$$\delta M_{tot}(n) = \sqrt{\delta M_{PT}^2(n) + \delta M_{UE}^2(n)} , \tag{4.76}$$

computed at $\eta = \eta_{opt}(n)$ for a given p_{t_H} and N_{PU}.

The results are plotted in figure 4.11. We can notice that the larger n, the narrower the peak, and thus the better the result. However, one should keep in mind that when n increases, the optimal $R_{\text{filt}} = \eta R_{bb}$ becomes small, and we have to deal with hadronisation corrections that grow as $1/R_{\text{filt}}$ [176] as well as detector resolution and granularity $\delta\eta \times \delta\phi =$

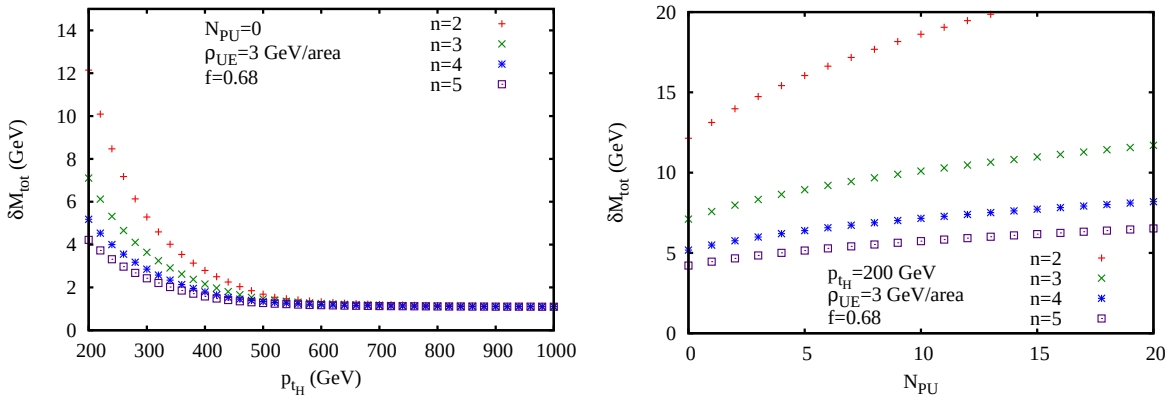

(a) (b)

Figure 4.11: δM_{tot} computed at $\eta = \eta_{opt}$ as a function of (a) p_{t_H} and (b) N_{PU} for different values of n.

0.1×0.1 that both start to have an important impact on the reconstructed Higgs width, and thus degrade the results presented here. In section 4.3.5 we will examine what happens when we include a very rough estimate for hadronisation corrections. However, at first sight, it seems that one should definitely not take $n = 2$. The value $n = 3$ chosen in the previous chapter is good, but it may be possible to do better with $n = 4$. Beyond this value, the optimal R_{filt} falls below ~ 0.2 (cf figure 4.9), which is too small for this study to be fully reliable, as we shall see in section 4.3.5.

4.3.4 Variations of the results with z and f

Until now, we have only presented some results for $f = 0.68$ and $z = 1/2$, z being defined as

$$z = \min\left(\frac{E_b}{E_H}, \frac{E_{\bar{b}}}{E_H}\right), \tag{4.77}$$

with E_i the energy of particle i in the Higgs splitting into $b\bar{b}$. What happens if we change these values?

Let us start with z. Though the Higgs splitting into $b\bar{b}$ is more often symmetric than in QCD events (and this is what we used in chapter 3 to distinguish it from pure QCD splittings), it still has a distribution in z that is uniform in the range:

$$\frac{1}{2}\left(1 - \frac{1}{\sqrt{1 + \frac{M_H^2}{p_{t_H}^2}}}\right) < z < \frac{1}{2}, \tag{4.78}$$

which is simply eq. (2.22). But in order to reduce the large QCD background, one usually cuts on small z, so that

$$z_{cut} < z < \frac{1}{2}, \tag{4.79}$$

with $z_{cut} \sim 0.1$. As an example, assume the b quark carries the fraction z of the Higgs splitting. In such a case, b and $\bar{b}$ are not equidistant from the Higgs direction: they are

respectively at an angular distance $(1-z)R_{bb}$ and zR_{bb} from H (see for instance figure B.1 in appendix B). Therefore, as UE/PU particles tend to cluster around the perturbative radiation, eq. (4.49) has to be modified:

$$\theta_{gH} \sim zR_{bb} \text{ or } \theta_{gH} \sim (1-z)R_{bb}\,, \tag{4.80}$$

for a given UE/PU particle g in the filtered jet. This leads to the modification of eq. (4.48) according to g being relatively close to b (region called "J_1") or $\bar{b}$ (region called "J_2"):

$$\begin{aligned}\Delta M &\simeq \frac{p_{t_H}}{M_H}\left(\sum_{g\in J_1} p_{t_g}\left(\frac{(1-z)^2R_{bb}^2}{2}+\frac{M_H^2}{2p_{t_H}^2}\right)+\sum_{g\in J_2} p_{t_g}\left(\frac{z^2R_{bb}^2}{2}+\frac{M_H^2}{2p_{t_H}^2}\right)\right)\,,\\ &\simeq \frac{M_H}{2p_{t_H}}\left(\frac{1}{z}\sum_{g\in J_1} p_{t_g}+\frac{1}{1-z}\sum_{g\in J_2} p_{t_g}\right)\,,\\ &= \frac{M_H}{2p_{t_H}}\left(\frac{1}{z}\rho A_1+\frac{1}{1-z}\rho A_2\right)\,.\end{aligned} \tag{4.81}$$

In this calculation we used eq. (4.47). To compute the dependence of the fluctuations on z, we take the simplest case $n=2$. For the σ and Σ fluctuations, the terms ρA_1 and ρA_2 vary independently, leading to the following contribution to δM_{UE}:[16]

$$\delta M_{UE,\sigma,\Sigma}^2 = 4\left(\frac{M_H\rho_{UE}}{2p_{t_H}}\right)^2\left(\frac{1}{z^2}\delta_{1,\sigma,\Sigma}^2+\frac{1}{(1-z)^2}\delta_{2,\sigma,\Sigma}^2\right)\,, \tag{4.82}$$

where

$$\delta_{1,\sigma,\Sigma}^2 = \delta_{2,\sigma,\Sigma}^2 = c_\sigma^2 e^{-2L}+c_\Sigma^2 e^{-4L}\,, \tag{4.83}$$

with c_σ and c_Σ given by eqs. (4.65,4.67) for $n=1$. Concerning the $\delta\rho$ fluctuations, the 2 terms ρA_1 and ρA_2 vary the same way from one event to another. Therefore, if it were only for the $\delta\rho$ term, we would write $\rho A_1 = \rho A_2$ leading to:

$$\delta M_{UE,\delta\rho}^2 = 4\left(\frac{M_H\rho_{UE}}{2p_{t_H}}\right)^2\frac{1}{z^2(1-z)^2}\delta_{\delta\rho}^2\,, \tag{4.84}$$

where

$$\delta_{\delta\rho}^2 = c_{\delta\rho}^2 e^{-4L}\,, \tag{4.85}$$

with $c_{\delta\rho}$ given by eq. (4.66) for $n=1$. Adding all these contributions,

$$\delta M_{UE}^2 = \delta M_{UE,\sigma,\Sigma}^2+\delta M_{UE,\delta\rho}^2\,, \tag{4.86}$$

this apparently leads to an enhancement of the width by a factor of $1/z$. But we have to take into account that the coefficients $c_{\delta\rho}$ and c_Σ also contain a factor R_{bb}^2 (eqs. (4.65,4.66)) leading to another factor $1/z$, and thus an enhancement $1/z^2$ at small z.[17] Therefore, we can conclude that the effect of $z\neq 1/2$ is to broaden the reconstructed Higgs peak. Such a factor may partly explain the width of ~ 14 GeV that was observed in [218], to be compared with the various widths found in the previous subsection (see for instance figure 4.11), and

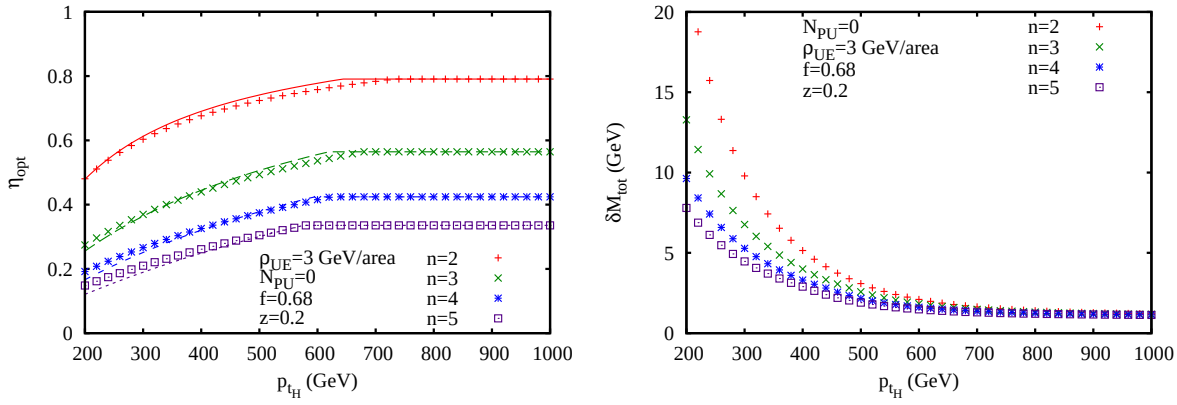

(a) (b)

Figure 4.12: (a) η_{opt} as a function of p_{t_H} when $f = 0.68$ and $z = 0.2$ for different values of n. The points correspond to the numerical determination of η_{opt}, found solving eq. (4.64) whose z dependence is derived in appendix C, whereas the curves correspond to its approximate analytical solutions. (b) $\delta M_{tot} = \sqrt{\delta M_{PT}^2 + \delta M_{UE}^2}$ computed at $\eta = \eta_{opt}$ as a function of p_{t_H} for $f = 0.68$ and $z = 0.2$.

should also lead to decreasing η_{opt}. This is illustrated in fig. 4.12, which was obtained with the results derived in appendix C, where we carry out the above analysis for a general n.

Now, we turn to the f value. As we explained in section 4.3.1, the choice $f = 0.68$ was made to correspond to a 2σ gaussian width, as we did for δM_{UE}, which is somewhat arbitrary. We would like to estimate how the results change when f is modified. We thus also consider a range of values for f between 0.5 and 0.8. In this case the $C_{PT}(n, f)$ constants characterising δM_{PT} are changed (see for instance eq. (4.42)), and δM_{UE} is also changed, i.e. eqs. (4.63,4.64,4.69) have to be slightly modified:

$$\delta M_{UE} = 2\sqrt{2}\,\mathrm{erf}^{-1}(f)\,\sqrt{A\sigma^2 + A^2\delta\rho^2 + \rho^2\Sigma^2}\,\frac{M_H}{p_{t_H}}\,, \tag{4.87}$$

$$= 2\sqrt{2}\,\mathrm{erf}^{-1}(f)\,\sqrt{c_\sigma^2 e^{-2L} + c_{\delta\rho}^2 e^{-4L} + c_\Sigma^2 e^{-4L}}\,\rho_{UE}\,\frac{M_H}{p_{t_H}}\,, \tag{4.88}$$

where $\mathrm{erf}(x)$ is the usual error function:

$$\mathrm{erf}(x) = \frac{2}{\sqrt{\pi}}\int_0^x e^{-u^2}\,du\,. \tag{4.89}$$

Notice that the constants c_σ, $c_{\delta\rho}$ and c_Σ are left unchanged with this convention. However

[16] the factor of 4 comes from the fact that we compute the width at 2σ.

[17] This is valid when $p_{t_H} > \frac{1}{\sqrt{z(1-z)}}\frac{M_H}{R_0}$, with R_0 the radius of the initial clustering of the event, in order for the b and $\bar{b}$ to be clustered together. For lower p_{t_H}, there is a kinematic cut on z and the enhancement is less strong.

C_{UE} becomes:

$$C_{UE}(n,f,N_{PU}) = \begin{cases} 2\sqrt{2}\,\mathrm{erf}^{-1}(f)\,0.6\sqrt{\pi}\sqrt{n}\sqrt{1+\frac{N_{PU}}{4}}\,, & \text{if the } c_\sigma \text{ term is dominant,} \\ 2\sqrt{2}\,\mathrm{erf}^{-1}(f)\,0.8\pi n\sqrt{1+\frac{N_{PU}}{4}}\,, & \text{if the } c_{\delta\rho} \text{ term is dominant,} \\ 2\sqrt{2}\,\mathrm{erf}^{-1}(f)\,0.26\pi\sqrt{n}\left(1+\frac{N_{PU}}{4}\right)\,, & \text{if the } c_\Sigma \text{ term is dominant.} \end{cases} \tag{4.90}$$

The bands corresponding to the uncertainties on η_{opt} that we obtain including these modifications are presented in figure 4.13. The uncertainty that we get, $\sim 20-30\%$, is not larger than the precision of the whole study, which limits itself to a large-N_c leading-log calculation. Notice that the variation with N_{PU} remains small.

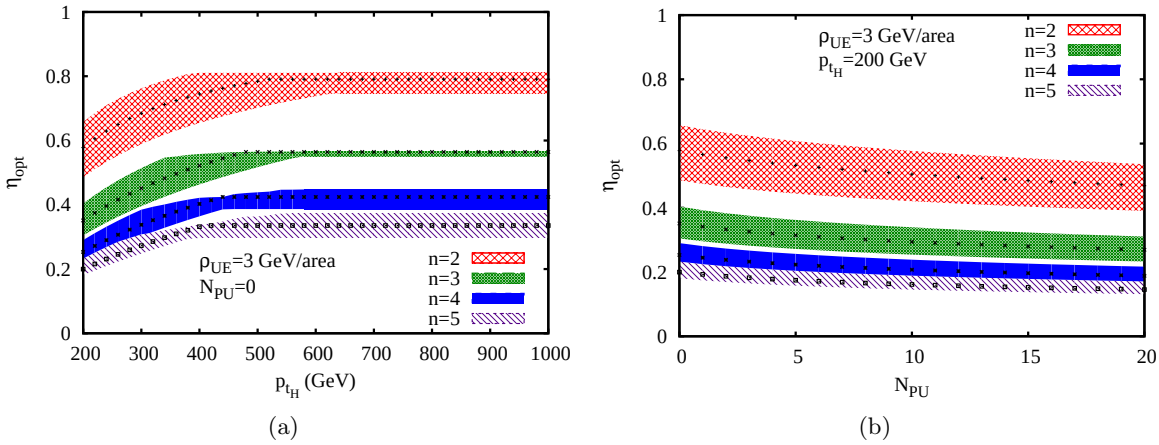

Figure 4.13: Uncertainty on η_{opt} when f varies from 0.5 to 0.8, for different values of n as a function of (a) p_{t_H} when $N_{PU}=0$ and (b) N_{PU} when $p_{t_H}=200$ GeV. The results for $f=0.68$ are also plotted as a reference.

One finally observes that $\eta_{sat}(n,f)$ is almost independent of f for $n=3$. In appendix C, we will show that it can be approximately written as:

$$\eta_{sat} \simeq e^{-0.58}\left(1+0.044\left(f-\frac{1}{2}\right)+\mathcal{O}\left(\left(f-\frac{1}{2}\right)^2\right)\right). \tag{4.91}$$

Because of the small coefficient of its first order correction, $\eta_{sat}=e^{-0.58}$ is a good approximation within less than 1% for a large range of f values. But this seems to be a coincidence with no deep physical reason.

4.3.5 Hadronisation corrections

It is difficult to calculate what happens during the process of hadronisation, though some analytical results can be found concerning jet studies for instance [176,219,220]. In particular, it was shown in [176] that such non-perturbative corrections lead to a p_t shift for QCD jets equals on average $\sim -\Lambda/R_{\text{filt}}C_i$ where $\Lambda=0.4$ GeV and $C_i=C_F$ or C_A depending on whether it is a quark jet or a gluon jet. This can be translated in our study by the following

averaged p_t shift for the filtered jet:

$$\begin{aligned}\langle \delta p_t \rangle_{had} &= -\left(2C_F + (n-2)C_A\right)\frac{\Lambda}{R_{\text{filt}}}\,, \\ &\simeq -\frac{(n-1)N_c\Lambda}{R_{\text{filt}}}\,,\end{aligned} \tag{4.92}$$

where the second equality holds in the large N_c limit. Unfortunately, there is no result concerning the dispersion of the p_t distribution, which is the relevant quantity to compute in our case. Therefore, we are going to assume that the spread is of the same order of magnitude as the shift. This is in principle a crude approximation, but the only aim here is to illustrate the consequences of including hadronisation corrections in order to emphasise the fact that taking n too large is certainly not a good choice. Therefore, we use eq. (4.48) to estimate very roughly the hadronisation corrections to the reconstructed Higgs mass peak width:

$$\delta M_{had} \sim \frac{(n-1)N_c\Lambda}{R_{\text{filt}}}\frac{M_H}{p_{t_H}} = \frac{(n-1)N_c\Lambda}{2\eta}\,, \tag{4.93}$$

when $z = 1/2$. As before, one should know how to combine perturbative radiation with UE/PU and hadronisation corrections in order to minimise the resulting combined width. However, we simply choose to minimise the quantity

$$\delta M_{tot} = \sqrt{\delta M_{PT}^2 + \delta M_{UE}^2 + \delta M_{had}^2}\,, \tag{4.94}$$

with respect to η and plot the resulting minimal δM_{tot} for different values of n (fig. 4.14).

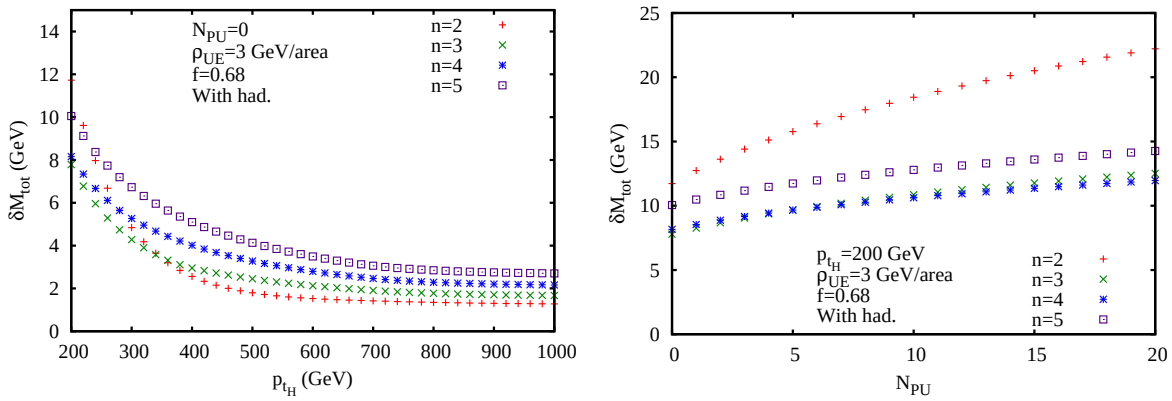

(a) (b)

Figure 4.14: δM_{tot} including hadronisation corrections computed at $\eta = \eta_{opt}$ as a function of (a) p_{t_H} and (b) N_{PU} for different values of n.

The first thing one can notice on these plots is that increasing n also increases the hadronisation corrections. For $n = 5$ they become so important that it is now clearly not an optimal filtering parameter contrary to what could be deduced from figure 4.11. The relevant p_t region in our study is roughly $200 - 400$ GeV where we find the major part of the Higgs cross-section above 200 GeV and where our results are more reliable (see section 4.3.3). In this region $n = 3$ gives the best result. And at high PU, $n = 3$ and $n = 4$ both seem optimal, whereas $n = 2$ is far from being as good.

To conclude, our estimates seem to indicate within the accuracy of our calculations that $n = 2$ is not a good choice, nor is $n \geq 5$. Taking $n = 3$ or $n = 4$ gives equally good quality to the mass peak. Increasing the hadronisation effects with respect to eq. (4.93), would lead to $n_{opt} = 3$, whereas if we lower them, we would find $n_{opt} = 4$. The only thing we can say is that $n = 3$ and $n = 4$ both seem to work rather well.

One way to go beyond these results would be to use event generators like HERWIG [97, 98] or PYTHIA [99], to compute directly the Higgs width in presence of UE/PU, perturbative radiation, ISR and hadronisation, and to find for which value of the couple (n, η) the reconstructed Higgs mass peak width δM_H becomes minimal (that would still depend on p_{t_H} and the level of UE/PU). But our study here aimed to understand as much as possible the physical aspects behind such an optimisation, the price to pay being larger uncertainties on the result because of the necessary simplifications that were made.

4.4 Conclusion

This work has investigated the effect of QCD radiation on the reconstruction of hadronically decaying boosted heavy particles, motivated in part by the analysis made in chapter 3 which uses a boosted search channel for the $H \to b\bar{b}$ decay. Though we took the Higgs boson as an example, all the results presented here can be applied to the W and Z bosons, as well as any new colourless resonance decaying hadronically that might be observed at the LHC. The main effect of the QCD radiation is to distort and spread out the boosted heavy resonance shape well beyond the intrinsic width of the resonance. The aim therefore is to calculate the resulting resonance lineshape. This is a function of the parameters of the reconstruction method, notably of the "filtering" procedure, which aims to limit contamination from underlying event and pile-up, but which causes more perturbative radiation to be lost than would otherwise be the case.

Calculations were performed in a leading (single) logarithmic and leading colour approximation, which is the state of the art for this kind of problem. Analytic results were provided up to $\alpha_s^2 \ln^2 \frac{M_H}{\Delta M}$ for $n = 2$, and all-orders analytic results for the cases $n = 2$ and $n = 3$ were given for the terms that dominate in the small η limit. Numerical fixed-order results up to $\alpha_s^5 \ln^5 \frac{M_H}{\Delta M}$ and all-orders resummed results were also given and are treated in more details in appendix E for a range of n and η. For the $n = 2$ and $n = 3$ cases there is quite acceptable agreement between the small-η analytic results and the full numerical results, even for values of $\eta \simeq 0.5$.

One unexpected feature that was observed was the behaviour of order-by-order expansion as compared to the resummed result: indeed there are indications that the series in $\alpha_s \ln \frac{M}{\Delta M}$ has a radius of convergence that is zero (but in a way that is unrelated to the renormalon divergence of the perturbative QCD series). This seems to be a general feature of the non-global logarithm series. Its practical impact seems to be greater for large η, or equivalently when the coefficients of the "primary" logarithms are small.

With these results in hand, it was then possible to examine how the perturbative width of the resonance peak depends on the parameters of the filtering. Though this was accessible only numerically for the full range of filtering parameters, figure 4.7(a) lends itself to a simple parametrisation for practically interesting parameter-ranges.

This parametrisation was then used in section 4.3.3 together with a parametrisation for the effect of UE and PU, so as to examine how to minimise the overall resonance width as

a function of the filtering parameters and of the physical parameters of the problem such as the resonance p_t and the level of UE/PU. The approximations used might be described as overly simple, yet they do suggest interesting relations between optimal choices of the filtering parameters and the physical parameters of the problem. Though it is beyond the scope of this analysis to test these relations in full Monte Carlo simulation, we believe that investigation of their applicability in realistic conditions would be an interesting subject for future work. It should also be noticed that the methods introduced in this chapter may be adapted to other reconstruction procedures like jet pruning [186] and jet trimming [188] as well as filtering as applied to jets without explicit substructure [141].

Chapter 5

Addressing giant QCD K-factors at the LHC

At the LHC, it is widely anticipated that signals of new physics, for example supersymmetry, may manifest themselves as large excesses of data compared to expected QCD and electroweak backgrounds at high momentum scales [140, 169, 221–225]. The estimation of these backgrounds will be one of the elements in ascertaining the presence of any new physics from such signals. Consequently, considerable effort is being invested across the particle physics community in the development of methods to understand and predict backgrounds (some of the issues involved are described nicely in ref. [226]).

Given the QCD methods that are available today, some of the best prospects for obtaining systematic, accurate predictions of backgrounds involve next-to-leading order (NLO) QCD calculations. By carrying out a systematic expansion in the strong coupling and obtaining the first two terms (leading order (LO) and NLO) for a given process, one often obtains predictions that are accurate to $10 - 20\%$, there being two ways to help judge the convergence of the series: the size of the NLO corrections relative to the LO result and the dependence of the NLO result on renormalisation and factorisation scales. The importance of NLO predictions in the LHC programme has motivated a large calculational effort destined to extend the range of processes known at NLO (for reviews, see refs. [227, 228]).

While the majority of NLO calculations show some degree of convergence relative to the LO results, we examined in chapter 3 a particular observable for which this was not the case: the p_t distribution of the highest-p_t jet ($p_{t,j1}$) in the Z+j process leads to K-factors up to 6 at high p_t. Several groups have also commented in recent years on the appearance of K-factors, that grow dramatically towards high transverse momenta [229–231] (similar behaviour is visible also in [232]). The problem generally occurs for hadronic observables (jet transverse momenta, etc.) in processes that involve heavy vector bosons or heavy quarks, at scales far above the boson or quark mass.

Fig. 5.1 illustrates this for Z+j at LHC (14 TeV) energies, which is our benchmark process. Besides $p_{t,j1}$, it also shows the distributions of 2 other observables that are non-zero for configurations involving a Z-boson and 1 or more partons: the transverse momentum of the Z boson, $p_{t,Z}$, and the effective mass (scalar sum of transverse momenta) of all jets ($H_{T,\text{jets}}$). At LO, all three distributions are identical. At NLO, the $p_{t,Z}$ observable is rather typical of a QCD observable: its distribution has a NLO K-factor of about 1.5, without too strong a dependence on $p_{t,Z}$. As already mentioned, the $p_{t,j1}$ distribution is more unusual,

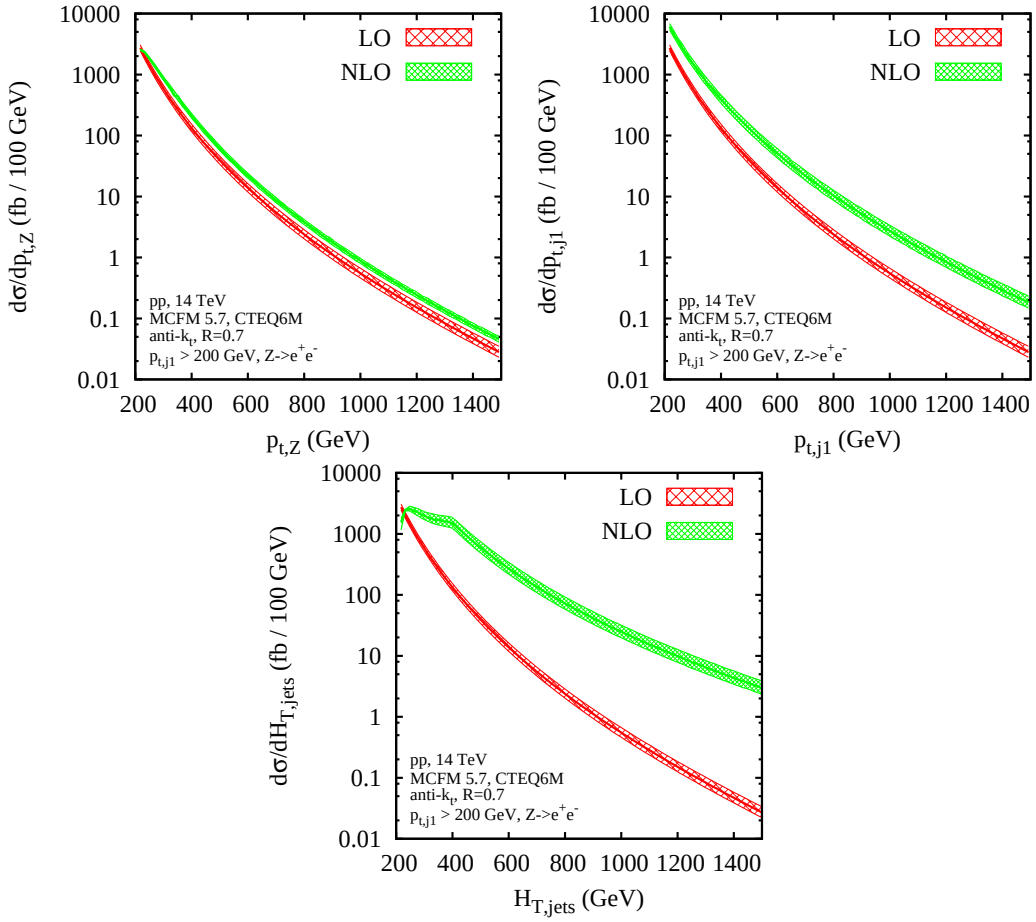

Figure 5.1: The LO and NLO distributions obtained with MCFM 5.7 for three observables in Z+jet production: the Z transverse momentum (upper left plot), the p_t of the hardest jet (upper right plot), and the scalar sum of the transverse momenta of all the jets, $H_{T,\text{jets}}$ (lower plot). The bands correspond to the uncertainty from a simultaneous variation of $\mu_R = \mu_F$ by a factor of two either side of a default $\mu_0 = \sqrt{p_{t,j1}^2 + m_Z^2}$. The jet algorithm is anti-k_t [78] with $R = 0.7$ and only events whose hardest jet passes a cut $p_t > 200\,\text{GeV}$ are accepted. The cross sections include the branching ratio $Z \to e^+e^-$.

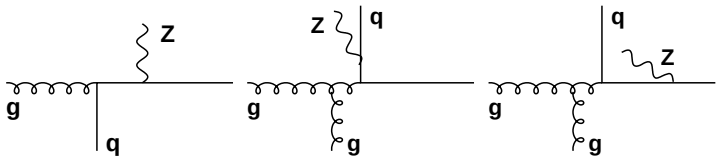

Figure 5.2: A) a LO contribution to Z+jet production; B) and C) two contributions that are NLO corrections to Z+jet observables but whose topology is that of a dijet event with additional radiation of a soft or collinear Z-boson either from a final-state quark (B) or an initial-state one (C).

with K-factors of about $4-6$ that grow noticeably at high p_t.[1] Of the three observables, $H_{T,\text{jets}}$ is by far the most striking: with K-factors of up to 100.

Given that fig. 5.1 involves momentum scales where $\alpha_s \sim 0.1$, one is driven to ask how it is that such "giant" K-factors can arise. As touched on in section 3.5, and discussed in more detail in [229, 230] for the $p_{t,j1}$ case, fig. 5.2 helps provide an answer: at LO the only event topology (A) is that of a Z-boson recoiling against a quark or gluon jet. At NLO, new topologies arise involving a dijet event with a Z-boson radiated collinearly or softly off outgoing (B) or incoming legs (C).

When considering the p_{tZ} distribution, it is easiest to produce a high p_t Z-boson from topologies like (A), because in (B) and (C) the Z-boson carries only part of the transverse momentum in the event, i.e. the event must have a higher overall momentum exchange in order to produce a Z with a given p_t.

When considering $p_{t,j1}$, topologies (B) and (C) dominate the NLO contribution at high p_t, because for fixed leading jet p_t one is free to integrate over the Z-momentum. This leads to a double logarithm that is absent from topology A — i.e. the relative size of the NLO correction is proportional to $\alpha_s \ln^2 p_t/M_Z$ rather than just α_s.[2] Additionally, topologies (B) and (C) can also be generated by qq scattering, which is important at high p_t but does not contribute to topology (A). The even larger K-factor for $H_{T,\text{jets}}$ arises as follows: whereas in diagrams such as A, $H_{T,\text{jets}} \simeq p_{t,j1} \simeq p_{t,Z}$, in diagrams like B and C, $H_{T,\text{jets}} \simeq 2p_{t,j1}$. Thus a given $H_{T,\text{jets}}$ can be obtained with a leading jet energy that is half as large at NLO as it needs to be at LO, vastly increasing the cross section.

While it is reassuring that we can understand the physical origins of the large K-factors in fig. 5.1, we are still left with doubts as to the accuracy of the NLO Z+jet prediction, since it is really just dominated by the LO result for the Z+2-parton topologies. One solution would be to calculate the next-to-next-to-leading order (NNLO) corrections to the Z+jet process. Since we do not expect further new topologies to arise in the NNLO contributions, their impact should be modest compared to NLO and should therefore help bring the perturbative series under control. However, while work is progressing on NNLO calculations of $2 \to 2$ processes with QCD final states (see [234] and references therein), results are not yet available; nor are they likely to become available any time soon for some of the more complex processes where giant K-factors have been observed (e.g. $pp \to Wb\bar{b}$ as studied in section 3.5).

[1] Notice that the PDFs for LO and the jet algorithm used in fig. 5.1 are different from that of fig. 3.13.

[2] This differs from double electroweak (EW) logarithms, which involve terms like $\alpha_{\text{EW}} \ln^2 p_t/M_Z$, which is usually much smaller. Examples do exist of "giant" EW effects when tagging flavour [233].

Alternatively one could simply try to avoid observables like $p_{t,j1}$ and $H_{T,\text{jets}}$ in inclusive event samples. For example, with additional cuts on the vector-boson momentum, we showed in the Higgs study that the K-factors are significantly reduced (this is also examined in [230]). Moreover, experimental cuts due to detector acceptances and lepton isolation requirements may also contribute to reducing the K-factors. However, there are good reasons for not wanting to rely on such restrictions: given the many analyses that are foreseen at the LHC, it is likely that at least a few will end up probing regions where giant K-factors are present, even if only inadvertently; should LHC see "fake" excesses of data compared to predictions, it is not unlikely that some will be for the cases with poorly controlled giant K-factors. It would be a shame if our QCD toolbox were not able to address these cases properly, especially as an inability of QCD to reproduce backgrounds in a handful of cases could affect broader perceptions of QCD's ability to reliably predict backgrounds.

This brings us to the main question of this chapter: is there any way of improving the predictions for observables with giant K-factors? Specifically, is there any way of improving on the NLO Z+j prediction for the $p_{t,j1}$ and $H_{T,\text{jets}}$ distributions, in the absence of a full NNLO Z+j calculation?

Since in the NLO Z+j calculations these observables are dominated by the LO Z+2j contribution, we would expect that the NNLO Z+j result would be dominated by the NLO Z+2j contribution. Of course, we cannot just carry out a NLO Z+2j calculation for $p_{t,j1}$ and $H_{T,\text{jets}}$, because the result would include the divergent NNLO real and 1-loop contributions to topologies of type (A), without corresponding cancellations from the 2-loop and squared 1-loop terms. However if we had a way of cancelling the divergences left over in the NLO Z+2j result, our remaining ignorance about the finite contribution of the 2-loop diagrams might well have a small impact, since it would be a finite term associated solely with the non-enhanced topology (A).

This is the motivation for a new approach that we introduce here (section 5.1), named LoopSim, which is based on unitarity. If we have an observable that is non-zero starting from Z+j configurations, then for each tree-level $2 \to$ Z+3-parton and 1-loop $2 \to$ Z+2-parton contribution that is present in Z+2j at NLO, we will generate related $2 \to 2$ configurations with weights such that all soft and collinear divergences are cancelled. The result including this approximation will be denoted "$\bar{n}$NLO" for Z+j, where the "$\bar{n}$" means that we have simulated the two-loop part of the NNLO result. Correspondingly, $\bar{n}$LO would mean that we simulated the one-loop part of a NLO result, $\bar{n}\bar{n}$LO the one and two-loop parts of a NNLO result.

Insofar as the LoopSim method is new, it will be important also to have some kind of independent validation for it. Firstly, for every observable that we calculate at $\bar{n}$NLO we will verify whether $\bar{n}$LO reproduces the NLO result — only for observables where this is the case should the $\bar{n}$NLO prediction teach us something new. Secondly, we will identify leptonic observables in Drell-Yan (DY) production that also have giant K-factors, so that we can legitimately compare the $\bar{n}$NLO DY result to a full NNLO one [235,236] (section 5.3). Thirdly, we will compare the LoopSim results with those from a "reference-observable method" (section 5.2): for example, in the Z+j case (section 5.4), we will take an observable such as the $p_{t,Z}$ distribution as a "reference," since it seems to have a reasonable NLO perturbative series, and add to it the NLO Z+2j calculation of the difference between the $p_{t,j1}$ (or $H_{T,\text{jets}}$) and $p_{t,Z}$ distributions. This should be similar in quality to the $\bar{n}$NLO result.

Of the various observables that we consider in Z+j production, we will see that those

belonging to the effective-mass (H_T) class are subject to significant corrections at $\bar{n}$NLO compared to NLO. To investigate this point in more detail, we will further examine these (and other) observables in pure jet production (section 5.5), where the NLO/LO result should be similar to $\bar{n}$NLO/NLO for Z+j. As well as casting light specifically on H_T type observables, the jet-study will also serve to illustrate the application of the LoopSim method to processes other than Z+j and its potential usefulness even in cases with large, but not "giant" K-factors.

5.1 Estimating higher orders: the LoopSim method

We now introduce the LoopSim method that we will use throughout this chapter. It allows one to merge different orders of perturbation theory. To understand how the LoopSim algorithm works, we consider the simple example of Z+j at NLO which was discussed in the introduction. Then, we give a general overview of the method before analysing in detail the simpler pure glue case at tree-level accuracy. We then explain how the procedure deals with flavour (quarks and Z). Finally, we extend the method beyond tree-level accuracy.

5.1.1 Sketch of the method on Z+j at $\bar{n}$LO

To understand the basic aspects of the LoopSim algorithm, let us start with a simple example about the aforementioned Z+j process, and let us assume that we want to generate the plots in fig. 5.1 using only $\mathcal{O}(\alpha_s\alpha_{\text{EW}})$ and $\mathcal{O}\big(\alpha_s^2\alpha_{\text{EW}}\big)$ tree-level calculations instead of a dedicated NLO generator like MCFM. Within our notation, this means that we want to compute Z+j at $\bar{n}$LO. We start by noticing that a Z+2j process at LO (written as Z+2j@LO) corresponds to the real part of the Z+j process at NLO (written as Z+j@NLO). Thus, one has to find out a way to simulate the virtual part of Z+j@NLO without explicitly computing it. The goal is to comply with unitarity, i.e. cancel the soft and collinear divergences that arise in the Z+2j@LO process.

Our procedure is only intended to be accurate in the presence of giant K-factors, so we expect to be able to reproduce with a good approximation the plots for p_{t,j_1} and $H_{T,\text{jets}}$ in fig. 5.1. For that, we generate tree-level Z+2j events. We noticed that the large correction comes from topologies like diagrams (B) and (C) in fig. 5.2, where the Z boson is either soft or collinear to an initial or final state parton. Therefore, our procedure has to consider these topologies as electroweak corrections to a high-p_t dijet process, i.e. generate a loop of the Z boson over the parton to which it is "mostly collinear" (we will define this aspect in a precise way below, when examining the general algorithm). Depending on whether we started with topology (B) or (C), we obtain one of the 1-loop events shown in fig. 5.3. But one may also face a Z+2j event where the Z boson is hard and one emits a soft gluon: this event has the topology of a QCD correction to a Z+j process, in which case it seems more natural that the gluon becomes virtual instead of the Z boson, which corresponds to topology (A). Therefore, for each Z+2j event, the LoopSim procedure will have to decide whether this event corresponds to topology (A), (B) or (C).[3]

Even if the procedure can lead to a "loop" of the Z-boson, one should be aware that the LoopSim method is not intended to address the issue of virtual electroweak corrections.

[3]Though not depicted in fig. 5.3, one could also imagine a topology (D) where the gluon is emitted from the beam, and the LoopSim method has to take care of it.

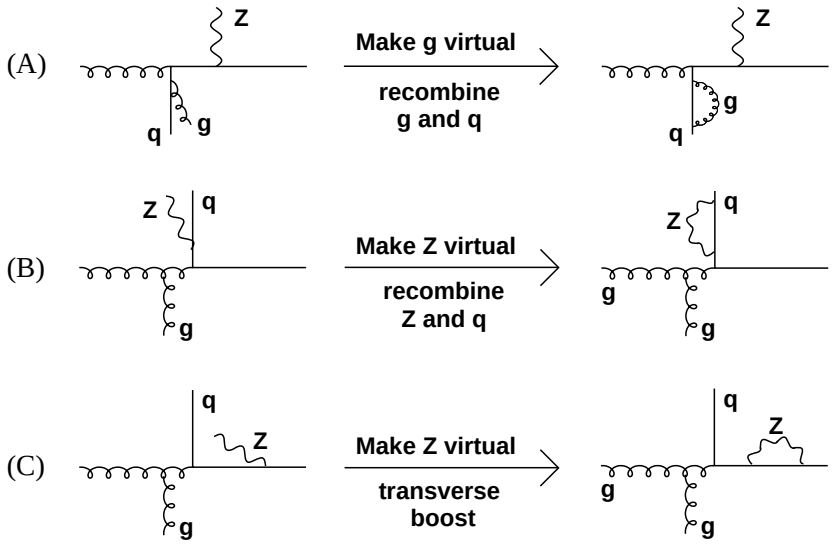

Figure 5.3: The 3 topologies (A), (B) and (C) of fig. 5.2 treated by the LoopSim method at $\bar{n}$LO, leading to 1-loop events.

In practice, the "virtual" Z is simply removed from the event and our method is used, in this case, to reveal the main dijet structure of the event. The LoopSim method is instead relevant to deal with virtual QCD corrections because they serve to cancel all infra-red and collinear divergences, whereas events where the Z-boson is looped are not considered because we require the presence of a Z-boson.

Anyway, how do we generate a loop in practice? In the case of diagrams (A) and (B), the loop of particle $j = g, Z$ with momentum p_j over the final state quark with momentum p_q results in a quark with momentum $p_j + p_q$, rescaled in a longitudinally boost invariant way such that it remains massless (this is explained in detail in appendix F.2). The "looped" particle is then removed from the event. In the case of diagram (C), the loop of the Z boson over a beam quark also means that we remove it from the event, which leads to a deficit in the total transverse momentum (that is 0 in proton-proton collision events). We take it into account by applying a transverse boost that brings the total transverse momentum to 0 (see also appendix F.2). Finally, to cancel soft and collinear divergences, we give the virtual event the opposite weight of that of the real one.

5.1.2 Sketch of the method on a general process

Before entering into the details of the LoopSim method, we give a general overview of it that will help in understanding the origin of each of its various steps. For that, let us assume that we have to analyse an event with n final state particles.

Firstly, one has to ascribe a structure to the event, i.e. know which particle has been emitted from whom. For instance, in the case of Z+j, one has to establish whether the gluon or the Z was emitted from the quark or from the beam. This question can be answered using a jet clustering. The clustering process recombines particles via "branchings" $ij \to k$ or $iB \to B$ where B corresponds to the beam. Therefore, the branching history gives us a kind of "emission" history: the clustering $ij \to k$ can be interpreted as the splitting of

particle k into particles i and j, whereas $iB \to B$ can be interpreted as the emission of particle i from the beam. The foundation of such a picture relies on the fact that the splitting of k into i and j usually results in i and j being close in angle to each other. However, when recombining them, one has to decide which one is the emitter and which one is emitted, an information which is not given by the clustering process. This is done using a measure of the particles' hardness, the general feature being that the emitter is the harder of the two recombined particles.

Secondly, one has to obtain the structure of the corresponding born event. For instance, when considering topology (A) in fig. 5.3, the born event is Z+j, whereas for topologies (B) and (C), the born event is QCD dijet. Based on the hardness of the branchings obtained from the previous clustering, the LoopSim method will tell us which of the final state particles are the "born" particles, i.e. the ones that cannot become virtual.

Thirdly, one has to "loop" the non-born particles, i.e. find a procedure to make them virtual in order to fulfil the unitarity requirement which implies the cancellation of all soft and collinear divergences. This was already briefly sketched in fig. 5.3. But one also has to pay attention to "secondary emitters", i.e. final-state particles which emit something. Such a particle does not get looped, even if it is not a born particle. This is detailed in appendix F.1.

Finally, to obtain soft and collinear safe results, one has to adequately combine all the loop diagrams generated by LoopSim. To avoid double counting in the cases where some loop calculations are done exactly at NLO (NNLO), we subtract in a soft and collinear safe way the one-loop (and two-loop) diagrams given by LoopSim.

5.1.3 Merging tree-level calculations: pure glue case

Following the main steps of our procedure given in the previous section, we now examine the exact procedure in the simple pure glue case. We will see the slight modifications that we have to make when we include flavour, i.e. quarks and Z bosons, in the next section. Moreover, we only consider here the combination of tree-level events, i.e. $\bar{n}$LO, $\bar{n}\bar{n}$LO and so on. The way to merge NLO, NNLO,... events will be explained in section 5.1.5.

We introduce the following notation:

- b: number of final-state particles in the lowest order event that will be relevant (i.e. the number of final-state "Born" particles). For instance $b = 2$ for Z+j at transverse momenta $p_t \gtrsim M_Z$.

- E_n: a generic event with n final state particles. For the Z+j@$\bar{n}$LO example, a tree-level Z+j event would be labelled E_2, a tree-level Z+2j event would be labelled E_3.

- U_l^b: an operator that acts on an event E_n and returns all the events at l loops obtained from E_n using the LoopSim method. For instance, fig. 5.3 shows the action of the operator $U_{l=1}^{b=2}$ on three different events E_3.

The central part of the LoopSim method relies on the construction of the operator U_l^b acting on E_n for all $l = 0 \dots n - b$ ($l \leq n - b$ because the number of real final state particles cannot be smaller than that of the lowest order event). First, as we previously saw, one has to decide which particles can be virtual, and which ones will always remain real. To decide that for a generic event E_n, one has to ascribe a structure to it. This is done via a

jet clustering, which makes use of the FastJet package, whose main steps can be described in the following way:

1. Number the particles in the event E_n such that each one has a unique index in the range 1 to n.

2. Run the Cambridge/Aachen (C/A) algorithm [71, 72] using a radius $R_{\rm LS}$ (LS stands for LoopSim). This means that the distance d_{ij} between 2 partons i and j is defined to be $d_{ij} = \Delta R_{ij}^2 / R_{\rm LS}^2$, where $\Delta R_{ij}^2 = (y_i - y_j)^2 + (\phi_i - \phi_j)^2$ is the usual angular distance squared in the (y, ϕ) plane. In the case where i and j are recombined into a particle k, define a special recombination scheme: particle k should acquire the index of particle i (j) if $p_{t_i} > p_{t_j}$ ($p_{t_i} < p_{t_j}$), where p_t is the transverse momentum with respect to the beam.

3. The clustering of the event can be reinterpreted in terms of a set of branchings $ij \leftarrow k$ and $iB \leftarrow B$ where B is the beam. Sort these branchings into decreasing relative transverse momentum between i and j or i and B, which is a measure of the hardness of the branching.[4]

4. Work through all the branchings in order of decreasing hardness. For a branching $ij \leftarrow k$, look at the harder of i and j, i.e. the one whose index equals that of k (cf. the recombination scheme defined above), and mark it as a "born" particle. Do the same for the softer particle if fewer than b particles have already been marked. If not, label the softer particle as clustering with the harder. For a branching $iB \leftarrow B$, mark i as a born particle. Repeat this process until b particles have been labelled as "born". The born particles will never become virtual.

5. Once the b born particles are found, continue to work through the branchings in order of decreasing hardness. For a branching $ij \leftarrow k$, assuming i is the harder particle, label j as clustering with i and label i as "non-clustering", which means that i is a secondary emitter as explained in appendix F.1. For a branching $iB \leftarrow B$, label i as clustering with the beam. In no case should existing born particles be relabelled, nor particles that have already been labelled as non-clustering. Repeat until all particles have been marked. As with born particles, particles labelled as non-clustering will never become virtual.

Our choice of the C/A algorithm comes from its close connection with angular ordering. It was shown in [71] to give a clustering sequence that matches well onto QCD divergences (avoiding the "junk jets" that appear in the k_t algorithm [70], and also leading to simpler resummations for jet rates [237]). In particular it ensures that if a hard parton independently emits multiple gluons, strongly ordered in angle, then each gluon will cluster with the hard parton rather than with one of the other gluons. Note also that our procedure for determining the Born particles, assigning a transverse-momentum measure of the hardness of branchings, is inspired by the use of separate angular and a transverse momentum distance measures in the original (full) version of the Cambridge algorithm [71].

[4] The hardness measure h_{ij} that we use between i and j is currently $h_{ij} = \min(p_{t_i}^2, p_{t_j}^2)\Delta R_{ij}^2$, but future versions of the code will define it as $h_{ij} = \min(p_{t_i}^2, p_{t_j}^2)\Delta R_{ij}^2 / R_{\rm LS}^2$ while keeping the hardness measure h_{iB} of a recombination with the beam as $h_{iB} = p_{t_i}^2$. This will only have an impact on the $R_{\rm LS}$ dependence of the results (the major part of the results presented in this chapter have $R_{\rm LS} = 1$).

The procedure described here allows one to decide which particles can become virtual when applying the LoopSim operator U_l^b: i.e. those particles that are labelled as clustering with something, whether the beam or another particle. Though the procedure was described only in the pure glue case, let us consider the simple Z+j@$\bar{n}$LO calculation as an example in order to illustrate all these definitions in a concrete case already examined. For diagram (A) in fig. 5.3, the quark and the Z boson are labelled as born whereas the gluon is labelled as clustering with the quark. For diagrams (B) and (C), the 2 partons are labelled as born. In diagram (B) the Z is labelled as clustering with q, whereas in diagram (C) it is labelled as clustering with the beam. All this seems rather intuitive.

Once every particle is labelled in an event E_n, one can compute the result of $U_l^b(E_n)$, which is a set of events E_{n-l}. For an event E_n with respectively b and n_c born and non-clustering particles, we define

$$v \equiv n - (b + n_c) \tag{5.1}$$

to be the maximum number of particles that can become virtual in an event. The operator U_l^b, when applied on an event E_n, generates all the $\binom{v}{l}$ diagrams in which l particles become virtual. For the virtual events to cancel the infra-red and collinear divergences that appear in the tree-level diagram, we need an infra-red and collinear (IRC) safe procedure to make particles virtual. For instance, the divergent weight of an event with two collinear partons i and j has to be cancelled by that of corresponding virtual event (j makes a loop over i) when computing the distribution of any IRC safe observable; and two collinear partons, if not virtualised, have to remain collinear when another particle becomes virtual.

There are two ways for a particle j to make a loop:

- If it is labelled as clustering with particle i, then one has to spread the momentum of particle j over i and all the particles that are labelled as clustering with it but which were emitted after j according to the C/A clustering sequence. This procedure is explained in detail in appendix F.2, and is designed to ensure that the recombination is collinear safe. When j is the only particle that clusters with i, then this procedure becomes equivalent to adding the momenta of particles i and j: $p_i + p_j = p_k$. Then, the momentum p_k is rescaled such that its mass is set to 0, leaving its transverse components p_x, p_y and its rapidity unchanged.

- If particle j is labelled as clustering with the beam, then, when it is looped, it is simply removed from the event. A p_t imbalance will result from this "looping" of particles with the beam, and so we subsequently apply transverse boosts to all remaining event particles, while conserving their rapidities, so as to bring the total transverse momentum to zero (see appendix F.2).

The operator U_l^b has the following properties

$$U_0^b = \mathbb{1}\,, \qquad U_l^b(E_n) = 0 \quad \text{if } l > v\,. \tag{5.2}$$

Moreover, if w_n is the weight of event E_n, then each of the events generated by the $U_l^b(E_n)$ operator has a weight

$$w_{n-l} = (-1)^l w_n\,. \tag{5.3}$$

In order to illustrate the action of the operator U_l^b, we give below some simple examples in the pure glue case. In each of these examples, the born particles are labelled with numbers

$$U_{l=1}^{b=2}$$ 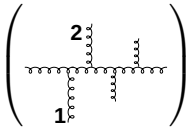

$$= -$$ 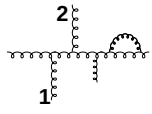

$$-$$ 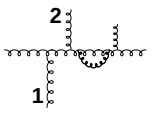

$$, \tag{5.4}$$

$$U_{l=2}^{b=2}$$ 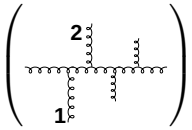

$$=$$ 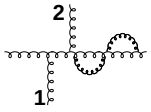

$$, \tag{5.5}$$

$$U_{l=2}^{b=2}$$ 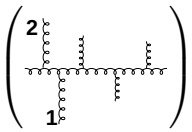

$$=$$ 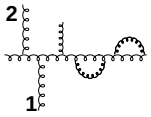

$$+$$ 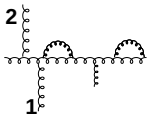

$$+$$ 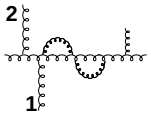

$$, \tag{5.6}$$

$$U_{l=2}^{b=3}$$ 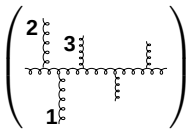

$$=$$ 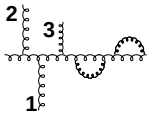

$$, \tag{5.7}$$

$$U_{l=2}^{b=2}$$ 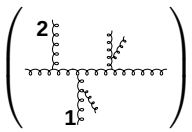

$$=$$ 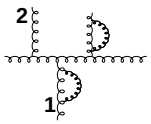

$$, \tag{5.8}$$

$$U_{l=3}^{b=2}$$ 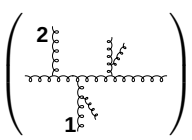

$$= 0\,. \tag{5.9}$$

Eq. (5.4) gives an example of 1-loop diagrams generated by LoopSim when studying QCD dijet at $\bar{n}\bar{n}$LO for instance. Eq. (5.5) shows the 2-loop diagrams generated from the same event. The next equation shows what happens if we still study a born configuration corresponding to dijet events but with one more particle in the final state. If we now put the number of born particles from the same event to be 3, we obtain only one 2-loop diagram instead of three, as represented in eq. (5.7). Finally, the last two equalities give a case with a splitting: the emitter is not looped, even if it is not a born particle.

Once all the $U_l^b(E_n)$ have been calculated for $l = 0 \dots n - b$, one has to combine them in order to subtract all the soft and collinear divergences that appear in the calculation of E_n and the virtual diagrams generated from it. This is done by the operator $U_\forall^b$, which is defined as

$$U_\forall^b \equiv \sum_{l=0}^{\infty} U_l^b\,. \tag{5.10}$$

It generates all the necessary loop diagrams that have the same order in α_s as the original tree-level diagram. It is straightforward to see that the total weight of the diagrams obtained from the $U_\forall^b$ operator is 0. Indeed, if we apply it to an event E_n whose maximum number of virtual particles is v, we get

$$w_n \sum_{l=0}^{v} (-1)^l \binom{v}{l} = 0\,, \tag{5.11}$$

for $v > 0$.

We give here a few examples of the action of this operator:

$U_\forall^2$ 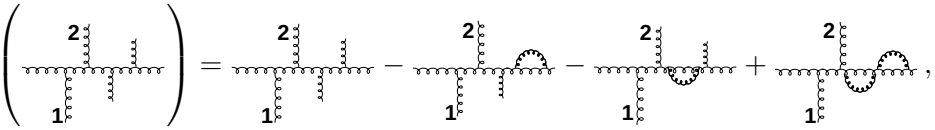 (5.12)

$U_\forall^2$ 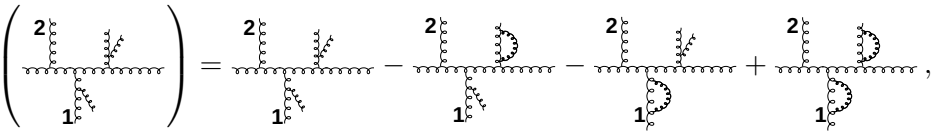 (5.13)

$U_\forall^2$ 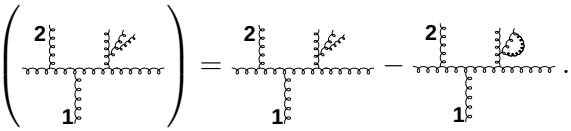 (5.14)

In the last case, only one particle can become virtual because there are two secondary emitters which cannot be looped.

5.1.4 Treatment of flavour within LoopSim

In the previous section, we saw how to cancel soft and collinear divergences using a procedure that generates loops from tree-level events in the pure glue case. We now would like to extend it to include quarks and Z bosons. This will lead us to define a kind of "flavoured" C/A algorithm.

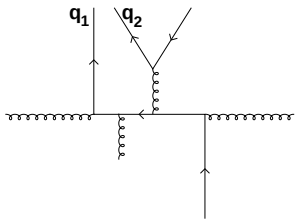

Figure 5.4: Example of an event where two quarks q_1 and q_2 get recombined by the C/A algorithm.

Let us start with quarks and consider the situation depicted in fig. 5.4. In this case, applying the C/A algorithm as in the previous section will lead to the recombination of the two quarks q_1 and q_2, which is clearly not possible: one can only recombine a quark with an antiquark (giving a gluon), or a quark with a gluon (giving a quark). Therefore, one should veto on such a clustering by defining for instance the clustering distance d_{qq} between two quarks to be infinite. But in event generators (like MCFM [88,89] and NLOJet++ [238] that we used to produce the results presented in this chapter), it is not possible to distinguish between light quarks and gluons, and one thus has to ignore these fake recombinations and still define the distance d_{ij} between two partons to be $\Delta R_{ij}^2/R_{\mathrm{LS}}^2$, regardless of whether i and j are quarks, antiquarks, or gluons. This is justified by the fact that these kind of recombinations should not occur frequently, because the corresponding divergence is very sub-leading [239]. Therefore, light quarks are treated exactly as gluons and we apply the procedure described in the pure glue case. However, should we wish to extend the LoopSim procedure to handle tagged heavy quarks like b or t, then it will become necessary to properly

take into account quark flavour in the clustering distances, for example through an extension to the C/A algorithm of the work in [239, 240]. This is a possible subject for future work.

What about Z bosons? Normally, a Z can only be emitted from quarks or antiquarks. So if one could distinguish between quarks and gluons, it would be possible to define the distance d_{gZ} between a Z and a gluon to be infinite. Since we cannot assume that we will know which partons are quarks or gluons, we instead adapt Frixione's isolation procedure [241] to decide if a Z boson relatively close in angle to a parton i is likely to have been emitted from i. More precisely, if

$$p_{t_i} > \sqrt{p_{t_Z}^2 + M_Z^2}\frac{\Delta R_{iZ}}{R_{\text{LS}}}\,, \tag{5.15}$$

then we define $d_{iZ} = \Delta R_{iZ}^2/R_{\text{LS}}^2$, otherwise $d_{iZ} = \infty$. Concerning the recombination scheme: if i and Z are recombined by the clustering procedure into a particle k, then define the index of k to be that of i (a quark and a Z give a quark). In practice, besides the particle's number in the event, the index of the particle also encodes its flavour (parton or Z).

Finally, for a recombination between a parton i and Z, we define the hardness of the branching h_{iZ} as[5]

$$h_{iZ} \equiv \min(p_{t_i}^2, p_{t_Z}^2 + M_Z^2)\frac{\Delta R_{iZ}^2}{R_{\text{LS}}^2}\,, \tag{5.16}$$

whereas a recombination of a Z with the beam has a hardness

$$h_{ZB} \equiv p_{t_Z}^2 + M_Z^2\,. \tag{5.17}$$

When a particle becomes virtual, the recoil procedure which keeps the total transverse momentum to 0 is the same as in the pure glue case. However, this procedure becomes more subtle when the Z decays, because one also has to define a longitudinally boost invariant way to recoil its decay products. This is described in appendix F.2.

5.1.5 Merging NLO calculations and beyond

Before explaining how we merge exact higher orders calculations, let us mention how we use the LoopSim method in practice on tree-level events at several different orders. The LoopSim procedure is simply to act on each of them with the $U_\forall^b$ operator. For instance, one can write

$$\text{Z@}\bar{n}\text{LO} = U_\forall^1(\text{Z@LO}) + U_\forall^1(\text{Z+j@LO})\,, \tag{5.18}$$

$$\text{Z+j@}\bar{n}\text{LO} = U_\forall^2(\text{Z+j@LO}) + U_\forall^2(\text{Z+2j@LO})\,, \tag{5.19}$$

$$\text{Z+j@}\bar{n}\bar{n}\text{LO} = U_\forall^2(\text{Z+j@LO}) + U_\forall^2(\text{Z+2j@LO}) + U_\forall^2(\text{Z+3j@LO})\,. \tag{5.20}$$

Notice that $U_\forall^1(\text{Z@LO}) = \text{Z@LO}$ and $U_\forall^2(\text{Z+j@LO}) = \text{Z+j@LO}$. The terms $U_\forall^1(\text{Z+j@LO})$ and $U_\forall^2(\text{Z+2j@LO})$ simulate up to one-loop corrections, and $U_\forall^2(\text{Z+3j@LO})$ simulates up to two-loop corrections.

Now, let us see how things work beyond tree-level accuracy. As an example we first consider the case where the one-loop corrections are computed exactly. We define $E_{n,l}$ to be a generic event at l loops (exactly calculated) with n particles in the final state. At one-loop accuracy, one can still apply the operator $U_\forall^b$ on tree-level events $E_{n,0}$, which generates up

[5] This will be true in a future version of the code, but currently $h_{iZ} = \min(p_{t_i}^2, p_{t_Z}^2)\Delta R_{iZ}^2$.

to $n-b$ loops. But to take into account that the one-loop corrections are exactly calculated, one has to subtract the one-loop part $U_1^b(E_{n,0})$ contained in $U_\forall^b(E_{n,0})$. But one cannot simply compute $U_\forall^b(E_{n,0}) - U_1^b(E_{n,0})$ because that would not be infrared and collinear safe (the total weight of the events is not zero). To comply with unitarity, we instead perform the operation $U_\forall^b(E_{n,0}) - U_\forall^b\left(U_1^b(E_{n,0})\right)$ and also apply the $U_\forall^b$ operator to $E_{n-1,1}$. To be more precise, at one-loop accuracy, we define a new operator $U_{\forall,1}^b$ such that:

$$U_{\forall,1}^b(E_{n,0}) = U_\forall^b(E_{n,0}) - U_\forall^b\left(U_1^b(E_{n,0})\right)\,, \tag{5.21}$$

$$U_{\forall,1}^b(E_{n-1,1}) = U_\forall^b(E_{n-1,1})\,, \tag{5.22}$$

the subscript 1 indicating that the calculation is done at one-loop accuracy. The action of $U_{\forall,1}^b$ depends on the number of loops computed exactly in the event: we subtract the one-loop contribution returned by LoopSim only in tree-level events. With this notation, one can compute the higher order corrections of eqs. (5.18−5.20) to one-loop accuracy

$$\text{Z@}\bar{n}\text{NLO} = \text{Z@NLO} + U_{\forall,1}^1(\text{Z+j@NLO}_{\text{only}})\,, \tag{5.23}$$

$$\text{Z+j@}\bar{n}\text{NLO} = \text{Z+j@NLO} + U_{\forall,1}^2(\text{Z+2j@NLO}_{\text{only}})\,, \tag{5.24}$$

$$\text{Z+j@}\bar{n}\bar{n}\text{NLO} = \text{Z+j@NLO} + U_{\forall,1}^2(\text{Z+2j@NLO}_{\text{only}}) + U_{\forall,1}^2(\text{Z+3j@NLO}_{\text{only}})\,, \tag{5.25}$$

where the "only" subscript on Z+nj@NLO$_{\text{only}}$ means that we take the highest order that contributes, i.e. here $\alpha_s^{n+1}\alpha_{\text{EW}}$, since the LO, $\alpha_s^n\alpha_{\text{EW}}$, piece of Z+$n$j@NLO, is already taken into account in the Z+$(n-1)$j@NLO contribution. Note that this implies that one should use consistent renormalisation and factorisation scale choices across all different orders of the calculation.

The extension of the procedure beyond one-loop accuracy is simple. For instance, at two-loop accuracy, one has to subtract the approximated two-loop contribution $U_2^b(E_{n,0}) - U_1^b\left(U_1^b(E_{n,0})\right)$ in eq. (5.21), and the other approximated two-loop contribution $U_1^b(E_{n,1})$ in eq. (5.22), giving

$$U_{\forall,2}^b(E_{n,0}) = U_\forall^b(E_{n,0}) - U_\forall^b\left(U_1^b(E_{n,0})\right) - U_\forall^b\left[U_2^b(E_{n,0}) - U_1^b\left(U_1^b(E_{n,0})\right)\right]\,, \tag{5.26}$$

$$U_{\forall,2}^b(E_{n-1,1}) = U_\forall^b(E_{n-1,1}) - U_\forall^b\left(U_1^b(E_{n-1,1})\right)\,, \tag{5.27}$$

$$U_{\forall,2}^b(E_{n-2,2}) = U_\forall^b(E_{n-2,2})\,. \tag{5.28}$$

Therefore, once Z+j@NNLO is calculated, one may compute for instance

$$\text{Z@}\bar{n}\text{NNLO} = \text{Z@NNLO} + U_{\forall,2}^1(\text{Z+j@NNLO}_{\text{only}})\,. \tag{5.29}$$

To be complete, let us mention the generalisation of our procedure to m-loop accuracy

$$U_{\forall,m}^b(E_{n-l,l}) = U_\forall^b(E_{n-l,l}) + \sum_{j=1}^{m-l}(-1)^j \sum_{\substack{l_1,\ldots,l_j\geq 1\\ l_1+\ldots+l_j\leq m-l}} U_\forall^b \circ U_{l_1}^b \circ \ldots \circ U_{l_j}^b(E_{n-l,l})\,. \tag{5.30}$$

5.1.6 Expected accuracy of the method

Let us briefly explain why the LoopSim method is expected to work in presence of huge K-factors. We consider an observable A computed respectively at NLO and $\bar{n}$LO. We define $K^{(A)}_{\text{NLO}}$ such that

$$\sigma^{(A)}_{\text{NLO}} = K^{(A)}_{\text{NLO}} \sigma^{(A)}_{\text{LO}} \,, \tag{5.31}$$

and we assume that $K^{(A)}_{\text{NLO}} \gg 1$. This huge K-factor may come from logarithmic enhancements in the real NLO diagram or the appearance of new scattering channels in the perturbative expansion. The computation of $\sigma^{(A)}_{\bar{n}\text{LO}}$ gives the exact real part of the NLO calculation as well as the divergent terms of the virtual correction. Therefore

$$\sigma^{(A)}_{\bar{n}\text{LO}} - \sigma^{(A)}_{\text{NLO}} = \mathcal{O}\left(\alpha_s \sigma^{(A)}_{\text{LO}}\right) \,, \tag{5.32}$$

where, in writing $\mathcal{O}(\alpha_s \sigma^{(A)}_{\text{LO}})$, we mean that the term missing in the $\bar{n}$LO calculation, the finite part of the 1-loop correction, is not especially enhanced. This leads to

$$\sigma^{(A)}_{\bar{n}\text{LO}} = \sigma^{(A)}_{\text{NLO}} \left(1 + \mathcal{O}\left(\frac{\alpha_s}{K^{(A)}_{\text{NLO}}}\right)\right) \,. \tag{5.33}$$

The relative difference between the approximate and exact NLO calculations is thus suppressed by the inverse K-factor.

Next, consider $\bar{n}$NLO accuracy. The difference between $\sigma^{(A)}_{\bar{n}\text{NLO}}$ and $\sigma^{(A)}_{\text{NNLO}}$ comes from the parts of the two-loop corrections that are finite and associated with the LO topology, so that they should be free of the enhancements that led to the large NLO K-factor. This implies

$$\sigma^{(A)}_{\bar{n}\text{NLO}} - \sigma^{(A)}_{\text{NNLO}} = \mathcal{O}\left(\alpha_s^2 \sigma^{(A)}_{\text{LO}}\right) \,. \tag{5.34}$$

If we define $K^{(A)}_{\text{NNLO}}$ such that $\sigma^{(A)}_{\text{NNLO}} = K^{(A)}_{\text{NNLO}} \sigma^{(A)}_{\text{LO}}$, we can then write

$$\sigma^{(A)}_{\bar{n}\text{NLO}} = \sigma^{(A)}_{\text{NNLO}} \left(1 + \mathcal{O}\left(\frac{\alpha_s^2}{K^{(A)}_{\text{NNLO}}}\right)\right) \,. \tag{5.35}$$

If $K^{(A)}_{\text{NLO}} \gg 1$, one can expect $K^{(A)}_{\text{NNLO}} \gg 1$ too.

5.2 Estimating higher orders: the reference-observable method

Using the large enhancement of the NLO corrections, one can also imagine an alternative method to compute approximately $\sigma^{(A)}_{\text{NNLO}}$ in some particular cases. We will use it for the Z+j and dijet processes as a powerful cross-check that will help us build our confidence in results of the LoopSim method.

Let us explain it for Z+j. We assume that we have a reference observable which is identical to the observable A at LO. For instance, one might consider ref $= p_{t,Z}$ and $A = p_{t,j}$.

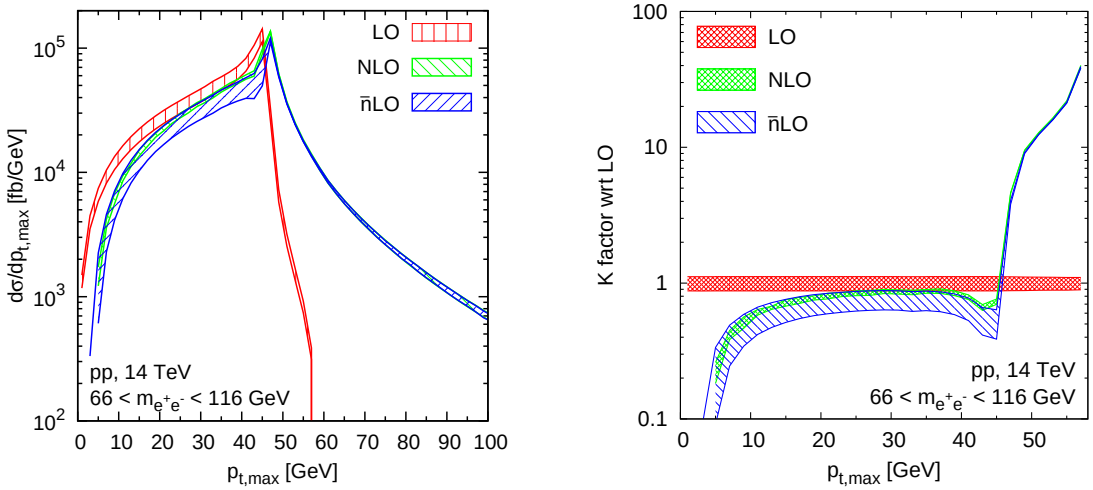

Figure 5.5: Comparison between simulated $\bar{n}$LO results from LoopSim (with $R_{\rm LS} = 1$) with exact results for Drell-Yan process at NLO. Transverse momentum spectra of the harder lepton are shown in the left plot while in the right plot the corresponding K-factors w.r.t. LO are given. The uncertainty bands were obtained by varying $\mu_R = \mu_F$ by a factor of $\frac{1}{2}$ and 2 around a default choice of M_Z.

We can write the NNLO Z+j prediction for A in terms of the NNLO prediction for the reference observable plus the NLO Z+2j difference between A and the reference distributions

$$\sigma^{(A)}_{\text{Z+j@NNLO}} = \sigma^{(\text{ref})}_{\text{Z+j@NNLO}} + (\sigma^{(A)} - \sigma^{(\text{ref})})_{\text{Z+j@NNLO}} \tag{5.36}$$

$$= \sigma^{(\text{ref})}_{\text{Z+j@NNLO}} + (\sigma^{(A)} - \sigma^{(\text{ref})})_{\text{Z+2j@NLO}} \tag{5.37}$$

The second equality is possible because 2-loop NNLO corrections to Z+j have the topology of Z+j at LO. Therefore, their contributions to the observables A and ref are identical and cancel in the difference in eq. (5.36).

If we have reason to believe that the perturbative expansion of the reference observable converges well, we can conclude that $\sigma^{(\text{ref})}_{\text{Z+j@NNLO}} - \sigma^{(\text{ref})}_{\text{Z+j@NLO}}$ is genuinely a small correction. Therefore

$$\sigma^{(A)}_{\text{Z+j@NNLO}} \simeq \sigma^{(\text{ref})}_{\text{Z+j@NLO}} + (\sigma^{(A)} - \sigma^{(\text{ref})})_{\text{Z+2j@NLO}}\,, \tag{5.38}$$

i.e. we approximate the NNLO distribution for A in terms of the NLO distribution for the ref observable and a NLO calculation for the difference between the A and ref distributions, both of which are exactly calculable. The missing part is suppressed by $1/K^{(A)}$ as for the LoopSim method. For Z+j, one can see on fig. 5.1 that $p_{t,Z}$ seems to be an acceptable reference observable for $p_{t,j1}$ and $H_{T,\text{jets}}$.

5.3 Validation: comparison to DY at NNLO

The cross section for the Drell-Yan process is known with exclusive final states up to NNLO accuracy [235, 236]. Above a certain value of lepton transverse momentum, one finds giant corrections to the lepton p_t spectra when going from LO to NLO and large ones from NLO

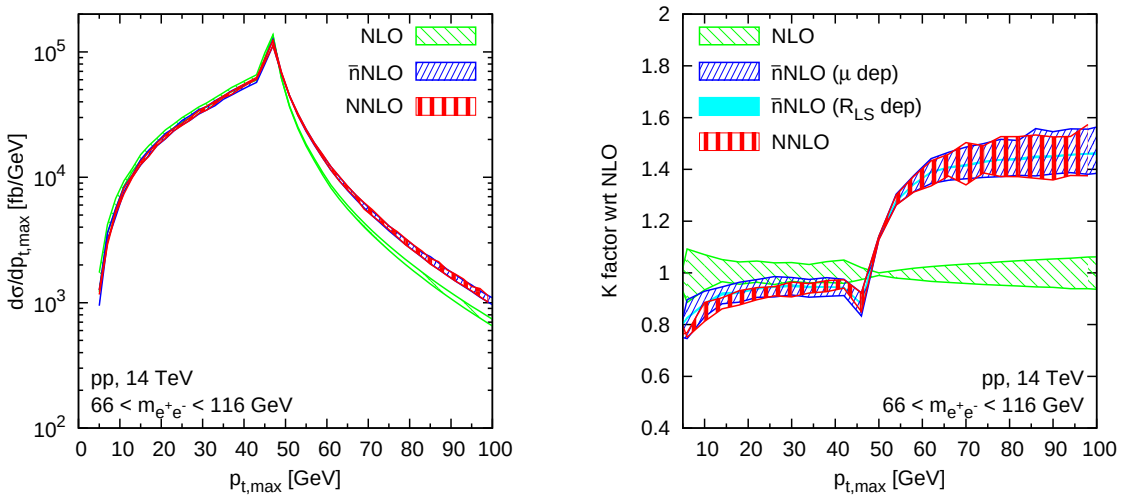

Figure 5.6: Comparison between simulated results from LoopSim (with $R_{\rm LS} = 1$) at $\bar{n}$NLO with available exact results for Drell-Yan process NNLO. Transverse momentum spectra of the harder lepton are shown in the left plot while in the right plot the corresponding K-factors w.r.t. NLO are given. The uncertainty bands come from varying the factorisation and renormalisation scales by factors 1/2 and 2. For $\bar{n}$NLO, the band related to changing the $R_{\rm LS}$ parameter from 0.5 to 1.5, at fixed $\mu_R = \mu_F = m_Z$, is also shown.

to NNLO. This gives us an opportunity to directly test the performance of the LoopSim method by comparing its $\bar{n}$NLO results to exact NNLO spectra for lepton pair production.

Fig. 5.5 gives the comparison of the $\bar{n}$LO, NLO and LO results for the production of an e^+e^- pair within the mass window of $66 < m_{e^+e^-} < 116$ GeV at a proton-proton centre of mass energy of 14 TeV. The left-hand plot shows the cross section differential in the transverse momentum of the harder of the two leptons. The right-hand plot gives the corresponding K-factor with respect to LO. The results were obtained with MCFM 5.3 [88, 89], with its default set of electroweak parameters and NNLO MSTW2008 parton distribution functions. The uncertainty bands in Fig. 5.5 correspond to varying the renormalisation and factorisation scales $\mu_{\rm R} = \mu_{\rm F}$ by a factor of $\frac{1}{2}$ and 2 around a default choice of M_Z. In the $\bar{n}$LO result we fixed the value of the LoopSim radius parameter to be $R_{\rm LS} = 1$, which naturally places interparticle-state and particle-beam clustering on the same footing (though the $\bar{n}$LO result here is actually independent of $R_{\rm LS}$, because there is at most one isolated QCD parton in the final state).

There are three relevant regions of transverse momentum in fig. 5.5. For $p_{t,\max} \lesssim \frac{1}{2}M_Z$ (low p_t) the distribution is dominated by on-shell Z-bosons and its shape is governed by the angular distribution of the Z decays in their centre-of-mass frame. The peak close to $\frac{1}{2}M_Z$ corresponds to Z-bosons that decay at right-angles to the beam. For $\frac{1}{2}M_Z \lesssim p_{t,\max} < 58\,\text{GeV}$ (intermediate p_t), the LO distribution comes from Z-bosons that are off shell, which allows the p_t of the lepton to be larger than $\frac{1}{2}M_Z$. The narrow width of the Z causes the distribution to fall very steeply. The 58 GeV upper edge of this region scale is controlled by our cut on $m_{e^+e^-}$. Above 58 GeV (high p_t) the LO distribution is zero.

In the low p_t region, the NLO correction is moderate and negative. There is no strong reason to believe that the LoopSim method should work here, but it turns out that the $\bar{n}$LO

result reproduces the structure of the correction, even if its scale dependence remains much larger than that of the NLO result. In the intermediate p_t region, we see a "giant" NLO K-factor. It comes about because initial-state radiation can give a boost to the Z-boson, causing one of the leptons to shift to higher p_t (it becomes the "max" lepton). The spectrum of QCD radiation falls much less steeply than the Z-boson lineshape, so this NLO correction dominates over the LO result. In this region the exact loop correction, proportional to the LO result, becomes almost irrelevant and we see near perfect agreement between $\bar{n}$LO and NLO. In the high-p_t region only the real emission diagrams of Z@NLO contribute and $\bar{n}$LO becomes identical to NLO (both correspond to the Z+j@LO result). Similar results hold for the $p_{t,e^\pm}$ distribution, while the $p_{t,\min}$ lacks the giant K-factor in the intermediate region.

A similar comparison between $\bar{n}$NLO and NNLO spectra is shown in fig. 5.6. The NNLO results were obtained with DYNNLO 1.0 [236,242] used with a set of electroweak parameters compatible with that of MCFM. When calculating contributions of $\bar{n}$NLO and NNLO, we imposed a cut of 1 GeV on the transverse momentum of the Z-boson to avoid configurations that adversely affect numerical convergence. At lower orders, we used a cut compatible with zero (0 for MCFM and 0.1 for DYNNLO). All the other parameters are identical with those adopted earlier at lower orders.

In the low-p_t region we find quite good agreement between the $\bar{n}$NLO and NNLO results (with somewhat larger uncertainty bands for $\bar{n}$NLO). Such a result was not guaranteed a priori. In the intermediate region, where the NNLO/NLO corrections are substantial, the agreement is excellent. This was expected. At high p_t the agreement should be exact, and does seem to be, within statistical fluctuations. The dependence on $R_{\rm LS}$ (shown in the right-hand plot) has been estimated by varying its value from 0.5 to 1.5. The effects are small.

Finally, we note that similar features and a similar level of agreement between $\bar{n}$NLO and NNLO are to be found in the $p_{t,\min}$ and $p_{t,e^\pm}$ distributions.

5.4 Results for the Z+jet process

In the previous section, we studied the Z production process and showed that our procedure correctly reproduces the p_t distribution of the hardest lepton at NNLO, even unexpectedly in regions where the K-factor is not large. In this section we study the Z+j process, whose NNLO cross-section is not known yet, but which leads to giant K-factors at NLO for some observables as explained in the introduction. Therefore, its NNLO contribution is expected to be accurately described by the LoopSim method. Throughout this section we use MCFM 5.7, including the Z+2j process at NLO [243], with the NLO CTEQ6M PDFs. We will take three different values for the renormalisation and factorisation scales: $\mu_R = \mu_F = \frac{1}{2}\mu_0$, μ_0 and $2\mu_0$, with

$$\mu_0 = \sqrt{M_Z^2 + p_{t,j1}^2}\,, \tag{5.39}$$

where $p_{t,j1}$ is the transverse momentum of the hardest jet. At high p_t, this scale choice should be quite similar to that used in [244] and has the same p_t scaling as those in [229,230]. The $R_{\rm LS}$ uncertainty is measured at $\mu_R = \mu_F = \mu_0$ using three different values for it: $R_{\rm LS} = 0.5$, 1, 1.5.

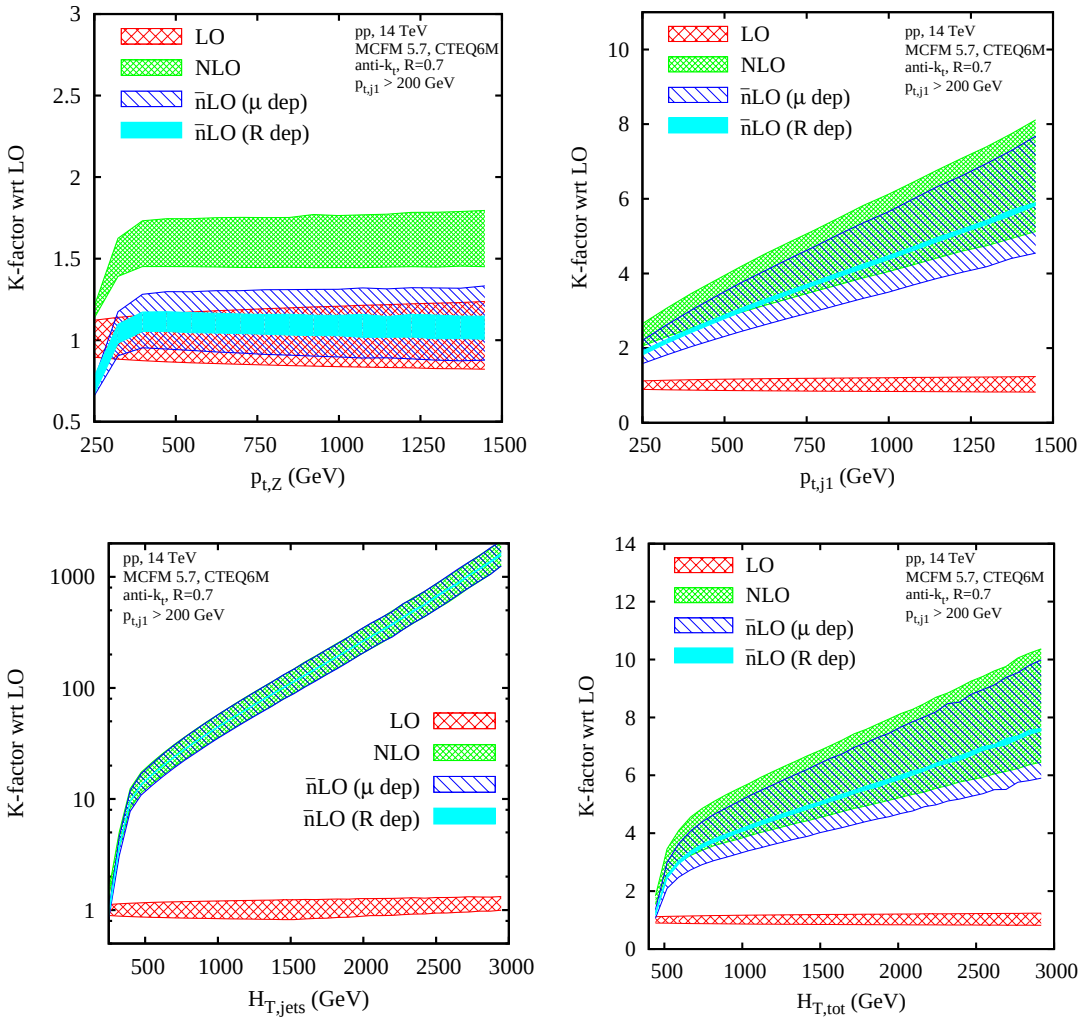

Figure 5.7: Comparison of the $\bar{n}$LO/LO K-factor with the NLO/LO K-factor, together with their scale and R_{LS} uncertainties for four observables.

In addition to the 3 observables shown in the introduction, $p_{t,Z}$, $p_{t,j1}$ and $H_{T,\mathrm{jets}} = \sum_{i=1}^{\infty} p_{t,ji}$, we will also consider

$$H_{T,\mathrm{tot}} \equiv H_{T,\mathrm{jets}} + p_{t,Z}\,. \tag{5.40}$$

We only include events for which $p_{t,j1} > 200\,\mathrm{GeV}$.

5.4.1 Validation at $\bar{n}$LO

As a first investigation of the performance of the LoopSim method, let us examine how the $\bar{n}$LO approximation compares to the full NLO result. Fig. 5.7 shows the K-factors for the $\bar{n}$LO and NLO predictions, with uncertainty bands from scale and R_{LS} variations.

In the upper-left plot, one sees that the $\bar{n}$LO prediction for the $p_{t,Z}$ distribution gives a somewhat smaller K-factor than the NLO result. This is because certain genuine loop effects are not taken into account by the LoopSim method, for example those related to threshold

logarithms which depend crucially on the factorisation scheme of the parton distribution functions. The $\bar{n}$LO result does, however, reproduce the p_t dependence of the K-factor, i.e. the dip towards $p_t = 200\,\text{GeV}$. This dip arises because of the requirement in our event selection that there should at least one jet with $p_t > 200\,\text{GeV}$. At LO this induces a step-function in the $p_{t,Z}$ distribution at 200 GeV. At NLO, soft and collinear emissions smoothen out that threshold and the $\bar{n}$LO calculation correctly reproduces the resulting interplay between real and virtual terms.

In the three remaining plots of fig. 5.7, for $p_{t,j1}$, $H_{T,\text{jets}}$ and $H_{T,\text{tot}}$, all of which have giant K-factors, one sees good agreement between the $\bar{n}$LO and NLO results. This is because the dominant NLO contribution comes from events in the B and C-type configurations for which there is no corresponding QCD loop correction. The LoopSim method merely serves to cancel the divergences that arise from soft and collinear emissions off A-type configurations and these are not dominant overall.

The R_{LS} dependence, also shown on these four plots, only comes from 1-loop events generated by LoopSim. Therefore, for an observable A studied in Z+j@$\bar{n}$LO with two different values R_0 and R_1 for R_{LS}, one can write:

$$\sigma^{(A)}_{\text{Z+j@}\bar{n}\text{LO},R_1} - \sigma^{(A)}_{\text{Z+j@}\bar{n}\text{LO},R_0} = \sigma^{(p_{t,Z})}_{\text{Z+j@}\bar{n}\text{LO},R_1} - \sigma^{(p_{t,Z})}_{\text{Z+j@}\bar{n}\text{LO},R_0} \tag{5.41}$$

as long as A coincides with $p_{t,Z}$ at LO (it does for each of $p_{t,j1}$, $H_{T,\text{jets}}$ and $\frac{1}{2}H_{T,\text{tot}}$). This means that the *absolute* uncertainty due to R_{LS} is the same for A and $p_{t,Z}$. Therefore, the *relative* uncertainty due to R_{LS} is expected to be roughly inversely proportional to the K-factor for A, in analogy with the discussion of sec. 5.1.6. This explains why the R_{LS} dependence (solid cyan band) looks significantly smaller for $p_{t,j1}$, $H_{T,\text{jets}}$ and $H_{T,\text{tot}}$ than it does for $p_{t,Z}$ plot.

5.4.2 Results at $\bar{n}$NLO

Results at $\bar{n}$NLO are given in fig. 5.8. In the case of $p_{t,Z}$ the result is similar to the NLO result, and the scale uncertainties remain largely unchanged. In other words, since Z+2j topologies do not dominate the high-$p_{t,Z}$ distribution, adding NLO corrections to them (i.e. $\bar{n}$NLO Z+1j) makes no difference either to the result or the uncertainties. We have also shown the dependence on the choice of R_{LS} in the LoopSim procedure. It is smaller than the scale dependence.

The $p_{t,j1}$ distribution gets a correction that is just within the NLO uncertainty band, with $\bar{n}$NLO uncertainties that are about half the size of the NLO band. Adding in the $\bar{n}$NLO term has made a real difference. This is precisely what we expect: the observable is dominated by Z+2-parton configurations, and these were only present at tree-level in the NLO Z+1j calculation. Our use of $\bar{n}$NLO provides the additional 1-loop Z+2-parton and tree-level Z+3-parton configurations that come with NLO Z+2j accuracy.

Given the improvement in scale uncertainty, we need to ask whether the uncertainty due to R_{LS} variation might somehow eliminate part of this benefit. It is, however, small. The reasons are similar to those given around eq. (5.41).

The $H_{T,\text{jets}}$ and $H_{T,\text{tot}}$ distributions get a significant $\bar{n}$NLO correction, with a $\bar{n}$NLO/NLO K-factor of about $1.7-2$ (with some reduction of the uncertainties in the $H_{T,\text{jets}}$ case). Absolute scale uncertainties increase slightly compared to NLO, but because of the large K-factor, relative scale uncertainties diminish. It is somewhat disturbing that the $\bar{n}$NLO and NLO

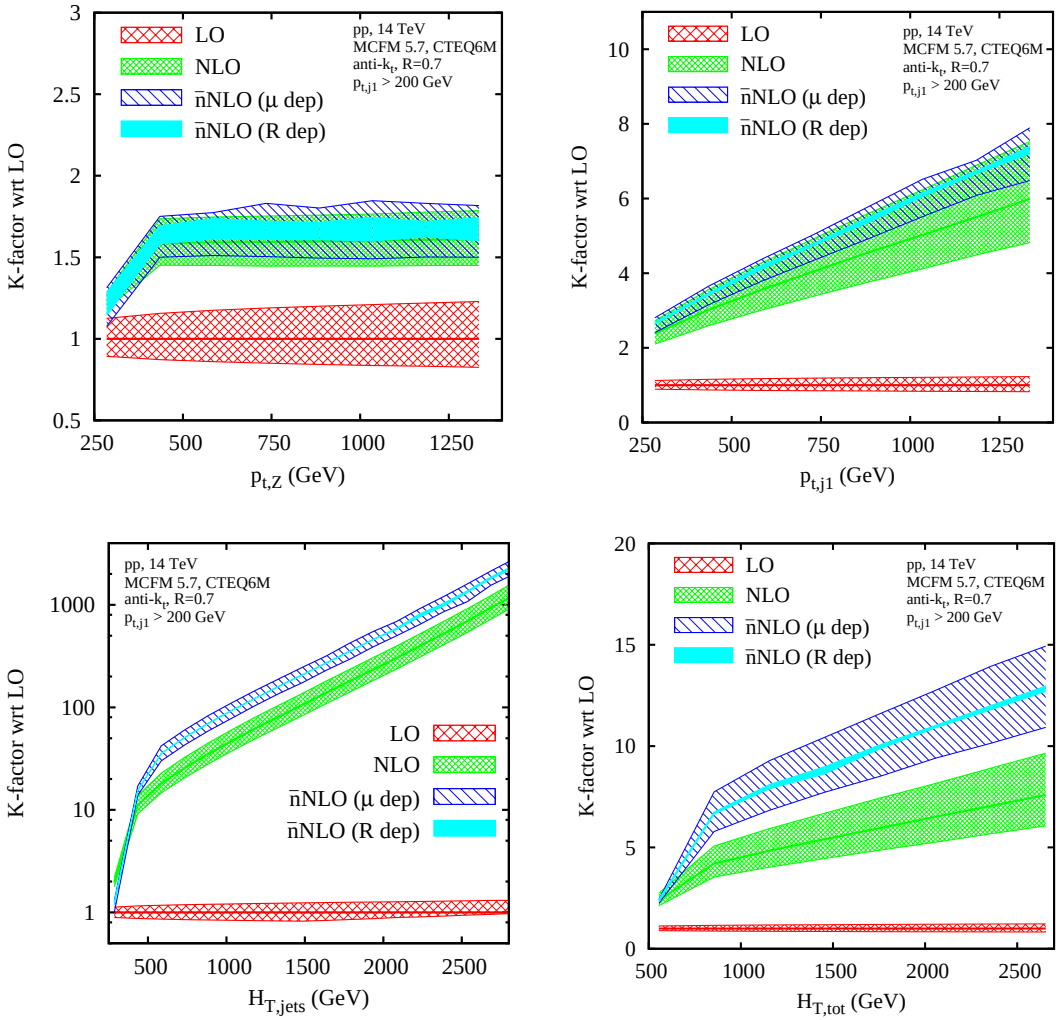

Figure 5.8: Comparison of the $\bar{n}$NLO/LO K-factor with the NLO/LO K-factor, together with their scale and R_{LS} uncertainties for four observables.

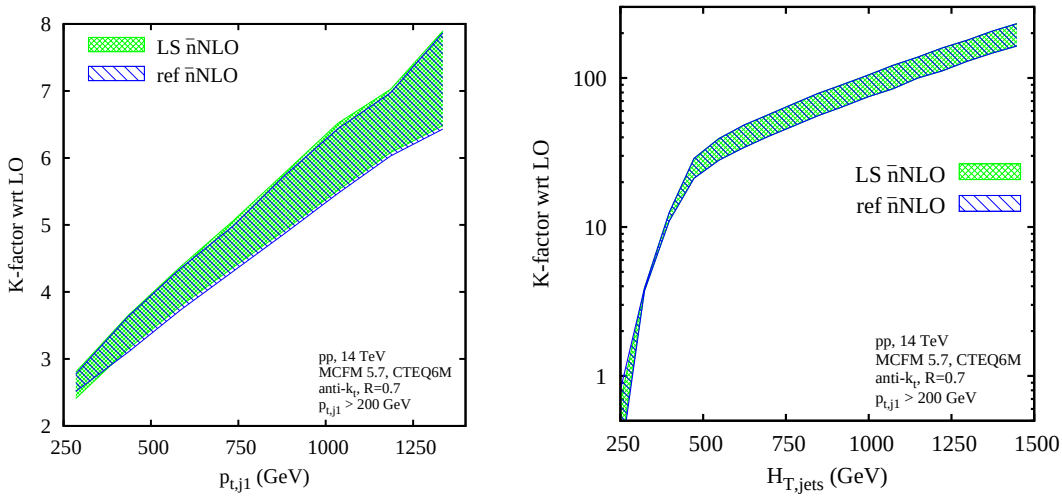

Figure 5.9: Comparison between the approximate NNLO/LO K-factor calculated using respectively the LoopSim and the "reference-observable" method for $p_{t,j1}$ and $H_{T,\text{jets}}$. As a reference observable we take the differential cross section for $p_{t,Z}$.

uncertainty bands don't overlap. Given the novelty of the LoopSim method, one should therefore ask whether this is reasonable and whether there is any way of cross-checking the result. Since $\bar{n}$NLO Z+1j is really NLO of the dominant Z+2j component, the large $\bar{n}$NLO correction that we see is comparable to an $\mathcal{O}(2)$ K-factor for going from LO to NLO in the Z+2j prediction. There are many contexts where NLO and LO results are not compatible within scale uncertainties, and so it is not unreasonable that the same should be seen here.

Still we would like to have some cross checks. A first option is to consider the alternative "reference-observable" method presented in section 5.2, which only makes use of standard NLO calculations to compute the approximate NNLO corrections. The comparison between the two methods is shown in fig. 5.9 for $H_{T,\text{jets}}$ and $p_{t,j1}$. One notices near perfect agreement for $H_{T,\text{jets}}$ and very good agreement for $p_{t,j1}$. This gives us some degree of confidence that the $\bar{n}$NLO LoopSim results provide an accurate description of the NNLO behaviour for these observables.

A second option for cross-checking these results is to examine whether H_T might generally be a "difficult" observable. To do so we examine this observable in the case of QCD jet events.

5.5 QCD jet events as a testing ground

We have seen that the $\bar{n}$NLO K-factors for the two effective-mass variables, $H_{T,\text{tot}}$ and $H_{T,\text{jets}}$, in Z+jet(s) events are about a factor of two above the NLO K-factor. We have already commented on the fact that so large an effect is somewhat disturbing and that it is natural to ask whether one can really trust it.

Since NLO is the first order at which we see the dominant "dijet" topology for the H_T variables in Z+jet(s), fig. 5.2B,C, it might be instructive to establish a correspondence with a simpler process, QCD dijet production. Having a NLO Z+j prediction is analogous to a LO dijet prediction; and the $\bar{n}$NLO Z+j predictions should be analogous to NLO dijet

predictions. NLO cross sections for dijet observables can be calculated exactly and therefore we can check whether NLO K-factors of order 2 appear for effective-mass observables in pure QCD events.

We will consider several effective-mass observables: an $H_{T,n}$ variable, which sums over the n hardest jets above some threshold ($p_{t,\min} = 40\,\text{GeV}$; such a cut is often imposed experimentally[6])

$$H_{T,n} = \sum_{i \in \text{jets with } p_{t,ji} > p_{t,\min}}^{n} p_{t,ji}\,, \tag{5.42}$$

where $p_{t,ji}$ is the transverse momentum of the i^{th} hardest jet. Upper limits on the number of jets included in the effective mass are common in SUSY searches [140, 169] (though it is not clear if that limit is always the same within a given experiment's search, e.g. compare [169] with [225]). We also define an effective mass for all jets above the $p_{t,\min}$ threshold,

$$H_T \equiv H_{T,\infty}\,, \tag{5.43}$$

which is more similar to the $H_{T,\text{jets}}$ and $H_{T,\text{tot}}$ observables of section 5.4. Finally, for completeness we consider the distributions of $p_{t,j1}$, $p_{t,j2}$ and the inclusive jet spectrum.

At LO the distributions of $\frac{1}{2}H_{T,n}$ ($n \geq 2$), $\frac{1}{2}H_T$, $p_{t,j1}$, and $p_{t,j2}$ will all be identical. The inclusive jet spectrum will have a distribution that is twice as large (because each of the two jets contributes). Note that we do not impose any rapidity acceptance limits on the jets: though such a cut would have been trivial to include in the LoopSim procedure, it would have complicated somewhat the reference-observable approach that we will consider at the end of the section.

Figure 5.10(left) shows the distributions for two observables, $\frac{1}{2}H_T$ and $p_{t,j2}$ at LO (where they are identical) and at NLO, as determined using NLOJet++ with CTEQ6M PDFs. A first comment is that H_T receives a NLO K-factor of order 2, just like the $\bar{n}$NLO enhancements in the Z+j case. This provides supporting evidence as to their legitimacy. A second comment is that the cross sections are large: these observables will be easily accessible with a few pb^{-1} of integrated luminosity at a 7 TeV LHC, allowing for an early experimental verification of the large K-factor for H_T.

The other observable in the left-hand plot of fig. 5.10, $p_{t,j2}$, has a very different K-factor, somewhat below 1. The right-hand plot shows the NLO K-factors for our full range of observables, focusing on a single bin of the left-hand one, from $400-500\,\text{GeV}$. The pattern that we see here allows us to make some deductions. Firstly, the $H_{T,2}$ variable, which sums the p_t's of the two leading jets, is free of large NLO enhancements. It is the addition of the third jet in $H_{T,3}$ and H_T that brings about the enhancement. A natural interpretation is the following: it is common for a third, soft jet to be present due to initial state radiation. This third jet shifts the H_T distribution to slightly larger values, and because the distribution falls very steeply, that leads to a non-negligible enhancement.

The pattern for $p_{t,j1}$ and $p_{t,j2}$ can also be explained in similar terms: a soft ISR emission boosts the hard dijet system, breaking the degeneracy between the p_t's of the two hardest jets. It is jet 1 that shifts to larger p_t (giving a K-factor > 1), while jet 2 shifts to lower p_t and so it gets a K factor below 1. For the inclusive jet spectrum, and for $H_{T,2}$, this effect

[6] In section 5.4 we did not apply this kind of cut on the H_T variables; one purpose in applying it here is to ascertain whether the large higher-order effects persist even with it.

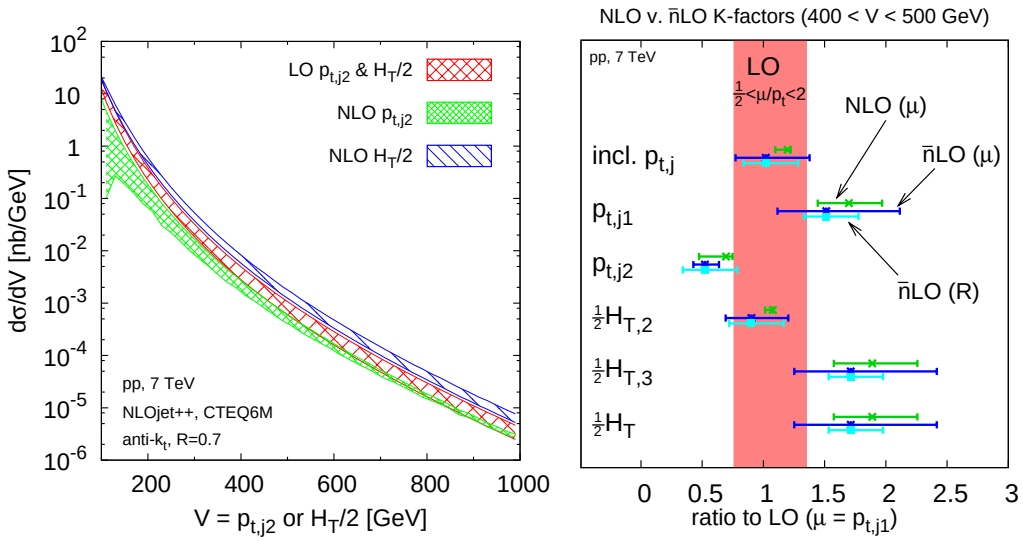

Figure 5.10: Left: differential cross sections for the $p_{t,j2}$ and $\frac{1}{2}H_T$ observables, at LO, where they are identical, and at NLO where they have substantially different K-factors. Right: the NLO K-factors for the $400 < V/\,\text{GeV} < 500$ bin for each choice of variable V among the following: the inclusive jet spectrum, the p_t distribution of the hardest ($p_{t,j1}$) and second hardest ($p_{t,j2}$) jets, (half) the effective mass of the two hardest jets ($H_{T,2}$), three hardest jets ($H_{T,3}$) and of all jets above 40 GeV (H_T). Also shown on the right are the $\bar{n}$LO results for the K-factors. The NLO and $\bar{n}$LO (μ) widths correspond to the uncertainty due to simultaneous renormalisation and factorisation scale variation by a factor of two around a central value $\mu = p_{t,j1}$. The $\bar{n}$LO(R) width shows the uncertainty from a variation of R_{LS} in the range $0.5 < R_{\text{LS}} < 1.5$.

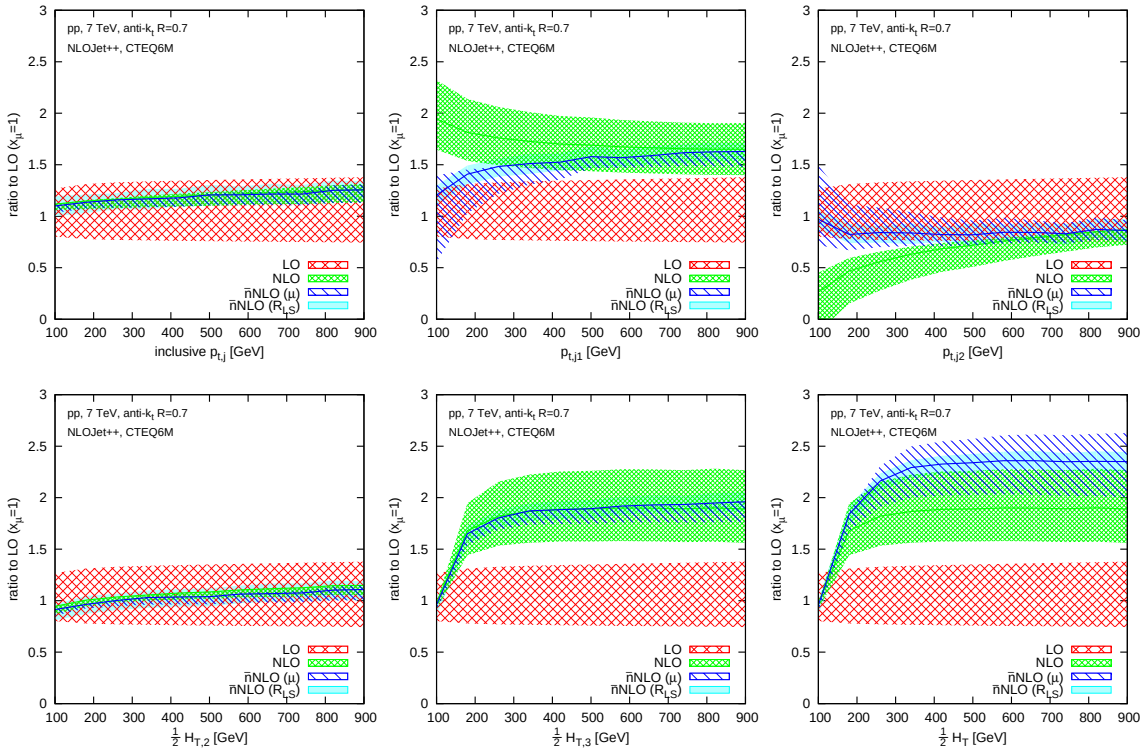

Figure 5.11: The $\bar{n}$NLO and NLO K-factors relative to the the LO predictions, as a function of p_t (or $\frac{1}{2}H_T$, etc.), for the collection of jet observables described in the text.

balances out. In addition, final-state radiation from one of the jets can cause it to shift to lower p_t (becoming the 2nd jet), further reducing the K-factor for its distribution.

Of the different variables, it is only the inclusive jet p_t and $H_{T,2}$ for which there is a clear reduction in scale uncertainty in going from LO to NLO.

Figure 5.10(right) also shows the $\bar{n}$LO results (including uncertainties both from scale variation and from the LoopSim parameter $R_{\rm LS}$). Despite the fact that none of the K-factors is parametrically large (except arguably for $H_{T,3}$ and H_T), the $\bar{n}$LO results are remarkably effective at reproducing the pattern of NLO K-factors, albeit with a small systematic shift and generally larger scale uncertainties. One can also verify that, to within $10-20\%$, the p_t dependence of the NLO K-factors is reproduced at $\bar{n}$LO.

Given this success of $\bar{n}$LO, and the observed limited convergence of some of the observables at NLO, it is interesting to examine what happens at $\bar{n}$NLO, where the additional 3j@NLO contribution that we require is again obtained with NLOJet++. Results are shown in fig. 5.11.

For the inclusive jet spectrum and $H_{T,2}$, which already saw large reductions in scale-dependence at NLO, the $\bar{n}$NLO corrections have essentially no meaningful effect: they neither significantly affect the central values, nor reduce the scale uncertainties. For these observables, NLO already converged well, and adding a subset of the NNLO corrections without the 2-loop part cannot improve the result.

For the other effective mass observables, the situation is quite different. With $H_{T,3}$, the $\bar{n}$NLO result is close to the NLO result and the scale uncertainty is much reduced, i.e. this

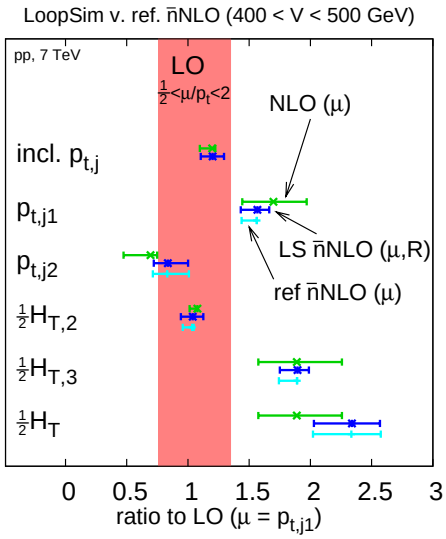

Figure 5.12: Comparison of LoopSim based $\bar{n}$NLO results with those from the reference-observable method, here using the inclusive jet p_t spectrum as the reference observable. In the LoopSim results (labelled $\bar{n}$NLO), the uncertainty bar spans the envelope of the scale and R_{LS} uncertainties. The results are for the $400 < V/\,\mathrm{GeV} < 500$ bin for each observable V, as in fig. 5.10.

observable seems to come under control at $\bar{n}$NLO. In contrast, H_T is subject to quite a large further correction, with the central value at $\bar{n}$NLO lying outside the NLO uncertainty band, and the $\bar{n}$NLO uncertainty band (dominated by scale variation) only marginally smaller than at NLO. Why is this? Perhaps we are seeing the effect of a second ISR emission, which shifts the H_T distribution to even higher values? Given that $H_{T,3}$ converges and H_T does not, such an explanation is not unattractive. It is also consistent with the decrease in K-factor at low H_T, where the 40 GeV p_t cutoff on the jets contributing to the H_T sum will eliminate the ISR enhancement. A definitive conclusion would however probably require further study.

For the remaining two observables, $p_{t,j1}$ and $p_{t,j2}$, the $\bar{n}$NLO contribution goes in the opposite direction from the NLO correction and at low p_t it seems that the series fails to converge. This is, we believe, closely related to observations of insufficiencies of NLO predictions for dijet cross sections in DIS and photoproduction when identical p_t cuts are imposed on both jets [200, 245–248] (equivalent to integrating the $p_{t,j2}$ distribution above that cut). The worse convergence at low p_t is probably due to larger fraction subprocesses that involve gluons in the underlying $2 \to 2$ scattering so that perturbative corrections tend to go as $(C_A\alpha_s)^n$ rather than as $(C_F\alpha_s)^n$ at higher p_t.

Considering that we do not have giant NLO K-factors for the jet processes shown here, one may question the validity of the information obtained from the LoopSim procedure. An important cross check comes from a comparison with the reference-observable technique. Examining fig. 5.10 (right), one sees two natural reference observables: the inclusive jet spectrum and $H_{T,2}$, both of which show "perturbative" K-factors and small scale dependence at NLO. Here we will use (half) the inclusive jet spectrum as the reference observable (results with $H_{T,2}$ would be almost identical).

Figure 5.12 provides a comparison of the LoopSim $\bar{n}$NLO results (showing the envelope of the scale and $R_{\rm LS}$ uncertainties) with the reference-observable $\bar{n}$NLO results. The comparison is given for all observables except the reference observable itself. The agreement between the two methods is striking, with the reference-observable method giving just a small shift of the K-factors relative to the LoopSim results. The shift is identical for all the observables, as it has to be: it is simply equal to the difference between the NLO and $\bar{n}$NLO results for the reference observable. Insofar as we believe the scale dependence to be representative of the true NLO uncertainty on the inclusive jet spectrum,[7] the results for the other observables should therefore be good approximations to the full NNLO results.

5.6 Conclusion

Several cases of LHC observables with giant NLO K-factors have come to light in recent years. They are characterised by the presence at NLO of new partonic scattering topologies that have large enhancements over the LO topologies. In these cases, NLO calculations, while important in highlighting the presence of the large K-factors, cannot on their own provide accurate predictions.

In this chapter we have examined how to address this problem by combining NLO results for different multiplicities, for example Z+1j@NLO with Z+2j@NLO. Our main, most flexible method, LoopSim, makes use of unitarity to cancel the infrared and collinear divergences that appear when one tries, say, to apply Z+2j@NLO calculations to observables that are non-zero starting from Z+1-parton. We referred to the result as Z+1j@$\bar{n}$NLO.

In introducing a new approximate method for estimating NNLO corrections, significant evidence needs to be provided that the method is meaningful.

Firstly, we gave reasons why, in cases with giant K-factors associated with new NLO topologies, we expect $\bar{n}$NLO results to be a good approximation to NNLO results.

As a next step, we carried out studies comparing Z/γ^*@$\bar{n}$NLO (DY) to NNLO predictions for the $pp \to Z/\gamma^* + X \to e^+e^- + X$ process. In comparing the DY lepton p_t $\bar{n}$NLO distributions to NNLO we found near-perfect agreement in the region of giant K-factors. Interestingly, even in the region where the NLO K-factor was not large, the $\bar{n}$NLO results provided a significantly better approximation to NNLO than did the plain NLO result. This needs not always be the case, but is, we believe, connected to the observation that our $\bar{n}$LO results reproduced much of the structure seen at NLO (recall, Z@$\bar{n}$LO means combining Z@LO with Z+1j@LO).

For Z+j production, part of our validation procedure was to compare $\bar{n}$LO and NLO. All observables with giant K-factors showed good agreement between the two (one with a moderately large K-factor did not). For those observables, $\bar{n}$NLO always appeared to provide extra information: in one case ($p_{t,j1}$) the $\bar{n}$NLO result suggested convergence of the perturbative series, with small corrections beyond NLO and significantly reduced scale uncertainty; in two other cases, both involving effective-mass type observables (H_T), the $\bar{n}$NLO results were almost a factor of 2 larger than the NLO ones, with, at best, limited reduction in the scale uncertainties. A second part of our validation procedure was to use

[7] The fact that the $\bar{n}$NLO uncertainty for the inclusive jet spectrum is larger than the NLO uncertainty suggests that our symmetric scale variation may well be underestimating somewhat the uncertainties present at NLO. To be conservative, it might have been safer to vary the renormalisation and factorisation scales independently.

an alternative, less flexible "reference-observable" $\bar{n}$NLO-type estimate.

The poor convergence that we saw for effective mass observables led us to examine a range of effective-mass and jet observables in pure jet events. The presence of significant a K-factor for the effective mass in the jet case turned out to depend on the maximal number of objects included in the H_T sum. Including just two, $H_{T,2}$, the K-factor was close to 1. But for $H_{T,n}$ with $n \geq 3$ the K-factor was $\mathcal{O}(2)$. In the Z+j case we did not have an upper limit and so the $\bar{n}$NLO/NLO ratios that we saw there are consistent with the NLO/LO K-factors in the pure jets case.

Even though the observables in the pure jets case did not display giant K-factors we let ourselves be tempted into an application of the LoopSim method there too. We found systematically good agreement between $\bar{n}$LO and NLO results, better than we could perhaps have expected. At the next order, $\bar{n}$NLO, the results suggested that $H_{T,2}$ remains stable, with $\bar{n}$NLO providing no extra information as compared to NLO; with our default scale choice, $H_{T,3}$ starts to converge at $\bar{n}$NLO, with a small correction relative to NLO and reduced scale uncertainties, now commensurate with those of $H_{T,2}$ at NLO; we also found that $H_{T,n}$ with $n \geq 4$ at best converges slowly. An interpretation of these results was given in the main text and we also confirmed them with a "reference-observable" $\bar{n}$NLO-type estimate.

Overall we have come to believe that $\bar{n}$NLO results in the LoopSim method provide significant information beyond NLO. Not only can we prove this in cases with giant K-factors, but we saw strong suggestions that it is true in a number of other cases too. Wherever one can calculate a $\bar{n}$NLO result one can also examine the $\bar{n}$LO prediction: its degree of agreement with NLO provides case-by-case information on the potential usefulness of the method. Moreover, we are inclined to think that the reference-observable method can often be adapted, on a case-by-case basis, to provide additional backup.

Let us finally mention the relation that exists between LoopSim and other predictive methods. Firstly there is a close connection between $\bar{n}$LO (or $\bar{n}\bar{n}$LO) and CKKW and MLM [249, 250] matching, because they also both provide ways of combining tree-level results with different multiplicities. Of course CKKW and MLM matching provide an interface with parton showers too, which the LoopSim method does not. On the other hand it is significantly easier to include multiple loop orders into the LoopSim method than it is within matrix-element/parton-showering matching procedures (though work is ongoing in this direction see e.g. [251]).

An interesting cross-check of the LoopSim method will come with the completion of the NNLO calculations for the Z+j and dijet processes. At that point the method could also, for example, be used to merge Z@NNLO with Z+j@NNLO, so as to provide an $\bar{n}$NNLO prediction for quantities like the Drell-Yan lepton p_t spectrum.

The value of the LoopSim method also goes hand-in-hand with progress on 1-loop calculations, especially with the prospect of automated of NLO calculations now on the horizon (for example [252–254]).

Note that currently, the LoopSim code can deal with processes involving any number of light partons and up to one single vector boson. It would benefit from further work to appropriately include heavy quarks and additional bosons.

Conclusion

In this thesis we have been interested in various topics related to LHC studies and predictions: light Higgs WH and ZH search channels at the LHC, reconstruction of the Higgs boson decaying into $b\bar{b}$, optimised using semi-analytical calculations, and approximation of higher-order corrections in presence of huge K-factors. This work has led to new tools (Mass Drop + filtering analysis, LoopSim) that can be used to expand the range of signals that may be expected to be seen at the LHC, and to gain insight into what happens when we include higher-order terms for some potentially "dangerous" background processes whose perturbative convergence is poor at lower orders.

More precisely, we first examined the reconstruction of massive particles decaying hadronically. In the boosted limit, such a decay often leads to one jet in the final state which looks similar to a QCD splitting. It thus becomes important to distinguish between these two configurations. This issue is relevant for light Higgs searches at the LHC, because in this case the Higgs boson predominantly decays into $b\bar{b}$. We showed in particular how the boosted kinematics allows one to recover the challenging WH and ZH production modes as promising search channels when the Higgs mass is around 120 GeV. For that, we used a novel subjet analysis procedure, called Mass Drop and Filtering analysis, which reduces the QCD background while enhancing the Higgs reconstruction efficiency. The Mass Drop procedure measures the hardness of the splitting and, to avoid the soft divergence of QCD, requires it to be large enough if it is to be tagged as a Higgs decay. Its originality relies on its ability to adapt itself to the p_t scale of the event, which is important for the LHC where a broad range of scales is expected. The Filtering analysis goes one step further as it reduces the effect of underlying event and pile-up on the jet mass reconstruction, which both lead to an important amount of additional soft particles in the Higgs jet neighbourhood. The main result of this part was the significance of 4.5σ obtained for the Higgs signal in the combined WH and ZH channels for a luminosity of 30 fb^{-1} at the LHC (14 TeV). The efficiency of our procedure in reconstructing the Higgs signal was later confirmed by the Atlas collaboration through a full detector simulation with only moderately smaller significance. The NLO corrections surprisingly gave rise to very large K-factors for the $Wb\bar{b}$ and $Zb\bar{b}$ processes but, after applying our procedure, they were found not to significantly affect the $S/\sqrt{B}$ results. It should be noted that our reconstruction method can be applied to any colourless massive particle decaying hadronically, and variants of it have been used by a number of authors [141, 174, 187, 188].

We then focused in particular on the filtering analysis. Its role is to balance two opposite effects: on one hand, soft noise from underlying event and pile-up increases the mass of the Higgs jet far beyond the nominal Higgs mass; on the other hand, QCD radiation from the $b\bar{b}$ dipole tends to decrease the Higgs jet mass. The purpose of this part was to optimise the parameters of the filtering analysis in order for the combination of these effects to have as

small an impact as possible, i.e. we require the reconstructed Higgs width to be minimal. To study the effect of QCD radiation on the Higgs jet mass, we performed analytical non-global calculations up to order $\mathcal{O}(\alpha_s^2)$ at leading single-logarithmic accuracy, and we provided some analytical estimates at all-orders in the large-N_c limit when the radius of the filtering analysis is small. We also numerically resummed the Higgs jet mass distribution at all-orders in the large-N_c limit and used the results obtained to model the value of the perturbative Higgs width as a function of the filtering parameters. We then introduced a simple model to examine the impact of underlying event and pile-up on the reconstructed Higgs width, which is a non-perturbative effect. Some approximations were finally needed to combine these two effects in a simple but physically reasonable way, which led to interesting relations between the optimal choices of the filtering parameters and the physical scales of the problem.

Finally, motivated by the very large K-factors discovered for some observables in the Z+j process while studying the WH and ZH search channels, we addressed the more general issue of giant K-factors at hadron colliders. The method that we developed, called "LoopSim", consists in approximating higher-order corrections by merging different orders of perturbation theory such that all infra-red and collinear divergences are cancelled. To validate the LoopSim procedure, we applied it to the DY process and saw a good agreement between our approximate NNLO and the exact NNLO results, even, surprisingly, in regions where the K-factor is not large. Encouraged by these results, and also using an alternative validation procedure called "the reference-observable method", we returned to the Z+j process, which was our original motivation for this work, and made our predictions for the dominant part of its NNLO corrections. We noted different kinds of behaviours depending on the observable. We focused especially on the effective-mass type observables (H_T) for which, contrary to $p_{t,j1}$, we did not observe a convergence of the perturbative series. In particular, we confirmed these results in the somewhat similar QCD dijet case at NLO and also showed that the LoopSim method could provide significant results at $\bar{n}$LO and $\bar{n}$NLO for this process in spite of the moderate K-factors involved. The LoopSim code still needs some extensions to include heavy quarks and multi-boson productions, yet it already provides useful and interesting insights in higher-order corrections for processes with (even not necessarily) huge K-factors.

Appendices

Appendix A

Colour algebra

In this appendix, we derive the relations eqs. (1.48−1.50).

A.1 Definition of the $SU(N_c)$ algebra

The $N_c^2 - 1$ $SU(N_c)$ generators t^A are traceless, hermitian, and generate the closed $SU(N_c)$ algebra:

$$[t^A, t^B] = i f^{ABC} t^C \,, \tag{A.1}$$

where f^{ABC} are the structure constants of the algebra, verifying

$$f^{ABC} = -f^{BAC} \,, \tag{A.2}$$

$$f^{ABC} = f^{CAB} \,. \tag{A.3}$$

The t^A matrices are normalised such that:

$$\mathrm{Tr}(t^A t^B) = T_R \delta^{AB} \,, \quad T_R = \frac{1}{2} \,. \tag{A.4}$$

The basic relations defining C_F and C_A are:

$$t^A t^A = C_F \mathbf{1} \,, \tag{A.5}$$

$$f^{ABC} f^{ABD} = C_A \delta^{CD} \,. \tag{A.6}$$

Once T_R is fixed, the values for C_F and C_A are completely determined. We compute them below.

A.2 The Fierz identity

The Fierz identity is at the heart of many complex relations involving $SU(N_c)$ algebra. We are going to derive it here.

Let M be a $N_c \times N_c$ matrix. It can then be expanded on the basis formed by the identity matrix $\mathbf{1}$ and the $N_c^2 - 1$ generators t^A of the $SU(N_c)$ algebra:

$$M = D_0 \mathbf{1} + D_A t^A \,. \tag{A.7}$$

We take as an example the matrix $M = M^l_j$, whose only non-zero component is the one at line j and column l:

$$\left(M^l_j\right)^i_k = \delta^i_j \delta^l_k \,. \tag{A.8}$$

If we take the trace of eq. (A.7), we obtain:

$$\delta^i_j \delta^l_i = D_0 N_c \,, \tag{A.9}$$

thus leading to

$$D_0 = \frac{1}{N_c} \delta^l_j \,. \tag{A.10}$$

If we now multiply eq. (A.7) by t^B and then we take the trace, we obtain:

$$\left(t^B\right)^l_j = \frac{1}{2} D_B \,, \tag{A.11}$$

which gives

$$D_A = 2 \left(t^A\right)^l_j \,. \tag{A.12}$$

Replacing D_0 and D_A by their corresponding value implies eq. (1.47), i.e. the Fierz identity:

$$\delta^i_j \delta^l_k = \frac{1}{N_c} \delta^i_k \delta^l_j + 2 (t^A)^i_k (t^A)^l_j \,. \tag{A.13}$$

A.3 Some useful formulae

The first application of the Fierz identity is the value of C_F. Contracting indexes i and j, we find:

$$\begin{aligned} N_c \delta^l_k &= \frac{1}{N_c} \delta^l_k + 2 \left(t^A t^A\right)^l_k \,, \\ &= \frac{1}{N_c} \delta^l_k + 2 C_F \delta^l_k \,. \end{aligned} \tag{A.14}$$

Therefore:

$$C_F = \frac{N_c^2 - 1}{2 N_c} \,. \tag{A.15}$$

Multiplying eq. (A.13) by $\left(t^B\right)^j_i$, one finds:

$$0 = \frac{1}{N_c} \left(t^B\right)^l_k + 2 \left(t^A t^B t^A\right)^l_k \,, \tag{A.16}$$

leading to:

$$t^A t^B t^A = -\frac{1}{2 N_c} t^B \,. \tag{A.17}$$

We finally derive the value for C_A and another important relation in the meantime. On one side we have:[1]

$$\begin{aligned} if^{ABC}t^A t^C &= if^{ABC}\left(\frac{1}{2}[t^A,t^C]+\frac{1}{2}\{t^A,t^C\}\right), \\ &= if^{ABC}\frac{1}{2}[t^A,t^C], \\ &= \frac{1}{2}if^{ABC}if^{ACD}t^D, \\ &= \frac{C_A}{2}t^B. \end{aligned} \tag{A.18}$$

On the other side, we get:

$$\begin{aligned} if^{ABC}t^A t^C &= t^A[t^A,t^B], \\ &= t^A t^A t^B - t^A t^B t^A, \\ &= C_F t^B + \frac{1}{2N_c}t^B. \end{aligned} \tag{A.19}$$

Therefore:

$$C_A = N_c. \tag{A.20}$$

A.4 Application to the calculation of colour factors in Feynman diagrams

We return to the diagrams of section 1.2.5. We can now easily derive their precise colour factor for finite values of N_c. Their topology is recalled on fig. A.1.

Diagram (a) is the simplest one. Averaging over the colour i and summing over the colour k, one gets (cf the Feynman rules in fig. 1.3):

$$\begin{aligned} (a) &= \alpha_s\frac{1}{N_c}\sum_i\sum_k \left(t^A\right)^j_k\left(t^A\right)^i_j, \\ &= \alpha_s\frac{1}{N_c}\sum_i\sum_k C_F\delta^i_k, \\ &= \alpha_s\frac{C_F}{N_c}\delta^i_i, \\ &= \alpha_s C_F. \end{aligned} \tag{A.21}$$

The 2 sums over i and k can be equivalently written as a trace over these indexes. We will use that property for the two other diagrams. This result leads to eq. (1.48) in the large-N_c limit.

[1] We use the anticommutator:

$$\{t^A,t^C\} = t^A t^C + t^C t^A.$$

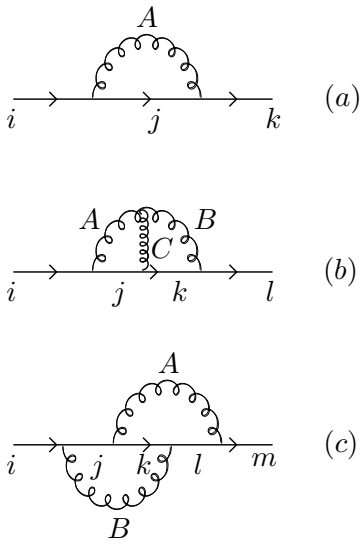

Figure A.1: The Feynman diagrams of section 1.2.5 with colour indexes explicitly written.

Diagram (b) can be derived in the same way:

$$\begin{aligned}(b) &= \alpha_s^2 \frac{1}{N_c} \mathrm{Tr}\left(\left(t^B\right)_l^k \left(t^C\right)_k^j \left(t^A\right)_j^i \right) i f^{ABC} \,, \\ &= \alpha_s^2 \frac{1}{N_c} \left(t^B\right)_i^k \left(-\frac{C_A}{2} \right) \left(t^B\right)_k^i \,, \\ &= -\alpha_s^2 \frac{C_F C_A}{2} \,. \end{aligned} \tag{A.22}$$

We used eq. (A.18) in this calculation. In the large-N_c limit, we finally obtain eq. (1.49).

Finally, diagram (c) gives:

$$\begin{aligned}(c) &= \alpha_s^2 \frac{1}{N_c} \mathrm{Tr}\left(\left(t^A\right)_m^l \left(t^B\right)_l^k \left(t^A\right)_k^j \left(t^B\right)_j^i \right) \,, \\ &= \alpha_s^2 \frac{1}{N_c} \left(-\frac{1}{2N_c} \right) \left(t^B\right)_i^j \left(t^B\right)_j^i \,, \\ &= -\alpha_s^2 \frac{C_F}{2N_c} \,. \end{aligned} \tag{A.23}$$

Here, we applied eq. (A.17), which finally leads to eq. (1.50) in the large-N_c limit.

Appendix B

Analytical considerations on the non-global structure of the perturbative expansion

In this appendix, we first briefly recall the difference between a global and a non-global observable, and then we derive all the results presented in section 4.1.

B.1 Global and non-global observables

In [199], a fundamental distinction is made between global and non-global observables. A global observable is sensitive to the emission of gluons in the entire phase space, as it is the case for event shape variables (thrust, C-parameter,...). The calculation that will be carried out in this appendix concerns a non-global observable at second order. We would like to see the main difference between these 2 kinds of observables. For that, let us consider a generic global observable τ. In this case, using eqs (4.14,4.17-4.19,4.20), we can write the second order contribution $I_2^{(G)}$ to the distribution $\Sigma(\tau)$ as:

$$\begin{aligned} I_2^{(G)}(\tau) &= \int dk_1 dk_2 (4\pi\alpha_s)^2 \Theta(E_1 - E_2) \Big[(W_1 + W_2)\Theta(\tau - \tau(k_1, k_2)) - \\ &\qquad - (W_1 + W_2)\Theta(\tau - \tau(k_1)) - W_1 \Theta(\tau - \tau(k_2)) + W_1 \Big] , \qquad \text{(B.1)} \\ &= \int dk_1 dk_2 (4\pi\alpha_s)^2 \Theta(E_1 - E_2) W_1 \Theta(\tau(k_2) - \tau) , \qquad \text{(B.2)} \end{aligned}$$

in the limit $E_1 \gg E_2$. Eq. (B.2) has to be compared with eq. (4.22): the function W_2 disappears from the calculation, and one is left with primary emissions only. One can actually show this result to all-orders: at leading-log (and even next-to-leading log) accuracy, the distribution of a global observable can be computed using only independent gluon emissions (primaries) from the original $q\bar{q}$ dipole.

The observable ΔM considered in chapter 4 is non-global because only the gluons emitted outside the filtered jet region contribute to it. We are now going to explicitly calculate its distribution.

B.2 The variables of the calculation

The Higgs boson is taken to move along the x direction and the angular coordinates (θ, ϕ) are defined with respect to the Higgs direction (so that $\theta = 0$ corresponds to the Higgs direction and $\phi = 0$ to the y axis for instance). As it is very boosted, the b and $\bar{b}$ resulting from its decay should be close to the Higgs, i.e. with $\theta_{b,\bar{b}} \ll 1$. Due to angular ordering, so will be the major part of the perturbative radiation from $b\bar{b}$. To take this property into account, the angular coordinates (θ, ϕ) are slightly changed into a two-dimensional vector $\vec{\alpha}$:

$$\begin{aligned} \vec{\alpha} &= \theta(\cos\phi, \sin\phi)\,, \\ d^2\vec{\alpha} &= \theta d\theta d\phi\,. \end{aligned} \tag{B.3}$$

This vector is useful because of the property that, at small θ, one can express the angle θ_{ij} between 2 particles i and j as:

$$\theta_{ij} = |\vec{\alpha}_i - \vec{\alpha}_j|\,. \tag{B.4}$$

$\vec{R}_{b\bar{b}}$ is defined to be the vector from b to $\bar{b}$ in the $\vec{\alpha}$ plane (see fig. B.1). Even if $|\vec{\alpha}| < \mathcal{O}(1)$, the integrations over α_x and α_y are extended to ∞. By doing so, the error made on a $\mathcal{O}(1)$ result is of order $\mathcal{O}\left(R_{b\bar{b}}^2\right)$.

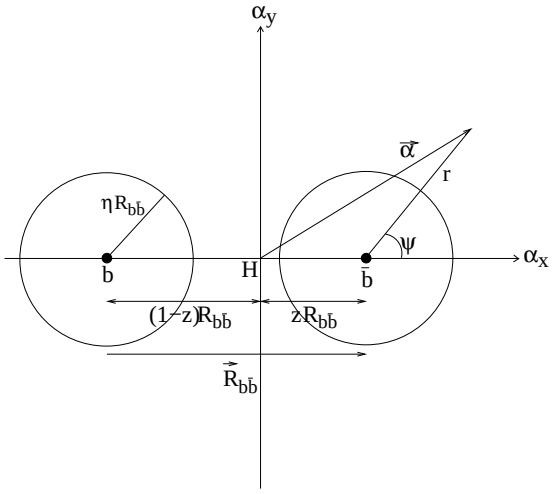

Figure B.1: The $\vec{\alpha}$ plane, with various variables used in the calculation and all along this study. In this figure, the b quark is supposed to carry a fraction z of the Higgs energy, and the centre of the frame coincides with the direction of the Higgs boson momentum.

B.3 Primary coefficients

Let us go back to the integral of eq. (4.9) and write it in the $\vec{\alpha}$ plane:

$$\begin{aligned} I(\Delta M) &= -\int_{\vec{k}\notin J_{b\bar{b}}} \frac{d^3\vec{k}}{(2\pi)^3 2|\vec{k}|}|M(k)|^2\Theta\left(\Delta M(k)-\Delta M\right)\,, \\ &= -\frac{\alpha_s C_F}{2\pi^2}\int_0^{p_{t_H}}\frac{dk_t}{k_t}\int_{\vec{\alpha}\notin J_{b\bar{b}}} d^2\vec{\alpha}\frac{2R_{bb}^2}{|\vec{\alpha}-z\vec{R}_{bb}|^2|\vec{\alpha}+(1-z)\vec{R}_{bb}|^2}\Theta\left(\Delta M(k)-\Delta M\right)\,. \end{aligned} \tag{B.5}$$

For $\Delta M(k) = M_H - M$ one easily finds

$$\Delta M(k) = k_t\frac{M_H}{p_{t_H}}A\left(\vec{\alpha}\right)\,, \tag{B.6}$$

with

$$A\left(\vec{\alpha}\right) = \frac{|\vec{\alpha}|^2 p_{t_H}^2}{2M_H^2}+\frac{1}{2}\,, \tag{B.7}$$

$$= \frac{|\vec{\alpha}|^2}{2z(1-z)R_{bb}^2}+\frac{1}{2}\,, \tag{B.8}$$

where we used eq. (2.7). With this expression, the integration over k_t is straightforward:

$$\begin{aligned} \int_0^{p_{t_H}}\frac{dk_t}{k_t}\Theta\left(\Delta M(k)-\Delta M\right) &= \int_{\frac{p_{t_H}}{M_H}\frac{\Delta M}{A(\vec{\alpha})}}^{p_{t_H}}\frac{dk_t}{k_t}\,, \\ &= \ln\frac{M_H}{\Delta M}+\ln A(\vec{\alpha})\,. \end{aligned} \tag{B.9}$$

Notice that $|\vec{\alpha}|\sim(1-z)R_{bb}$ or $|\vec{\alpha}|\sim zR_{bb}$, depending on whether the perturbative gluon emission is relatively close to b or $\bar{b}$ (due to the collinear divergence of QCD). Thus, given that a Higgs splitting is most of the time roughly symmetric ($z\sim 1/2$), this leads to $A\left(\vec{\alpha}\right)=\mathcal{O}(1)$. Therefore:

$$\ln A(\vec{\alpha}) \ll \ln\frac{M_H}{\Delta M}\,, \tag{B.10}$$

and the $\ln A(\vec{\alpha})$ term can be neglected in a leading-log calculation. One thus obtains:

$$I(\Delta M) = -\frac{\alpha_s C_F}{\pi}\ln\left(\frac{M_H}{\Delta M}\right)J(\eta)\,, \tag{B.11}$$

with $J(\eta)$ the remaining angular integral. Introducing the coordinates (r,ψ) defined in fig. B.1, $J(\eta)$ can be rewritten in the following form:[1]

$$\begin{aligned} J(\eta) = J_0(\eta) &= \frac{1}{\pi}\int_{\eta R_{bb}}^{+\infty}\frac{dr}{r}\int_{-\arccos(-\frac{R_{bb}}{2r})}^{\arccos(-\frac{R_{bb}}{2r})}d\psi\frac{2R_{bb}^2}{r^2+2rR_{bb}\cos\psi+R_{bb}^2} \quad \text{if} \quad \frac{1}{2}<\eta<1\,, \\ &= J_0\left(\frac{1}{2}\right)+\frac{1}{\pi}\int_{\eta R_{bb}}^{\frac{R_{bb}}{2}}\frac{dr}{r}\int_{-\pi}^{\pi}d\psi\frac{2R_{bb}^2}{r^2+2rR_{bb}\cos\psi+R_{bb}^2} \qquad \text{if} \quad \eta<\frac{1}{2}\,. \end{aligned} \tag{B.12}$$

[1] A simple shift of the $\vec{\alpha}$ coordinates gets rid of the z dependence, for instance $\vec{\alpha}' = \vec{\alpha}-\left(z-\frac{1}{2}\right)\vec{R}_{b\bar{b}}$

Performing the ψ integration and the r one (for $\eta < 1/2$), one arrives at the formulae (4.11,4.12), where all the R_{bb} dependence is cancelled.

One remark: if $\eta > 1$, the b and $\bar{b}$ quarks cluster together, and the result then depends on the z fraction of the splitting. For instance, if $\eta > 2$, $J(\eta)$ can now be written:[2]

$$J(\eta, z) = \ln\left(\frac{(\eta^2 + z(1-z))^2}{(\eta^2 - z^2)(\eta^2 - (1-z)^2)}\right). \tag{B.13}$$

B.4 Non-Global coefficients

The starting point here is eq. (4.22) for I_2^{NG}:

$$I_2^{NG}(\Delta M) = -\int dk_1 dk_2 (4\pi\alpha_s)^2 \Theta(E_1 - E_2)\Theta(k_1 \in J_{b\bar{b}})\Theta(k_2 \notin J_{b\bar{b}})W_2\Theta(\Delta M(k_2) - \Delta M)\,.$$

In the same way as the primary case, using the $\vec{\alpha}$ plane and integrating over the energies of the 2 gluons, one arrives at:

$$I_2^{NG}(\Delta M) = \frac{1}{2}C_F C_A \left(\frac{\alpha_s}{\pi}\log\left(\frac{M_H}{\Delta M}\right)\right)^2 S_2(\eta)\,, \tag{B.14}$$

with

$$S_2(\eta) = -\frac{R_{bb}^2}{2\pi^2}\int_{\vec{\alpha}_1 \in J_{b\bar{b}}} d^2\vec{\alpha}_1 \int_{\vec{\alpha}_2 \notin J_{b\bar{b}}} d^2\vec{\alpha}_2 \left(-\frac{R_{bb}^2}{|\vec{\alpha}_1 - z\vec{R}_{bb}|^2||\vec{\alpha}_1 + (1-z)\vec{R}_{bb}|^2|\vec{\alpha}_2 - z\vec{R}_{bb}|^2||\vec{\alpha}_2 + (1-z)\vec{R}_{bb}|^2}\right.$$
$$\left. + \frac{1}{|\vec{\alpha}_1 + (1-z)\vec{R}_{bb}|^2|\vec{\alpha}_1 - \vec{\alpha}_2|^2|\vec{\alpha}_2 - z\vec{R}_{bb}|^2} + \frac{1}{|\vec{\alpha}_1 - z\vec{R}_{bb}|^2|\vec{\alpha}_1 - \vec{\alpha}_2|^2|\vec{\alpha}_2 + (1-z)\vec{R}_{bb}|^2}\right). \tag{B.15}$$

In all this part, $\eta < 1/2$ is assumed. To deal with this integral, the frame is centred around $\bar{b}$ for instance, and 2 quantities are computed: S_{tot} where gluon 1 is in the jet region $J_{\bar{b}}$ around $\bar{b}$ and gluon 2 covers the whole phase space except $J_{\bar{b}}$, from which is subtracted S_{int} where gluon 2 covers J_b, the jet region around b (fig. B.2). Therefore:

$$S_2(\eta) = 2(S_{tot}(\eta) - S_{int}(\eta))\,, \tag{B.16}$$

where the factor 2 is for the symmetric case (gluon 1 in J_b).

B.4.1 Calculation of S_{tot}

Using the variables $\left(u = \frac{r}{\eta R_{bb}}, \psi\right)$ (fig. B.1), S_{tot} can be written

$$S_{tot}(\eta) = -\frac{1}{2\pi^2}\int_0^1 u_1 du_1 \int_1^{+\infty} u_2 du_2 \int_0^{2\pi} d\psi_1 \int_0^{2\pi} d\psi_2 \Big($$
$$- \frac{1}{u_1^2 u_2^2 (1 + 2\eta u_1\cos\psi_1 + \eta^2 u_1^2)(1 + 2\eta u_2\cos\psi_2 + \eta^2 u_2^2)}$$
$$+ \frac{1}{u_1^2(1 + 2\eta u_2\cos\psi_2 + \eta^2 u_2^2)(u_1^2 - 2u_1u_2\cos(\psi_1 - \psi_2) + u_2^2)}$$
$$+ \frac{1}{u_2^2(1 + 2\eta u_1\cos\psi_1 + \eta^2 u_1^2)(u_1^2 - 2u_1u_2\cos(\psi_1 - \psi_2) + u_2^2)}\Big)\,. \tag{B.17}$$

[2] the intermediate case $1 < \eta < 2$ has a more complicated phase space integration and is not presented here.

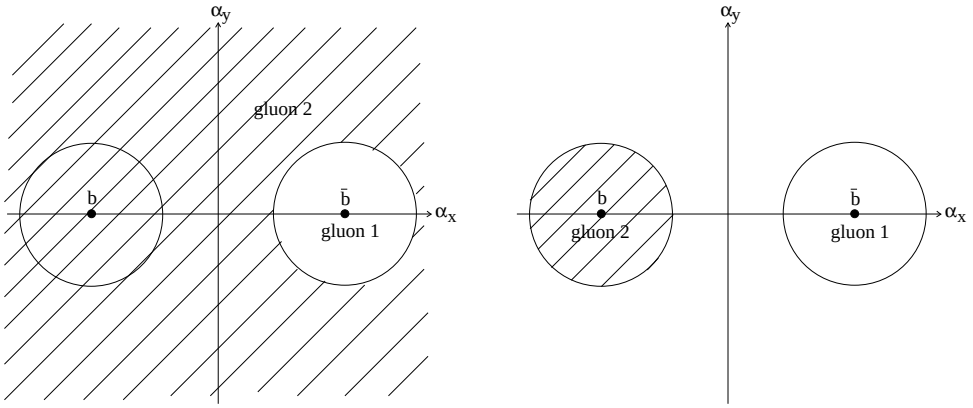

(a) S_{tot} (b) S_{int}

Figure B.2: regions of integration (dashed region) for gluon 2 when computing S_{tot} (left) and S_{int} (right).

Doing the angular integrations, one arrives at:

$$S_{tot}(\eta) = -4\int_0^1 du_1 \frac{u_1}{1-\eta^2 u_1^2}\int_1^{\frac{1}{\eta}} \frac{du_2}{u_2}\frac{1}{u_2^2-u_1^2}\,. \tag{B.18}$$

2 remarks about this result:

1. The first and second terms have divergences in $u_1 = 0$ and $u_2 = \frac{1}{\eta}$, so respectively when gluon 1 is collinear to $\bar{b}$ and gluon 2 is collinear to b, but they cancel when adding these terms.

2. The part of the integral corresponding to $u_2 > \frac{1}{\eta}$, i.e. $r_2 > R_{bb}$, is null, which can be simply interpreted as a manifestation of the angular ordering.

Performing this integration with Maple for instance gives the following result:

$$\begin{aligned} S_{tot}(\eta) = \frac{\pi^2}{2} - \frac{3}{2}\ln^2(1-\eta) + \ln(2\eta)\ln(1-\eta) - \ln 2\ln(1+\eta) - \\ - 2\Re\left(\mathrm{dilog}\left(\frac{\eta}{\eta-1}\right)\right) - 2\mathrm{Li}_2(1-\eta) - \mathrm{Li}_2\left(\frac{1}{1+\eta}\right) + \mathrm{Li}_2\left(-\eta\right) + \mathrm{Li}_2\left(\frac{1-\eta}{1+\eta}\right) - \mathrm{Li}_2\left(\frac{-2\eta}{1-\eta}\right)\,, \end{aligned} \tag{B.19}$$

where

$$\mathrm{dilog}(x) = \int_1^x dt \frac{\ln t}{1-t}\,, \tag{B.20}$$

$$\mathrm{Li}_2(x) = \int_x^0 dt \frac{\ln(1-t)}{t}\,. \tag{B.21}$$

This is rather complicated, but that expression can be greatly simplified using the relations:

$$\forall x > 0 \ , \ \mathrm{dilog}(x) = \mathrm{Li}_2(1-x)\,, \tag{B.22}$$

$$\mathrm{dilog}(-x) = \frac{\pi^2}{3} - \frac{1}{2}\ln^2(1+x) - \mathrm{Li}_2\left(\frac{1}{1+x}\right) - i\pi\ln(1+x)\,, \tag{B.23}$$

$$\forall x \text{ with } 0 < x < 1 \ , \ \mathrm{Li}_2(x) + \mathrm{Li}_2(1-x) = \frac{\pi^2}{6} - \ln(x)\ln(1-x)\,, \tag{B.24}$$

$$\mathrm{Li}_2(1-x) + \mathrm{Li}_2(1-1/x) = -\frac{1}{2}\ln^2 x\,. \tag{B.25}$$

The final answer is then:

$$S_{tot}(\eta) = -\frac{\pi^2}{6}\,. \tag{B.26}$$

The remarkable point to notice is of course that S_{tot} does not depend on η. But no simple explanation was found to interpret this result.

B.4.2 Calculation of S_{int}

S_{int} must now be subtracted from S_{tot}. The computation is similar to the previous one and is not detailed here. However, contrary to S_{tot}, a simple analytical result was not obtained, only the following expansion:

$$S_{int}(\eta) = -4\int_0^1 \frac{du_1}{u_1}\int_0^1 \frac{du_2}{u_2}\left(\frac{1}{\sqrt{(1-\eta^2(u_1^2+u_2^2))^2 - 4\eta^4 u_1^2 u_2^2}} - \frac{1}{1-\eta^2(u_1^2+u_2^2)}\right)\,, \tag{B.27}$$

$$= -2\eta^4 - 6\eta^6 - \frac{31}{2}\eta^8 - 40\eta^{10} - \frac{1921}{18}\eta^{12} - \frac{889}{3}\eta^{14} - \frac{20589}{24}\eta^{16} - \frac{7643}{3}\eta^{18} + \mathcal{O}(\eta^{20})\,. \tag{B.28}$$

Using eq. (B.16) with the 2 previous results, one arrives at the expression eq. (4.26).

Appendix C

Analytical considerations on the dependence of the results on z and f

C.1 Dependence on z

It is interesting to understand analytically how η_{opt} evolves when the decay of the Higgs boson occurs with a z fraction different from 1/2. In fact, we obtain the same result as eqs. (4.74,4.75) up to a modification of the constant C_{UE} (more generally, we have to modify the coefficients c_σ, $c_{\delta\rho}$ and c_Σ, see eqs. (4.64-4.67)). The starting point is eq. (4.81) generalised to any value of n:

$$\Delta M \simeq \frac{M_H}{2p_{t_H}} \sum_{i=1}^{n} a_i(z) \rho A_i \,, \tag{C.1}$$

where $a_i(z)$ is either $\frac{1}{z}$ or $\frac{1}{1-z}$ depending on whether subjet i is in the J_1 region (around the b quark) or in the J_2 region (around the $\bar{b}$ quark). This is because the UE/PU particles tend to cluster around the perturbative radiation, which itself is emitted close to b and $\bar{b}$. We call a "configuration" the set of all the coefficients $a_i(z)$.

The result on the fluctuations depends on which ones are considered. Let us start with the fluctuations originating from the σ and Σ terms. In this case the ρA_i terms vary independently, thus leading to a contribution to δM_{UE} similar to that of eq. (4.82) for $n = 2$:

$$\delta M^2_{UE,\sigma,\Sigma,\{a_i\}} = 4 \left(\frac{M_H \rho_{UE}}{2p_{t_H}} \right)^2 \sum_{i=1}^{n} a_i(z)^2 \delta^2_{i,\sigma,\Sigma} \,, \tag{C.2}$$

with (see eq. (4.83)):

$$\begin{aligned} \delta^2_{i,\sigma,\Sigma} &= c_\sigma^2 e^{-2L} + c_\Sigma^2 e^{-4L} \,, \\ &\equiv \delta^2_{\sigma,\Sigma} \,. \end{aligned} \tag{C.3}$$

The coefficients c_σ and c_Σ are still computed for $n = 1$ in this formula. But eq. (C.2) is only valid for a given configuration $\{a_i\}$. We thus have to average over all the 2^{n-2} possible

configurations (the b and $\bar{b}$ subjets are fixed). As the perturbative radiation pattern does not depend on z (for z not too small), each configuration arises with the same probability. Therefore, if k is the number of subjets in the J_1 region and $n-2-k$ the number of subjets in the J_2 region apart from the b and $\bar{b}$ subjets, we obtain:

$$\delta M^2_{UE,\sigma,\Sigma} = 4\left(\frac{M_H \rho_{UE}}{2p_{t_H}}\right)^2 \frac{1}{2^{n-2}} \sum_{k=0}^{n-2} \binom{n-2}{k} \left(\frac{k+1}{z^2} + \frac{n-1-k}{(1-z)^2}\right) \delta^2_{\sigma,\Sigma}\,, \tag{C.4}$$

$$= 4\left(\frac{M_H \rho_{UE}}{p_{t_H}}\right)^2 \frac{n}{8} \frac{1-2z(1-z)}{z^2(1-z)^2} \delta^2_{\sigma,\Sigma}\,. \tag{C.5}$$

We can follow a similar reasoning for the $\delta\rho$ fluctuations, except that the ρA_i terms in eq. (C.1) vary the same way from one event to the next. Therefore, for a given configuration $\{a_i\}$, one can deduce the following contribution to δM_{UE}:

$$\delta M^2_{UE,\delta\rho,\{a_i\}} = 4\left(\frac{M_H \rho_{UE}}{2p_{t_H}}\right)^2 \left(\sum_{i=1}^{n} a_i(z)\right)^2 \delta^2_{\delta\rho}\,, \tag{C.6}$$

with $\delta_{\delta\rho}$ given by eq. (4.85). As before, we have to average this result over all the 2^{n-2} possible configurations, leading to:

$$\delta M^2_{UE,\delta\rho} = 4\left(\frac{M_H \rho_{UE}}{2p_{t_H}}\right)^2 \frac{1}{2^{n-2}} \sum_{k=0}^{n-2} \binom{n-2}{k} \left(\frac{k+1}{z} + \frac{n-1-k}{1-z}\right)^2 \delta^2_{\delta\rho}\,, \tag{C.7}$$

$$= 4\left(\frac{M_H \rho_{UE}}{p_{t_H}}\right)^2 \frac{n^2 + (n-2)(1-2z)^2}{16z^2(1-z)^2} \delta^2_{\delta\rho}\,. \tag{C.8}$$

One can absorb all the dependence of the resulting δM^2_{UE} in n and z into the coefficients c_σ, $c_{\delta\rho}$ and c_Σ, and define new coefficients c' such that

$$\delta M_{UE} = 2\sqrt{c'^2_\sigma \eta^2 + c'^2_{\delta\rho}\eta^4 + c'^2_\Sigma \eta^4} \frac{M_H \rho_{UE}}{p_{t_H}}\,, \tag{C.9}$$

with

$$c'_\sigma(n, N_{PU}, R_{bb}, z) \simeq 0.6\sqrt{\pi}\sqrt{n} \frac{\sqrt{1-2z(1-z)}}{2\sqrt{2}z(1-z)} R_{bb} \sqrt{1 + \frac{N_{PU}}{4}}\,, \tag{C.10}$$

$$c'_{\delta\rho}(n, N_{PU}, R_{bb}, z) \simeq 0.8\pi \frac{\sqrt{n^2 + (n-2)(1-2z)^2}}{4z(1-z)} R^2_{bb} \sqrt{1 + \frac{N_{PU}}{4}}\,, \tag{C.11}$$

$$c'_\Sigma(n, N_{PU}, R_{bb}, z) \simeq 0.26\pi\sqrt{n} \frac{\sqrt{1-2z(1-z)}}{2\sqrt{2}z(1-z)} R^2_{bb} \left(1 + \frac{N_{PU}}{4}\right)\,. \tag{C.12}$$

With these results in hand, we can easily generalise eq. (4.74) for any value z of the Higgs splitting. One only has to modify the value of C_{UE}. For instance, the curves in fig. 4.12(a) were obtained using eqs. (4.71−4.75) with:

$$C_{UE}(n, N_{PU}, z) = 1.6\pi \frac{\sqrt{n^2 + (n-2)(1-2z)^2}}{4z(1-z)} \sqrt{1 + \frac{N_{PU}}{4}}\,, \tag{C.13}$$

where we just use the dominant $c'_{\delta\rho}$ term.

There is also another source of fluctuations that we haven't accounted for so far. Indeed, even if the values of ρ and of the jets area were constant, we should consider the fact that the filtered subjets can be either in the J_1 or in the J_2 region. The calculation of its effect is similar to that of the fluctuations in σ, $\delta\rho$ and Σ. Its contribution on δM^2_{UE} can be written:

$$\delta M^2_{UE,\text{other}} = 4\left(\frac{M_H \rho_{UE}}{p_{t_H}}\right)^2 c'^2_{\text{other}} \eta^4 \,, \tag{C.14}$$

with

$$c'_{\text{other}}(n, N_{PU}, R_{bb}, z) = \pi \frac{\sqrt{n-2}|1-2z|}{4z(1-z)} R^2_{bb}\left(1 + \frac{N_{PU}}{4}\right) . \tag{C.15}$$

But we checked that its effect on δM^2_{UE} is negligible compared to that from the dominant $\delta\rho$ fluctuation,[1] and therefore we did not include it.

C.2 Comments on the uncertainty due to the choice of f

Let us return to the observation of section 4.3.4 that $\eta_{sat}(n, f)$ is almost independent of f for $n = 3$. To understand why, we have to estimate $t_{sat}(f)$ and $C_{PT}(3, f)$ (cf eq. (4.45)). t_{sat} can be deduced from the equation:

$$\Sigma^{(n)}(\eta = 1, t_{sat}) = f \,, \tag{C.16}$$

for any value of n, as t_{sat} only depends on f (see for instance figs. (4.6,4.7(a))). To be simple, we can use the function $\Sigma^{(2)}$ which was widely studied in this paper. Unfortunately we cannot take the primary emission result eq. (4.10) because the non-global part becomes important when $\eta = 1$. However, as an approximation, we can numerically compute the second order coefficient $a_2 \simeq -3$ of $\Sigma^{(2)}(\eta = 1, t)$ and solve:

$$1 - J(1)N_c t_{sat} + a_2 t^2_{sat} \simeq f \,, \tag{C.17}$$

which simply leads to

$$t_{sat}(f) \simeq \frac{J(1)N_c - \sqrt{J(1)^2 N_c^2 - 4a_2(1-f)}}{2a_2} \,. \tag{C.18}$$

This expression can be shown numerically to give $t_{sat}(f)$ with a precision better than 1% for $f \in [0.5, 0.8]$. $C_{PT}(3, f)$ is harder to evaluate. One must solve

$$\Sigma^{(3)}(L, t) = f \,, \tag{C.19}$$

in the limit of large L. Using eq. (4.29), which is valid in this limit, and defining the function h such that $h(4N_c Lt) = \Sigma^{(3)}(L, t) - f$, we can use Newton's method with only one iteration

[1] This effect is strictly null when $z = 1/2$. When $z = 0.2$, we obtain:

$$\delta M^2_{UE,\delta\rho} \simeq 16.6\, \delta M^2_{UE,\text{other}} \,,$$

for $p_{t_H} = 200$ GeV and $N_{PU} = 0$.

on h, evaluated numerically for $4N_cLt = 1$,[2] to solve approximately eq. (C.19):

$$\begin{aligned} 4N_cLt &\simeq 1 - \frac{h(1)}{h'(1)}\,, \\ &\simeq 2.543 - 2.334f\,, \\ &\equiv 4N_cC_{PT}(3,f)\,, \end{aligned} \tag{C.20}$$

which gives $C_{PT}(3,f)$ within a few %. Therefore, eq. (4.45) leads to

$$\begin{aligned} \eta_{sat}(3,f) &= e^{-\frac{C_{PT}(3,f)}{t_{sat}}}\,, \\ &\simeq e^{-0.58}\left(1 + 0.044\left(f - \frac{1}{2}\right) + \mathcal{O}\left(\left(f - \frac{1}{2}\right)^2\right)\right)\,, \end{aligned} \tag{C.21}$$

which is eq. (4.91).

To be complete, the same analysis can be done when $n = 2$, using eq. (4.42) for $C_{PT}(2,f)$, to obtain $\eta_{sat}(2,f)$. We will just mention that

$$\lim_{f\to 1} \eta_{sat}(2,f) = e^{-\frac{J(1)}{4}} \simeq 0.85\,. \tag{C.22}$$

[2]Starting from $4N_cLt \sim 1$ quickly converges to the true solution.

Appendix D

Numerical non-global calculations

This appendix is intended to show how one can construct an all-orders program that resums the leading non-global logarithms in the large-N_c limit (see section 1.2.5) and a fixed-order program which gives the coefficients of the first few leading logarithms from the all-orders expansion, still in the large-N_c approximation.

D.1 The matrix elements squared in the large-N_c limit

The basic thing to know in resummation is the matrix element squared $M_n(k_1, \ldots, k_n)$ to emit n energy-ordered gluons $E_1 \gg E_2 \gg \ldots \gg E_n$ from the dipole $b\bar{b}$. Unfortunately, the colour structure is difficult to deal with in general and one usually resorts to the large-N_c approximation to calculate the matrix elements at high orders.

D.1.1 Case of n real gluons

In the case of n real gluons, the result was derived a long time ago and can be written as (see for instance [40, 212]):

$$M_n(k_1 \text{ real}, \ldots, k_n \text{ real}) = \frac{(4\pi\alpha_s N_c)^n}{E_1^2 \ldots E_n^2} \left(\sum_{\Pi_n} \frac{(b\bar{b})}{(bi_1)(i_1 i_2) \ldots (i_{n-1} i_n)(i_n \bar{b})} + \mathcal{O}\left(\frac{1}{N_c^2}\right) \right), \tag{D.1}$$

where the sum is over all the $n!$ permutations Π_n of $\{1, \ldots, n\}$, and where we define

$$(ij) \equiv 1 - \cos\theta_{ij}\,. \tag{D.2}$$

Notice that eq. (D.1) is invariant over the permutation of the n gluons, so that it is valid for any strong energy-ordering of the n gluons. One can rewrite it in a different way that

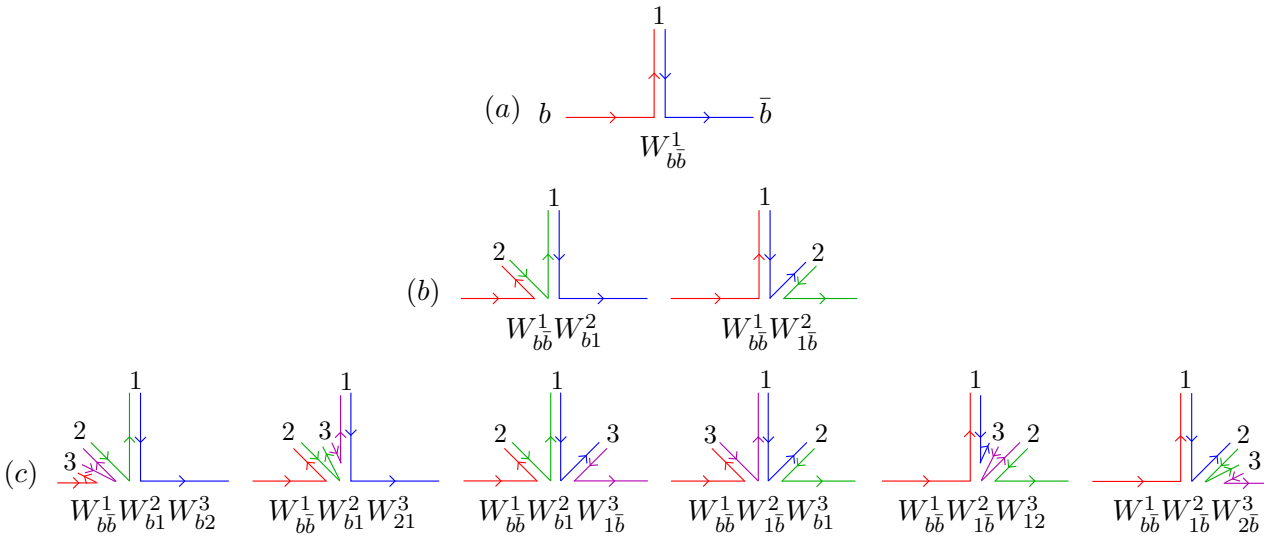

Figure D.1: Real gluon-emission diagrams in the large-N_c limit and their corresponding weight (products of some W_{ij}^k): (a) gluon 1 emitted from the $(b\bar{b})$ dipole; (b) gluon 2 emitted from the dipoles $(b1)$ and $(1\bar{b})$ respectively (from left to right); (c) gluon 3 emitted from the dipoles $(b2)$, (21), $(1\bar{b})$, $(b1)$, (12) and $(2\bar{b})$ respectively (from left to right).

will be more convenient to deal with. For instance, the 3 first orders are rewritten as:

$$M_1(k_1) = \frac{4\pi\alpha_s N_c}{E_1^2}\frac{(b\bar{b})}{(b1)(1\bar{b})}\,, \tag{D.3}$$

$$M_2(k_1,k_2) = \frac{(4\pi\alpha_s N_c)^2}{E_1^2E_2^2}\frac{(b\bar{b})}{(b1)(1\bar{b})}\left(\frac{(b1)}{(b2)(21)}+\frac{(1\bar{b})}{(12)(2\bar{b})}\right)\,, \tag{D.4}$$

$$\begin{aligned} M_3(k_1,k_2,k_3) = \frac{(4\pi\alpha_s N_c)^3}{E_1^2E_2^2E_3^2}\frac{(b\bar{b})}{(b1)(1\bar{b})}\Bigg[&\frac{(b1)}{(b2)(21)}\left(\frac{(b2)}{(b3)(32)}+\frac{(21)}{(23)(31)}+\frac{(1\bar{b})}{(13)(3\bar{b})}\right)+\\ &+\frac{(1\bar{b})}{(12)(2\bar{b})}\left(\frac{(b1)}{(b3)(31)}+\frac{(12)}{(13)(32)}+\frac{(2\bar{b})}{(23)(3\bar{b})}\right)\Bigg]\,. \end{aligned} \tag{D.5}$$

Eq. (D.4) is the same as eq. (4.14) in the large-N_c limit ($C_F = N_c/2$ and $C_A = N_c$). The emission of gluon 2 from the $(b\bar{b})$ dipole is suppressed by powers of $1/N_c$ so that we do not consider it at this accuracy.

This rewritting explicitly reveals the dipole structure of the emissions in the large-N_c limit when they are strongly ordered $E_1 \gg \ldots \gg E_n$: 1 is emitted from the dipole $b\bar{b}$, 2 is emitted from the dipoles $(b1)$ and $(1\bar{b})$, 3 is emitted from the dipoles $(b2)$, $(21) = (12)$, $(1\bar{b})$, $(b1)$ and $(2\bar{b})$. And so on for more gluons. Generally, each time a gluon k is emitted from a dipole (ij), this gives a factor W_{ij}^k with:

$$W_{ij}^k = \frac{4\pi\alpha_s N_c}{E_k^2}\frac{(ij)}{(ik)(kj)}\,. \tag{D.6}$$

In the large-N_c limit, we can draw a diagrammatic picture of these emissions (fig. D.1) in

terms of colour flows which is very easy to generalize at higher orders and which will reveal itself useful when examining the virtual corrections in the next section.

Line (a) in fig. D.1 gives simply $W^1_{b\bar{b}}$ which is eq. (D.3). The sum of the diagrams in line (b) gives $W^1_{b\bar{b}}\left(W^2_{b1}+W^2_{1\bar{b}}\right)$, which is simply eq. (D.4). This is similar for line (c). Note that, in the large-N_c limit, a gluon can only be emitted from *colour connected* partons, forming a dipole. In diagram (a) of fig. D.1 for instance, the gluon 1 is colour connected to the quark b and the anti-quark $\bar{b}$, but b and $\bar{b}$ are not connected to each other.

D.1.2 Virtual gluons emission

In the previous section, we saw how to compute the matrix element squared for the emission of n real gluons in terms of dipoles. We are now going to see how one can compute the matrix elements in the large-N_c limit when some gluons become virtual. Here, we simply aim to understand intuitively how this computation can be implemented.

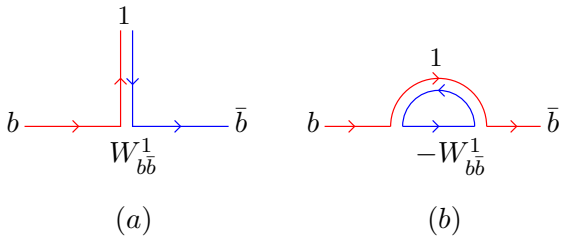

Figure D.2: Real and virtual diagrams at order α_s and their corresponding weight.

First we start with the one-gluon emission (fig. D.2). We know that the divergences of the virtual and real diagrams have to cancel exactly. Therefore, in the soft limit, the virtual part is simply the opposite of the real part. The $\mathcal{O}(\alpha_s)$ contribution $I_1(\tau)$ to the distribution of a generic observable τ (which is 0 if there is no emission) can thus be written as:[1]

$$I_1(\tau) = \int dk_1\, W^1_{b\bar{b}}\Big(\Theta(\tau-\tau(k_1))-1\Big)\,, \tag{D.7}$$

which is exactly eq. (4.9).

We now examine the virtual diagrams of the two-gluon emission case with $E_1 \gg E_2$. There are two possible configurations:

1. If gluon 1 is real, then we have to "emit" a virtual gluon 2 from the two dipoles $(b1)$ and $(1\bar{b})$ of diagram (a) in fig. D.2, which leads to an additional factor $-W^2_{b1}$ and $-W^2_{1\bar{b}}$ respectively, the minus sign accounting for a virtual emission (fig. D.3(b)).

2. If gluon 1 is virtual, then we have to emit a gluon 2 from the configuration (b) in fig. D.2. And this emission can only occur from the $(b\bar{b})$ dipole in red. Therefore, a real or virtual emission of gluon 2 from this configuration leads to an additional factor $\pm W^2_{b\bar{b}}$ (fig. D.3(c)).

[1] As usual:

$$dk = \frac{d^3\vec{k}}{(2\pi)^3 2|\vec{k}|}\,.$$

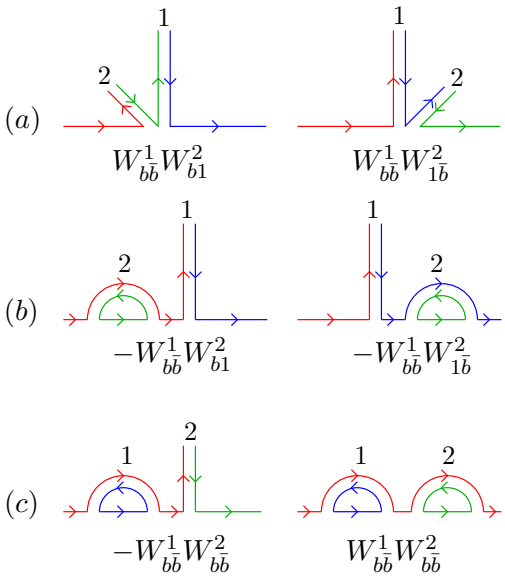

Figure D.3: (a) The two diagrams for a real emission of gluon 1 followed by a real emission of gluon 2; (b) The two diagrams for a real emission of gluon 1 followed by a virtual emission of gluon 2; (c) The two diagrams for a virtual emission of gluon 1 followed by a real or virtual emission of gluon 2. All these diagrams are given with their corresponding weight.

Therefore, the $\mathcal{O}(\alpha_s^2)$ contribution $I_2(\tau)$ to the distribution of τ in the large-N_c limit is expressed as:

$$I_2(\tau) = \int dk_1 dk_2\, \Theta(E_1 - E_2) W^1_{b\bar{b}} \Big((W^2_{b1} + W^2_{1\bar{b}}) \left(\Theta(\tau - \tau(k_1,k_2)) - \Theta(\tau - \tau(k_1))\right) - \\ - W^2_{b\bar{b}} \left(\Theta(\tau - \tau(k_2)) - 1\right) \Big), \tag{D.8}$$

where $\tau(k_i)$ means that k_i is real and may contribute to the observable τ, but not necessarily, especially if τ is non-global (one may have to separate the integration into different phase space regions as was done in eq. (4.21)).[2]

This approach can be easily generalized to higher orders. A gluon number k (real or virtual) is emitted coherently from the set of all the previous *real* gluons. For each pair (ij) of real colour connected partons, inserting the gluon k costs a factor W^k_{ij}. As an example, let us write explicitly the $\mathcal{O}(\alpha_s^3)$ contribution $I_3(\tau)$ to the distribution of τ in the large-N_c limit:

$$I_3(\tau) = \int dk_1 dk_2 dk_3\, \Theta(E_1 - E_2)\Theta(E_2 - E_3) W^1_{b\bar{b}} \Big[\\ W^2_{b1}\Big(W^3_{b2}(\Theta_{123} - \Theta_{12}) + W^3_{21}(\Theta_{123} - \Theta_{12}) + W^3_{1\bar{b}}(\Theta_{123} - \Theta_{12} - \Theta_{13} + \Theta_1) - W^3_{b1}(\Theta_{13} - \Theta_1)\Big) \\ + W^2_{1\bar{b}}\Big(W_{b1}(\Theta_{123} - \Theta_{12} - \Theta_{13} + \Theta_1) + W^3_{12}(\Theta_{123} - \Theta_{12}) + W^3_{2\bar{b}}(\Theta_{123} - \Theta_{12}) - W^3_{1\bar{b}}(\Theta_{13} - \Theta_1)\Big) \\ - W^2_{b\bar{b}}\Big(W^3_{b2}(\Theta_{23} - \Theta_2) + W^3_{2\bar{b}}(\Theta_{23} - \Theta_2) - W^3_{b\bar{b}}(\Theta_3 - 1)\Big)\Big], \tag{D.9}$$

[2] Eq. (D.8) is the large-N_c limit approximation of eq. (4.21). One simply notices that $(4\pi\alpha_s N_c)^2(W_1 + W_2)$ in eq. (4.21) equals to $W^1_{b\bar{b}}(W^2_{b1} + W^2_{1\bar{b}})$ in eq. (D.8) and that $(4\pi\alpha_s N_c)^2 W_1$ equals to $W^1_{b\bar{b}}W^2_{b\bar{b}}$ in the large-N_c limit.

where

$$\Theta_{i_1,\ldots,i_n} \equiv \Theta\left(\tau - \tau(k_{i_1},\ldots,k_{i_n})\right) . \tag{D.10}$$

The W^2_{b1} and $W^2_{1\bar{b}}$ terms (second and third lines) correspond to gluon 1 being real, while the $-W^2_{b\bar{b}}$ term (last line) corresponds to gluon 1 being virtual. In the same way, one separates in each line the case where gluon 2 is real and where it is virtual (idem for gluon 3).

D.2 The dipole's frame

Once the matrix elements are known, one has to carry out the integrations. In general, for a gluon k emitted from a dipole (ij), one will have to face integrals of the form:

$$\begin{aligned} I_{ij} &= \int \frac{d^3\vec{k}}{(2\pi)^3 2|\vec{k}|} W^k_{ij} \,, \\ &= \frac{\alpha_s N_c}{2\pi} \int \frac{d|\vec{k}|}{|\vec{k}|} \int \sin\theta d\theta \frac{d\phi}{2\pi} \frac{(ij)}{(ik)(kj)} \,, \end{aligned} \tag{D.11}$$

cf eqs. (D.2,D.6). Numerically, this kind of integration suffers from instabilities due to the soft and collinear divergences. Here, we are essentially interested in the angular integrations because they are at the heart of the non-global property of the observable. To deal with them, it is convenient to introduce the dipole (ij)'s frame, in which the momentum k can be written with respect to the momenta p_i and p_j of partons i and j:

$$k = \frac{k_t}{\sqrt{2(u_i.u_j)}} \left(e^{-y} u_i + e^{y} u_j\right) + k_t \cos\phi \, u_{t_1} + k_t \sin\phi \, u_{t_2} \,, \tag{D.12}$$

where the 4-vectors u_i, u_j, u_{t_1} and u_{t_2} can be expressed as:

$$u_i = \frac{p_i}{E_i} = \left(1, \frac{\vec{p}_i}{|\vec{p}_i|}\right) = (1, \vec{u}_i) \text{ (similarly for } u_j) \,, \tag{D.13}$$

$$u_{t_1} = \left(\sqrt{\frac{1+\vec{u}_i.\vec{u}_j}{1-\vec{u}_i.\vec{u}_j}}, \frac{1}{\sqrt{1-(\vec{u}_i.\vec{u}_j)^2}}(\vec{u}_i + \vec{u}_j)\right) \,, \tag{D.14}$$

$$u_{t_2} = \left(0, \frac{\vec{u}_i \wedge \vec{u}_j}{|\vec{u}_i \wedge \vec{u}_j|}\right) . \tag{D.15}$$

One can easily check the following properties:

$$k^2 = 0 \,, \tag{D.16}$$

$$u_i^2 = u_j^2 = 0 \,, \tag{D.17}$$

$$u_{t_1}^2 = u_{t_2}^2 = -1 \,, \tag{D.18}$$

$$u_i.u_{t_1} = u_j.u_{t_1} = 0 \,, \tag{D.19}$$

$$u_i.u_{t_2} = u_j.u_{t_2} = 0 \,. \tag{D.20}$$

In terms of the variables (k_t, y, ϕ), one also has:

$$|\vec{k}| = \frac{k_t}{\sqrt{u_i.u_j}} \left(\sqrt{2} \cosh y + \sqrt{2 - u_i.u_j} \cos\phi \right) , \tag{D.21}$$

$$(ik) = (ij) \frac{e^y}{2\cosh y + \sqrt{2}\sqrt{2 - u_i.u_j}\cos\phi} , \tag{D.22}$$

$$(kj) = (ij) \frac{e^{-y}}{2\cosh y + \sqrt{2}\sqrt{2 - u_i.u_j}\cos\phi} , \tag{D.23}$$

$$(ik) = (kj) e^{2y} , \tag{D.24}$$

where we recall that $(ij) = 1 - \cos\theta_{ij} = u_i.u_j$. As a cross-check, one can compute the rapidity y for $\phi = 0$ as a function of the angle θ between k and j, and θ_{ij}:

$$y = -\ln \left(\frac{\sin\frac{\theta}{2}}{\sin\left(\frac{\theta_{ij}-\theta}{2}\right)} \right) , \tag{D.25}$$

which corresponds to the usual formula $y = -\ln\tan\frac{\theta}{2}$ when $\theta_{ij} = \pi$, i.e. in the dipole's center of mass frame.

Now, returning to the integral (D.11), one can express the integration in terms of the variables (k_t, y, ϕ):

$$\frac{d^3\vec{k}}{|\vec{k}|} = k_t dk_t \, dy \, d\phi \, . \tag{D.26}$$

This leads to the following remarkable property:

$$\begin{aligned} \frac{d|\vec{k}|}{|\vec{k}|} \sin\theta \, d\theta \, d\phi \, \frac{(ij)}{(ik)(kj)} &= \frac{k_t dk_t}{|\vec{k}|^2} \, dy \, d\phi \, \frac{(ij)}{(ik)^2} e^{2y} , \\ &= \frac{dk_t}{k_t} \, dy \, d\phi \, \frac{(ij)^2}{(ik)^2} \frac{e^{2y}}{\left(\sqrt{2}\cosh y + \sqrt{2 - u_i.u_j}\cos\phi\right)^2} , \\ &= 2\frac{dk_t}{k_t} \, dy \, d\phi \, , \end{aligned} \tag{D.27}$$

so that the angular integration is strictly uniform in the (k_t, y, ϕ) variables, and is therefore easier to deal with numerically. The angular divergence when k is collinear to parton i or j is shifted to the integration on y, which runs from $-\infty$ to ∞ and has to be regularized via a cut-off y_{max}.

D.3 Monte-Carlo programs for non-global calculations

D.3.1 Fixed-order program

Given a dimensionless observable τ, one wants to compute the first few coefficients c_n of the expansion of its distribution $\Sigma(\tau)$:

$$\Sigma(\tau) = \sum_{n=0}^{\infty} c_n t^n \, , \tag{D.28}$$

where t is given for instance in eq. (4.31), or, in a fixed coupling framework, by:

$$t = \frac{\alpha_s}{2\pi} \ln \frac{1}{\tau} \,. \tag{D.29}$$

Building a fixed-order program simply means computing the integrals given in eqs .(D.7,D.8,D.9) and similarly for higher orders. In this section, we give the way it was constructed to produce the results shown in appendix E, though it is certainly possible to find a more efficient method. We call D_k the dipole (ij) that emitted the gluon number k (for instance D_1 always equals $(q\bar{q})$), and we define v_k to be the virtuality of gluon k (v_k is either "real" or "virtual"). We call a *dipole configuration* the knowledge of all the couples (D_k, v_k) for $k = 1, \ldots, n$. The complexity of the fixed-order program grows like $\mathcal{O}(n!)$, which roughly corresponds to the number of dipole configurations when there are n gluons in the final state. In practice, it was found too hard to go beyond $n = 6$.

To compute the order n coefficient c_n, the principle is simple: one considers all the possible dipole configurations, and for each of them, one randomly generates the gluons in the various dipoles' frames according to the D_k. Then, given all the v_k, one checks if the real gluons configuration changes the observable, i.e. if $\Theta_{i_1,\ldots,i_p} = 0$ or 1 (cf eq. (D.10)), where p is the number of real gluons.[3] Notice that for the program to be relatively efficient, one has to ensure the cancellation of the collinear divergences event by event, but we will not enter into details here.

D.3.2 All-orders program

Here, the goal is to compute numerically the whole distribution $\Sigma(t)$. To build an all-orders program, one has to know the probability for no emission from a given dipole configuration. This is given by the sum of all virtual corrections obtained from the configuration. For instance, let us start with a simple $b\bar{b}$ dipole. Then the probability that there is no gluon emission with energy in $[E, E']$ from $b\bar{b}$ can be written as (fig. D.4 (a)):

$$\begin{aligned}
\Delta(E, E') &= 1 - \int dk_1 \, W^1_{b\bar{b}} + \frac{1}{2} \int dk_1 dk_2 \, W^1_{b\bar{b}} W^2_{b\bar{b}} - \ldots \,, \\
&= e^{-\int dk_1 \, W^1_{b\bar{b}}} \,, \\
&= e^{-\frac{\alpha_s N_c}{2\pi} \int_E^{E'} \frac{d|\vec{k}|}{|\vec{k}|} \int \sin\theta d\theta \frac{d\phi}{2\pi} \frac{(b\bar{b})}{(b1)(1\bar{b})}} \,, \\
&= e^{-\frac{\alpha_s N_c}{\pi} \ln \frac{E'}{E} \int dy \frac{d\phi}{2\pi}} \,,
\end{aligned} \tag{D.30}$$

where we used eq. (D.27) in the last equality. There is a divergence in the integration on the rapidity y in the $(b\bar{b})$ dipole's frame, so one has to regularise it using cutoffs y_{min} and y_{max}. If we use the variable $t = \frac{\alpha_s}{2\pi} \ln \frac{Q}{E}$ (with Q a hard scale in the process) and if we integrate over ϕ and y ($\Delta y_{b\bar{b}} = y_{max} - y_{min}$), we obtain:

$$\Delta(t, t + \Delta t) = e^{-2N_c \Delta y_{b\bar{b}} \Delta t} \,. \tag{D.31}$$

$\Delta y_{b\bar{b}}$ can be seen as the "logarithmic size" of the dipole $b\bar{b}$, i.e. the allowed phase space region in rapidity for the emission of a gluon from this dipole.

[3] In this work the energy integration has already been carried out, giving the factor t^n, so that $\Theta_{i_1,\ldots,i_p}$ only depends on the angles now, and not on τ anymore. For example, the ΔM observable in chapter 4 is changed if one real gluon is outside the filtered jet region.

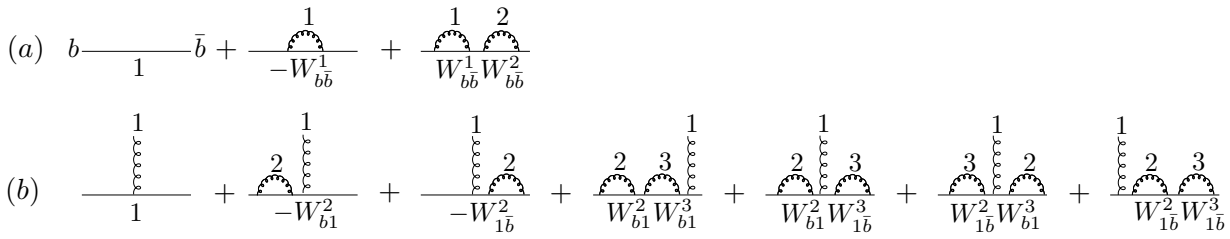

Figure D.4: (a) Diagrams up to 2 loops arising in the computation of the probability for no gluon emission from the $b\bar{b}$ dipole with their corresponding weight; (b) The same but for the $(b1) + (1\bar{b})$ dipole configuration.

If one real gluon 1 has already been emitted, then we now have 2 dipoles: $(b1)$ and $(1\bar{b})$. One can also compute the probability that there is no gluon emission from this dipole configuration (fig. D.4 (b)) between t and $t + \Delta t$:

$$\begin{aligned}\Delta(t, t+\Delta t) &= 1 - \int dk_2 \left(W^2_{b1} + W^2_{1\bar{b}}\right) + \frac{1}{2}\int dk_2 dk_3 \left(W^2_{b1}W^3_{b1} + W^2_{b1}W^3_{1\bar{b}} + W^2_{1\bar{b}}W^3_{b1} + W^2_{1\bar{b}}W^3_{1\bar{b}}\right) - \dots ,\\ &= e^{-\int dk_2 \left(W^2_{b1}+W^2_{1\bar{b}}\right)} ,\\ &= e^{-2N_c \Delta t (\Delta y_{b1} + \Delta y_{1\bar{b}})} . \end{aligned} \tag{D.32}$$

For the last line, we introduce the logarithmic sizes Δy_{b1} and $\Delta y_{1\bar{b}}$ of the dipoles $(b1)$ and $(1\bar{b})$ respectively, as we did for $\Delta y_{b\bar{b}}$. The generalisation of this formula to any dipole configuration gives:

$$\Delta(t, \Delta t) = e^{-2N_c \Delta y_{tot} \Delta t} , \tag{D.33}$$

where $\Delta y_{tot} = \Delta y_{bi_1} + \Delta y_{i_1 i_2} + \dots + \Delta y_{i_n \bar{b}}$ is the total logarithmic size in rapidity of the dipole configuration.

In practice, we can define for instance the (ij) dipole's logarithmic size as:

$$\Delta y_{ij} = 2y_{max} + \ln \frac{(ij)}{2} , \tag{D.34}$$

where y_{max} is a parameter. This equality means that there is less phase space region for gluon emission in a narrow dipole. When i and j are too close in angle, there is no possibility to emit a gluon from (ij).

The algorithm to compute all-orders non-global logarithms is the following:

1. Start from $t = 0$ and the $(b\bar{b})$ dipole.
2. Given a configuration of dipoles with size Δy_{tot}, one increases t according to a distribution proportional to $\exp(-2N_c \Delta y_{tot} \Delta t)$.
3. Choose a dipole (ij) from the dipole configuration with a probability $\Delta y_{ij}/\Delta y_{tot}$ and emit a gluon from (ij) uniformly in the (y, ϕ) variables defined with respect to the dipole's frame.
4. Repeat steps 2 and 3 until one reaches a value t_{max} for t (the cutoff for soft emissions), or the last emitted gluon changes the observable (for instance it is emitted outside the filtered jet region for the ΔM observable in chapter 4)

5. Fill the corresponding bin in t for the $\Sigma(t)$ histogram.

Appendix E

Convergence of the non-global series

In this appendix, we go back to the study of the convergence of the non-global series that was already briefly examined in section 4.2.2, trying to understand a little more what may be behind the observed behaviour.

E.1 Case $n_{\text{filt}} = 2$

First, we start by studying the convergence of the non-global perturbative series when $n = 2$ for η small, where the primary coefficients are known to be enhanced with respect to the purely non-global ones because of the presence of large collinear logarithms (cf section 4.1.2). Figure E.1 compares the fixed-order results to the all-orders one up to α_s^5. On these 2 plots

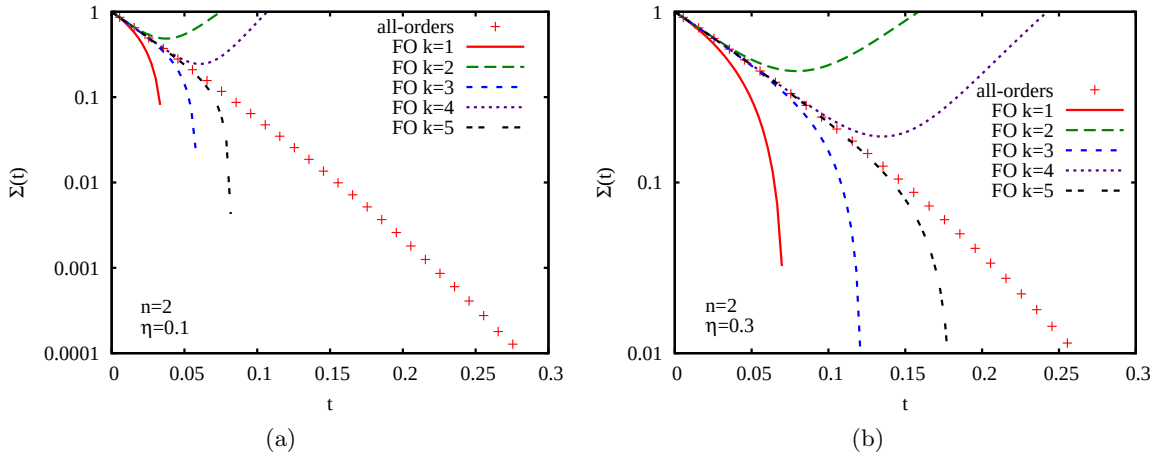

Figure E.1: Comparison between fixed-order (FO) expansion and all-orders result when $n = 2$ for (a) $\eta = 0.1$ and (b) $\eta = 0.3$.

one can notice that the series seems to converge, as was already shown in section 4.2.2. In other respects, the convergence looks better when η is larger. This may be understood using the following simple explanation: if we make an expansion up to order k, then the series starts to diverge from the exact result when the term of order $k+1$ becomes roughly

of the same size as the function itself. In the $\Sigma^{(2)}(L,t)$ case, using the analytic expression (eq. (4.27)), this can be translated to

$$\frac{(4N_cLt)^{k+1}}{(k+1)!} \sim e^{-4N_cLt}\,, \tag{E.1}$$

with $L = \ln\frac{1}{\eta}$. At large k,[1] the solution gives

$$t \sim \frac{k+1}{4N_cL}\,. \tag{E.2}$$

So the convergence is better when k and η increase.

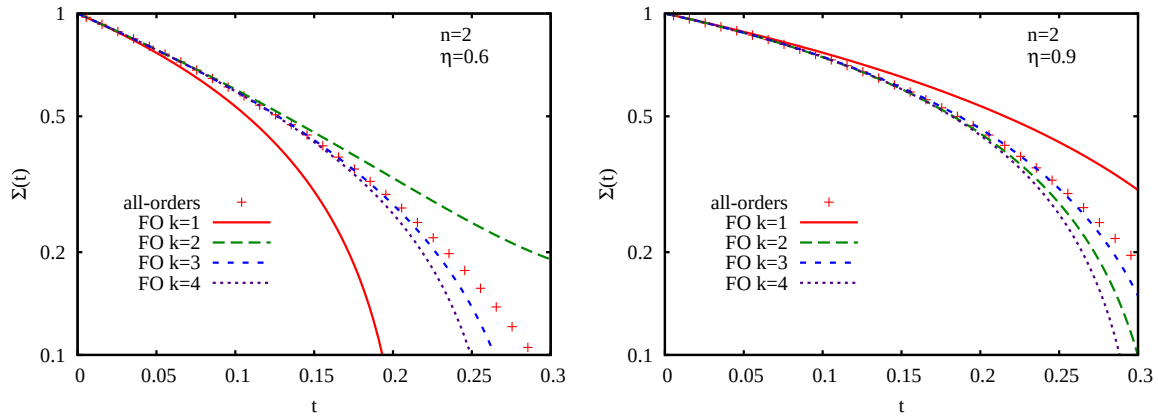

Figure E.2: Comparison between fixed-order (FO) expansion and all-orders result when $n = 2$ for (a) $\eta = 0.6$ and (b) $\eta = 0.9$.

Let us go to larger η, where there is no large collinear logarithm anymore, and check what happens. This is done for $\eta = 0.6$ and $\eta = 0.9$ on figure E.2. One striking feature of these plots is that the convergence seems acceptable up to the third order, but the 4^{th} order does not give as good a result, and the situation becomes worse as η increases. Said another way, the perturbative expansion can be trusted until the third order, but then it starts to diverge. The fact that the convergence looks better for small η may come from the dominant behavior of the primary series, which converges very well to a nice exponential function. However, if one could go to sufficiently high orders, it might be possible to observe the same divergence as in figure E.2, when the purely non-global coefficients become of the same order of magnitude as the primary ones.

To get an idea of these coefficients, the series of the plots are explicitly written below:

$$\Sigma^{(2)}(\eta = 0.1, t) = 1 - 27.57t + 368.8t^2 - 3195t^3 + 20200t^4 - 99300t^5 + \mathcal{O}\left(t^6\right)\,, \tag{E.3}$$

$$\Sigma^{(2)}(\eta = 0.3, t) = 1 - 13.88t + 87.49t^2 - 334t^3 + 860t^4 - 1500t^5 + \mathcal{O}\left(t^6\right)\,, \tag{E.4}$$

$$\Sigma^{(2)}(\eta = 0.6, t) = 1 - 4.656t + 6.53t^2 - 6.7t^3 - 10t^4 + \mathcal{O}\left(t^5\right)\,, \tag{E.5}$$

$$\Sigma^{(2)}(\eta = 0.9, t) = 1 - 2.320t - 2.27t^2 + 1.9t^3 - 12t^4 + \mathcal{O}\left(t^5\right)\,. \tag{E.6}$$

[1] the derivation was done at large k, but the result seems to be reasonable even for $k = 2$.

For η small, the growth of these coefficients comes from the powers of the large collinear logarithm L. For η near 1, the small growth that one can start to observe at the 4^{th} order essentially comes from the purely non-global part. Indeed, at the 4^{th} order, the primary coefficient is positive, and it is not the case for $\eta > 0.6$. This non-global growth will be confirmed at higher orders for the slice observable in section E.3.

Let us now see what happens if the perturbative series is exponentiated. This means that instead of plotting $g(t) = 1 + \sum_{i=1}^{k} a_i t^i$, which is the perturbative series, one plots $e^{f(t)}$ where

$$f(t) = \sum_{i=1}^{k} c_i t^i \text{ and } e^{f(t)} = g(t) + \mathcal{O}\left(t^{k+1}\right) , \tag{E.7}$$

so that

$$c_1 = a_1 , \tag{E.8}$$

$$c_2 = a_2 - \frac{a_1^2}{2} , \tag{E.9}$$

$$\dots$$

Notice that the exponentiated first order corresponds to the analytical estimate for $n = 2$. One can observe on figure E.3 a nice convergence for $\eta = 0.1$ until the 4^{th} order. Concerning the order 5, it seems that it diverges a little, but if the coefficients of the series are varied within their respective errors, then it can coincide with the all-orders curve. However, one can guess that it should not converge at the end because the all-orders function is not strictly a simple exponential. This will be confirmed later with the slice. When $\eta = 0.9$, the exponentiated 4^{th} order surprisingly almost fits the all-orders result. Even more surprising, if the 5^{th} order coefficient (not shown here) is varied within its error band, it seems that the exponentiated fit is still improved. Is it accidental? Here again, the slice example and good sense lead us to answer yes but we cannot be completely sure.

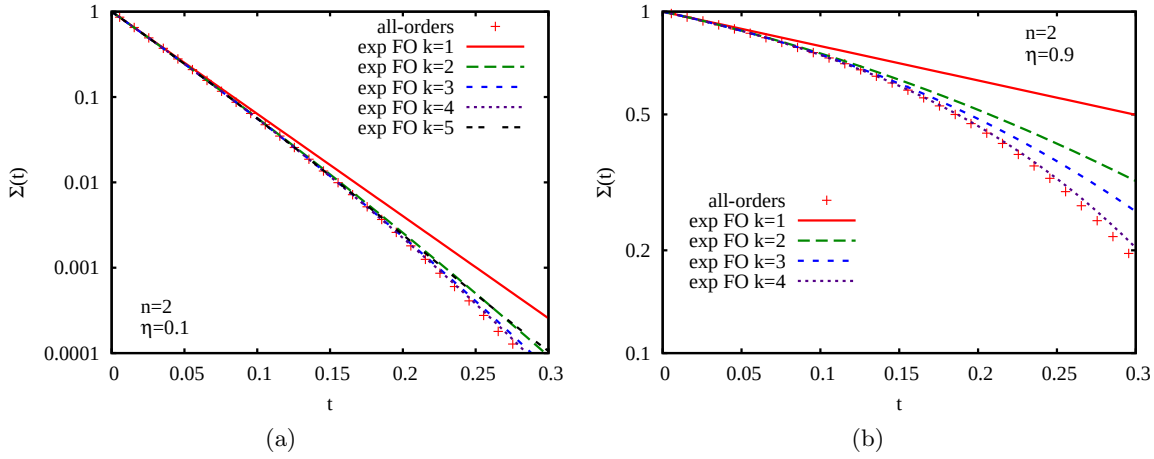

Figure E.3: Comparison between exponentiated fixed-order (exp FO) expansion and all-orders result when $n = 2$ for (a) $\eta = 0.1$ and (b) $\eta = 0.9$.

E.2 Case $n_{\text{filt}} = 3$

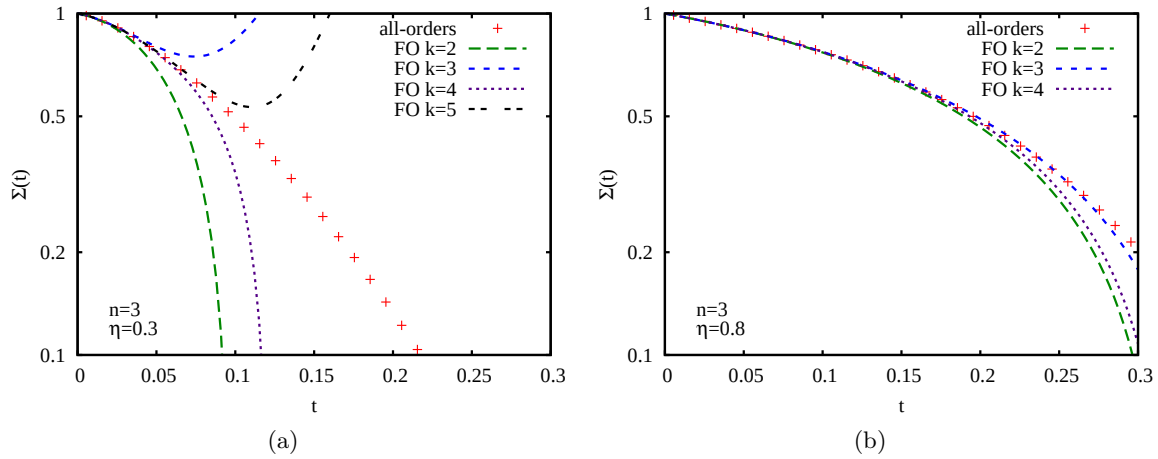

Figure E.4: Comparison between fixed-order expansion and all-orders result when $n = 3$ for (a) $\eta = 0.3$ and (b) $\eta = 0.8$.

For small enough η, it was found analytically in section 4.1.3 that the all-orders result for the Higgs ΔM distribution can be expressed as a simple function of t (eq. (4.29)), which is of the form $g(4N_c Lt)$ with:

$$g(t) = e^{-t}\left(1 + \int_0^t dt' \frac{1 - e^{t'}}{t'}\right) . \tag{E.10}$$

The radius of convergence of the Taylor series for g is infinite as the coefficients a_k resulting from its expansion can be shown to be bounded for large k by:

$$|a_k| < \frac{1}{k!}(2^k + \mathcal{O}(1)) . \tag{E.11}$$

As the expansion of this function converges, one would expect the same to occur for the curves obtained numerically. However, the expansion does not converge as fast as for the exponential, so that the t window for which there is a convergence should be smaller than what was obtained for $n = 2$. This is indeed what is observed in figure E.4(a) for $\eta = 0.3$, if it is compared for instance with the plot E.1(b).

In other respects, the curves on the plot E.4(b) for η near 1 behave similarly as for $n = 2$, i.e. a perturbative series that converges until the 3^{rd} order, and that starts to diverge from the 4^{th} order. Notice that the same behaviour is observed for $n > 3$.

E.3 The Slice case

The Slice observable, studied for instance in [205], gives an interesting example of the strange behaviour of the non-global leading-log series. It is simply defined by the sum of all the particles' energy flowing into a region Ω of the phase space corresponding to a rapidity $y \in [-y_0, y_0]$, with y_0 a parameter of the observable (figure E.5). Here, we work in the $q\bar{q}$ center of mass frame and the quarks are assumed to move along the z axis. This observable is non-global as shown in fig. E.5, and it is interesting in 2 ways:

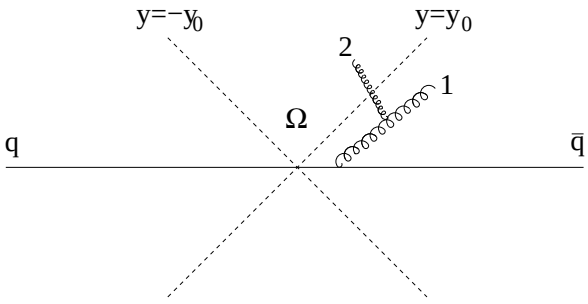

Figure E.5: The region Ω between the 2 dashed lines, and the gluon's configuration leading to the appearance of non-global logarithms.

- A simple change of frame[2] shows that it is more or less equivalent in the leading-log approximation to the ΔM observable in the filtering analysis using anti-k_t with $n = 2$ and $\eta = e^{-y_0}$ when $\eta \ll 1$, while being faster to compute numerically due to the absence of clustering.
- When $e^{-y_0} \sim 1$, which should very approximately correspond to $\eta = \mathcal{O}(1)$, the strange behaviour of the non-global series, observed in section 4.2, is clearly confirmed with the addition of the 5^{th} and 6^{th} orders.

The series are represented in figure E.6 for 2 different values of y_0. The plot for $y_0 = 2.3$ is here for a comparison with figure E.1(a), i.e. when $n = 2$ and $\eta = 0.1$. One can notice that until order 5 the behaviours of the 2 series are very similar. The slight difference comes from the fact that the C/A algorithm was used there instead of anti-k_t. This can also be seen on the expansions eqs. (E.3,E.12). However, a remarkable effect is the 6^{th} order curve which does not improve the fit with the all-orders result anymore (it even makes it worse). When $y_0 = 0.5$ (fig. E.6(b)), this effect is enhanced: indeed, one notices that the 3^{rd} order gives the best result, with the 2^{nd} order even worse than the 1^{st} one. And here again, adding more orders shifts point of disagreement to smaller t.

To get an idea of the coefficients in this case, the series of the plots are given below:

$$\Sigma(y_0 = 2.3, t) = 1 - 27.6t + 351.1t^2 - 2673t^3 + 13900t^4 - 99500t^5 + 2\,10^6 t^6 + \mathcal{O}(t^7)\,, \tag{E.12}$$

$$\Sigma(y_0 = 0.5, t) = 1 - 6t - 9.108t^2 + 114t^3 + 1740t^4 - 68400t^5 + 1.6\,10^6 t^6 + \mathcal{O}(t^7)\,. \tag{E.13}$$

The growth of the coefficients for $y_0 = 2.3$ until the 5^{th} order essentially comes from the powers of $4N_c y_0$ when expanding the primary result, which is the expression of the collinear divergence near q and $\bar{q}$, whereas, for $y_0 = 0.5$, it essentially takes its origin from the purely non-global part. There is no large enhancement due to collinear divergence which can explain it. As an example, we also show the function $S(y_0, t)$, which is defined as in [199, 205] to contain the purely non-global part of the result:

$$S(y_0, t) \equiv \frac{\Sigma(y_0, t)}{\Sigma^{(P)}(y_0, t)}\,, \tag{E.14}$$

[2] or more simply comparison between primary results, eq. (2.5) from [205] and eq. (4.10) from this paper.

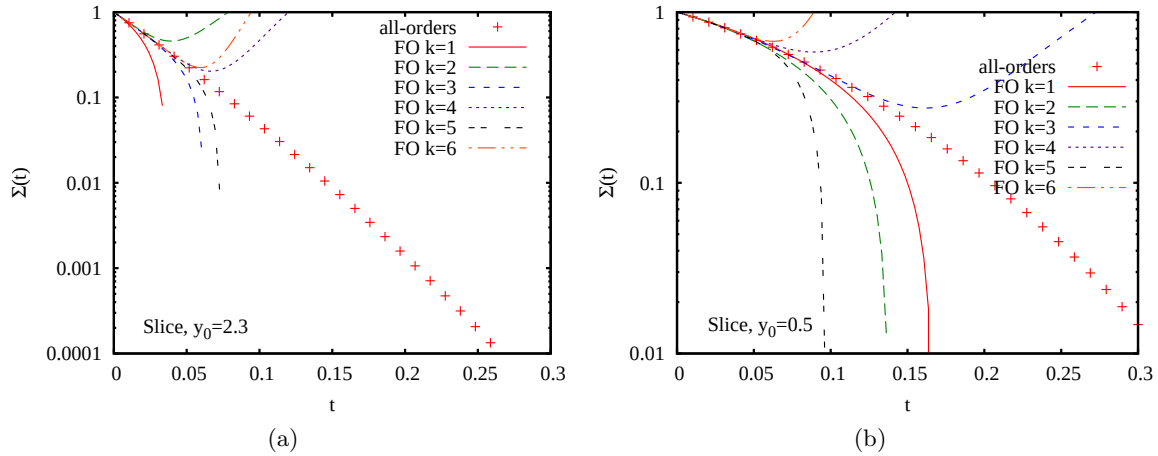

Figure E.6: Comparison between all-orders and fixed-order results for the Slice when (a) $y_0 = 2.3$ and (b) $y_0 = 0.5$.

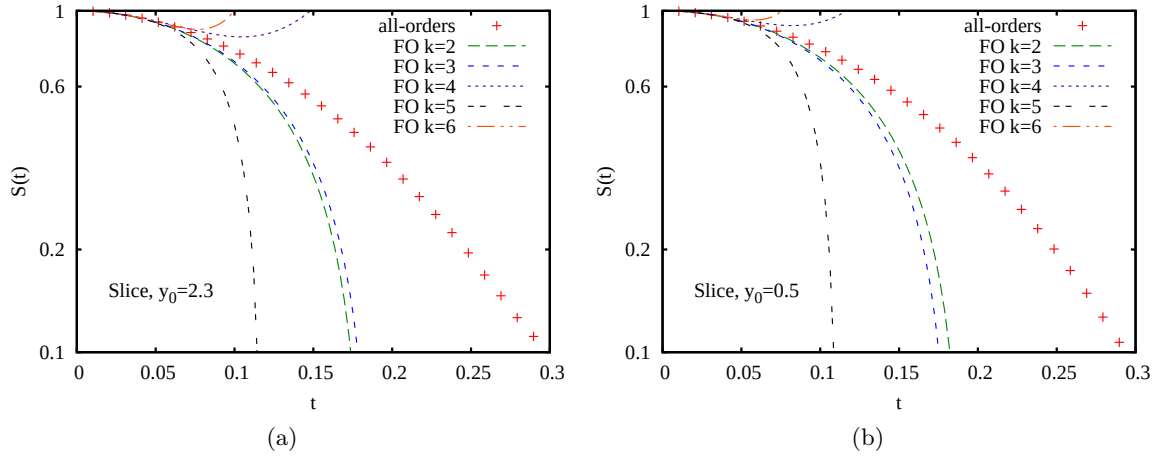

Figure E.7: Comparison between all-orders and fixed-order results for the purely non-global part $S(t)$ of the Slice when (a) $y_0 = 2.3$ and (b) $y_0 = 0.5$.

where, for the slice, the primary contribution $\Sigma^{(P)}$ can be written as:

$$\Sigma^{(P)}(y_0, t) = e^{-4N_c y_0 t}\,, \tag{E.15}$$

in the large-N_c limit. The plots for $S(y_0, t)$ are shown in fig. E.7. One observes the saturation property noticed in [205] which leads to very similar plots for $y_0 = 0.5$ and $y_0 = 2.3$. There is clearly no convergence of the perturbative series.

Therefore, the non-global leading-log large-N_c series seems to behave badly at high orders. Does this mean that it is an asymptotic series like the Standard Model is known to be [255]?[3] This study cannot answer such a question but, at least, one should be aware of the strange behaviour of the non-global series.

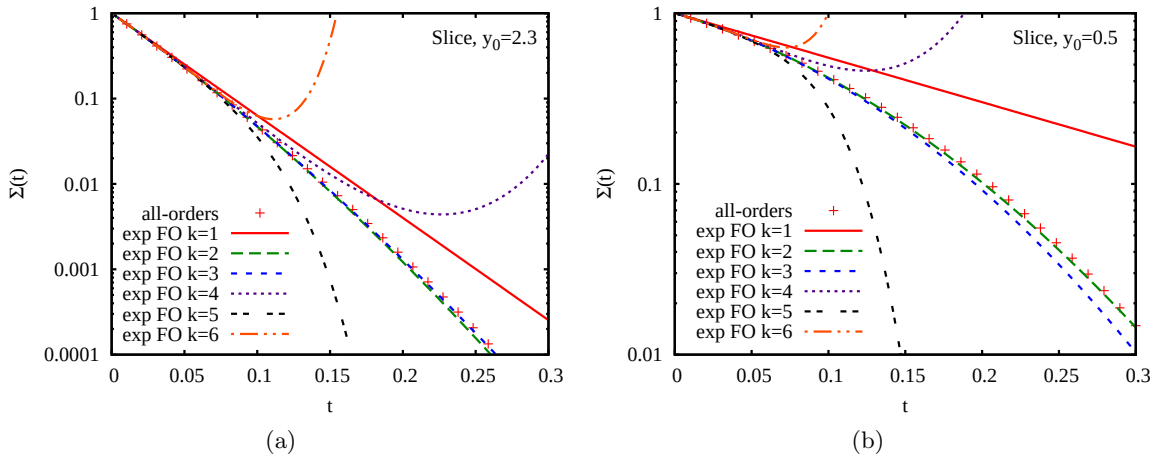

Figure E.8: Comparison between all-orders and exponentiated fixed-order results for the Slice when (a) $y_0 = 2.3$ and (b) $y_0 = 0.5$.

To finish, let us mention the exponentiated results represented in figure E.8. They show that the convergence observed in the case $n = 2$ is clearly only illusory. One point to notice is that the case $y_0 = 2.3$ is slightly different from its $\eta = 0.1$ counterpart as the divergence starts to be visible at order 4 instead of 5. This may be because using the C/A algorithm in the filtered Higgs mass observable reduces the impact of the non-global logarithms [206, 207] and the primaries still dominate at order 4, whereas it is not the case anymore for the slice. Notice also the very nice fit given by the exponentiated 2^{nd} order curve when $y_0 = 0.5$.

[3] though the origin would be different if it were the case.

Appendix F

Some key points of the LoopSim algorithm

This appendix is intended to examine three important points of the LoopSim method explained in section 5.1: first we see why "non-clustering" particles cannot become virtual, then we give the details of our recoil procedure, and finally we illustrate why the LoopSim method is sensible even in the presence of incoming hadrons.

F.1 The non-clustering status

Apart from the born particles, in general one has to take into account possible "secondary emitters", i.e. non-born particles which emit something. These kind of particles, whose status is defined as "non-clustering", do not get looped. Indeed, when particle j makes a loop over i, this means that there is a collinear enhancement of the matrix element coming from i and j being close in angle. But the emission of the same j from the configuration where i is virtual does not give such a collinear enhancement, so one must not take it into account.

Another way to understand it might be to consider the example of 2-gluons emission from a $q\bar{q}$ dipole. We saw in section 4.1.2 that the squared matrix element for the emission of 2 real energy-ordered ($E_1 \gg E_2$) gluons, g_1, g_2, can be expressed as

$$M(k_1, k_2) = (4\pi\alpha_s)^2 (C_F^2 W_1 + C_F C_A W_2)\,, \tag{F.1}$$

with

$$W_1 = 4\frac{(p_q.p_{\bar{q}})}{(p_q.k_1)(k_1.p_{\bar{q}})}\frac{(p_q.p_{\bar{q}})}{(p_q.k_2)(k_2.p_{\bar{q}})}\,, \tag{F.2}$$

$$W_2 = 2\frac{(p_q.p_{\bar{q}})}{(p_q.k_1)(k_1.p_{\bar{q}})}\left(\frac{(p_q.k_1)}{(p_q.k_2)(k_2.k_1)} + \frac{(p_{\bar{q}}.k_1)}{(p_{\bar{q}}.k_2)(k_2.k_1)} - \frac{(p_q.p_{\bar{q}})}{(p_q.k_2)(k_2.p_{\bar{q}})}\right)\,. \tag{F.3}$$

As the W_1 term diverges when g_2 is collinear to q or $\bar{q}$ (unlike the W_2 term), it becomes relevant when g_2 is considered to have been emitted from q or $\bar{q}$ independently of g_1. The W_2 term diverges when g_2 is collinear to g_1 (unlike W_1), so it becomes relevant when g_2 is considered to have been emitted from g_1. This is depicted in fig. F.1, where are also represented the virtual corrections whose study can be found in [213]. One notices that the

W_2 term only appears when g_1 is real. The diagrams where g_1 is virtual are taken into account when g_2 is emitted from q or $\bar{q}$. Therefore, g_1 cannot become virtual when g_2 makes a loop over it.

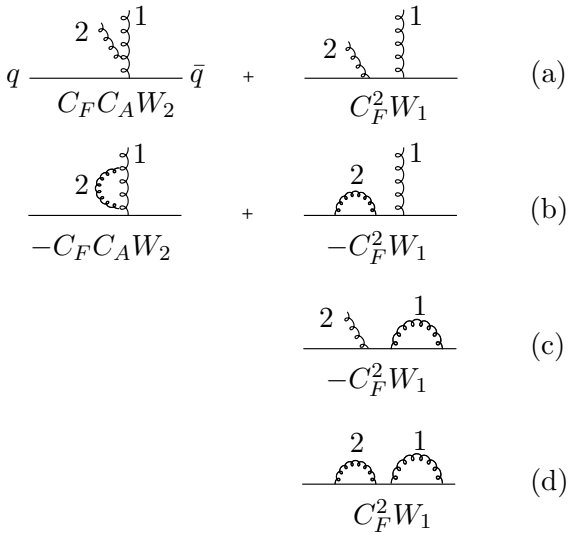

Figure F.1: Matrix elements for two gluons emitted from a $q\bar{q}$ dipole: (a) gluons 1 and 2 real; (b) gluon 1 real and 2 virtual; (c) gluon 1 virtual and 2 real; (d) gluons 1 and 2 virtual. In each case, when needed, we separate what can be seen as the emission of gluon 2 from gluon 1, and what can be seen as the emission of gluon 2 directly from $q\bar{q}$.

F.2 Recoil procedure

We now describe a little more precisely how we perform the recoil of an event when a particle becomes virtual, and we also consider the decay products of the Z boson. We first examine the simpler case of a particle making a loop with the beam, then we show how to deal with a particle that makes a loop with another particle.

F.2.1 A particle recombines with the beam

Let us assume that particle number i_0 has to make a loop over the beam. To simulate it, do the following procedure:

1. For each particle $i \neq i_0$, store its rapidity y_i.

2. Perform a separate longitudinal boost on each particle so as to bring its rapidity to 0 (i.e. get a purely transverse event).

3. Compute
$$E_{tot} = \sum_{i \neq i_0} E_i \,, \tag{F.4}$$
where E_i is the energy of particle i in the purely transverse event.

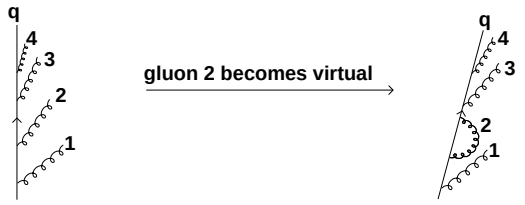

Figure F.2: Case where four gluons are emitted from the same quark. Gluon 1 is the last to be clustered with the quark (which roughly corresponds to an early time emission) and gluon 4 is the first to be clustered. In the event where gluon 2 makes a loop over the quark, we spread the gluon 2's momentum over the quark's momentum and the momenta of gluons that were emitted *after* it, i.e. gluons 3 and 4 (an earlier time emission like gluon 1 cannot be affected).

4. Define
$$k = (E = E_{tot}, \vec{p}_t = \vec{p}_{t,i_0}, p_z = 0) \ , \tag{F.5}$$
and boost all particles into the rest frame of k (so that the total transverse momentum balances).

5. Perform a longitudinal boost on each particle so that it recovers its original rapidity y_i.

For the case where two particles are looped with the beam, i_0 and i_1, replace $i \neq i_0$ with $i \neq i_0, i_1$ and in eq. (F.5) replace $\vec{p}_{t,i_0}$ with $\vec{p}_{t,i_0} + \vec{p}_{t,i_1}$; etc. In the case where the Z decays, for instance into 2 leptons, the procedure is exactly the same except that we apply to them the same longitudinal boosts as for the Z (the rapidity of the leptons is thus non necessarily 0 when we apply the transverse boost). This conserves the property that the sum of the leptons' momenta is still the Z momentum in the "looped" event.

The logic of the above procedure is that if we had attempted to apply a transverse boost without stages 3 and 5, we would have found that our choice of transverse boost, and the corresponding mapping of high-p_t particles' momenta, would be affected by the presence of energetic particles collinear to the beam. This would have made the procedure collinear unsafe.

F.2.2 A particle recombines with another particle

Let us consider the situation depicted in fig. F.2: four gluons are emitted from the same quark, but at different angles:

$$\theta_{1q} \gg \theta_{2q} \gg \theta_{3q} \gg \theta_{4q} \, , \tag{F.6}$$

and gluon 2 becomes virtual. The virtualisation of gluon 2 over the quark cannot have an impact on gluon 1, which was emitted earlier in an angular-ordered picture. But it has an impact on gluons 3 and 4. More precisely, we define

$$p_{t,tot} = p_{t,q} + p_{t,3} + p_{t,4} \, . \tag{F.7}$$

If we call p the momenta in the original event and p' the momenta in the event where gluon 2 is virtual, we have:

$$p'_i = p_i + \frac{p_{t,i}}{p_{t,tot}} p_2 \quad \text{for } i = q,\, 3,\, 4\,, \tag{F.8a}$$

$$p'_1 = p_1\,. \tag{F.8b}$$

This procedure is applied as many times as is necessary to account for all the looped particles (in eqs. (F.7,F.8a) it is always the original particle momenta that are used to determine the $p_{t,i}/p_{t,tot}$ ratio). Subsequently each particle is rescaled such that its mass is 0 (or M_Z if gluon 3 is replaced with a Z boson for instance), keeping its transverse components p_x, p_y and its rapidity unchanged.

This can be easily generalised to any number of particles recombining on the same hard one: we spread the looped particle over the hard particle h and over the ones which were emitted after it and recombine with h. This procedure is designed to ensure collinear safety: if, for instance, the gluon 4 is collinear to the quark in the original event, then it remains collinear in the looped event. And in the case where the gluon 2 is collinear to the quark, this means that it was emitted after all the other gluons, in which case only the quark momentum is rescaled (and its direction does not change).

In the case where the Z decays into 2 leptons, one applies the following procedure to each of the leptons:

1. Perform a longitudinal boost of the Z boson respectively in the original event and the looped event such that it has 0 rapidity in each case. Call the momenta obtained $p_{Z,0} = (E_0, \vec{p}_{t,0}, 0)$ and $p_{Z,1} = (E_1, \vec{p}_{t,1}, 0)$ respectively.

2. Perform a longitudinal boost of the lepton from the original event into the frame where the initial Z has 0 rapidity.

3. Define a purely transverse vector k such that $p_{Z,0}$ is transformed to $p_{Z,1}$ if it is boosted into k's rest frame:

$$k = \left(E_1 + E_0, \frac{2}{1+C}(\vec{p}_{t,1} - \vec{p}_{t,0}), 0\right)\,, \tag{F.9}$$

   with

$$C = \frac{(\vec{p}_{t,1} - \vec{p}_{t,0})^2}{(E_1 + E_0)^2}\,. \tag{F.10}$$

4. Boost the lepton's momentum into k's rest frame.

5. Apply to the lepton the longitudinal boost that brings $p_{Z,1}$ to its true rapidity in the looped event.

We are aware of the somewhat cumbersome nature of these procedures. A simplification of the procedures that retained the relevant collinear-safety properties would certainly be of interest.

F.3 The LoopSim method and incoming partons

Without going into a full proof, we shall here illustrate why the LoopSim method is sensible even in the presence of incoming hadrons, by considering what happens at $\bar{n}$LO. We start with a LO cross section for a process producing n hard objects

$$\sigma_n^{\mathrm{LO}} = \int dx_a dx_b \, d\Phi_n \, \frac{d\hat{\sigma}_{ij\to n}(x_a p_a, x_b p_b)}{d\Phi_n} \, f_{i/a}(x_a, \mu_{\mathrm{F}}^2) f_{j/b}(x_b, \mu_{\mathrm{F}}^2) \, C(p_1, \ldots, p_n) \tag{F.11}$$

For compactness of notation, we have dropped the μ_{R} dependence in the differential tree-level partonic cross section $d\hat{\sigma}_{ij\to n}/d\Phi_n$. We have also not yet specified our choice for the factorisation scale μ_{F}. We assume that $d\hat{\sigma}_{ij\to n}/d\Phi_n$ contains the necessary constraints to relate the incoming partonic momenta to the outgoing momenta. We further integrate over the phase-space $dx_a dx_b d\Phi_n$, and include a function $C(p_1, \ldots, p_n)$, which is 1 if the momenta pass our cuts and 0 otherwise.

We now imagine that there is some transverse-momentum scale Q_0 below which no radiation takes place. To $\mathcal{O}(\alpha_s)$, the PDFs $f_{i/a}(x_a, \mu_{\mathrm{F}}^2)$ can be written in terms of PDFs at scale Q_0:

$$f_{i/a}(x_a, \mu_{\mathrm{F}}^2) = f_{i/a}(x_a, Q_0^2) + \frac{\alpha_s}{2\pi} \sum_k \int_{Q_0^2}^{\mu_F^2} \frac{dk_t^2}{k_t^2} \int \frac{dz}{z} P_{ik}(z) f_{k/a}(x/z, Q_0^2) \tag{F.12}$$

where we also define an unregularised splitting function $p_{ik}(z)$ such that $P_{ik}(z) = p_{ik}(z) - \delta(1-z) \int dz' \bar{p}_{ik}(z')$, with $\bar{p}_{ik}(z')$ embodying the virtual parts of the splitting function (it is zero for $i \neq k$).

Next, we can write the LO cross section in terms of a PDF for proton a that has been evaluated at scale Q_0:

$$\begin{aligned}\sigma_n^{\mathrm{LO}} = &\int dx_a dx_b \, d\Phi_n \, \frac{d\hat{\sigma}_{ij\to n}(x_a p_a, x_b p_b)}{d\Phi_n} \, f_{j/b}(x_b, \mu_{\mathrm{F}}^2) \, C(p_1, \ldots, p_n) \\ &\times \left[f_{i/a}(x_a, Q_0^2) + \frac{\alpha_s}{2\pi} \int_{Q_0^2}^{\mu_{\mathrm{F}}^2} \frac{dk_t^2}{k_t^2} dz \, \left(\frac{p_{ik}(z)}{z} f_{k/a}(x_a/z, Q_0^2) - \bar{p}_{ik}(z) f_{i/a}(x_a, Q_0^2) \right) \right] . \end{aligned} \tag{F.13}$$

Note that the first term in round brackets on the second line corresponds to real emission of a parton. However that parton is not taken into account in the $C(p_1, \ldots, p_n)$ factor.

Next we examine the structure of the $\bar{n}$LO contribution,

$$\begin{aligned}\sigma_n^{\bar{n}\mathrm{LO}} = \sigma_n^{\mathrm{LO}} + \int dx_a dx_b \, d\Phi_{n+1} \, &\frac{d\hat{\sigma}_{ij\to n+1}(x_a p_a, x_b p_b)}{d\Phi_{n+1}} \, f_{i/a}(x_a, \mu_{\mathrm{F}}^2) f_{j/b}(x_b, \mu_{\mathrm{F}}^2) \\ &\times \left[C(p_1, \ldots, p_{n+1}) - C(p_1^{\mathrm{LS}}, \ldots, p_n^{\mathrm{LS}}) \right] , \end{aligned} \tag{F.14}$$

where the $p_1^{\mathrm{LS}} \ldots p_n^{\mathrm{LS}}$ represent the momenta after application of the LoopSim procedure to p_{n+1}. In the limit in which p_{n+1} is collinear to incoming parton i, with momentum $p_{n+1} = (1-z) x_a p_a$, the $n+1$-parton differential cross section and phase-space simplify

$$dx_a d\Phi_{n+1} \frac{d\hat{\sigma}_{ij\to n+1}(x_a p_a, x_b p_b)}{d\Phi_{n+1}} = dx'_a d\Phi_n \frac{d\hat{\sigma}_{kj\to n}(x'_a p_a, x_b p_b)}{d\Phi_n} \cdot \frac{\alpha_s}{2\pi} \frac{dz}{z} \frac{dk_{t,n+1}^2}{k_{t,n+1}^2} p_{ki}(z) \tag{F.15}$$

where $x'_a = z x_a$. By "collinear" we will mean $k_{t,n+1} \ll Q$ where Q is the momentum transfer in the hard process. In this limit we also have that $p_i^{\mathrm{LS}} \simeq p_i$ (for $i \leq n$). So, still working within the collinear limit, we can now rewrite eq. (F.14) as

$$\sigma_n^{\bar{n}\mathrm{LO}} \simeq \sigma_n^{\mathrm{LO}} + \int dx'_a dx_b \, d\Phi_n \, \frac{d\hat{\sigma}_{kj\to n}(x'_a p_a, x_b p_b)}{d\Phi_n} \, f_{j/b}(x_b, \mu_{\mathrm{F}}^2) \\ \times \frac{\alpha_s}{2\pi} \int_{Q_0^2}^{Q^2} \frac{dk_{t,n+1}^2}{k_{t,n+1}^2} \frac{dz}{z} \, p_{ki}(z) \left[C(p_1, \ldots, p_{n+1}) - C(p_1, \ldots, p_n) \right] f_{i/a}(x'_a/z, \mu_{\mathrm{F}}^2) \,. \quad \text{(F.16)}$$

Next, we exchange $i \leftrightarrow k$, replace $x'_a \to x_a$ and change the scale μ_{F}^2 in $f_{i/a}(x'_a/z, \mu_{\mathrm{F}}^2)$ to be Q_0^2, which is allowed because it corresponds to an $\mathcal{O}\big(\alpha_s^2\big)$ change (while here we consider only $\mathcal{O}(\alpha_s)$):

$$\sigma_n^{\bar{n}\mathrm{LO}} \simeq \sigma_n^{\mathrm{LO}} + \int dx_a dx_b \, d\Phi_n \, \frac{d\hat{\sigma}_{ij\to n}(x_a p_a, x_b p_b)}{d\Phi_n} \, f_{j/b}(x_b, \mu_{\mathrm{F}}^2) \\ \times \frac{\alpha_s}{2\pi} \int_{Q_0^2}^{Q^2} \frac{dk_{t,n+1}^2}{k_{t,n+1}^2} \frac{dz}{z} \, p_{ik}(z) \left[C(p_1, \ldots, p_{n+1}) - C(p_1, \ldots, p_n) \right] f_{k/a}(x_a/z, Q_0^2) \,. \quad \text{(F.17)}$$

Note now that if we take $\mu_{\mathrm{F}}^2 \sim Q^2$ then the second term in square brackets in eq. (F.17) cancels the first term in round brackets in the second line of eq. (F.13). In other words for initial-state radiation, the action of LoopSim is not so much to provide virtual corrections as to cancel the real-emission terms already included implicitly through the PDFs in the leading order cross section. In contrast, the true virtual terms are already included through the PDFs themselves, i.e. through the second term in round brackets in eq. (F.13).

As an example, consider $pp \to Z$. At $\bar{n}$LO we will have events such as $gq \to Zq$, where the outgoing quark comes from collinear initial-state splitting $g \to q\bar{q}$, with an underlying hard subprocess $\bar{q}q \to Z$. From these events LoopSim will generate a configuration in which the outgoing quark is "looped". This will come in with a PDF weight that is the product of a gluon distribution and a quark distribution, so it appears that we have a (negative) $gq \to Z$ contribution, which would be unphysical. However in the LO cross section with a factorisation scale $\mu_{\mathrm{F}} \sim Q$, when we write $\bar{q}q \to Z$, part of the $\bar{q}$ PDF comes from $g \to \bar{q}q$ splitting. If we were just to add the real $gq \to Zq$ diagram to the LO cross section alone, then in the collinear limit we would be double counting the part already included in the PDF. With the negative "$gq \to Z$" LoopSim contribution, what happens is that we simply remove the $\bar{q}$ PDF component, generated from $g \to \bar{q}q$ splitting, that was implicitly included at LO with an incorrect final state (i.e. lacking an outgoing quark), since we are now putting it in with the correct final state through the real $gq \to Zq$ diagram.

Note that we have not yet worked out the full extension of this discussion to higher orders. The details would depend on the precise higher orders that we have in mind, for example $\bar{n}\bar{n}$LO versus $\bar{n}$NLO. However, regardless of these details, the fundamentally unitary nature of the LoopSim procedure is important in ensuring that the simulated "loops" simply bring about an overall consistent set of final states while maintaining the total cross section as calculated with a sensible factorisation scale choice.

Bibliography

[1] C. Itzykson and J. B. Zuber, *Quantum field theory*, . New York, Usa: Mcgraw-hill (1980) 705 P.(International Series In Pure and Applied Physics).

[2] M. E. Peskin and D. V. Schroeder, *An Introduction to quantum field theory*, . Reading, USA: Addison-Wesley (1995) 842 p.

[3] I. J. R. Aitchison and A. J. G. Hey, *Gauge theories in particle physics: a practical introduction*, . BRISTOL, UK: HILGER (1989) 571p.

[4] T. P. Cheng and L. F. Li, *Gauge theory of elementary particle physics*, . Oxford, Uk: Clarendon (1984) 536 P. (Oxford Science Publications).

[5] T. Muta, *Foundations of quantum chromodynamics. Second edition*, *World Sci. Lect. Notes Phys.* **57** (1998) 1–409.

[6] S. L. Glashow, *Partial Symmetries of Weak Interactions*, *Nucl. Phys.* **22** (1961) 579–588.

[7] S. Weinberg, *A Model of Leptons*, *Phys. Rev. Lett.* **19** (1967) 1264–1266.

[8] A. Salam, *Weak and Electromagnetic Interactions*, . Originally printed in *Svartholm: Elementary Particle Theory, Proceedings Of The Nobel Symposium Held 1968 At Lerum, Sweden*, Stockholm 1968, 367-377.

[9] T. D. Lee and C.-N. Yang, *Question of Parity Conservation in Weak Interactions*, *Phys. Rev.* **104** (1956) 254–258.

[10] C. S. Wu, E. Ambler, R. W. Hayward, D. D. Hoppes, and R. P. Hudson, *Experimental test of parity conservation in beta decay*, *Phys. Rev.* **105** (1957) 1413–1414.

[11] F. Englert and R. Brout, *Broken symmetry and the mass of gauge vector mesons*, *Phys. Rev. Lett.* **13** (Aug, 1964) 321–323.

[12] P. W. Higgs, *Broken symmetries and the masses of gauge bosons*, *Phys. Rev. Lett.* **13** (Oct, 1964) 508–509.

[13] G. S. Guralnik, C. R. Hagen, and T. W. B. Kibble, *Global conservation laws and massless particles*, *Phys. Rev. Lett.* **13** (Nov, 1964) 585–587.

[14] A. Djouadi, *The Anatomy of electro-weak symmetry breaking. I: The Higgs boson in the standard model*, *Phys. Rept.* **457** (2008) 1–216, [hep-ph/0503172].

[15] B. W. Lee, C. Quigg, and H. B. Thacker, *The Strength of Weak Interactions at Very High-Energies and the Higgs Boson Mass*, *Phys. Rev. Lett.* **38** (1977) 883–885.

[16] N. Cabibbo, L. Maiani, G. Parisi, and R. Petronzio, *Bounds on the Fermions and Higgs Boson Masses in Grand Unified Theories*, *Nucl. Phys.* **B158** (1979) 295–305.

[17] M. Lindner, M. Sher, and H. W. Zaglauer, *Probing Vacuum Stability Bounds at the Fermilab Collider*, *Phys. Lett.* **B228** (1989) 139.

[18] C. Ford, D. R. T. Jones, P. W. Stephenson, and M. B. Einhorn, *The Effective potential and the renormalization group*, *Nucl. Phys.* **B395** (1993) 17–34, [hep-lat/9210033].

[19] G. Altarelli and G. Isidori, *Lower limit on the Higgs mass in the standard model: An Update*, *Phys. Lett.* **B337** (1994) 141–144.

[20] J. A. Casas, J. R. Espinosa, and M. Quiros, *Improved Higgs mass stability bound in the standard model and implications for supersymmetry*, *Phys. Lett.* **B342** (1995) 171–179, [hep-ph/9409458].

[21] **LEP Working Group for Higgs boson searches** Collaboration, R. Barate *et. al.*, *Search for the standard model Higgs boson at LEP*, *Phys. Lett.* **B565** (2003) 61–75, [hep-ex/0306033].

[22] A. Falkowski, J. T. Ruderman, T. Volansky, and J. Zupan, *Hidden Higgs Decaying to Lepton Jets*, arXiv:1002.2952.

[23] A. Collaboration *et. al.*, *Precision Electroweak Measurements and Constraints on the Standard Model*, arXiv:0911.2604.

[24] **CDF** Collaboration, *Combined CDF and D0 Upper Limits on Standard Model Higgs- Boson Production with 2.1 - 5.4 fb-1 of Data*, arXiv:0911.3930.

[25] **CDF and D0** Collaboration, T. Aaltonen *et. al.*, *Combination of Tevatron searches for the standard model Higgs boson in the W+W- decay mode*, *Phys. Rev. Lett.* **104** (2010) 061802, [arXiv:1001.4162].

[26] J. Baglio and A. Djouadi, *Predictions for Higgs production at the Tevatron and the associated uncertainties*, arXiv:1003.4266.

[27] A. Djouadi, J. Kalinowski, and M. Spira, *HDECAY: A program for Higgs boson decays in the standard model and its supersymmetric extension*, *Comput. Phys. Commun.* **108** (1998) 56–74, [hep-ph/9704448].

[28] *http://diablo.phys.northwestern.edu/pc/brs.html*, .

[29] A. Djouadi, *The Anatomy of electro-weak symmetry breaking. II. The Higgs bosons in the minimal supersymmetric model*, *Phys. Rept.* **459** (2008) 1–241, [hep-ph/0503173].

[30] N. Arkani-Hamed, A. G. Cohen, E. Katz, and A. E. Nelson, *The littlest Higgs*, *JHEP* **07** (2002) 034, [hep-ph/0206021].

[31] G. Panico, M. Serone, and A. Wulzer, *A model of electroweak symmetry breaking from a fifth dimension*, *Nucl. Phys.* **B739** (2006) 186–207, [hep-ph/0510373].

[32] M. Carena, A. D. Medina, B. Panes, N. R. Shah, and C. E. M. Wagner, *Collider Phenomenology of Gauge-Higgs Unification Scenarios in Warped Extra Dimensions*, *Phys. Rev.* **D77** (2008) 076003, [arXiv:0712.0095].

[33] C. Csaki, J. Hubisz, and P. Meade, *Electroweak symmetry breaking from extra dimensions*, hep-ph/0510275.

[34] M. Gell-Mann, *A Schematic Model of Baryons and Mesons*, *Phys. Lett.* **8** (1964) 214–215.

[35] G. Zweig, *An SU(3) model for strong interaction symmetry and its breaking*, . CERN-TH-401.

[36] G. Zweig, *An SU(3) model for strong interaction symmetry and its breaking. 2*, . CERN-TH-412.

[37] R. M. Barnett, C. D. Carone, D. E. Groom, T. G. Trippe, C. G. Wohl, B. Armstrong, P. S. Gee, G. S. Wagman, F. James, M. Mangano, K. Mönig, L. Montanet, J. L. Feng, H. Murayama, J. J. Hernández, A. Manohar, M. Aguilar-Benitez, C. Caso, R. L. Crawford, M. Roos, N. A. Törnqvist, K. G. Hayes, K. Hagiwara, K. Nakamura, M. Tanabashi, K. Olive, and K. Honscheid, *Review of particle physics*, *Phys. Rev. D* **54** (Jul, 1996) 1–708.

[38] R. K. Ellis, W. J. Stirling, and B. R. Webber, *QCD and collider physics*, *Camb. Monogr. Part. Phys. Nucl. Phys. Cosmol.* **8** (1996) 1–435.

[39] S. Bethke, *Experimental tests of asymptotic freedom*, *Prog. Part. Nucl. Phys.* **58** (2007) 351–386, [hep-ex/0606035].

[40] A. Bassetto, M. Ciafaloni, and G. Marchesini, *Jet Structure and Infrared Sensitive Quantities in Perturbative QCD*, *Phys. Rept.* **100** (1983) 201–272.

[41] V. S. Fadin, *Double logarithmic asymptotics of the cross-sections of e+ e- annihilation into quarks and gluons. (in Russian)*, *Yad. Fiz.* **37** (1983) 408–423.

[42] B. I. Ermolaev and V. S. Fadin, *Log - Log Asymptotic Form of Exclusive Cross-Sections in Quantum Chromodynamics*, *JETP Lett.* **33** (1981) 269–272.

[43] A. H. Mueller, *On the Multiplicity of Hadrons in QCD Jets*, *Phys. Lett.* **B104** (1981) 161–164.

[44] Y. L. Dokshitzer, V. S. Fadin, and V. A. Khoze, *Double Logs of Perturbative QCD for Parton Jets and Soft Hadron Spectra*, *Zeit. Phys.* **C15** (1982) 325.

[45] G. 't Hooft, *A planar diagram theory for strong interactions*, *Nucl. Phys.* **B72** (1974) 461.

[46] E. Witten, *Baryons in the 1/N Expansion*, *Nucl. Phys.* **B160** (1979) 57.

[47] J. R. Ellis, M. K. Gaillard, and G. G. Ross, *Search for Gluons in e+ e- Annihilation*, *Nucl. Phys.* **B111** (1976) 253.

[48] M. R. Pennington, *Cornerstones of QCD*, *Rept. Prog. Phys.* **46** (1983) 393.

[49] C. G. Bollini and J. J. Giambiagi, *Dimensional Renormalization: The Number of Dimensions as a Regularizing Parameter*, *Nuovo Cim.* **B12** (1972) 20–25.

[50] G. 't Hooft and M. J. G. Veltman, *Regularization and Renormalization of Gauge Fields*, *Nucl. Phys.* **B44** (1972) 189–213.

[51] J. F. Ashmore, *A Method of Gauge Invariant Regularization*, *Lett. Nuovo Cim.* **4** (1972) 289–290.

[52] G. M. Cicuta and E. Montaldi, *Analytic renormalization via continuous space dimension*, *Nuovo Cim. Lett.* **4** (1972) 329–332.

[53] F. Bloch and A. Nordsieck, *Note on the Radiation Field of the electron*, *Phys. Rev.* **52** (1937) 54–59.

[54] T. Kinoshita, *Mass singularities of Feynman amplitudes*, *J. Math. Phys.* **3** (1962) 650–677.

[55] T. D. Lee and M. Nauenberg, *Degenerate Systems and Mass Singularities*, *Phys. Rev.* **133** (1964) B1549–B1562.

[56] E. Farhi, *A QCD Test for Jets*, *Phys. Rev. Lett.* **39** (1977) 1587–1588.

[57] A. De Rujula, J. R. Ellis, E. G. Floratos, and M. K. Gaillard, *QCD Predictions for Hadronic Final States in e+ e- Annihilation*, *Nucl. Phys.* **B138** (1978) 387.

[58] H. Georgi and M. Machacek, *A Simple QCD Prediction of Jet Structure in e+ e- Annihilation*, *Phys. Rev. Lett.* **39** (1977) 1237.

[59] C. L. Basham, L. S. Brown, S. D. Ellis, and S. T. Love, *Electron - Positron Annihilation Energy Pattern in Quantum Chromodynamics: Asymptotically Free Perturbation Theory*, *Phys. Rev.* **D17** (1978) 2298.

[60] C. L. Basham, L. S. Brown, S. D. Ellis, and S. T. Love, *Energy Correlations in electron - Positron Annihilation: Testing QCD*, *Phys. Rev. Lett.* **41** (1978) 1585.

[61] C. L. Basham, L. S. Brown, S. D. Ellis, and S. T. Love, *Energy Correlations in electron-Positron Annihilation in Quantum Chromodynamics: Asymptotically Free Perturbation Theory*, *Phys. Rev.* **D19** (1979) 2018.

[62] R. K. Ellis, D. A. Ross, and A. E. Terrano, *The Perturbative Calculation of Jet Structure in e+ e- Annihilation*, *Nucl. Phys.* **B178** (1981) 421.

[63] G. Sterman and S. Weinberg, *Jets from Quantum Chromodynamics*, *Phys. Rev. Lett.* **39** (1977) 1436.

[64] G. Hanson *et. al.*, *Evidence for Jet Structure in Hadron Production by e+ e- Annihilation*, *Phys. Rev. Lett.* **35** (1975) 1609–1612.

[65] **OPAL** Collaboration, *http://opal.web.cern.ch/Opal/events/opalpics.html*, .

[66] S. Catani, Y. L. Dokshitzer, M. H. Seymour, and B. R. Webber, *Longitudinally invariant K_t clustering algorithms for hadron hadron collisions*, *Nucl. Phys.* **B406** (1993) 187–224.

[67] S. D. Ellis and D. E. Soper, *Successive combination jet algorithm for hadron collisions*, *Phys. Rev.* **D48** (1993) 3160–3166, [hep-ph/9305266].

[68] **JADE** Collaboration, W. Bartel *et. al.*, *Experimental Studies on Multi-Jet Production in e+ e- Annihilation at PETRA Energies*, *Z. Phys.* **C33** (1986) 23.

[69] **JADE** Collaboration, S. Bethke *et. al.*, *Experimental Investigation of the Energy Dependence of the Strong Coupling Strength*, *Phys. Lett.* **B213** (1988) 235.

[70] S. Catani, Y. L. Dokshitzer, M. Olsson, G. Turnock, and B. R. Webber, *New clustering algorithm for multi - jet cross-sections in e+ e- annihilation*, *Phys. Lett.* **B269** (1991) 432–438.

[71] Y. L. Dokshitzer, G. D. Leder, S. Moretti, and B. R. Webber, *Better Jet Clustering Algorithms*, *JHEP* **08** (1997) 001, [hep-ph/9707323].

[72] M. Wobisch and T. Wengler, *Hadronization corrections to jet cross sections in deep-inelastic scattering*, hep-ph/9907280.

[73] M. H. Seymour, *Jet shapes in hadron collisions: Higher orders, resummation and hadronization*, *Nucl. Phys.* **B513** (1998) 269–300, [hep-ph/9707338].

[74] G. P. Salam and G. Soyez, *A practical Seedless Infrared-Safe Cone jet algorithm*, *JHEP* **05** (2007) 086, [arXiv:0704.0292].

[75] G. P. Salam, *Towards Jetography*, arXiv:0906.1833.

[76] M. Cacciari and G. P. Salam, *Dispelling the N^3 myth for the k_t jet-finder*, *Phys. Lett.* **B641** (2006) 57–61, [hep-ph/0512210].

[77] G. Salam, M. Cacciari, and G. Soyez, *http://www.lpthe.jussieu.fr/ salam/fastjet/*, .

[78] M. Cacciari, G. P. Salam, and G. Soyez, *The anti-k_t jet clustering algorithm*, *JHEP* **04** (2008) 063, [arXiv:0802.1189].

[79] G. Altarelli and G. Parisi, *Asymptotic Freedom in Parton Language*, *Nucl. Phys.* **B126** (1977) 298.

[80] Y. L. Dokshitzer, D. I. Dyakonov, and S. I. Troyan, *Hard processes in quantum chromodynamics*, *Physics Reports* **58** (1980), no. 5 269 – 395.

[81] S. Catani and M. H. Seymour, *The Dipole Formalism for the Calculation of QCD Jet Cross Sections at Next-to-Leading Order*, *Phys. Lett.* **B378** (1996) 287–301, [hep-ph/9602277].

[82] S. Frixione, Z. Kunszt, and A. Signer, *Three jet cross-sections to next-to-leading order*, *Nucl. Phys.* **B467** (1996) 399–442, [hep-ph/9512328].

[83] S. Frixione, *A General approach to jet cross-sections in QCD*, *Nucl. Phys.* **B507** (1997) 295–314, [hep-ph/9706545].

[84] G. Heinrich, *Sector Decomposition*, *Int. J. Mod. Phys.* **A23** (2008) 1457–1486, [arXiv:0803.4177].

[85] D. A. Kosower, *Antenna factorization of gauge-theory amplitudes*, *Phys. Rev.* **D57** (1998) 5410–5416, [hep-ph/9710213].

[86] J. M. Campbell, M. A. Cullen, and E. W. N. Glover, *Four jet event shapes in electron positron annihilation*, *Eur. Phys. J.* **C9** (1999) 245–265, [hep-ph/9809429].

[87] D. A. Kosower, *Antenna factorization in strongly-ordered limits*, *Phys. Rev.* **D71** (2005) 045016, [hep-ph/0311272].

[88] J. M. Campbell and R. K. Ellis, *An update on vector boson pair production at hadron colliders*, *Phys. Rev.* **D60** (1999) 113006, [hep-ph/9905386].

[89] J. M. Campbell and R. K. Ellis, *Radiative corrections to Z b anti-b production*, *Phys. Rev.* **D62** (2000) 114012, [hep-ph/0006304].

[90] Z. Nagy and Z. Trocsanyi, *Multi-jet cross sections in deep inelastic scattering at next-to-leading order*, *Phys. Rev. Lett.* **87** (2001) 082001, [hep-ph/0104315].

[91] T. Hahn and M. Perez-Victoria, *Automatized one-loop calculations in four and D dimensions*, *Comput. Phys. Commun.* **118** (1999) 153–165, [hep-ph/9807565].

[92] T. Binoth, J. P. Guillet, G. Heinrich, E. Pilon, and T. Reiter, *Golem95: a numerical program to calculate one-loop tensor integrals with up to six external legs*, *Comput. Phys. Commun.* **180** (2009) 2317–2330, [arXiv:0810.0992].

[93] W. T. Giele and G. Zanderighi, *On the Numerical Evaluation of One-Loop Amplitudes: The Gluonic Case*, *JHEP* **06** (2008) 038, [arXiv:0805.2152].

[94] C. F. Berger *et. al.*, *An Automated Implementation of On-Shell Methods for One-Loop Amplitudes*, *Phys. Rev.* **D78** (2008) 036003, [arXiv:0803.4180].

[95] A. van Hameren, C. G. Papadopoulos, and R. Pittau, *Automated one-loop calculations: a proof of concept*, *JHEP* **09** (2009) 106, [arXiv:0903.4665].

[96] G. Ossola, C. G. Papadopoulos, and R. Pittau, *CutTools: a program implementing the OPP reduction method to compute one-loop amplitudes*, *JHEP* **03** (2008) 042, [arXiv:0711.3596].

[97] G. Corcella *et. al.*, *HERWIG 6.5: an event generator for Hadron Emission Reactions With Interfering Gluons (including supersymmetric processes)*, *JHEP* **01** (2001) 010, [hep-ph/0011363].

[98] G. Corcella *et. al.*, *HERWIG 6.5 release note*, hep-ph/0210213.

[99] T. Sjostrand, S. Mrenna, and P. Z. Skands, *PYTHIA 6.4 Physics and Manual*, *JHEP* **05** (2006) 026, [hep-ph/0603175].

[100] T. Gleisberg *et. al.*, *Event generation with SHERPA 1.1*, *JHEP* **02** (2009) 007, [arXiv:0811.4622].

[101] S. Frixione and B. R. Webber, *Matching NLO QCD computations and parton shower simulations*, *JHEP* **06** (2002) 029, [hep-ph/0204244].

[102] R. P. Feynman, *Photon-hadron interactions*, . Reading 1972, 282p.

[103] J. D. Bjorken, *Asymptotic Sum Rules at Infinite Momentum*, *Phys. Rev.* **179** (1969) 1547–1553.

[104] V. N. Gribov and L. N. Lipatov, *Deep inelastic e p scattering in perturbation theory*, *Sov. J. Nucl. Phys.* **15** (1972) 438–450.

[105] L. N. Lipatov, *The parton model and perturbation theory*, *Sov. J. Nucl. Phys.* **20** (1975) 94–102.

[106] Y. L. Dokshitzer, *Calculation of the Structure Functions for Deep Inelastic Scattering and e+ e- Annihilation by Perturbation Theory in Quantum Chromodynamics*, *Sov. Phys. JETP* **46** (1977) 641–653.

[107] G. Curci, W. Furmanski, and R. Petronzio, *Evolution of Parton Densities Beyond Leading Order: The Nonsinglet Case*, *Nucl. Phys.* **B175** (1980) 27.

[108] W. Furmanski and R. Petronzio, *Singlet Parton Densities Beyond Leading Order*, *Phys. Lett.* **B97** (1980) 437.

[109] E. G. Floratos, C. Kounnas, and R. Lacaze, *Higher Order QCD Effects in Inclusive Annihilation and Deep Inelastic Scattering*, *Nucl. Phys.* **B192** (1981) 417.

[110] S. Moch, J. A. M. Vermaseren, and A. Vogt, *The three-loop splitting functions in QCD: The non-singlet case*, *Nucl. Phys.* **B688** (2004) 101–134, [hep-ph/0403192].

[111] A. Vogt, S. Moch, and J. A. M. Vermaseren, *The three-loop splitting functions in QCD: The singlet case*, *Nucl. Phys.* **B691** (2004) 129–181, [hep-ph/0404111].

[112] J. Pumplin *et. al.*, *New generation of parton distributions with uncertainties from global QCD analysis*, *JHEP* **07** (2002) 012, [hep-ph/0201195].

[113] A. D. Martin, R. G. Roberts, W. J. Stirling, and R. S. Thorne, *NNLO global parton analysis*, *Phys. Lett.* **B531** (2002) 216–224, [hep-ph/0201127].

[114] D. A. Kosower, *Evolution of parton distributions*, *Nucl. Phys.* **B506** (1997) 439–467, [hep-ph/9706213].

[115] P. G. Ratcliffe, *A matrix approach to numerical solution of the DGLAP evolution equations*, *Phys. Rev.* **D63** (2001) 116004, [hep-ph/0012376].

[116] **NNPDF** Collaboration, L. Del Debbio, S. Forte, J. I. Latorre, A. Piccione, and J. Rojo, *Neural network determination of parton distributions: the nonsinglet case*, *JHEP* **03** (2007) 039, [hep-ph/0701127].

[117] A. Cafarella, C. Coriano, and M. Guzzi, *Precision Studies of the NNLO DGLAP Evolution at the LHC with CANDIA*, *Comput. Phys. Commun.* **179** (2008) 665–684, [arXiv:0803.0462].

[118] G. P. Salam and J. Rojo, *A Higher Order Perturbative Parton Evolution Toolkit (HOPPET)*, *Comput. Phys. Commun.* **180** (2009) 120–156, [arXiv:0804.3755].

[119] J. C. Collins and D. E. Soper, *The Theorems of Perturbative QCD*, *Ann. Rev. Nucl. Part. Sci.* **37** (1987) 383–409.

[120] Y. I. Azimov, Y. L. Dokshitzer, V. A. Khoze, and S. I. Troyan, *Similarity of Parton and Hadron Spectra in QCD Jets*, *Z. Phys.* **C27** (1985) 65–72.

[121] X. Artru and G. Mennessier, *String model and multiproduction*, *Nucl. Phys.* **B70** (1974) 93–115.

[122] M. G. Bowler, *e+ e- Production of Heavy Quarks in the String Model*, *Zeit. Phys.* **C11** (1981) 169.

[123] B. Andersson, G. Gustafson, and B. Soderberg, *A General Model for Jet Fragmentation*, *Z. Phys.* **C20** (1983) 317.

[124] B. Andersson, G. Gustafson, and B. Soderberg, *A probability measure on parton and string states*, *Nucl. Phys.* **B264** (1986) 29.

[125] **TPC/Two Gamma** Collaboration, H. Aihara *et. al.*, *Tests of models for quark and gluon fragmentation in e^+e^- annihilation $\sqrt{s} = 29$ GeV*, *Z. Phys.* **C28** (1985) 31.

[126] R. D. Field and S. Wolfram, *A QCD Model for e+ e- Annihilation*, *Nucl. Phys.* **B213** (1983) 65.

[127] B. R. Webber, *A QCD Model for Jet Fragmentation Including Soft Gluon Interference*, *Nucl. Phys.* **B238** (1984) 492.

[128] T. D. Gottschalk, *A Realistic Model for e+ e- Annihilation Including Parton Bremsstrahlung Effects*, *Nucl. Phys.* **B214** (1983) 201.

[129] T. Sjostrand and M. van Zijl, *A Multiple Interaction Model for the Event Structure in Hadron Collisions*, *Phys. Rev.* **D36** (1987) 2019.

[130] J. M. Butterworth, J. R. Forshaw, and M. H. Seymour, *Multiparton interactions in photoproduction at HERA*, *Z. Phys.* **C72** (1996) 637–646, [hep-ph/9601371].

[131] T. Sjostrand and P. Z. Skands, *Transverse-momentum-ordered showers and interleaved multiple interactions*, *Eur. Phys. J.* **C39** (2005) 129–154, [hep-ph/0408302].

[132] M. Bahr, S. Gieseke, and M. H. Seymour, *Simulation of multiple partonic interactions in Herwig++*, *JHEP* **07** (2008) 076, [arXiv:0803.3633].

[133] R. Corke and T. Sjostrand, *Multiparton Interactions and Rescattering*, *JHEP* **01** (2010) 035, [arXiv:0911.1909].

[134] S. Alekhin *et. al.*, *HERA and the LHC - A workshop on the implications of HERA for LHC physics: Proceedings Part A*, hep-ph/0601012.

[135] F. W. Bopp, R. Engel, and J. Ranft, *Rapidity gaps and the PHOJET Monte Carlo*, hep-ph/9803437.

[136] T. Sjostrand *et. al.*, *High-energy physics event generation with PYTHIA 6.1*, *Comput. Phys. Commun.* **135** (2001) 238–259, [hep-ph/0010017].

[137] T. Sjostrand, L. Lonnblad, S. Mrenna, and P. Z. Skands, *Pythia 6.3 physics and manual*, hep-ph/0308153.

[138] M. Cacciari and G. P. Salam, *Pileup subtraction using jet areas*, *Phys. Lett.* **B 659** (2008) 119–126, [0707.1378].

[139] Atlas, *ATLAS detector and physics performance. Technical design report. Vol. 2*, . CERN-LHCC-99-15.

[140] **CMS** Collaboration, G. L. Bayatian *et. al.*, *CMS technical design report, volume II: Physics perfomance*, *J. Phys.* **G34** (2007) 995–1579.

[141] M. Cacciari, J. Rojo, G. P. Salam, and G. Soyez, *Quantifying the performance of jet definitions for kinematic reconstruction at the LHC*, *JHEP* **12** (2008) 032, [arXiv:0810.1304].

[142] **CDF** Collaboration, D. E. Acosta *et. al.*, *Measurement of the $t\bar{t}$ production cross section in $p\bar{p}$ collisions at $\sqrt{s} = 1.96$ TeV using dilepton events*, *Phys. Rev. Lett.* **93** (2004) 142001, [hep-ex/0404036].

[143] **CDF** Collaboration, D. E. Acosta *et. al.*, *Measurement of the cross section for $t\bar{t}$ production in $p\bar{p}$ collisions using the kinematics of lepton + jets events*, *Phys. Rev.* **D72** (2005) 052003, [hep-ex/0504053].

[144] **CDF** Collaboration, L. Cerrito, *Measurement of the t anti-t production cross section in $p\bar{p}$ collisions at $\sqrt{s} = 1.96$-TeV using multijet events*, hep-ex/0510002.

[145] **CDF** Collaboration, T. Aaltonen *et. al.*, *First simultaneous measurement of the top quark mass in the lepton + jets and dilepton channels at CDF*, *Phys. Rev.* **D79** (2009) 092005, [arXiv:0809.4808].

[146] M. H. Seymour, *Searches for new particles using cone and cluster jet algorithms: A Comparative study*, *Z. Phys.* **C62** (1994) 127–138.

[147] J. M. Butterworth, B. E. Cox, and J. R. Forshaw, *WW scattering at the CERN LHC*, *Phys. Rev.* **D65** (2002) 096014, [hep-ph/0201098].

[148] J. M. Butterworth, J. R. Ellis, and A. R. Raklev, *Reconstructing sparticle mass spectra using hadronic decays*, *JHEP* **0705:033** (2007) [hep-ph/0702150].

[149] J. Thaler and L.-T. Wang, *Strategies to Identify Boosted Tops*, *JHEP* **07** (2008) 092, [arXiv:0806.0023].

[150] D. Graudenz, M. Spira, and P. M. Zerwas, *QCD corrections to Higgs boson production at proton proton colliders*, *Phys. Rev. Lett.* **70** (1993) 1372–1375.

[151] M. Spira, A. Djouadi, D. Graudenz, and P. M. Zerwas, *Higgs boson production at the LHC*, *Nucl. Phys.* **B453** (1995) 17–82, [hep-ph/9504378].

[152] T. Han, G. Valencia, and S. Willenbrock, *Structure function approach to vector boson scattering in p p collisions*, *Phys. Rev. Lett.* **69** (1992) 3274–3277, [hep-ph/9206246].

[153] M. Spira, *QCD effects in Higgs physics*, *Fortsch. Phys.* **46** (1998) 203–284, [hep-ph/9705337].

[154] T. Han and S. Willenbrock, *QCD correction to the p p → W H and Z H total cross-sections*, *Phys. Lett.* **B273** (1991) 167–172.

[155] W. Beenakker *et. al.*, *Higgs radiation off top quarks at the Tevatron and the LHC*, *Phys. Rev. Lett.* **87** (2001) 201805, [hep-ph/0107081].

[156] W. Beenakker *et. al.*, *NLO QCD corrections to t anti-t H production in hadron collisions. ((U))*, *Nucl. Phys.* **B653** (2003) 151–203, [hep-ph/0211352].

[157] R. V. Harlander and W. B. Kilgore, *Next-to-next-to-leading order Higgs production at hadron colliders*, *Phys. Rev. Lett.* **88** (2002) 201801, [hep-ph/0201206].

[158] C. Anastasiou and K. Melnikov, *Higgs boson production at hadron colliders in NNLO QCD*, *Nucl. Phys.* **B646** (2002) 220–256, [hep-ph/0207004].

[159] V. Ravindran, J. Smith, and W. L. van Neerven, *NNLO corrections to the total cross section for Higgs boson production in hadron hadron collisions*, *Nucl. Phys.* **B665** (2003) 325–366, [hep-ph/0302135].

[160] A. Djouadi and P. Gambino, *Leading electroweak correction to Higgs boson production at proton colliders*, *Phys. Rev. Lett.* **73** (1994) 2528–2531, [hep-ph/9406432].

[161] U. Aglietti, R. Bonciani, G. Degrassi, and A. Vicini, *Two-loop light fermion contribution to Higgs production and decays*, *Phys. Lett.* **B595** (2004) 432–441, [hep-ph/0404071].

[162] G. Degrassi and F. Maltoni, *Two-loop electroweak corrections to Higgs production at hadron colliders*, *Phys. Lett.* **B600** (2004) 255–260, [hep-ph/0407249].

[163] S. Actis, G. Passarino, C. Sturm, and S. Uccirati, *NLO Electroweak Corrections to Higgs Boson Production at Hadron Colliders*, *Phys. Lett.* **B670** (2008) 12–17, [arXiv:0809.1301].

[164] R. Hamberg, W. L. van Neerven, and T. Matsuura, *A Complete calculation of the order $\alpha - s^2$ correction to the Drell-Yan K factor*, *Nucl. Phys.* **B359** (1991) 343–405.

[165] O. Brein, A. Djouadi, and R. Harlander, *NNLO QCD corrections to the Higgs-strahlung processes at hadron colliders*, *Phys. Lett.* **B579** (2004) 149–156, [hep-ph/0307206].

[166] M. L. Ciccolini, S. Dittmaier, and M. Kramer, *Electroweak radiative corrections to associated W H and Z H production at hadron colliders*, *Phys. Rev.* **D68** (2003) 073003, [hep-ph/0306234].

[167] M. Grazzini, *NNLO predictions for the Higgs boson signal in the $H \to WW \to l\nu l\nu$ and $H \to ZZ \to 4l$ decay channels*, *JHEP* **02** (2008) 043, [arXiv:0801.3232].

[168] C. Anastasiou, K. Melnikov, and F. Petriello, *Fully differential Higgs boson production and the di- photon signal through next-to-next-to-leading order*, *Nucl. Phys.* **B724** (2005) 197–246, [hep-ph/0501130].

[169] **The ATLAS Collaboration** Collaboration, G. Aad *et. al.*, *Expected Performance of the ATLAS Experiment - Detector, Trigger and Physics*, arXiv:0901.0512.

[170] **GEANT4** Collaboration, S. Agostinelli *et. al.*, *GEANT4: A simulation toolkit*, *Nucl. Instrum. Meth.* **A506** (2003) 250–303.

[171] R. Lafaye, T. Plehn, M. Rauch, D. Zerwas, and M. Duhrssen, *Measuring the Higgs Sector*, *JHEP* **08** (2009) 009, [arXiv:0904.3866].

[172] *www-hep.uta.edu/∼brandta/ATLAS/AFP/JulyAnswers.pdf*, .

[173] J. M. Butterworth, A. R. Davison, M. Rubin, and G. P. Salam, *Jet substructure as a new Higgs search channel at the LHC*, *Phys. Rev. Lett.* **100** (2008) 242001, [arXiv:0802.2470].

[174] T. Plehn, G. P. Salam, and M. Spannowsky, *Fat Jets for a Light Higgs*, arXiv:0910.5472.

[175] R. K. Ellis, I. Hinchliffe, M. Soldate, and J. J. van der Bij, *Higgs Decay to tau+ tau-: A Possible Signature of Intermediate Mass Higgs Bosons at the SSC*, *Nucl. Phys.* **B297** (1988) 221.

[176] M. Dasgupta, L. Magnea, and G. P. Salam, *Non-perturbative QCD effects in jets at hadron colliders*, *JHEP* **02** (2008) 055, [arXiv:0712.3014].

[177] *Atlas sensitivity to the standard model higgs in the hw and hz channels at high transverse momenta*, Tech. Rep. ATL-PHYS-PUB-2009-088. ATL-COM-PHYS-2009-345, CERN, Geneva, Aug, 2009.

[178] L. G. Almeida, S. J. Lee, G. Perez, I. Sung, and J. Virzi, *Top Jets at the LHC*, *Phys. Rev.* **D79** (2009) 074012, [arXiv:0810.0934].

[179] D. E. Kaplan, K. Rehermann, M. D. Schwartz, and B. Tweedie, *Top Tagging: A Method for Identifying Boosted Hadronically Decaying Top Quarks*, *Phys. Rev. Lett.* **101** (2008) 142001, [arXiv:0806.0848].

[180] W. Skiba and D. Tucker-Smith, *Using jet mass to discover vector quarks at the LHC*, *Phys. Rev.* **D75** (2007) 115010, [hep-ph/0701247].

[181] B. Holdom, *t' at the LHC: The physics of discovery*, *JHEP* **03** (2007) 063, [hep-ph/0702037].

[182] J. M. Butterworth, J. R. Ellis, A. R. Raklev, and G. P. Salam, *Discovering baryon-number violating neutralino decays at the LHC*, *Phys. Rev. Lett.* **103** (2009) 241803, [arXiv:0906.0728].

[183] U. Baur and L. H. Orr, *Searching for $t\bar{t}$ Resonances at the Large Hadron Collider*, *Phys. Rev.* **D77** (2008) 114001, [arXiv:0803.1160].

[184] P. Fileviez Perez, R. Gavin, T. McElmurry, and F. Petriello, *Grand Unification and Light Color-Octet Scalars at the LHC*, *Phys. Rev.* **D78** (2008) 115017, [arXiv:0809.2106].

[185] Y. Bai and Z. Han, *Top-antitop and Top-top Resonances in the Dilepton Channel at the CERN LHC*, *JHEP* **04** (2009) 056, [arXiv:0809.4487].

[186] S. D. Ellis, C. K. Vermilion, and J. R. Walsh, *Recombination Algorithms and Jet Substructure: Pruning as a Tool for Heavy Particle Searches*, arXiv:0912.0033.

[187] G. D. Kribs, A. Martin, T. S. Roy, and M. Spannowsky, *Discovering the Higgs Boson in New Physics Events using Jet Substructure*, arXiv:0912.4731.

[188] D. Krohn, J. Thaler, and L.-T. Wang, *Jet Trimming*, arXiv:0912.1342.

[189] S. Catani, G. Turnock, B. R. Webber, and L. Trentadue, *Thrust distribution in e+ e- annihilation*, *Phys. Lett.* **B263** (1991) 491–497.

[190] S. Catani, Y. L. Dokshitzer, F. Fiorani, and B. R. Webber, *Average number of jets in e+ e- annihilation*, *Nucl. Phys.* **B377** (1992) 445–460.

[191] S. Catani, L. Trentadue, G. Turnock, and B. R. Webber, *Resummation of large logarithms in e+ e- event shape distributions*, *Nucl. Phys.* **B407** (1993) 3–42.

[192] S. Catani, G. Turnock, and B. R. Webber, *Jet broadening measures in e^+e^- annihilation*, *Phys. Lett.* **B295** (1992) 269–276.

[193] S. Catani and B. R. Webber, *Resummed C-parameter distribution in e+ e- annihilation*, *Phys. Lett.* **B427** (1998) 377–384, [hep-ph/9801350].

[194] Y. L. Dokshitzer, A. Lucenti, G. Marchesini, and G. P. Salam, *On the QCD analysis of jet broadening*, *JHEP* **01** (1998) 011, [hep-ph/9801324].

[195] V. Antonelli, M. Dasgupta, and G. P. Salam, *Resummation of thrust distributions in DIS*, *JHEP* **02** (2000) 001, [hep-ph/9912488].

[196] S. J. Burby, *The four-jet rate in e+ e- annihilation*, *Phys. Lett.* **B453** (1999) 54–58, [hep-ph/9902305].

[197] S. J. Burby and E. W. N. Glover, *Resumming the Light Hemisphere Mass and Narrow Jet Broadening distributions in e^+e^- annihilation*, *JHEP* **04** (2001) 029, [hep-ph/0101226].

[198] A. Banfi, G. Marchesini, Y. L. Dokshitzer, and G. Zanderighi, *QCD analysis of near-to-planar 3-jet events*, *JHEP* **07** (2000) 002, [hep-ph/0004027].

[199] M. Dasgupta and G. P. Salam, *Resummation of non-global QCD observables*, *Phys. Lett.* **B512** (2001) 323–330, [hep-ph/0104277].

[200] A. Banfi and M. Dasgupta, *Dijet rates with symmetric E(t) cuts*, *JHEP* **01** (2004) 027, [hep-ph/0312108].

[201] A. Banfi, G. P. Salam, and G. Zanderighi, *Resummed event shapes at hadron - hadron colliders*, *JHEP* **08** (2004) 062, [hep-ph/0407287].

[202] A. Banfi, G. P. Salam, and G. Zanderighi, *Principles of general final-state resummation and automated implementation*, *JHEP* **03** (2005) 073, [hep-ph/0407286].

[203] T. Becher and M. D. Schwartz, *A Precise determination of α_s from LEP thrust data using effective field theory*, *JHEP* **07** (2008) 034, [arXiv:0803.0342].

[204] G. Dissertori *et. al.*, *Determination of the strong coupling constant using matched NNLO+NLLA predictions for hadronic event shapes in e+e- annihilations*, *JHEP* **08** (2009) 036, [arXiv:0906.3436].

[205] M. Dasgupta and G. P. Salam, *Accounting for coherence in interjet E(t) flow: A case study*, *JHEP* **03** (2002) 017, [hep-ph/0203009].

[206] Y. Delenda, R. Appleby, M. Dasgupta, and A. Banfi, *On QCD resummation with k(t) clustering*, *JHEP* **12** (2006) 044, [hep-ph/0610242].

[207] R. B. Appleby and M. H. Seymour, *Non-global logarithms in inter-jet energy flow with kt clustering requirement*, *JHEP* **12** (2002) 063, [hep-ph/0211426].

[208] A. Banfi, G. Marchesini, and G. Smye, *Away-from-jet energy flow*, *JHEP* **08** (2002) 006, [hep-ph/0206076].

[209] Y. Hatta and T. Ueda, *Jet energy flow at the LHC*, *Phys. Rev.* **D80** (2009) 074018, [arXiv:0909.0056].

[210] H. Weigert, *Non-global jet evolution at finite N(c)*, *Nucl. Phys.* **B685** (2004) 321–350, [hep-ph/0312050].

[211] J. R. Forshaw, A. Kyrieleis, and M. H. Seymour, *Super-leading logarithms in non-global observables in QCD*, *JHEP* **08** (2006) 059, [hep-ph/0604094].

[212] F. Fiorani, G. Marchesini, and L. Reina, *Soft gluon factorization and multi-gluon amplitude*, *Nucl. Phys.* **B309** (1988) 439.

[213] Y. L. Dokshitzer, G. Marchesini, and G. Oriani, *Measuring color flows in hard processes: Beyond leading order*, *Nucl. Phys.* **B387** (1992) 675–714.

[214] Y. Dokshitzer, V. Khoze, A. Mueller, and S. Troyan, *Basics of Perturbative QCD*. Editions Frontières, Gif-sur-Yvette, France, 1991.

[215] C. Buttar *et. al.*, *Standard Model Handles and Candles Working Group: Tools and Jets Summary Report*, arXiv:0803.0678.

[216] M. Cacciari, G. P. Salam, and G. Soyez, *The catchment area of jets*, *JHEP* **0804:005** (2008) [0802.1188].

[217] M. Cacciari, G. P. Salam, and S. Sapeta, *On the characterisation of the underlying event*, arXiv:0912.4926.

[218] M. Rubin, *Light Higgs searches at the LHC using jet substructure*, arXiv:0905.2124.

[219] G. P. Korchemsky and G. Sterman, *Nonperturbative corrections in resummed cross-sections*, *Nucl. Phys.* **B437** (1995) 415–432, [hep-ph/9411211].

[220] M. Dasgupta and Y. Delenda, *On the universality of hadronisation corrections to QCD jets*, *JHEP* **07** (2009) 004, [arXiv:0903.2187].

[221] I. Hinchliffe, F. E. Paige, M. D. Shapiro, J. Soderqvist, and W. Yao, *Precision SUSY measurements at CERN LHC*, *Phys. Rev.* **D55** (1997) 5520–5540, [hep-ph/9610544].

[222] **CMS** Collaboration, S. Abdullin *et. al.*, *Discovery potential for supersymmetry in CMS*, *J. Phys.* **G28** (2002) 469, [hep-ph/9806366].

[223] M. Spiropulu, *SUSY@LHC.CERN.CH*, arXiv:0801.0318.

[224] **ATLAS** Collaboration, T. Yamazaki, *Data-driven Estimation of SM Backgrounds for SUSY Searches at the LHC*, arXiv:0805.3883.

[225] **ATLAS** Collaboration, S. Yamamoto, *Strategy for early SUSY searches at ATLAS*, arXiv:0710.3953.

[226] M. L. Mangano, *Standard Model backgrounds to supersymmetry searches*, *Eur. Phys. J.* **C59** (2009) 373–387, [arXiv:0809.1567].

[227] **NLO Multileg Working Group** Collaboration, Z. Bern *et. al.*, *The NLO multileg working group: Summary report*, arXiv:0803.0494.

[228] **SM and NLO Multileg Working Group** Collaboration, J. R. Andersen *et. al.*, *The SM and NLO multileg working group: Summary report*, arXiv:1003.1241.

[229] C. W. Bauer and B. O. Lange, *Scale setting and resummation of logarithms in $pp \to V$ + jets*, arXiv:0905.4739.

[230] A. Denner, S. Dittmaier, T. Kasprzik, and A. Muck, *Electroweak corrections to W + jet hadroproduction including leptonic W-boson decays*, *JHEP* **08** (2009) 075, [arXiv:0906.1656].

[231] A. Banfi, G. P. Salam, and G. Zanderighi, *Accurate QCD predictions for heavy-quark jets at the Tevatron and LHC*, *JHEP* **07** (2007) 026, [arXiv:0704.2999].

[232] T. Binoth, T. Gleisberg, S. Karg, N. Kauer, and G. Sanguinetti, *NLO QCD corrections to ZZ+jet production at hadron colliders*, *Phys. Lett.* **B683** (2010) 154–159, [arXiv:0911.3181].

[233] P. Ciafaloni and D. Comelli, *The importance of weak bosons emission at LHC*, *JHEP* **09** (2006) 055, [hep-ph/0604070].

[234] E. W. N. Glover and J. Pires, *Antenna subtraction for gluon scattering at NNLO*, arXiv:1003.2824.

[235] K. Melnikov and F. Petriello, *Electroweak gauge boson production at hadron colliders through O(alpha(s)**2)*, *Phys. Rev.* **D74** (2006) 114017, [hep-ph/0609070].

[236] S. Catani, L. Cieri, G. Ferrera, D. de Florian, and M. Grazzini, *Vector boson production at hadron colliders: a fully exclusive QCD calculation at NNLO*, *Phys. Rev. Lett.* **103** (2009) 082001, [arXiv:0903.2120].

[237] A. Banfi, G. P. Salam, and G. Zanderighi, *Semi-numerical resummation of event shapes*, *JHEP* **01** (2002) 018, [hep-ph/0112156].

[238] Z. Nagy, *Next-to-leading order calculation of three jet observables in hadron hadron collision*, *Phys. Rev.* **D68** (2003) 094002, [hep-ph/0307268].

[239] A. Banfi, G. P. Salam, and G. Zanderighi, *Infrared safe definition of jet flavor*, *Eur. Phys. J.* **C47** (2006) 113–124, [hep-ph/0601139].

[240] S. Hoeche, F. Krauss, S. Schumann, and F. Siegert, *QCD matrix elements and truncated showers*, *JHEP* **05** (2009) 053, [arXiv:0903.1219].

[241] S. Frixione, *Isolated photons in perturbative QCD*, *Phys. Lett.* **B429** (1998) 369–374, [hep-ph/9801442].

[242] S. Catani and M. Grazzini, *An NNLO subtraction formalism in hadron collisions and its application to Higgs boson production at the LHC*, *Phys. Rev. Lett.* **98** (2007) 222002, [hep-ph/0703012].

[243] J. M. Campbell, R. K. Ellis, and D. L. Rainwater, *Next-to-leading order QCD predictions for W + 2jet and Z + 2jet production at the CERN LHC*, *Phys. Rev.* **D68** (2003) 094021, [hep-ph/0308195].

[244] C. F. Berger *et. al.*, *Next-to-Leading Order QCD Predictions for Z,gamma* +3-Jet Distributions at the Tevatron*, arXiv:1004.1659.

[245] M. Klasen and G. Kramer, *Dijet cross-sections at o (alpha alpha-s**2) in photon - proton collisions*, *Phys. Lett.* **B366** (1996) 385–393, [hep-ph/9508337].

[246] S. Frixione and G. Ridolfi, *Jet photoproduction at HERA*, *Nucl. Phys.* **B507** (1997) 315–333, [hep-ph/9707345].

[247] **ZEUS** Collaboration, S. Chekanov *et. al.*, *Dijet production in neutral current deep inelastic scattering at HERA*, *Eur. Phys. J.* **C23** (2002) 13–27, [hep-ex/0109029].

[248] **H1** Collaboration, A. Aktas *et. al.*, *Inclusive dijet production at low Bjorken-x in deep inelastic scattering*, *Eur. Phys. J.* **C33** (2004) 477–493, [hep-ex/0310019].

[249] S. Catani, F. Krauss, R. Kuhn, and B. R. Webber, *QCD Matrix Elements + Parton Showers*, *JHEP* **11** (2001) 063, [hep-ph/0109231].

[250] J. Alwall *et. al.*, *Comparative study of various algorithms for the merging of parton showers and matrix elements in hadronic collisions*, *Eur. Phys. J.* **C53** (2008) 473–500, [arXiv:0706.2569].

[251] N. Lavesson and L. Lonnblad, *Extending CKKW-merging to One-Loop Matrix Elements*, *JHEP* **12** (2008) 070, [arXiv:0811.2912].

[252] R. Keith Ellis, K. Melnikov, and G. Zanderighi, *W+3 jet production at the Tevatron*, *Phys. Rev.* **D80** (2009) 094002, [arXiv:0906.1445].

[253] C. F. Berger *et. al.*, *Next-to-Leading Order QCD Predictions for W+3-Jet Distributions at Hadron Colliders*, *Phys. Rev.* **D80** (2009) 074036, [arXiv:0907.1984].

[254] G. Bevilacqua, M. Czakon, C. G. Papadopoulos, and M. Worek, *Dominant QCD Backgrounds in Higgs Boson Analyses at the LHC: A Study of $pp \to t\bar{t}$ + 2 jets at Next-To-Leading Order*, *Phys. Rev. Lett.* **104** (2010) 162002, [arXiv:1002.4009].

[255] M. Beneke, *Renormalons*, *Phys. Rept.* **317** (1999) 1–142, [hep-ph/9807443].